IDENTIFICATION OF EPITHELIAL OVARIAN TUMOR SPECIFIC APTAMERS THAT BIND AND INTERNALIZE INTO TARGET CELLS

by

Gregory Benedetto

A dissertation submitted to the faculty of
The University of North Carolina at Charlotte
in partial fulfillment of the requirements
for the degree of Doctor of Philosophy in
Biology

Charlotte

2015

Approved by:

_____
Dr. Christine Richardson

_____
Dr. Daniel Nelson

_____
Dr. Laura Schrum

_____
Dr. Didier Dreau

_____
Dr. Anthony Fodor

ABSTRACT

GREGORY BENEDETTO: Tumor specific aptamer directed nanoparticles increase the efficacy of the front line chemotherapy Paclitaxel in epithelial ovarian cancer (Under the direction of DR. CHRISTINE RICHARDSON)

New clinical tools that aid in the early diagnosis of ovarian malignancies will significantly help reduce mortality and improve current long-term survival rates. The objective of the work presented here was to identify ovarian tumor specific single stranded DNA probes termed aptamers that bind to cell surface structures with high affinity and specificity. First I identified aptamers using a random screening protocol known as Cell-SELEX that bind and internalize to target cells. All aptamers identified demonstrate unique binding kinetics and internalized by the endocytic pathway. Next I assessed the internalization kinetics of identified aptamers when used to label the surface of polymeric organic nanoparticles. I was able to demonstrate that the high specificity exhibited by aptamers promotes localization and uptake of tethered nanoparticles by specific cell populations. Finally a preliminary pilot study looking at the *in vivo* stability of aptamers and their ability to promote retention and honing of nanoparticles at tumors was conducted. The experiments described here demonstrate the effective combinatorial use of aptamer and nanoparticle technologies for the direct targeting of tumor cell populations.

DEDICATION

This work is dedicated to my mother Rita Benedetto. Thank you for all your support and love throughout the years. You are the strongest person I know. To my entire family old and new thank you for the support that has made this journey possible.

ACKNOWLEDGEMENTS

I want to express my sincerest and deepest gratitude to my advisor Dr. Christine Richardson for her continuous support and help. Thank you for your continuous dedication to ensure my success on multiple levels in academia and for helping me develop my research skills. I am very thankful for all of her guidance which enabled the development and ultimate fruition of this project.

I am also grateful to my committee members Dr. Laura Schrum, Dr. Daniel Nelson, Dr. Didier Dreau, and Dr. Anthony Fodor for their support and feedback that helped me in my research. I appreciate the time and energy they put in to help me achieve my degree.

I would like to thank our past research technician Mina Masrorpour for all the laboratory training and her willingness to provide me with technical assistance and advice. Dr. Bhawana Bariar who began this journey with me was and is a constant pillar of support and encouragement. The many members of the Richardson lab: Noelle Cornelio, Deborah Nwafor, Peter Wasserman, Warren Endclave, and Tien Troung for their assistance and support in the laboratory. I would like to thank Dr. Eric Hastie and Carol Greer Vestal for helping with statistical analysis and the constant evolution of the project. Dr. Didier Dreau and David Gray for their expertise and training regarding confocal microscopy and flow cytometry. Additionally I would like to thank Dr. Kenneth Pillar for his endless advice and wisdom particularly in trouble shooting the TOPO cloning experiments.

The collaboration with the Ogle laboratory in the Chemistry department at UNC-Charlotte was instrumental to the success of present and future works. Thank you for

providing the necessary nanoparticles and helping to develop the *in vivo* experimentation. Dr. Cory Brouwer of the Bioinformatics department who made the Next Generation sequencing possible as well as Dr. Wie Song for his analysis of the sequencing data. Very special thanks to Timm Hamp whose expertise in sequencing made him instrumental in the success of this project.

Lastly, I would like to thank all the friends and colleagues that have enhanced my own experience at UNC-Charlotte, particularly Michelle Pass, Taghi and Zahra Mostafavi for helping with the ovarian cell lines and primary tumor cells, and the entire Biology office staff who is always willing to accommodate the students' needs.

TABLE OF CONTENTS

LIST OF TABLES

LIST OF FIGURES

LIST OF ABBREVIATIONS

EOC	epithelial ovarian cancer
HOSE	human ovarian surface epitheial
PEG	polyethylene glycol
NPs	nanoparticles
PLGA	poly-lactic-glycolic acid
ssDNA	single stranded DNA
dsDNA	double stranded DNA
MDR	multi-drug resistance
EPR	enhance permeability and retention
ICG	indocyanine green
Ptx	Paclitaxel
EPR	enhanced permeability and retention
NIR	near infrared
ASO	antisense oligonucleotide
AMD	age-related macular degeneration
NGS	next generation sequencing
AMD	age-related macular degeneration

CHAPTER 1: INTRODUCTION

1.1 Epithelial Ovarian Cancer

Recent statistics project a total of 1,658,370 new cancer cases and 589,430 cancer deaths to occur in the United States in 2015 [1]. The majority of primary solid tumors are treated by invasive surgery to remove accessible malignant tissue, followed by adjuvant nonselective chemotherapy and/or radiation therapy with high dose-limiting toxicities [2, 3]. Epithelial ovarian cancer (EOC) is one of the most lethal gynecological malignancies in the United States affecting woman today. A woman's chance of being diagnosed with invasive ovarian cancer in their lifetime is 1 in 72 [4]. As the fifth most common cause of cancer-related deaths in American women this disease is responsible for an estimated 14,000 deaths with approximately 22,000 new cases diagnosed each year and over 250,000 cases worldwide [4, 5].

Due to the asymptomatic nature of early stages in disease progression, stage I diagnosis is rare. Localized stage I EOC has a 92% 5-year mean survival rate but is only diagnosed in 15% of new cases [4, 6]. More problematic is that early symptoms are similar to common ailments such as gastrointestinal inflammation and diagnosis often requires invasive pelvic or transvaginal ultrasound [7]. The majority of diagnosed EOCs occur at stage II or later where there are fewer treatment options for patients and poor long-term prognosis with a 5-year mean survival rate of 44%. The relative survival rate decreases to 27% when the disease is diagnosed at stage III which constitutes almost 62%

of all new cases each year [7]. Moreover, the recurrence rate is high in woman diagnosed with EOC even after surgical debulking of abnormal tissue and adjuvant chemotherapy. Recurrence is often linked with chemoresistance making treatment difficult. The progression of the disease to carcinosis is common preventing further help from invasive surgeries [8].

Of the three most common tissue type progenitors (sex chord <10%, germ line 5%, and epithelial), epithelial derived malignancies of the female reproductive tract constitute 85% of all new ovarian related cases diagnosed each year [9]. There is a need to develop more sensitive diagnostic tools to identify early stage EOC. In addition it is important to develop more aggressive and targeted primary treatment protocols to combat late stage ovarian malignancies.

1.2 Epithelial Ovarian Cancer Subtypes and Diagnosis

The origin of tumors is difficult to understand since the physical development of cyst-like structures within the ovary is uncharacteristic of normal epithelial ovarian tissue [10]. Additionally, EOC neoplasms resemble cancers of the peritoneal and fallopian tube with evidence suggesting that the tissue of origin could be a common embryonic precursor from the distal tubal fimbria [3, 10, 11]. Ovarian tumors often present with chromosomal aberrations that have been detected by conventional comparative genomic hybridization (CGH) showing aneuploidy and tetraploidy genomes. The most prevalent sites of chromosomal gain seen in human tumor samples have been found to be located within 1q, 3q, 8q, 11q, 12p, 17q and 20q, with common DNA amplification at 3q, 7q, 8q, 12p, 17q, 19q, and 20 q [12-14]. Frequent sites of copy number decreases were seen within 4q, 5q, 6q, 9q, 12q, 13q, 16q, 17q, and 22q across a panel of 25 human EOC

samples [13]. Data show that aberrations are linked to sites that code for putative oncogenes and tumor suppressor genes that are dysregulated contributing to the pathogenesis of ovarian malignancies [15]. Candidate oncogenes that are over-expressed in ovarian cancers include PIK3CA (3q26.3), c-Myc (8q24), PAK1 (11q), K-ras (12p), p16, and STK15 (20q), PTEN, and ARID1A [12, 16-19].

Epithelial ovarian cancers are classified by histopathological grade determined by invasiveness and progression (I, II, and III). Additionally they are identified by morphologically determined subtypes. The most common of these are serous (~75% of EOC cases), endometrioid, and mucinous while more rare subtypes include clear cell, transitional cell, squamous cell, mixed epithelial, and undifferentiated epithelial [3, 9]. Serous derived tumors originate from the lining of the fallopian tube. Histologic markers identify serous epithelial by concentric rings of calcification known as psammoma bodies [20, 21]. Serous EOCs are commonly divided into a two-tiered system described as low-grade and high-grade serous EOC [20]. Somatic genetic aberrations are often associated with subtype specific neoplasms. High-grade (II-III) serous tumors display defects in BRCA1/2 and p53 signaling pathways leading to aberrant DNA repair with genetic aberrations in PIK3CA, K-ras, and p16 [22, 23]. In a study done looking at paraffin embedded micro-dissected tissue of 47 ovarian epithelial tumors of high-grade serous carcinomas—chromosomal analysis by CGH showed more than twice as many chromosomal imbalances compared to low-grade serous carcinomas [16]. Low-grade serous neoplasms often present exclusively with K-ras or BRAF mutations and are of low malignant potential (LMP) [24]. Data did suggest that serous LMP tumors compared to an invasive carcinoma carry unique genetic aberrations which indicate that pre-existing

LMPs seldom progress to an invasive carcinoma [16]. Thus LMP and high-grade serous EOCs could originate from a common progenitor but undergo unique translational pathways promoting differentiation.

Mucinous tumors are usually large with a median diameter of 18 to 20 cm and tend to remain confined to the ovaries [25]. Mucinous tumors are morphologically similar to intestinal or endocervical epithelium [21, 26]. Primary ovarian mucinous tumors can be difficult to distinguish from metastatic mucinous tumors from the colon or rectum as well as the appendix, cervix or pancreas [21]. In a study done in 2003 looking at 104 different EOC tumors, they found a high incidence of K-ras mutations within mucinous derived EOC tumors (>50%) [27]. Endometrioid and some clear cell carcinoma (morphologically clear) tumors are hypothesized to arise from the foci of endometriosis [21]. Both are associated with slightly better survival when compared to serous adenocarcinoma regardless of disease stage [28]. Both clear cell and endometrioid tumors frequently display loss of PTEN or mismatch repair gene functions [17]. Additionally, clear cell related tumors present with mutations in ARID1A a component of the SWI-SNF chromatin remodeling complex [18] and PIK3CA [29]. Poor prognosis is associated with clear cell type EOCs due to an increased risk of venous thromboembolism and platinum-taxane resistance [30]. Transitional cell tumors (Branner's tumor) resemble transitional epithelium of the bladder and are often benign [21]. Histology shows that neoplasms present with nests of transitional-type epithelial cells characterized by longitudinal nuclear grooves located in fibrous stroma [21]. While many altered oncogenic proteins can exist within these subtypes there is not always a clear correlation between genetic lesions and tumor diagnosis. Histochemical analysis on

47 ovarian carcinomas showed that there is overexpression or amplification of c-Myc and Cyclin D1 gene products in serous, endometrioid, mucinous, and clear cell EOC but not necessarily correlated with a histologic subtype [31].

Ovarian cancer serum proteomic profiling and array-CGH have generated a large number of potential tumor biomarkers including CA-125, SMRP and WFDC2 (HE4) proteins that can be instrumental in diagnosis [5, 32, 33]. Additionally an increased CD44+ and CK18+ stem cell load correlates with a high risk of recurrence in EOC cases [8]. A widely accepted assessment to differentiate between a malignancy and a benign abdominal mass is the Risk of Malignancy Index (RMI) developed in 1990 [34]. The criteria used include a woman's age, ultrasound score, menopausal status, a clinical impression score, and a serum CA-125 count. The Risk of Malignancy Algorithm (RMA) improved upon RMI by including an additional EOC related biomarker (HE4) [35], and the OVA1 blood test includes a panel of five biomarkers which include CA125 and HE4 as well as transferrin, prealbumin, and β2 microglobulin [36]. Comprehensive serum studies evaluating the effectiveness of RMI, ROMA, and OVA1 blood tests to properly distinguish between a malignant and benign mass have given conflicting results [5, 26]. One suggested that a more stringent nine biomarker assessment can increase positive diagnosis by over 25% [26]. It is important to note that the major limitation of algorithm based diagnosis is that they only infer information about an existing condition and fail to promote early detection. All three methods are used as preoperative risk assessments to facilitate triage of women to primary care providers but do little to diagnose early stage EOC. Ovarian tumorigenesis is aggressive and often asymptomatic; there is substantial evidence within the clinical field that calls for more sensitive

diagnostic tools to aid in the early detection of this disease and development of more effective targeted drug therapies.

1.3 Epithelial Ovarian Cancer Treatment

Treatment options offered to an individual patient are determined by multiple factors including subtype, stage and location, as well as the patient's age and history of prior disease. The majority of primary solid tumors are treated by invasive surgery to remove accessible malignant tissue followed by adjuvant nonselective chemotherapy and/or radiation therapy with high dose-limiting toxicities [3]. Following tumor resection current protocols for treatment regimens include adjuvant platinum-taxane combination therapy. Platinum-taxanes that disrupt mitotic division and inhibit DNA repair such as Cisplatin, Carboplatin, and Paclitaxel are front-line therapeutics used to treat ovarian tumors [37]. Paclitaxel and Carboplatin often show a high rate of initial response following tumor debulking when administered alone [37]. However, current treatment protocols often administer high dose combination therapies and demonstrate a synergistic effect that show a 10-14 month improvement in patient's survival and lower rates of recurrence [2, 37, 38]. Depending on the desired rate of infusion the most common administered dosage is a combination of 175 mg/m^2 Paclitaxel with Docetaxel or Carboplatin (patient specific). In addition to adjuvant IV chemotherapy [2, 39], surgeries could include intraperitoneal chemotherapy to treat residual disease as well as heated intraperitoneal chemotherapy (HIPC) [40-42]. Unfortunately local recurrence is seen in 60% to 75% of patients often progressing aggressively (< 6 months) and demonstrate decreased sensitivity to platinum-taxane therapies and carry poor long term prognosis [2, 39, 43]. Development of newer agents administered in combination with platinum-

taxanes is ongoing. Phase II and III clinical trials administering second-line agents that target unique molecular mechanisms include: Trabectedin (alkylation of guanine residues) [44], poly-ADP ribose polymerase (PARP) inhibitors (interruption of DNA repair mechanisms) [45], Bevacizumab (inhibiton of VEGF/anti-angiogetic) [46, 47], and Farletuzumab (folate inhibitor) [48] in patients showing reduced platinum sensitivity [37, 49].

1.4 Aptamer Identifcation by SELEX

Aptamers are single stranded RNA/DNA anti-sense oligonucleotides (ASOs) engineered to a specified length. Aptamers have more generally been used as reagents for identifying cell surface proteins and for cell typing [50]. Aptamers form stable secondary structures under normal conditions that are variations of large central loops with protruding hairpin loops leaving the negative charged phosphate backbone exposed. These compact structures form high affinity bonds in the active sites of protein targets by interacting with positive charged amino acid residues. The typical methodology for identifying aptamers utilizes protein targets that are isolated or purified. However, additional methodology has been adapted over time that does not exclusively utilize protein targets but whole cells as well as *in silico* computer modeling to predict aptamer-target binding affinities. The emergence of multiple library screening protocols to identify aptamers with therapeutic potential has led to an abundance of both agonistic and antagonistic aptamer-based therapies [51]. The first report of ASOs binding to a target molecule was presented by Tuerk and Gold describing methodology used to identify short RNA molecules that bind to T4 bacteriophage DNA polymerase [52]. The methods they presented which identified ASOs that bind to polymerase were known as the

Systematic Evolution of Ligands by Exponential enrichment (SELEX). Almost simultaneously, the term "aptamers" was presented by Ellington and Szostak describing random RNA oligos that preferentially bind to organic dyes [53].

Aptamers have an average length of 40-80 nucleotides that bind with high affinity and specificity to specific protein or non-protein targets by folding into complex secondary and tertiary structures. Commercially available aptamers can be engineered to a desired length and offer a variety of post sequencing modifications that allow for aptamer design flexibility. Post sequencing modifications can increase stability to promote bioavailability or conjugate a fluorescent reporter to terminal ends that could be used for *in vitro* tracking. Aptamers display a conventional binding behavior similar to that of antibodies with dissociation constants (Kd) measuring on the order of μM to pM ranges [54, 55]. Aptamers possess several advantages over antibodies or small molecules (reviewed in [56]) for their therapeutic targeting potential [57]. Biologically, aptamers are (1) smaller in size promoting greater tissue penetration, (2) elicit little to no immunogenic effects, and (3) demonstrate rapid renal clearance [51, 58-60]. Commercially, aptamers are chemically synthesized; thus they (1) can be readily modified to alter targeting kinetics, (2) are readily and cheaply produced with low batch variability, (3) can be transported at ambient temperatures, and (4) remain stable for long periods even under adverse conditions [56, 60-64]. Aptamers are multifunctional molecules that can be used as an antagonistic pharmaceutical agent, a molecular chaperone conjugated to therapeutics, or as a diagnostic tool for imaging. Aptamers have been used to treat age-related macular degeneration (AMD) [65, 66], thrombotic thrombocytopenia purpura [67], diabetic nephropothy [68], and cancer [69].

The SELEX process consists of iterative rounds of affinity, purification, and PCR amplification. Initial aptamer libraries are designed with a randomized central active site flanked by two known PCR primer sequences. The sequential process produces pools of enriched aptamers that bind to target molecules with high specificity and affinity [70]. Targets can include small molecules such as proteins, nucleic acids, and lipids, as well as more complex structures that include cells, bacteria, and viruses [55, 70-72]. Some targets of SELEX identified aptamers include: E and P-selectin [73, 74], HER3 [75], PDGFβ [76], stem-cell marker CD133[77] and HIV protein gp120 [78].

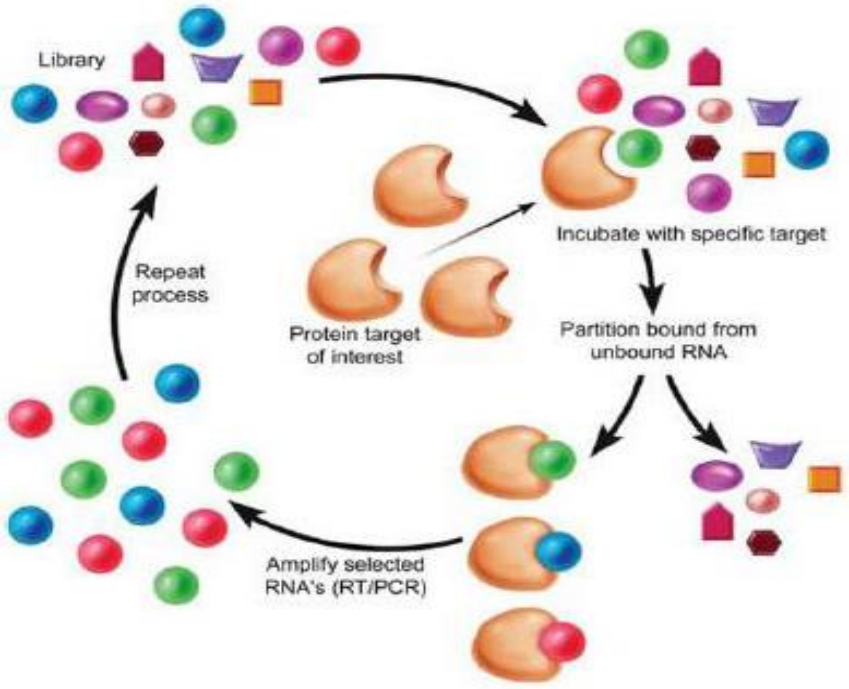

Figure 1: Aptamer identification by SELEX. The SELEX protocol uses a random library selected against a known protein target. Through iterative rounds of selection and amplification target specific aptamer populations grow each with unique binding affinities.

To date a number of aptamers have been reported and are in various stages of preclinical and clinical development (reviewed in [56, 79-81]). Aptamers such as

pegaptanib can bind to a VEGF isoform and can be administered as a drug treatment for AMD. Although pegaptanib is the only FDA approved aptamer currently in use today, there are 13 additional aptamers identified by SELEX protocols that are in phase I, II, or III clinical trials [70]. In addition, research groups have attempted to develop *in silico* theoretical methods to speed up the SELEX process by pre-designing optimal aptamer libraries. Computation design of structured random pools modifies RNA aptamer structures to enrich initial libraries with complex oligonucleotides to increase the probability of identifying novel RNA aptamers [82, 83]. Additionally the potential of a virtual screening process can facilitate aptamer identification. The 3D modeling of aptamer secondary structures can help design optimal initial libraries. Secondary structures of aptamers can then be fitted to potential targets thus creating a high-throughput virtual screening of aptamer libraries to potential targets [84, 85]. This type of library optimization has been successfully employed to identify aptamers that inhibit HIV proliferation by disrupting viral RNA and subsequent replication [86].

1.5 Aptamer Identification by Cell-SELEX for Tumor Specific Aptamers

Although SELEX is typically performed using a highly purified target molecule, it has been effective against mammalian cells and complex organisms. In contrast to early aptamers engineered against known specific ligands, a major advantage of aptamers for biomedical applications is that they may be identified through random library screens without knowledge of their direct ligand on the cell membrane surface. This was experimentally confirmed by the identification of aptamers against red blood cell ghosts [87] and followed by the identification against live African trypanosomes [88]. Cell-SELEX was initially described as an *in vitro* identification scheme to enrich a small pool

of cell-specific aptamers from randomly generated libraries identified through binding to specific cell types and counter-selected against negative cell types. The addition of a negative selection step promotes identification of target cell specific aptamers. Cell-SELEX protocols have been continually modified and improved to *in vivo* screens and localization and internalization-specific screens [50, 55, 89-92]. Aptamers identified by Cell-SELEX can bind to small molecules or proteins in their native structure on the cell surface [55, 93, 94]. Information on the structural interface between target and the tertiary structure of aptamers can provide information regarding catalytic binding moieties and lead to modifications that improve design and delivery [95] [84] [60]. While Cell-SELEX screening is based on binding interactions to the cell surface, other positive and negative screening approaches have been based on cell internalization into target cell populations as shown effectively in a prostate cancer cell model [92].

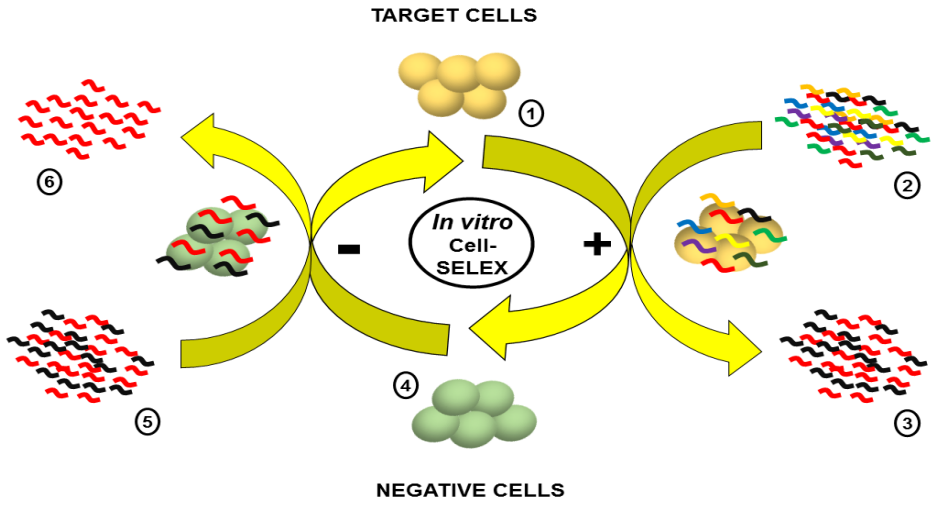

Figure 2: Aptamers identified by Cell-SELEX can be done using live cells. The *in vitro* Cell-SELEX protocol: (1) Target cells are chosen and (2) incubated with randomly generated size specific aptamer library; Aptamers that bind to target cells are eluted and will be incubated with pre-selected negative selection cells (4); Eluted aptamers (5) are incubated with negative selection cells; (6) Unbound aptamers are collected and are unique to target cells. Subsequent PCR amplification is done to enrich the aptamer library and the process is repeated.

1.6 Post Sequencing Modifications of Aptamers

Despite the advantages of aptamer-based treatments and promising results *in vitro*, it is still debated if their efficacy will be reduced *in vivo* due to lack of bioavailability, unstable circulation time, minimal cellular internalization, or susceptibility to nuclease attack [71, 92]. Post-sequencing modifications can increase structural integrity to promote bioavailability within the blood stream such as conjugation of larger molecules such as cholesterol or polyethylene glycol (PEG; PEGylation) to the aptamer [96]. It has been shown that 40 kDa PEGylated aptamers have a higher circulatory half-life than non-PEGylated aptamers, and the extended systemic exposure appears to facilitate distribution of aptamers to distal tissues and highly perfused organs [58]. Additionally, structural substitutions on DNA or RNA purine or pyrimidine moieties decrease susceptibility to nuclease attack and chemical degradation as well as improve pharmacokinetics [97]. Table 1 describes the effective uses of nucleic acid base modifications to aptamers. However, a key drawback for the synthesis of integrated modifications is the requirement of a polymerase capable of adding bulky groups rather than standard wild-type T7 RNA and *Taq* polymerases with high specificity [96]. Multivariate T7 RNA polymerase can synthesize 2'-modified nucleotide triphosphate nucleic acid aptamers that include 2'-azido, 2'-O-methyl (A, C, and U), and 2'-fluoro pyrimidines [96, 98, 99]. Many reported modifications (see Table 1) utilize a combination of wild-type T7 polymerase and Taq polymerase. The T7 polymerase variant Y639F and the multivariate Y639F/H784A polymerase and can be used in a combinatorial manner to add bulky groups that increase the half-life of aptamers *in vivo* up to 23 hours [97, 98, 100].

Table 1: Aptamer mdifications to increase stability and promote *In Vivo* targeting *

Pyrimidine Modification	Potential Effects	Current Aptamers	Pol.	Ref.
2'-Amino pyrimidine	-Increase aptamer stability in urine and human blood serum -Increase T_m of aptamer -Increase binding affinities by addition of available hydrogen binding sites	-Human neutrophil elastase -Fibroblast growth factor -Thyroid stimulating hormone -Prion protein specific aptamer	+	[96], [101], [102], [103], [104]
4'-Thio pyrimidine	-Increase nuclease resistance -Thermal stability	-Human α-Thrombin aptamer	+	[96], [105]
Phosphoro-thioate (S-oligo-nucleotide)	-Increase nuclease resistance -Greater inhibition of gene expression in combination with propyne analogs	-Anti viral drug -TGF-β1 aptamer -Syrian Hamster Prion	+	[96], [106], [107], [108]
2'-*O*-methyl nucleotide	-Increase nuclease resistance -Flexibility in desired sites of modification and often combined with other pyrimidine modifications	-Anti $VEGF_{165}$ aptamer -Thrombin aptamer -IL-23 aptamer	●	[96], [109], [110]
Borano-phosphate	-Increase endo and exonuclease resistance -Increase PCR efficiency and DNA fragment capture post digestion	-Boron neutron capture therapy (experimental treatment that could use any existing aptamer) -ATP aptamers	+	[96], [111], [108], [112]
5'-Modified pyrimidine	-Increase nuclease resistance -Increase PCR efficiency	-Thrombin aptamer -Sialyllactose aptamer	+, ●	[96], [113], [114]
2'-Fluoro pyrimidine	-Increase thermodynamic stability -Promote RNA-type sugar conformations -Increase stability in human plasma	-Anti-Factor IXa (aptamer RB006) -Anti-C5 aptamer -Prostate-specific membrane antigen (PSMA) aptamer	●	[96], [114], [115], [116]
Locked Nucleic Acids (LNA)	-Demonstrate increased binding to plasmid DNA -Increase stability and T_m	-TD05 aptamer for Burkitt's lymphoma	+, ●	[117], [118], [119], [120]

Table 1: continued

5' & 3' modification	-5' Terminal capping (dialkyl-glycerol) -3' nucleotide inversions decrease susceptibility to exonuclease	-Anti $VEGF_{165}$ aptamer -RB006 (REG1 anticoagulant) -ARC1905 (Ophthotech Corp)	N/A	[109], [121], [122]
Aptamer PEGylation	-Reduce renal clearance and increases bioavailability (RNA and DNA aptamers currently in clinical trials contain PEG conjugates)	-Anti $VEGF_{165}$ aptamer -RB006 (REG1 anticoagulant) -E10030	N/A	[122], [123]

+ T7 and Taq polymerase (wild-type)
● T7 double mutant Y639F/H784A
Pol. Polymerase
T_m =Melting Temperature
* Post-sequencing modifications that can be made to aptamers which can increase the overall stability of the structure, increase PCR efficiency, as well as reduce susceptibility to nuclease enzymes. Custom designing of these oligonucleotide can be done to specify location and amount of substitutions on the aptamer and wild-type or modified polymerase can be used to introduce or reproduce base analog substitutions.

1.7 Aptamers as Single Antagonists

Aptamers alone have been shown to bind to target molecules on cell surface membranes and typically internalize into cells via canonical endocytosis pathways [91, 124]. Recently one group has demonstrated a unique internalization mechanism whereby gold Au nanoparticles coated with an amphiphilic organic monolayer can spontaneously insert into lipid bilayers on the cell surface through hydrophobic–hydrophobic contact between the core of the bilayer and the monolayer of the Au nanoparticle dependent on the stochastic protrusion of an aliphatic lipid tail into solution [125].

Similar to canonical protein-protein interactions, aptamer-target molecule recognition and interaction can lead to inhibition of target molecule activity or function. Aptamer-target interactions have been shown to be sufficient to block signaling pathways

important in cell proliferation, and thus identification of molecules with this property has been long recognized for their significant therapeutic potential [126]. It has been well established that the aptamer pegaptinib will inhibit the $VEGF_{165}$ isoform without effecting similar isoforms necessary for physiological vascularization [127]. Pegaptinib has been used to target the retina in cases of age related macular degeneration where $VEGF_{165}$ is elevated under hypoxic conditions [127, 128]. Given the high prevalence of VEGF activation in multiple tumor types, this approach could be explored for other cancers.

Similar paradigms have been used to study aptamers that target additional signal transduction pathways. The Axl tyrosine kinase receptor has been recognized as a potential anti-tumor therapeutic target for the last decade [129, 130]; several small molecule and protein inhibitors and an anti-Axl monoclonal antibody have been described [131-133]. The aptamer GL21.T binds to Axl and inhibits phosphorylation of Erk and Akt downstream targets, inhibits cell migration and invasion, and reduces tumor growth in an *in vivo* xenograft lung tumor model [134]. PDGFRβ tyrosine kinase receptor is overexpressed in multiple tumor types including glioma. The same group that identified GL21.T now reports an aptamer Gint4.T selectively binds to PDGFRβ but not other tyrosine kinases. Aptamer Gint4.T inhibits dimerization and ligand dependent signaling, inhibits cell migration and proliferation, induces differentiation, and reduces tumor growth in an *in vivo* xenograft glioblastoma tumor model [135]. The anti-C5 aptamer ARC1905 is a potent inhibitor of factor C5 of the complement cascade, and inhibition of this signaling pathway prevents the formation of pro-inflammatory fragments inhibiting the release of angiogenic stimulating molecules [136].

1.8 Aptamer Toxicity

Aptamer toxicity can vary in species and be altered by post sequencing modifications (Table 1). Physiologically high doses of oligonucleotides (>100µg/mL) have triggered adverse immunogenic effects in non-human rodent and primate models [137]. When antisense oligonucleotides are dosed systemically in rodents, injury to the liver and kidneys is often seen as this is a major site of oligonucleotide accumulation [138, 139]. Swayze *et. al.* showed that antisense oligonucleotides (ASOs) accumulate in the liver confirmed by post-mortem liver necropsy with subsequent histopathological microscopy as well as increased serum levels of aminotransferases ALT and AST. Moreover they looked at ASOs containing either 2'-O-methyl or LNA modifications and found that LNA modified aptamers showed increased levels of hepatotoxicity for multiple sequences targeting three different biological targets (*Mus Amuscus* PTEN, TNFRSF1A, and apo-lipoprotein B) in additional to a mismatch control ASO with no target [138]. Multiple adverse effects have been seen with phosphorothioate modifications. Granule formation is seen in kidney and liver epithelial cells that are responsible for filtration and clearance of antisense oligonucleotides and their metabolite species [72, 140-142]. Further continued chronic exposure to phosphorothioate modified antisense oligonucleotides resulted in plasma accumulation which could affect coagulation of the blood [137]. Both high and low concentrations of ASOs in the liver can cause adverse hepatic function, but individual ASOs can exhibit unique hepatotoxic potential [138, 139]. Hagedorn *et. al.* developed computer based software to evaluate and distinguishing between locked nucleic acid modified oligonucleotides with low or high potential for hepatotoxicity [143]. Slow intravenous infusions are likely to

significantly lower circulatory plasma levels decreasing accumulation versus direct injection and to reduce these effects [144]. Additionally, RNA and DNA based oligonucleotides have promoted immune-stimulatory effects through toll-like receptors 3, 7, 8, and 9 signaling [145]. Such immunological responses could result in hyperplasia in the lymph nodes, mononuclear cell infiltration, and accumulation of basophilic granules. However these studies utilized naked aptamers and conjugation to therapeutics or nanoparticle delivery vehicles has altered both bioavailability and toxicity profiles.

1.9 Aptamer-Based Photodynamic Therapy

Photodynamic therapy (PDT) uses a photosensitizer or photosensitizing agent that, after injection, is exposed to a specific wavelength of light to produce a form of oxygen that kills nearby cells. PDT is currently available for prostate, breast, and esophageal cancers [146-151]. Newer models linking PDT to aptamers for targeting are being explored in translational studies. Aptamer TD05 was identified using SELEX targeting the Burkitt's lymphoma Ramos cell line [152] then conjugated to the photosensitizer reagent chlorin e_6 (Ce_6) to create an aptamer-photosensitizer conjugate (APS) [153]. When this APS was incubated with target Ramos cells and followed by light irradiation, >70% of cells exhibited cell death as determined by propidium iodide incorporation, and overall 50-60% more cell death in target cells was observed when compared to four control cell lines (CEM, T-cell leukemia; K562, human bone marrow; NB4, human acute promyelocytic leukemia; HL60, promyelocytic leukemia). Randomly generated aptamers conjugated to Ce_6 photosensitizer exhibited little to no cell death in target cells showing both the efficacy and the high specificity of the complex [153]. Similarly, the nucleolin targeting guanine-rich aptamer AS1411 has been conjugated to

six molecules of the cationic porphyrin TmPyP4 that intercalates into the G-quadruplex structures of AS1411 [154, 155]. When MCF7 breast cancer cells were incubated with AS1411-TmPyP4 complexes, an average of 30% more cell death was observed as compared to incubation with TmPyP4 alone. Similar results have been obtained with systems that utilize MUC-1 aptamers for targeting of epithelial cancer cells, aptamer R13 for targeting lung carcinoma, and protein kinase 7 (PTK7) aptamer sgc8 for targeting T-ALL [154, 156-158]. Also, Han et al. have developed a novel aptamer-based DNA nanocircuit which not only targets Ramos cells but demonstrates an amplified photodynamic therapeutic effect [159].

1.10 Aptamer-Based Anti-Viral Therapies

Aptamer-target molecule recognition and inhibition of target activity has been exploited in anti-viral therapies [160-162]. In at least one model system, aptamer-virus interactions act at the initial infection step and potentially inhibit mechanisms necessary for virus internalization [163]. Human papillomavirus (HPV) is linked to high incidence of cervical cancer worldwide as well as multiple other neoplastic diseases [164]. More aggressive types of HPV, such as HPV-16, express the E6 and E7 oncoproteins that degrade the tumor suppressor p53 and disrupt cell cycle checkpoints by destabilizing phosphorylated Rb [165]. Several other groupsm have isolated aptamers that internalize into cells and bind to the E7 oncoprotein as well [164-167]. 2'-fluoro modified aptamer A2 showed affinity for the N-terminal residues of E7, a reduction in E7 and pRb interactions, and increased cell mediated apoptosis of human epithelial cells [165, 167]. Additionally, Gourronc *et. al.* isolated aptamers that demonstrated variable rates of

internalization when incubated with E6/E7 HPV-16 transformed human tonsillar epithelial cells (HTECs) as compared to internalization into primary HTECs [164].

1.11 Aptamer-Drug Conjugates

Not all aptamer-target molecule interactions are inhibitory. Direct conjugation of aptamers to chemotherapeutic compounds through chemically labile linkers or self-assembly DNA drug nano-structures facilitate internalization into specific tumor cells [91, 124, 168]. Aptamer A10 recognizing prostate-specific membrane antigen (PMSA) conjugated to epirubicin [169, 170] led to increased cellular internalization and cell toxicity when administered *in vitro* to LNCaP ($PMSA^+$) cells as compared to PC3 ($PMSA^-$) cells [170]. The PTK7 T-ALL (T-cell acute lymphoblastic leukemia) aptamer sgc8c has been covalently conjugated to doxorubicin or daunorubicin via a functional thiol group at the 5' terminus [124, 171]. The bond between aptamer and drug is mediated by a hydrazone linker that has a nucleophilic attraction for the terminal carbonyl on the doxorubicin molecule [124], and the hydrazone linker promotes release of the drug in the acidic conditions of an internalized vesicle [172]. Aptamer sgc8c-doxorubicin conjugates were as effective as doxorubicin alone demonstrating approximately 80% cell death in CCRF-CEM T-ALL cell line within 48 hours post-exposure. Moreover, incubation with a randomly synthesized aptamer-doxorubicin complex prevented internalization and demonstrated less than 25% toxicity [124]. Similarly, doxorubicin has been conjugated to aptamers HB5 for breast cancer, EpCAM for retinoblastoma, TSL11 for liver cancer, and MA3 against MUC-1 for lung and breast cancers [173-176]. However, it should be noted that thus far all of these have only been tested in cell lines.

1.12 Nanoparticles

Nanoparticles technology is rapidly integrating into multiple fields in both research and industrial commercial products. Nanoparticles are used in the manufacturing of biomedical and electronic devices as well as in the textile industries. Nanoparticles can be used in sunscreens (titanium dioxide NPs, TiO_2) [177], antimicrobial wound dressings (silver NPs, Ag) [178], nanoimprinting lithography (zincoxide NPs, ZnO), and solar cells (silver, Ag and metaloxide NPs) [179]. Nanoparticles can be manufactured from organic or inorganic materials with sizes ranging from 10-200 nm in length and/or diameter. Nanoparticles are formulated into a wide range of structures including lipid-based liposomes, polymer-based particles or micelles, or poly-amido-amine dendrimers, silica-based particles, carbon-based nanotubes, and metallic nanoparticles, nanotubes, or nanocrystals [180, 181]. (We will hereafter refer to all collectively as nanoparticles.) Nanoparticles are produced either by a process that involve the breakdown of larger particles through milling, or by the assembly and precipitation that allow for incorporation of multiple molecules within their cores or tailored surface functionalities [182, 183]. At the nanoscale both optical and physical properties of NPs change in ways uncharacteristic to the base material improving their functionality beyond delivery of small molecules. For example nanoparticles composed of TiO_2 have the same chemical composition as macro-molecule TiO_2 in conventional sunscreen products. However, TiO_2 NPs are transparent and unique optical properties is one advantage of using NP technology. Quantum dots (nanocrystals) made of semiconductor material exhibit quantum mechanical properties. Quantum dots

are often utilized for their optical and electronic properties for super-resolution imaging [184] and diode lasers [185].

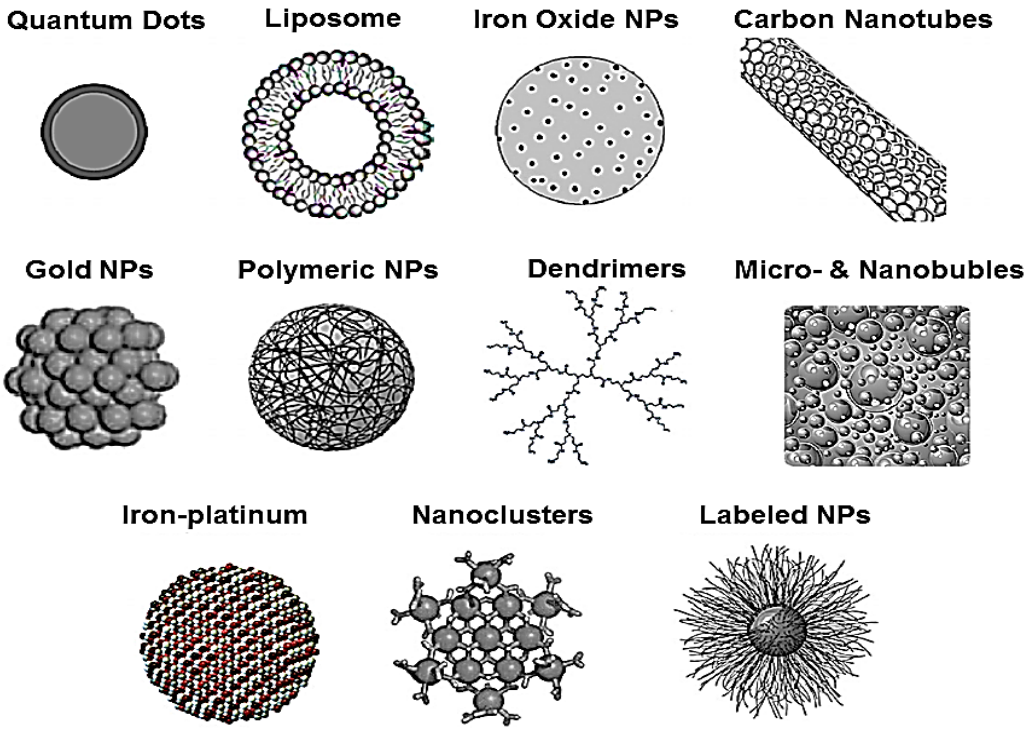

Figure 3: Nanoparticles can be made from a variety of inorganic and organic materials with unique physical properties. The figure above shows the variety of "nano-carriers" that can be utilized for packaging and delivery of small molecules. The NPs above can be used to carry molecular inhibitors, chemotherapeutics, small proteins, fluorescent dyes, and antibiotics.

More so recently, nanotechnology has been used in molecular research particularly as a drug delivery vehicle. The relatively small size of nanoparticles makes them optimal delivery vehicles as they can be phagocytosed by the cell through clathirin-mediated endocytosis and fluid phase pinocytosis [186, 187]. Moreover, the surface of NPs can be labeled, or functionalized, to promote active targeting of cell types [188, 189]. Targeted drug delivery systems can localize cytotoxic agents at tumor sites and could potentially enhance current protocols by (i) overcoming non-specific toxicity (ii)

delivering a more effective dose per treatment cycle, and (iii) overcome canonical multidrug resistance (MDR) pathways seen in incidences of recurrence. In many cases, compartmentalizing drugs in polymeric and organic nanoparticles (NP) has shown potential for drug delivery. Drug loaded nano-carriers have been developed using poly-lactic-co-glycolic acid (PLGA) [190], gold [191], silicon [192], and silver [193] to deliver drugs to tumor cells or to isolate and identify malignant cells *in vitro* and *in vivo* [194, 195]. The structure of NPs promotes long-term circulation throughout the body by reducing renal clearance and because of inconsistencies in vascular pore size associated with tumors, NPs readily accumulate due to the enhanced permeability and retention (EPR) effect [196, 197]. Thus NPs can be used for active targeting but also possess intrinsic passive targeting properties which exploit the incomplete vasculature of the tumor microenvironment.

Molecules such as chemotherapeutics, vaccines, proteins, miRNAs, anti-fungals, and inhibitors can be encapsulated within nanoparticles and delivered to target cells [186, 187, 198]. Nanoparticles that contain chemotherapeutics demonstrate consistently increased accumulation within tumors over free drug [55, 199-204] and also increase biodistribution to both primary tumors and distant metastatic sites, increase bioavailability of hydrophobic agents and maximum tolerated doses, and improve clearance from the circulatory system [156, 182, 205]. Depending on the type of monomeric subunits used to form the nanoparticle, polymer encapsulation of chemotherapeutics can help to (1) solubilize otherwise insoluble compounds, (2) minimize physiological drug degradation, (3) increase blood circulation half-life, (4) prolong systemic activity by reducing physiological secretion by the kidneys, and (5)

prevent recognition of therapeutic hydrophobic compounds by the reticulo-endothelial system [187, 206-208].

Multiple factors such as particle size, composition, surface chemistry, mobility, stability, and shape can alter *in vivo* particle dynamics and toxicity [209]. Moreover the mode of exposure including: (i) inhalation, (ii) oral/digestive, and (iii) dermal absorption can alter toxicity. It was shown in rats that persistent exposure to ZnO NPs within the gastric system could lead to pancreatitis [210]. However there is limited correlation between ZnO based skin protection and skin cancer--this is most likely due to the effective barrier skin provides against NPs and other toxic chemicals [211]. An observable difference in toxicity between carbon nanotube inhalation versus dermal and oral exposure has been reported as well [212]. As research continues current data suggest that the presence of nanomaterials is overly cytotoxic but the reactivity associated with raw NP material could be and would vary on the exposure metrics [213]. Due to the increased demand of NPs in molecular biology research, investigations how NPs can cause reproduction toxicity [214] or be involved with heritable genetic traits following long-term exposure [215] have been conducted.

1.13 Organic Polymeric Nanoparticles

Nanoparticles derived from organic-based compounds are used in a variety of biomedical and clinical settings and can be employed for imaging and delivery due to their delocalized electron structure giving them unique optical and magnetic properties. Polymer-based nanoparticles are spherical structures that range in size and can exist in a colloidal suspension [216]. Their three-dimensional amphipathic cage-like structure promotes encapsulation of most drugs and small molecules as well as solubility of

hydrophobic compounds [217, 218]. Structure and size can alter pharmaceutical properties such as half-life, cellular uptake, and drug release kinetics [219]. Polymeric drug encapsulation has been used for effective treatment for malignant gliomas for almost 20 years with intraparietal placement of carmustine wafers or carmustine-loaded polymers for effective controlled drug release over time without adverse systemic effects [220, 221]. Polymeric nanoparticles can be constructed from a wide range of monomeric organic molecules or commercially available synthetic compounds [187] including block polymer constituents such as PLGA, polystyrene (PS), and poly-ethelene-glycol (PEG) to form three dimensional amphipathic structures [187]. The experimentation described in Chapters 2, 3, and 4 utilize NPs composed of the di-block polymer poly (lactic-co-glycolic acid, PLGA) and poly-capro-lactone (PCL) with 5% polyethylene glycol (PEG).

PLGA based nanoparticle vehicles offer an FDA-approved biodegradable drug carrier that is metabolized by the body into monomeric subunits with limited toxicity [187]. Although no current human clinical trials utilize PLGA based NPs, they have been effective in the context of a drug delivery vehicle *in vitro*. PLGA based NPs have effectively carried Gemcitabine to pancreatic tumor cells [222] and Paclitaxel to lung cancer cells [223]. Polymer and copolymers are hydrolyzed into metabolite monomers that are easily consumed by cells through normal respiratory mechanisms such as the Krebs cycle [199]. There are multiple methods of formulation that allow for the encapsulation of both both hydrophobic [224] and hydrophilic drugs [225]. Moreover physio-chemical analysis can be run on a batch-by-batch basis to optimize subsequent NP surface fuctionalization. Polydispersity and particle size can be measure by dynamic light scattering and further evaluated by electron microscopy. PEGylation to nanoparticle

formulations further increases circulation time and bioavailability in the blood stream, and reduces renal clearance and has a well-established safety record in both clinical and commercial settings. PEGylation is common for aptamers to increase circulation by circumventing renal clearance[71, 97], in nanoparticles to increase biodistribution [198, 199], lipid based liposomal carriers [226] and chemotherapeutics [227].

1.14 Silica Nanoparticles

Silica is found ubiquitously in nature in both single- and multi-cellular organisms. The abundance of silanol groups within the silica matrix provides biocompatibility and promotes affinity towards phospholipids facilitating uptake by endocytosis [228-230]. Mesoporous silica and core-shell silica-based nanoparticles can be easily produced and modified to manipulate structural characteristics such as fluorescence, magnetism, surface area, controlled drug delivery, and pore size [192, 228, 231]. Uniquely, silica nanoparticles can promote slow or modulated release from their cores [232]. Modulation of pore size altered the kinetics of paclitaxel release *in vitro* that correlated with early and late (sustained) levels of apoptosis of MCF-7 (breast adenocarcinoma) cells in culture [233]. Kinetics of drug release is governed foremost by the electrostatic interactions between the drug and the silica surface while drug loading is dictated by pore and particle size [229]. Secondary stimuli such as pH, heat, light, or hydrolysis of structural scaffolding can be used to promote delayed or sustained release of bioactive materials or chemotherapeutics such as doxorubicin [232, 234-236]. Variation of material composition within the particles can also modulate release activity; hybrid porous silica-calcium phosphate nano-composite particles were developed to demonstrate an initial burst release of 5-FU followed by sustained release of a therapeutically relevant dose (up

to 32 days) and decreased tumor growth *in vivo* using a subcutaneous 4T1 breast cancer xenograft mouse model [237].

Similar to polymer-based nanoparticles, silica-based nanoparticles allow functionalization through covalent linkage of targeting molecules on their surface. Functionalization promotes solubility, prevents degradation, and increases delivery of encapsulated compounds [234, 238]. Dextran coating is associated with increased biocompatibility in mice and increased sensitivity for tumor imaging [239]. Conjugation of MUC-1 specific RNA aptamers to the surface of silica nanoparticles has been used to identify MCF-7 breast cancer cells *in vitro* [240]. A red salt crystalline reporter (RuBPY) incorporated in silica nanoparticles allows for quantification of the amount of aptamer species available on the nanoparticle surface as well as the amount of internalization into MCF-7 cells [240]. They also demonstrated a reduction in photobleaching likely due to electrostatic interactions when organic dyes are absorbed between the porous landscape of the silica core and shell [240]. Additional detection assays have utilized α-thrombin aptamers and a nucleolin aptamer conjugated to fluorescein-loaded mesoporous silica nanoparticles in MDA-MB-231 (breast adenocarcinomal) cell lines [241, 242]. In combinatory photodynamic and photothermal therapy [243, 244] a dual phototherapeutic effect was observed by near infrared irradiation of phthalocyanine, as well as 5-fold decrease in KB cell (cervical carcinoma) viability in a dose dependent manner, and a reduction in tumor burden with a 100% survival ratio in an *in vivo S180* sarcoma xenograft mouse model [244].

1.15 Inert Metallic Nanoparticles

Inert metals (gold Au, silver Ag) are used in multiple diagnostic modalities for basic biological and biomedical research including imaging, oligonucleotide delivery, detection, photodynamic therapies, biosensors, and drug encapsulation and release [193, 245, 246], although their use in anti-cancer therapies has been less widely utilized [180, 247-249]. Both Au and Ag nanoparticles demonstrate high permeability often showing retention at tumor sites due to the permissive and incomplete vascularization of tumors [250]. The permeability of these particles has been demonstrated *in vitro* with a model micro-vasculature membrane analogous to the blood-brain barrier. A linear progression and size dependence of Au nanoparticle permeability was demonstrated over 20 hr that could be most beneficial to patients with malignant brain tumors unable to undergo surgical tumor excision [251]. Au and Ag nanoparticles are readily linked to biomaterials, amino acids, proteins, and short oligonucleotides through thiol and amine group linker mediators to promote both cellular internalization and potentially higher tolerated doses of therapeutics [252-257].

Both Au and Ag nanomaterials exhibit intrinsic anti-angiogenic properties that may be exploited in anti-tumor therapeutics [258, 259]. Au nanoparticles inhibited the heparin-binding domain of $VEGF_{165}$ in human umbilical vascular endothelial cells (HUVECs) as well as $VEGF_{165}$-induced migration and RhoA activity [260]. Similar results were obtained with Ag nanoparticles on bovine retinal endothelial cells (BRECs) and *in vivo* studies using mice and rat models implanted with VEGF+/VEGF- matrigel plugs [259]. C57BL/6 mice administered Ag nanoparticles (500nM) in matrigel plugs for 7 days exhibited no significant vascularization and demonstrated results similar to those

mice administered anti-angiogenic pigment epithelium-derived factor. BRECs treated with the angiogenic stimulating compound Streptozotocin and Ag nanoparticles showed reduced AKT phosphorylation, and little to no angiogenic response when compared to Streptozotocin treatments alone. These results suggest that Ag nanoparticles themselves may mitigate multiple angiogenic and proliferative cellular pathways characteristic of malignant cells [259]. In support of this, reduction of fibroblast growth factor (FGF-2)-mediated angiogenesis has been shown in both chick chorioallontoic membrane models and in mouse matrigel models. Further, an increase in toxicity with cisplatin-loaded Au nanoparticles in both lung epithelial and colon cancer cell lines was reported [256, 261]. Recently one group has demonstrated a unique internalization mechanism whereby gold Au nanoparticles coated with an amphiphilic organic monolayer can spontaneously insert into lipid bilayers on the cell surface through hydrophobic–hydrophobic contact between the core of the bilayer and the monolayer of the Au nanoparticle dependent on the stochastic protrusion of an aliphatic lipid tail into solution [125].

Because of the increase in the commercial use of Ag, cytotoxicity of Ag exposure has been studied extensively. Ag nanomaterials exhibit many of the same properties observed with Au nanomaterials and produce minimal cytotoxicity and accumulation in respiratory and systemic organs [180, 262-265] as well as some antioxidant properties by interacting and depleting reactive oxygen species and peroxidase metabolites at the cellular level [213, 266, 267]. However, in one study, Sprague-Dawley rats highly dosed with Ag nanoparticles (~20µg/m^3) showed both respiratory and renal accumulation while rats receiving 0.04µg/m^3 showed no adverse effects [263]. Results may be governed by specific preparation, particle surface modulations, and even sex differences [251, 268-

270]. Sub-chronic inhalation of Au nanoparticles in Sprague-Dawley rats showed that both females and males accumulated NPs (diameter 4-5nm) in lungs in a dose dependent manner, accompanied by tissue histological changes, macrophage infiltrate, and inflammatory response, but accumulation in the kidneys only in females [263]. Au nanoparticles, at least, demonstrate a size-dependence on physiochemical properties. In lung cancer tumor cell lines A549 and 95D cells, incubation with 10nm Au nanoparticles promoted endocytosis and growth inhibition. However, despite the growth inhibition, cell invasion increased and correlated with increased expression of matrix metalloprotease-9 and intercellular adhesion molecule-1 [271]. By contrast, larger particles of 20nm and 40nm did not promote invasion pointing to the need for intensive pre-clinical testing [271].

1.16 Aptamer-Nanoparticle Conjugates

To date, no aptamer directed NP conjugates are being investigated as a viable treatment option. However, there are over 25 clinical trials that utilize aptamers as single antagonists. The majority utilize pegaptanib and E10030 to inhibit $VEGF_{165}$ in age related macular degeneration [50] and related diseases [122, 272, 273]. Clearly there is a clinical precedence regarding the use of aptamers as single antagonists which localize to specific molecular targets within the body. This would suggest that conjugating small molecules, such as cytotoxic drugs, could localize therapeutics to target sites as well. Distinct expression surface receptors or biomarkers give individual cancer subtypes unique molecular signatures that may be identified and bound by aptamers [51, 274]. When aptamers are covalently linked directly to drugs or drug carriers the resulting

aptamer-drug conjugate creates a circulating and actively targeting cytotoxic “smart bomb” [124, 275].

By themselves, internalization of nanoparticles into target tumor cells depends largely on passive targeting that is based on the enhanced permeability and retention (EPR) effect that is dependent on leaky vasculature or dysfunctional lymphatic drainage characteristic of tumors [158, 226]. Similar to small molecules, antibodies, and antigen-binding fragments (reviewed in [56]), aptamers have been used to functionalize nanoparticle surfaces and promote active targeting to tumor cells through multiple endocytosis mechanisms. The generation of such dual-functional “smart bomb” complexes that are both loaded with anti-tumor drugs and also conjugated to aptamers have multiple clinical advantages and their development by both basic research teams and biotechnology industry has significantly increased in the past several years (Table 2) [79, 80, 276, 277]. First, such a design will preferentially, or even exclusively, target tumor cell populations. Second, such a design facilitates active rather than passive targeting with both target cell recognition and endocytosis of the complex. Third, such recognition and internalization may circumvent multidrug resistance based chemoresistance mechanisms [188-190, 278]. Although density of aptamer coating on nanoparticles is central to the kinetics of cell binding and internalization, ratios need to be optimized for each model system. It has been demonstrated in at least one report that with a polymer-based system, excessive linkage of aptamers to the nanoparticle surface may mask PEG composition, thus altering surface charge and decreasing tumor cell uptake [277, 279].

Several groups have reported using aptamers to target nanoparticles to cells while also controlling release kinetics of therapeutics through “gating“ whereby short ssDNA

that forms hairpin structures prevent the release of the encapsulated biomolecule, and presence of complementary ssDNA sequences or binding molecules present inside target cells remove the hairpin structure and permit biomolecule release. In one such study, treatment with camptothecin-loaded nanoparticles gated by an ATP-specific aptamer showed a 40% higher incidence of cell death in MDA-MB-231 cell lines as compared to a fibrocystic normal MCF-10a cell line. The higher incidence of cell death was related to the higher metabolic synthesis of ATP in the cancerous cells [280]. Porous nanoparticles may be gated by strongly-bound biomolecules within the pores. One group gated mesoporous silica nanoparticle pores with desthiobiotin-avidin molecules. While T-ALL aptamer sgc8c conjugated to their surface promoted interaction and internalization into PTK7 expressing CEM cells, the subsequent cytosolic interaction of desthiobiotin-avidin with vitamin H, a hallmark of some tumor types, ungated the pores to allow release of encapsulated doxorubicin [281].

In a similar approach to controlled release, folic acid-conjugated mesoporous silica nanoparticles containing the photosensitizing agent TmPyP4, "capped" the TmPyP4 molecules through interactions with a G-quadruplex DNA species [282]. The folic acid promoted tumor targeting to folate receptors that commonly overexpressed on the surface of multiple tumor cell types and long used for targeted therapy [283-286]. After internalization, light irradiation generated reactive oxygen species that caused cleavage of the DNA cap and release and activation of TmPyP4 to facilitate cell killing in HepG2 liver cancer cell line as compared to folate receptor-deficient murine 3T3 cells [282]. Other groups using temperature and affinity modifications have demonstrated *in vitro* controlled release of neomycin from multiple aptamer-conjugated Au nanoparticles,

suggesting that these too could be utilized in therapeutic strategies [248]. Due to the plasmonic resonance and low quantum yield of Au, optical illumination will promote highly efficient conversion of photon energy into heat. Exploiting this property, Au nanoparticles conjugated to both the T-ALL PTK7 aptamer sgc8c and doxorubicin demonstrated efficient internalization into the CCRF-CEM T-ALL cell line [249]. Further treatment with a continuous 532 nm wave laser stimulated release of doxorubicin into cells and increased cell killing [249].

Similar to the traditional combination therapies using chemotherapeutics, combinatorial approaches with nanoparticle delivery have shown to be more effective particularly against late stage or chemoresistant tumors [287, 288]. Given that standard cancer treatment regimens include combination therapy, an advantage of nanoparticles as delivery vehicles is their property that individual cores can encapsulate multiple therapeutic compounds for ensured simultaneous delivery to an individual target cell. One group reported synthesis of polymer nanoparticles that carry precise molar ratios of doxorubicin, camptothecin, and cisplatin that allow photo-triggered release of all three drugs from a single nanoparticle [289]. Using the OVCAR3 ovarian carcinoma cell line, these particles showed effective internalization into tumor cells and significantly increased cytotoxicity following 365 nm UV light exposure [289]. In a second study, PSMA specific aptamers were conjugated to polyethyeneimine-PEG nanoparticles to deliver both doxorubicin and Bcl-xL shRNA to an LNCaP PSMA upregulated cell line [290]. Combination therapy with nanoparticles loaded with both doxorubicin and Bcl-xL shRNA was 60% more cytotoxic than either treatment with doxorubicin alone or with nanoparticles with encapsulated Bcl-xL shRNA alone [290]. In addition the co-delivery

of both compounds had a synergistic cytotoxic effect when compared to LNCaP cells treated with a mixture of doxorubicin and shRNA polyethyeneimine-PEG nanoparticles simultaneously [290].

Despite the large amount of promising initial data (see Table 2), the move from benchtop to bedside with aptamer-directed anti-cancer therapies has been slow. Aptamer-nanoparticle conjugates either alone or as "smart bombs" loaded with chemotherapeutics have not yet reached phased clinical trial stages of development [277]. However aptamers as single antagonists and various chemotherapeutic-loaded nanoparticle formulations have been clinically tested.

Table 2: "Smart Bomb" aptamer-conjugated nanoparticles in development for anti-cancer therapy and detection

Therapy	Aptamer	Target	Nanoparticle polymer	Findings
Cisplatin	A10 (RNA)	Prostate specific membrane antigen	PLGA-b-PEG	In vitro (PSMA+ LNCaP cells) -internalization/cell viability [190]
	A10 (RNA)	Prostate specific membrane antigen	PLGA-b-PEG	In vivo (Sprague Dawley Rats) -In vivo toxicity (NUDE BALB/c) -xenograph imaging/ antitumor effects [194]
Doxorubicin	KMF2 (DNA)	Her2/Erb2	Drug-aptamer conjugate	In vitro (MCF-10AT1) -internalization/cell viability [291]
	HB5 (DNA)	Her2/Erb2	Drug-aptamer conjugate	In vitro (MDA-MB-231, SK-BR-3) -internalization/cell viability [175]
	sgc8c (DNA)	PTK7	Silica (SiO_2)	In vitro (Ramos, CCRF-CEM cells) -internalization/cell viability In vivo (BALB/c) -Ex vivo organ imaging [292]

Table 2: continued

Doxorubicin (continued)	sgc8c (DNA) A9 (RNA) TDO5-sgc8c-sgd5a	PTK7 Prostate specific membrane antigen mIGm (B-cell receptor) Protein Kinase 7 Toledo cells (B-cell lymphoma)	Silica ($MP\text{-}SiO_2$) PAMAM-succinamic acid dendrimer Trimeric aptamer linked to Dox (3-D nucleic acid structure)	In vivo (Toledo, Ramos) -internalization/cell viability [281] In vitro (RAW264.7 murine monocytes) -immune response (LNCaP, 22RV1) -anticancer effects In vivo (BALB/c) -antitumor effects [180] In vivo (CCRF-CEM, Toledo, Ramos, NB4) -internalization/cell viability [168]
Epirubicin	MUC-1 (DNA) A-10 (RNA)	Mucin-1 Prostate specific membrane antigen	Iron oxide ($FeNO_3$) PEGylated aptamer	In vitro (CHO-K1, C532 Murine Colon) -anticancer effects In vivo (BALB/c) -antitumor effects -Mag. Res. Imaging [293] In vitro (PSMA+ LNCaP) -internalization/cell viability [170]
Paclitaxel	MUC-1 (DNA) AS1411 (DNA) AS1411 (DNA)	Mucin-1 Nucleolin Nucleolin	PLGA PLGA-PEG PLGA-Lecitin-PEG	In vitro (MCF-7, HepG2) -internalization/cell viability [294] In vitro (C6-rat glioma) -internalization/cell viability In vivo (Sprague Dawley rats, Wistar rats, NUDE mice) -antitumor, tissue distribution, pharmokinetics[195] In vitro (GI-1, L929, MCF-7) -internalization [295]
Camptothecin	ATP specific (DNA)	ATP recruitment promotes release	Mesoporous silica ($MP\text{-}SiO_2$)	In vitro (MDA-MB-231, MCF-10a) -internalization/cell viability [280]
Vinorelbine	AS1411 (DNA)	Nucleolin	PLGA-PEG	In vitro (MDA-MB-231, MCF-10a) -internalization [296]

Table 2: continued

Curcumin	EpCAM (RNA)	Epithelial cell adhesion molecule	PLGA-lecithin-PEG	In vitro (HT29, HEK293) -internalization/cell viability [296]
Daunorubicin	MUC-1 (DNA)	Mucin-1	NIR-$CulSn_2$ Quantum Dots	In vitro (MUC-1+ PC-3M, HepG2) -cell viability [297]
siRNA delivery	AS1411 (DNA)	Nucleolin	PEG liposome	In vitro (A375, HEK293) -internalization/cell viability In vivo (NUDE BALB/c) -tissue biodistribution, antitumor effects [275]
SN-38 (irinotecan metabolite)	MUC-1 (DNA)	Mucin-1	Chitosan	In vitro (MUC-1+ HT-29, CHO) -internalization/cell viability [298]
Doxorubicin & $TMPyP_4$	AS1411 (DNA)	Nucleolin	Gold (Au)	In vitro (HeLa, MCF-7, MCF-7R) -internalization/cell viability [191]
Docetaxel & Cisplatin	A10 (RNA)	Prostate specific membrane antigen	PLGA-PEG	In vitro (PSMA+ LNCaP cells) -internalization/cell viability [299]
Bcl-xL shRNA & Doxorubicin	A10 (RNA)	Prostate specific membrane antigen	PEI-PEG	In vitro (PSMA+ LNCaP cells) -internalization/cell viability [290]

1.17 Clinical Applications of Aptamers and Nanoparticles

To date there have been 27 clinical trials that utilize aptamers as single antagonists, although the majority of these do not target cancer but rather utilize pegaptanib and E10030 to inhibit $VEGF_{165}$ in age related macular degeneration and related diseases [122, 272, 273]. Four studies determining the efficacy of single aptamer therapies for cancer-related malignancies were completed in the last eight years, one with EYE001and three with AS1411. PEGylated aptamer EYE001 has high affinity toward isoforms of VEGF, and the genetic mutation found in Hippel-Lindau (VHL) disease up-regulates the production of VEGF. An open label phase I study concluded in 2008

piloted the use of anti-VEGF therapy (EYE001) in 5 patients as a treatment for retinal angioma associated with late stage VHL (NCT00056199). The nucleolin AS1411 aptamer [300] readily internalizes into cells, and is believed to have intrinsic pro-apoptotic properties at least in part through disruption of Bcl-2 mRNA transcripts, as demonstrated in breast cancer cell lines MCF-7 & MDA-MB-231 [155]. A phase I trial (NCT00881244) of patients with nonspecific advanced solid tumors determined tolerable dosage profiles and pharmacokinetics followed by a single arm phase II trial (NCT00740441) as a neoadjuvant therapy in patients suffering from metastatic renal cell carcinoma (MRCC), as well as an open-label randomized controlled dose escalating phase II trial (NCT00512083) as an adjuvant therapy in combination with cytarabine in patients with primary refractory or relapsed AML (acute myeloid leukemia). Subsequent additional arms of the trial were granted concerning patients with AML between the years 2009 to 2011 but were terminated (NCT01034410). Unfortunately no study results have been posted for any of the completed trials but the continued progression of aptamer development and the push toward aptamers as primary treatments is encouraging.

Currently nearly 300 clinical trials deliver chemotherapeutic or alternative cytotoxic payload encapsulated by nanoparticles to patients with solid tumors and recurring malignancies (*clinicaltrials.gov*). The majority of ongoing trials utilize paclitaxel-loaded micelles (nab-paclitaxel, ABI-007) composed of a negatively charged albumin shell which creates both an amphipathic surface to promote cell interaction as well as a hydrophobic core which promotes solubility of lipophilic paclitaxel and reduces cytotoxic allergic reactions [301]. Adjuvant nab-paclitaxel has been investigated as a

treatment for pancreatic, breast, ovarian, melanoma, peritoneal, lung, bladder, gastric, and esophageal cancers.

Other formulations include: (i) paclitaxel-loaded PEG-polyaspartate copolymers (NK105) [302] that are currently in a multi-national phase III clinical study comparing NK105 versus Paclitaxel in patients with metastatic or recurrent breast cancer malignancies (NCT01644890); (ii) Rapamycin-loaded albumin-based micelles (nab-rapamycin) structurally identical to nab-paclitaxel were used in a phase I trial for advanced non-hematologic malignancies (NCT00635284); (iii) an active phase II trial with docetaxel-loaded polystyrene nanoparticles (BIND-014) used in patients with non-small cell lung carcinoma (NSCLC, NCT02283320); (iv) campothecin loaded cyclodextrin polymeric nanoparticles (CRLX101, C-VISA BikDD) were used in a completed phase II trial in patients with advanced metastatic NSCLC (NCT01380769), and two currently recruiting phase I/II trials in combination with Bevacizumab for recurrent ovarian and peritoneal cancer (NCT01652079) or in combination with Capecitabine for rectal cancer (NCT02010567); (v) campothecin semisynthetic analogue irinotecan hydrochloride has been loaded into nanoliposomes (nl cpt-11) and albumin nanoparticle (FOLFIRABAX) used in phase I (NCT00734682) or I/II trials (NCT02333188) respectively in patients with multiple malignant disorders; and finally (iv) an alternative approach using direct linkage of Au nanoparticles to platinum-based oxaliplatin and PEGylated-TNF allowed higher tolerated doses and possibly treatment efficacy in a phase I trial [257].

The incorporation of gene therapy plasmids or small interfering RNA (siRNA) into lipid-based nanoparticles for anti-tumor targeting has become one of the more

promising areas of translational development. The anti-cyclin G1 gene construct (Rexin-G) in a stable lipid particle suspension had promising results in both phase I and phase II trials for breast (NCT00505271), soft tissue sarcoma (NCT00505713), osteosarcoma (NCT00572130), and pancreatic cancer (NCT00504998) but no results have been reported. Despite this success, anti-cyclin G1 Rexin-G is a paradigm in the length of time to bring new therapeutics to bedside. Cyclin G1 was identified more than a decade ago, followed by laboratory mouse studies, Phillipine FDA approval (2007) [111]. A similar gene therapy approach with FUS1 tumor suppressor gene expression plasmid-loaded nanoparticles for lung cancer has also reached phase I trials (NCT01455389). Incorporation of siRNA into lipid-based nanoparticles include: (i) anti-myc DCR-MYC currently in two phase I/II trials for patients with advanced solid tumors, multiple myeloma, lymphoma, hepatocellular carcinoma non-Hodgkins lymphoma (NCT02110563 & NCT02314052); (ii) anti-PLK1 TKM-080301 currently in phase I trials for liver tumors [303], and anti-ribonucleotide reductase CALAA-01 previously in a phase 1a/1b trial for non-specific solid malignancies that initially gave promising results with similar pharmacokinetic profiles to treatments in rat, mice, and primate models but which was subsequently terminated prematurely [304].

New experimental treatment approaches synergize the advantages between nanoparticle technology and ionizing radiation for anti-cancer therapy. Hafnium oxide nanoparticles (NBTXR3) have a high electron density enable the transfer of high dose energy to target cells following ionizing radiation treatments. The increased radio-enhancement could increase the efficacy of current radiation therapies while maintaining low exposure levels in neighboring tissues[305], [306]. A NBTXR3 intra-tumor

implantation phase I trials was recently concluded in patients with soft tissue sarcomas (NCT01433068) as well as phase II trials in progress for patients with soft tissue sarcomas (NCT02379845) will ascertain the efficacy of nanoparticle-based ionizing radiation therapy.

Several nanoparticle-based technologies are in clinical trials for imaging of tumors that aid not only in early detection and diagnosis but also in direct surgical removal of malignant tissue or cells. MagProbe is a clinical tool for detection of multiple hematopoietic malignancies including acute leukemia. Phase I trials began in 2011 with an estimated enrollment of 60 patients and was concluded in December 2013 but no results have been disclosed (NCT01411904). The system utilizes ultra-small superparamagnetic iron oxide nanoparticles conjugated to a CD34 antibody [307]. The inherent magnetic property enables both a more sensitive assay for detecting minimal residual disease as well as the isolation of CD34+ malignant cells from relatively small bone marrow samples. In theory this method can be used to clear these tumor cells from patients.

1.18 My Thesis

The goals of my research are as follows: (i) **I will identify aptamers that specifically bind membrane structures and internalize into individual ovarian tumor cell lines.** Then by conjugating these aptamers to a fluorescent Cy5 reporter, I can calculate the unique apparent binding constant for each aptamer as well as characterize the mechanistic internalization pathway. Unique aptamers specific to tumors could potentially be used as a diagnostic tool or molecular chaperone to localize tethered molecules to cells and promote internalization. (ii**) I will demonstrate that aptamer**

labeled NPs will promote internalization and retention of both fluorescent protein loaded and Paclitaxel loaded NPs in an *in vitro* and *in vivo* model.

Specific Aim 1: Identify aptamers by the Cell-SELEX system that bind with high affinity and internalize into Caov-3, SW626, and SK-OV-3 cells.

Specific Aim 2: To determine if Cell-SELEX identified aptamers that specifically bind and internalize into EOC tumor cells can facilitate endocytosis and internalize an aptamer labeled NP.

2.1: Measure the cellular uptake of Cell-SELEX identified aptamer labeled fluorescein diacetate loaded NPs

2.2: Measure the altered cellular proliferation after treatment with Cell-SELEX identified aptamer labeled Paclitaxel loaded NPs.

Specific Aim 3: Observe the aptamer mediated targeting and retention capabilities of an ovarian tumor specific Cell-SELEX identified aptamer labeled ICG loaded NP *in* vivo.

The methods described here could potentially lead to personalized aptamer guided drug treatments that are based on tumor specific morphology. Aptamer development in conjunction with polymeric NPs can deliver therapeutic payloads as front-line therapy for cancer treatment.

CHAPTER 2: IDENTIFICATION OF EOC SPECIFIC APTAMERS BY CELL-SELEX THAT INTERNALIZE INTO TARGET CELLS

2.1 Introduction

The objective of the work presented here was to identify ovarian tumor specific single stranded DNA probes, termed aptamers, which bind with high affinity to unique structural moieties on the cell surface. To identify epithelial ovarian cancer cell-specific aptamers I have adopted a widely used protocol named Cell-SELEX. I have modified the selection process to identify aptamers that can distinguish between neoplastic ovarian epithelial cells and non-transformed ovarian epithelial cells. The identified aptamers have been shown to specifically recognize target cells with an apparent equilibrium dissociation constant (K_d) measured in the nanomolar range but show minimal interaction with physiologically similar epithelial tumor cells and non-transformed cell lines. Further, I show that aptamers internalize into target cells thus having the potential to be utilized clinically as a diagnostic tool to aid in initial tumor detection and visualization including evidence of tumor metastasis or to direct and localized aptamer-chemotherapeutic conjugates at tumor sites.

2.2 Materials and Methods

Cell Lines and Cultures

The human ovarian adenocarcinoma cell lines Caov-3 (HTB-75), SK-OV-3 (HTB-77), and SW626 (HTB-78) were obtained from ATCC (Manassas, VA) and maintained in tissue culture 37°C 5% CO_2. Caov-3 cell lines were maintained in

Dulbecco's minimal essential medium (DMEM, GIBCO) supplemented with 10% fetal bovine serum (FBS, GIBCO) and 1% penicillin−streptomycin (GEMINI). SK-OV-3 cell lines were maintained in McCoys5a media (ATCC) supplemented with 10% FBS (heat-inactivated, GIBCO), 1% penicillin−streptomycin (GEMINI). SW626 cell lines were maintained in Leibovitz media (ATCC) supplemented with 10% FBS (heat-inactivated, GIBCO), 1% penicillin- streptomycin (GEMINI), and 1% sodium bicarbonate (7.5% w/v, Cellgro). The pancreatic carcinoma cell line Hs766T (ATCC, HTB-134) and Suit-2 [308], human cervical adenocaricoma HeLA (ATCC, CCL-2), breast adenocarcinoma cell lines MCF-7 (ATCC, HTB-22) and MDA-MB-231 (ATCC, CRM-HTB-26), murine embryonic fibroblast NIH/3T3 (ATCC, CRL-1658) were all maintained in DMEM supplemented with 10% FBS (heat-inactivated, GIBCO), 1% penicillin−streptomycin (GEMINI). Normal epithelial cell lines HEK-293 (ATCC, CRL-1573) maintained in DMEM supplemented with 10% FBS (heat-inactivated, GIBCO), 1% penicillin−streptomycin (GEMINI). The HPV immortalized human ovarian epithelial (HOSE 6-3) cells [309] maintained in Medium199/MCDB105 media (1:1, Sigma Aldrich) supplemented with 10% FBS (heat-inactivated, GIBCO), 1% penicillin--streptomycin (GEMINI), 1% sodium bicarbonate (7.5% w/v, Cellgro).

Whole Cell-SELEX

An HPLC-purified ssDNA aptamer library (Integrated DNA Technologies (IDT)) contained a centralized random sequence of 20 nucleotides flanked by fixed 5’ and 3’ 20 nucleotide sequences for PCR enrichment (5’-CTCCTCTGACTGTAACCACG-N_{20}-GCATAGGTAGTCCAGAAGCCA-3’). 2 μL of the aptamer library (100 μM) in TE was added to 8 μL H_2O with target Caov-3 cells. Samples were denatured 95°C 5 min

and cooled on ice for 5 min before treating target cells. Cooled suspension were added to 980 µL binding buffer (BB, PBS (GIBCO) supplemented with 1% *w/v* Bovine Serum Albumin (BSA, Cellgro), 4.5 g/L glucose (Sigma Aldrich), 5mM $MgCl_2$ (Sigma Aldrich). Aptamers were incubated on a monolayer of Caov-3 cells (seeded at 2.0×10^6 48 hrs prior, 37ºC 5% CO_2) in T25 flask 4°C 30 min under constant agitation in the absence of competitor. After washing with PBS (3X) for 1 min, adhesive cells were collected. Cells with aptamers were centrifuged 12,000 rpm 2 min. The supernatant was discarded and bound aptamers were eluted 95°C 5 min in 50µL 1X PBS. Eluted aptamers were collected, resuspended in 950µL BB and used for negative selection against HOSE 6-3 cells (seeded at 2.0×10^6 48 hrs prior, 37º 5% CO_2) in T25 flask 4°C 30 min under constant agitation in the absence of competitor. 1mL of BB was collected and aptamers eluted by ethanol precipitation resuspended in 20µL TE. The collected aptamers were amplified by PCR (GE HEALTHCARE illustra PuReTaq Ready-To-Go PCR beads): Primer A: 5'-gaggagactgacattggtgc, Primer B: cgtatccatcaggtcttcgga-5', Cycle: 94°C 5 min, (35 cycles) 94°C 30 sec, 62°C 30 sec, and 72°C 45 sec, followed by elongation 72°C 10 min. PCR product was concentrated using DNA Clean & Concentrator™-5 (Zymo Research) and the total volumes of recovered aptamers were used for proceeding rounds of selection. Concentrations, as detected by NanoDrop, were significantly less than initial starting concentration at the conclusion of round 1. Subsequent treatment concentration of aptamers was maintained (~100 ng) following elution of aptamers and PCR enrichment.The first and second rounds of SELEX eliminated the counter selection step, but were introduced during the 3^{rd}, 5^{th}, 7^{th} and subsequent odd rounds of selection. A total of 15 rounds of whole-cell SELEX were performed on the target cell line. Wash

strength was enhanced gradually from 1 to 2 min and flask sizes increased from T25 to T75 following and including round 10 of positive selection. To monitor the presence of aptamers through rounds of selection, aptamers from rounds 5, 8, and 12 were cloned into *Escherichia coli* by manufacturers' recommendations using a One Shot TOPO10A cloning kit (Invitrogen) then analyzed by Sequetech DNA Sequencing Service (Mountain View, California). Global sequence panels were obtained after 15 rounds of selection by Ion Torrent Next Generation Sequencing (University of North Carolina-Charlotte).

Next Generation Ion Torrent Sequencing

100 ng dsDNA PCR products was confirmed by Quant-iT™ PicoGreen® dsDNA Assay Kit (Invitrogen) and were used as template in the Ion Xpress Plus Fragment Library Kit (Invitrogen) following the protocol for short amplicons. Amplification of the prepared library was required; therefore the protocol to amplify and purify the library was followed. The amplified library was quantified using the Kapa Biosystems Library Quantification Kit for the Ion Torrent platform on a Bio-Rad MyIQ iCycler to determine the Template Dilution Factor (TDF) to be used with the Ion PGM Template OT2 200 Kit and the OneTouch 2 instrument. After emulsion PCR, the clonally amplified sample was run on the Ion Torrent PGM instrument using the Ion PGM Sequencing 200 Kit v2 and a 314 chip. Run conditions included 260 flows on the PGM instrument for sample 1 and 500 flows for sample 2.

Flow Cytometry (Binding Kinetics).

To test the binding capacity of selected ovarian aptamers-RLA01, RLA02, and RLA03 were obtained from IDT labeled with a Cy5 fluorescent dye. The binding affinity of aptamers was determined by incubating cell lines on 6-well plates (seeded at 1.0×10^{6},

incubated 48 hours) with varying concentrations of Cy5 labeled aptamer. 25µL aptamer pool in TE was added to 1 mL of cell line specific media and incubated at 37°C 5% CO_2 2 hours agitating slightly every 30 min. Cells were then washed twice with 2 mL 1X PBS, scraped in 1 mL 1X PBS, and filtered through a 35µm nylon mesh cell strainer polystyrene tube (BD Falcon). Cells were subjected to flow cytometric analysis within 1 min and fluorescent events were determined with a Becton Dickinson LSRFortessa Flow Cytometer by counting 50,000 events. A Cy5 labeled randomized unselected 60mer oligo was used as negative control. Mean fluorescent events (n=3) were recorded and used to calculate an apparent dissociation constant (K_d) for specific binding. The K_d of the fluorescent aptamers were obtained by fitting the dependence of fluorescence intensity of specific binding on the concentration of the ligands to the equation Y = B_{max*}X^h/(K_d^h + X^h) using GraphPad Prism software (2236 Avenida de la Playa, La Jolla, CA 92037). When calculating respective K_d values baseline fluorescence for untreated cells was not pre-subtracted off since detected initial auto fluorescence made no significant impact on the calculated K_d values. Concentrations of Cy5-aptamer conjugates were brought to 1600 nM to saturate the system and obtain sigmoidal curves giving the most accurate K_d values for post hoc analysis.

Flow Cytometry (Endosomal internalization)

To determine the percent internalization of Cy5-aptamer conjugates pHrodo® Red Transferrin Conjugate was used (Invitrogen). Aptamers (500 nM) were added to 1 mL cell specific media and incubated on Caov-3 cells (6-well plates seeded at 1.0×10^6 48 hrs prior, 37º 5% CO_2) and observed at 30, 60, 90, and 120 min post treatment. 30 min before pre-determined time points staining with endosomal specific marker pHrodo®

Transferrin Conjugate was done by the manufacturers' recommended protocol (25 µg/mL). Cells were then washed twice with 2 mL 1X PBS, scraped in 1 mL 1X PBS, and filtered through a 35µm nylon mesh cell strainer polystyrene tube (BD Falcon). Cells were subjected to flow cytometric analysis within 1 min and fluorescent events were determined with a Becton Dickinson LSRFortessa Flow Cytometer by counting 100,000 events. Percent internalization was calculated by the following equation: (# of dual Cy5 pHrodo Red events - # of pHrodo Red untreated background)/ # of Cy5 events.

Confocal Imaging.

Cells were seeded at 5.0×10^4 per well/plate and incubated 37°C 5% CO_2 48 hrs. 2µL Cy5-aptamer conjugates at concentration ranges of 1 µM to 25 µM was added to 1 mL cell specific media and incubated on target cells 37°C 5% CO_2 2 hours agitating slightly every 30 min on a 35, 0/10 mm glass bottom culture dish and 35, 0/10 mm glass bottom 24 well plate (Greiner bio-one). Cells were washed with PBS (3x) and fixed with 2ml heptane (1:8.25 PBS: 37% Formaldehyde (Sigma Aldrich)) 37°C 10 min. For endosomal internalization specific microscopy, cells were treated with pHrodo® Red Transferrin Conjugates by the manufacturers' recommended protocol 30 min before fixing. Endosomal internalization was observed at 30, 60, 90, and 120 min time points post initial treatment with Cy5-aptamer conjugates. Cells were washed with PBS (3x) and fixed with 2ml heptane (1:8.25 PBS: 37% Formaldehyde (Sigma Aldrich)) 37°C 10 min. Subsequent staining of fixed cells was performed with DAPI (10 ng/µL, 10 min), or cell membrane stain Wheat Germ Agglutinin Alexa 488 conjugate (1µg/µL, 10 min, Invitrogen) using standard procedures. Imaging of the cells was done with an Olympus

FluoView 1000 confocal microscope using DAPI (blue), Alexa448 (green), pHrodo® Red (orange), and Cy5 (red) filters.

2.3 Results

Cell-SELEX for Identification of Ovarian Tumor Specific Aptamers

Whole Cell-SELEX was adapted to identify aptamers that bind and potentially internalize into Caov-3, SK-OV-3, and SW626 ovarian epithelial adenocarcinoma cells [94, 310]. The Caov-3 adenocarcinoma cell line is of epithelial morphology and corresponds to late stage ovarian cancer and has been shown to express upregulated tumor biomarkers such as NB/70K, Ca-1, CEA, and Ba-2 [311]. Histological analysis confirms Caov-3 as a serous tumor subtype derived from primary tumor tissue [312]. The SK-OV-3 cell line has been characterized as a grade 1/2 serous epithelial adenocarcinoma that was isolated from peritoneal cavity fluid (ascite) [312]. Tumor associated antigen analysis of SK-OV-3 shows no evidence of NB/70K, OC-125, Ca-1, CEA, and Ba-2 [311]. Additonally, SK-OV-3 cells are characterized as resistant to multiple cytotoxic drugs including platinum taxanes [312, 313]. Although SW626 was isolated as an ovarian adenocarcinoma, genome expression evidence recently indicated it likely originated as a colorectal tumor metastasized to the ovary [314]. The SW626 cell line is representative of a grade III adenocarcinoma. All three cell lines have been shown to be tumorigenic in mouse models and genetic karyotyping shows Caov-3, SK-OV-3, and SW626 genomes to be hypotriploid, hypertriploid, and hypertetraploid respectively. To ensure aptamer target cell specificity, rounds of negative selection were carried out on human papilloma virus (HPV) immortalized human ovarian surface epithelial cells (HOSE 6-3) [309]. Morphologically HOSE 6-3 cells exhibited structurally identical

cytoskeleton filaments with that of normal ovarian epithelial cells and show no up-regulation of known ovarian tumor specific markers such as CA-125 after immortalization [309]. The non-transformed immortalized HOSE 6-3 cell line has demonstrated to be non-tumorigenic when inoculated into nude mice after 20 passages [309]. The use of HOSE 6-3 cells for negative selection was deemed significant for potential in vivo therapeutic applications in which aptamers would need to bind to malignant cells but not to neighboring non-tumor cells of otherwise similar cell type or origin. Potential aptamers were identified from an initial randomly generated ssDNA 60bp oligonucleotide library in a dual positive and negative selection process consisting of selection rounds followed with PCR enrichment prior to the subsequent round. Negative selection was done at rounds 3, 5, 7, 9, 11, and 13 which promoted identification of aptamers highly specific to malignant cells.

Monitoring Aptamer Selection and Identification of Ovarian Tumor-Specific Aptamers

Two methods to ensure complete 60mer and 80mer aptamer sequences were being recovered and enriched during the Cell-SELEX protocol. Firstly, aptamer pools from rounds 3, 8, and 12 of whole Cell-SELEX on Caov-3, SK-OV-3, and SW626 cell lines were sampled and transformed by TA TOPO10A cloning kit according to the manufacturers recommended protocol. An EcoRI digest of the DNA shows clones transformed with aptamer DNA of varying sizes as seen in Figure 4. Clones showing bands within the gel were further analyzed by Sanger sequencing. Results indicated that full length aptamers were being recovered and enriched throughout the Cell-SELEX protocol for Caov-3 and SK-OV-3 cells (Figure 4). This was confirmed by identifying PCR flanking sequences in 60mer and 80mer aptamer populations. Although positive

transformation of aptamer DNA specific to SW626 Cell-SELEX was never achieved, recovery of aptamer DNA and enrichment by PCR was continuously confirmed by NanoDrop.

The EcoRI digestion of clonal DNA result in a ~10 bp overhang on both 5' and 3' ends of the aptamer. This explains 80mer aptamers recovered in round 3 specific for Caov-3 cells showing a band at 100 bp (lane 5, 7, 10, 11, and 12 Figure 4). Sanger sequencing revealed that bands larger than expected for indicated aptamer sizes was the result of contcatemerized or 3' to 5' ligated full length aptamers. Clones analyzed from round 3 of Caov-3 Cell-SELEX (Figure 4) showed 11 distinct aptamer species with one subgroup representing 67% of the population. Additionally, sequencing of clones from round 12 of selection specific to Caov-3 cells (Figure 4) provided 10 distinct aptamer species with one of these aptamer species representing 33% of the sequenced population. Similar data was observed with SK-OV-3 specific Cell-SELEX aptamer transformations (Figure 4). Larger band sizes were the result of multiple full length aptamers intercalating into the bacterial genome during transformation. Although full length 3' to 5' ligated aptamers were seen, no clear subpopulation of aptamers was recognized. This data strongly suggests that aptamers are recovered following progressive rounds of Cell-SELEX. Additionally, as described earlier for my specific protocol, round 3 of selection was the first round involving both positive and negative selection. Aptamers from this round were exposed to two different cell lines and TOPO cloning confirmed recovery. Moreover, the results seen in rounds 3 and 8 for Caov-3 cells confirms positive enrichment of aptamers as seen by Sanger sequencing showing identical aptamer inserts in multiple clones.

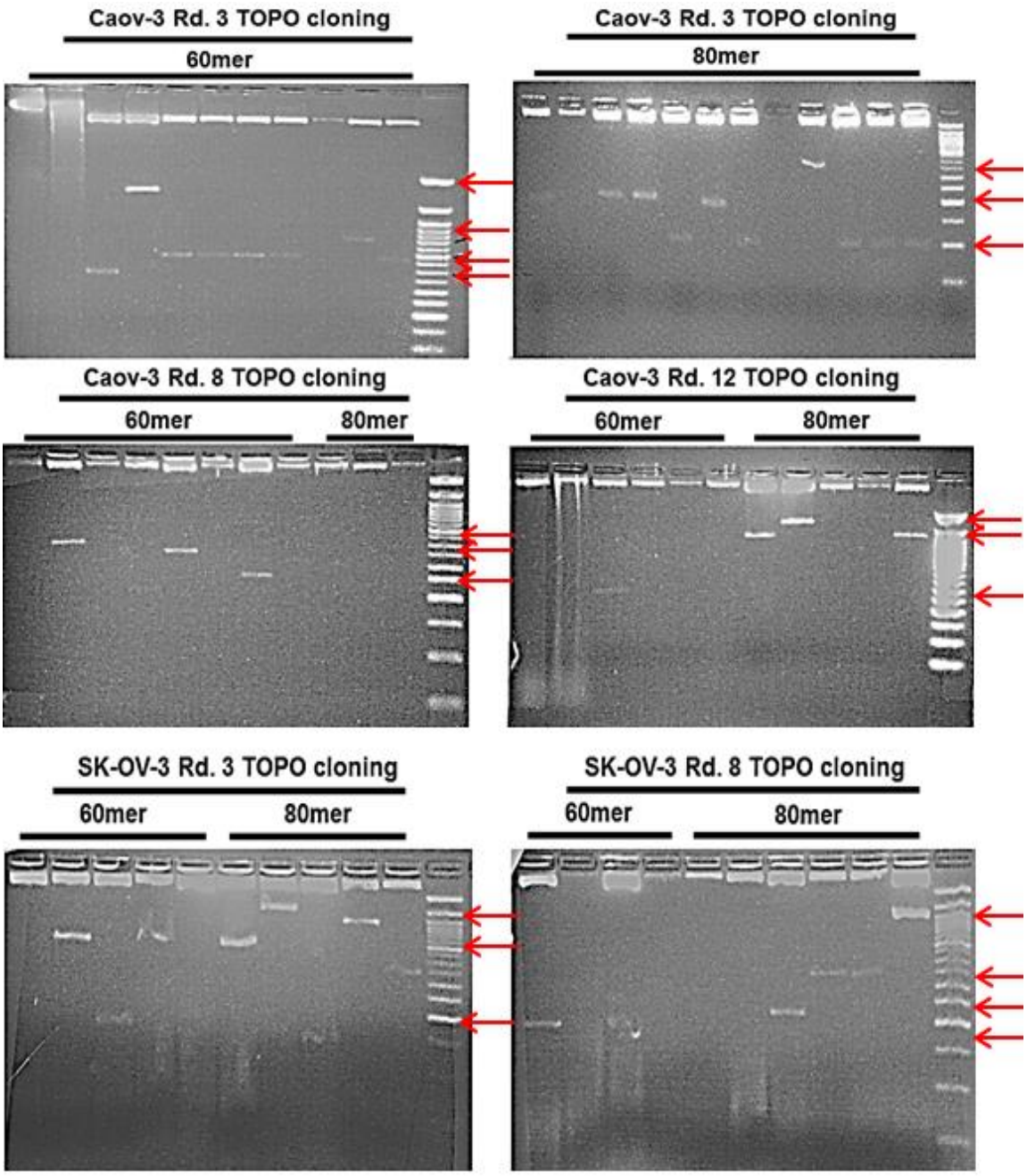

Figure 4: EcoRI digest of transformed clonal DNA shows positive recovery of aptamers during progressive rounds of Cell-SELEX for SK-OV-3 and Caov-3 cells. Clones scored by X-gal (5-Bromo-3-indolyl β-D-galactopyranoside) metabolism for positive intercalation of aptamer DNA were isolated and expanded at 37º overnight in ampicillin-LB broth. Following DNA extraction 2µg of clone specific DNA was subjected to digestion by EcoRI enzyme for 2 hours 37º. Digested DNA showing presence of inserted DNA from rounds of Cell-SELEX selection were analyzed by Sanger sequening.

A second way of monitoring aptamer enrichment is by observing the increase of fluorescent events between successive rounds of Cell-SELEX with Cy5 labeled aptamers. Again aptamers from round 3, 8, and 12 of selection were sampled and enriched by PCR. Pools of Cy5 labeled aptamers were generated using 5' Cy5 labeled and 3' biotin labeled primers for PCR. This creates a double stranded PCR product consisting of a 5'-Cy5 labeled aptamer and a 3'-biotin labeled antisense strand. The PCR product was cleaned and concentrated with a Zymo DNA cleaner kit by the manufacturers recommended protocol. Cleaned PCR product was heated at 95ºC to dissociate the dsDNA and mixed with streptavidin beads. The beads bind with antisense biotin labeled ssDNA strands that are then isolated when exposed to a magnetic field. The remaining supernatant is rich with Cy5 labeled aptamers and quantified by NanoDrop.

I added 500 ng of Cy5 labeled aptamer stock from the indicated rounds of selection to cell specific media. Cells and aptamers incubated for 2 hours, washed twice with 1x PBS, and collected by scraping. Cells were passed through a nylon mesh to prevent clumping and immediately analyzed by flow cytometry. Populations of SK-OV-3, Caov-3, or SW626 cell lines that bind to cell specific Cy5 labeled aptamers were quantified and shown in Figure 5. In addition to PCR amplifying fluorescently labeled aptamers from rounds 3, 8, and 12 of Cell-SELEX, I amplified the initial random library to establish any baseline fluorescent activity and demonstrate the importance of the selection process. The right shift in the histograms is showing an increase in fluorescent events when cells are treated with successive rounds of cell specific Cy5 aptamer pools. Levels of detectable fluorescence in round 3 (blue) are similar to the fluorescent events seen when cells are treated with aptamers from the initial random library (red). For all

cell lines round 8 (orange) and round 12 (green) cell specific aptamer treatments yielded significantly higher populations of cells with Cy5 associated fluorescence. This is due to the increase of cell line specific aptamers being enriched during Cell-SELEX and adhering or internalizing into target cells.

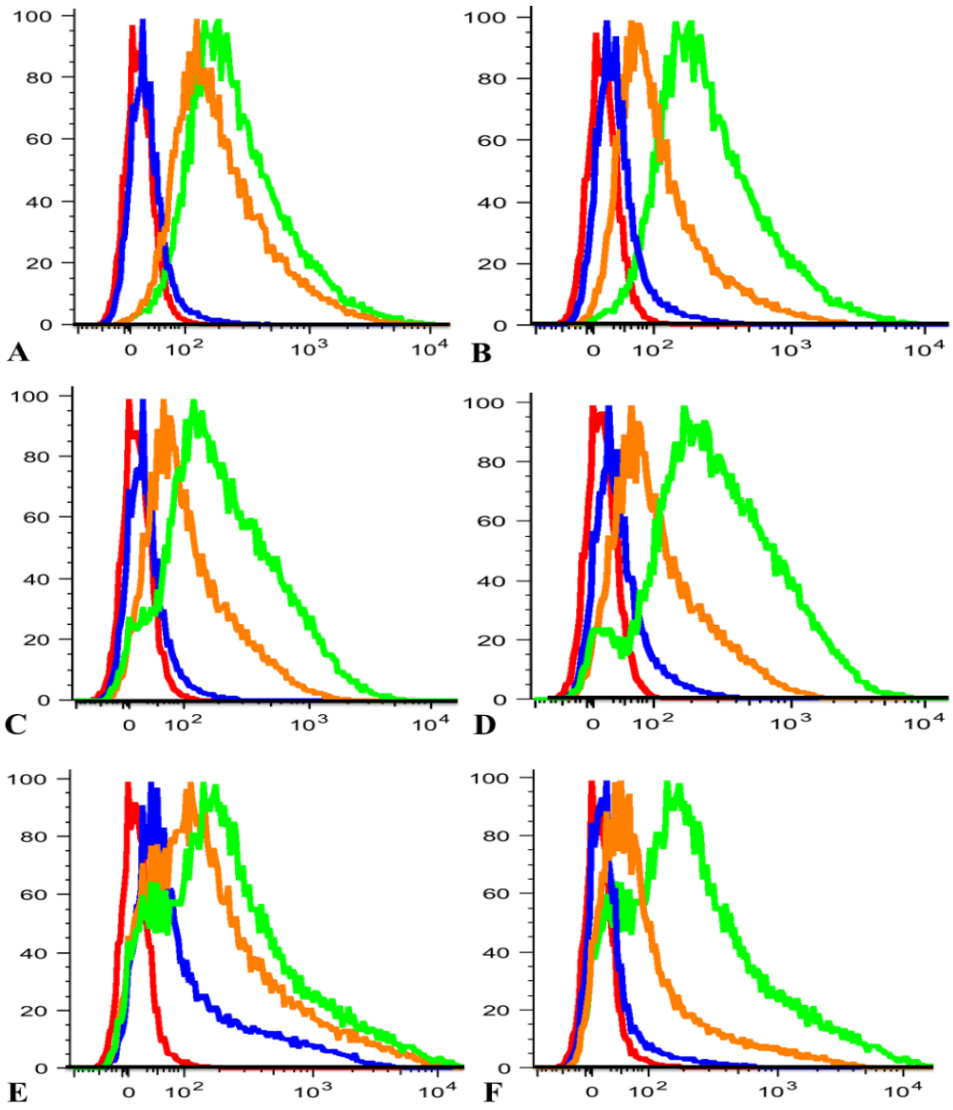

Figure 5: Monitoring the enrichment of aptamers by flow cytometry. Flow cytometry histograms are shown for Cy5-labeled aptamer pools from successive rounds of Cell-SELEX incubated on Caov-3 (A & B), SK-OV-3 (C& D), and SW626 (E & F) cells. Cells were treated with Cy5 labeled aptamers and incubated at 37°C 5% CO_2 2 hours. Aptamer rounds of selection: initial random library ( ), round 3 ( ), round 8 ( ) and round 12 ( ).

In order to characterize the complete aptamer population at the final round of selection, I used Next Generation Sequencing (NGS) on the Ion Torrent Personal Genome Machine (PGM) platform. After round 15 of Cell-SELEX on Caov-3, SK-OV-3, and SW626 cell lines I did a final enrichment by PCR and cleaning to concentrate respective pools of aptamers. To sequence the aptamer pools I followed the manufacturer's operating procedure for the PGM instrument and Ion PGM Sequencing 200 Kit v2. One modification from within the protocol was made; the option to electrophoretically elute size specific aptamers by Pippin Prep was omitted. Due to the sequencing data produced after TOPO cloning analysis data suggests that there could be end-to-end aptamer ligation during the initial preparation of the aptamer DNA pool with the Ion Xpress Plus Fragment Library Kit. A step requiring the ligation of PCR flanking regions to amplify the existing aptamer pool before sequencing could lead to unexpected ligation of aptamers that would result in larger than predicted aptamer sizes. I felt it necessary to not limit potential reads that could elucidate more information about aptamer sequence homology within the final round 15 pool of cell specific aptamers.

Aptamer pool libraries specific to SW626 (60mer) were analyzed after sequencing on an Ion Torrent 314 chip and resulted in 44% chip loading efficiency returning 9% usable reads. This resulted in 34,613 DNA reads but subsequent sequencing analysis returned no evidence of full length aptamers within the pool. However, analysis was only done searching for known forward and reverse PCR flanking regions of aptamers. In order to identify any potential sub-populations of sequences showing homology within the SW626 pool, more analysis must be done on the sequenced library. Sequencing of the SK-OV-3 (80mer) aptamer pool returned less than 5% loading efficiency resulting in

less than 10,000 usable reads. Mean read lengths of the pool were lower than expected and subsequent sequencing analysis has identified no aptamer species or sequence homology. At this time neither SK-OV-3 nor SW626 specific apatmer pools have been re-sequenced despite evidence of aptamer DNA recovery as seen by TOPO cloning and flow cytometry (Figure 4 & 5). These data strongly suggest that aptamer DNA has been both recovered and enriched throughout the Cell-SELEX process on both SW626 and SK-OV-3 cell lines, and the poor results from sequencing could be due to loading error or a preparatory step within the sequencing protocol.

Ion Torrent sequencing for both 60mer and 80mer Caov-3 specific aptamer pools resulted in more promising data. When analyzing the 80mer Caov-3 aptamer pool data showed a 49% loading efficiency resulting in 144,441 reads. Searches for forward and reverse known PCR flanking regions returned 3 unique sub-populations of truncated aptamers. Aptamer populations contained complete 5' PCR flanking regions but no 3' region. Truncated complimentary antisense stands were also recovered in the sequencing pool. It was evident that the three sub-populations of aptamers contained a unique 40mer random sequence. Alignment of the 40mer random sequence within the sub-population shows 98% to 100% homology. It is also noteworthy that sequencing identified aptamer sub-populations numbering in the hundreds and in some cases several thousand aptamers. The aptamers recovered were truncated but this data strongly suggest that aptamers were selected for and enriched through the Cell-SELEX protocol. During analysis of the 60mer aptamer pool data showed a 53% loading efficiency resulting in over 293,000 reads. Subsequent searching for aptamer PCR flanking regions returned full length aptamers from the sequencing data. From an initial random pool of approximately 4^{20}

sequences, my sequencing data identified 7 full-length aptamers within the final aptamer pool. Aptamers were identified in a 5' to 3' configuration as well as complimentary anti-sense strands. Given the flow cytometry data and the identification of 7 unique aptamers in sequencing data from the initial randomized pool, the Cell-SELEX protocol was terminated after 15 rounds. Here I will report on three of these aptamers termed RLA01, RLA02, and RLA03. Table 3 highlights all the sequences identified within the 60mer Caov-3 aptamer pool.

Table 3: Sequences of identified aptamers by Cell-SELEX specific for Caov-3 ovarian tumor cell lines

Aptamer	Sequence
RLA01	CTCCTCTGACTGTAACCACGCGGAAAGCATCAGGGTTGAGCATAGGTAGTCCAGAAGCCA
RLA02	CTCCTCTGACTGTAACCACGAGAAGGTCCAGAGAGTAGTGGCATAGGTAGTCCAGAAGCCA
RLA03	CTCCTCTGACTGTAACCACGCTACGGTTCGGAGGACACCCGCATAGGTAGTCCAGAAGCCA
RLA04	CTCCTCTGACTGTAACCACGCGAGGGGCGGACAGGGGAGGCATAGGTAGTCCAGAAGCCA
RLA05	CTCCTCTGACTGTAACCACGGATCAGGGGAAACTCCAGTGGCATAGGTAGTCCAGAAGCCA
RLA06	CTCCTCTGACTGTAACCACGTGACTAATTAGAGGTGGATCGCATAGGTAGTCCAGAAGCCA
RLA07	CTCCTCTGACTGTAACCACGTTATGAATTGGCGCCGGGGAGCATAGGTAGTCCAGAAGCCA
Scrambled Aptamer	ACTCAACGAACGCTGTGGATGCGACATAGCTAGCAGCGCATATGTATGTACATGGACATCT

Predicting Tertiary Structures of Aptamers

In order to predict the most stable structure for RLA01, RLA02, and RLA03, I used UNAfold (Rensselaer Polytechnic Institute). Ranking of the stability for aptamers RLA01, LA02, and RLA03 is based on Gibbs free energy and yielded ΔG values of -2.4, -4.91, -4.24 kcal/mol respectively. RLA01 and RLA02 exhibit a large central loop with small hairpin tructures radiating from the main loop. RLA03 will form a longer structure consisting of an external loop-hairpin-loop-hairpin-loop structure. Figures detailing the top energetically stable secondary structures of aptamers RLA01, RLA02, and RLA03 are available in supplemental data (Figure 6).

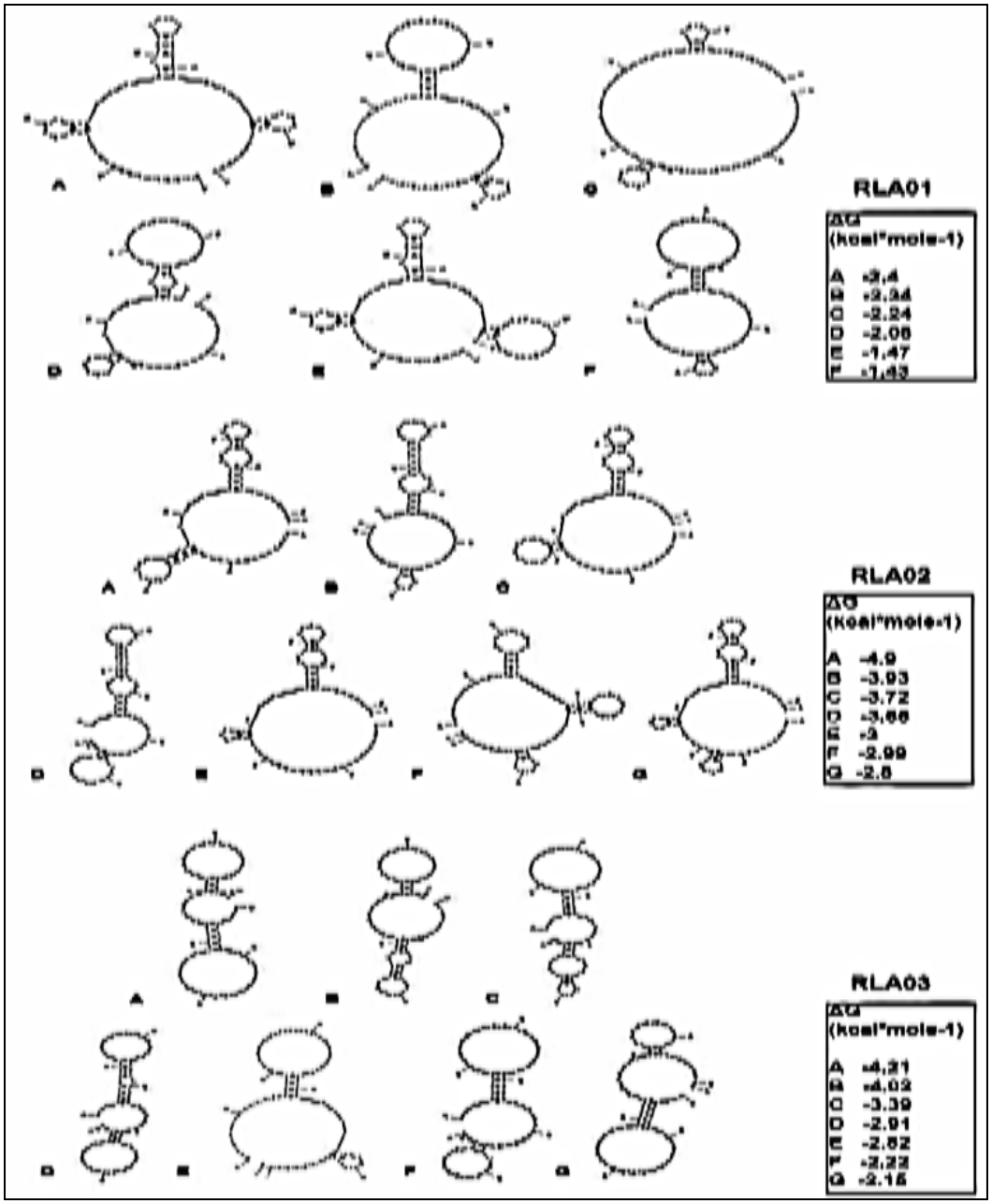

Figure 6: Predicting energetically stable tertiary structures of aptamaers RLA01, RLA02, and RLA03. To predict probable secondary structures of aptamers, nucleotide sequences were analyzed by UNAFold software. The top energetically stable structures as determined by Gibbs free energy equation analyzed at 20°C are shown for aptamers RLA01, RLA02, and RLA03. Corresponding ΔG values are given for each structure in tables provided above.

Specificity of aptamer binding and internalization to target cells: Determining Aptamer Binding Kinetics

Flow cytometry was used to quantify aptamer binding activity. RLA01, RLA02, and, RLA03 were evaluated to determine the binding kinetics of each and calculate apparent equilibrium dissociation constants (K_d). The aptamers were conjugated to cyanine dye Cy5 on the 5' end to enable detection by flow cytomerty and quantify the number of cells that bind to the target aptamer. Additionally, a random scrambled aptamer also conjugated to Cy5 was used as a negative control to demonstrate specificity. Target EOC Caov-3 cells were treated with increasing molar concentrations of Cy5-aptamers for 2 hr. Following washing of excess unbound aptamer, cells were analyzed by flow cytometry to quantify Cy5 fluorescence. To establish baseline fluorescence, untreated Caov-3 cells were also analyzed and gating of the background fluorescence was set to 0.01% of the total population analyzed (data not shown). As expected, no fluorescent events above the background gate were observed when Caov-3 cells were incubated with the random scrambled aptamer at concentrations up to 1.6 µM (data not shown). RLA01, RLA02, and RLA03 all demonstrated a dose-dependent increase in binding to target Caov-3 cells (data not shown). Binding of each of the aptamers to Coav-3 cells was highly specific since minimal binding events were detectable by flow cytomerty when any were incubated with either of the analogous epithelial ovarian tumor cell lines SK-OV-3 or SW626 (data not shown). From the flow cytomerty data (Figure 7), respective apparent K_d values for RLA01, RLA02, and RLA03 to Caov-3 cells were calculated in the nanomolar range as 16.02 ± 4.14 nM, 12.73 ± 2.29 nM, and 118 ± 7.64 nM, respectively (Table 4).

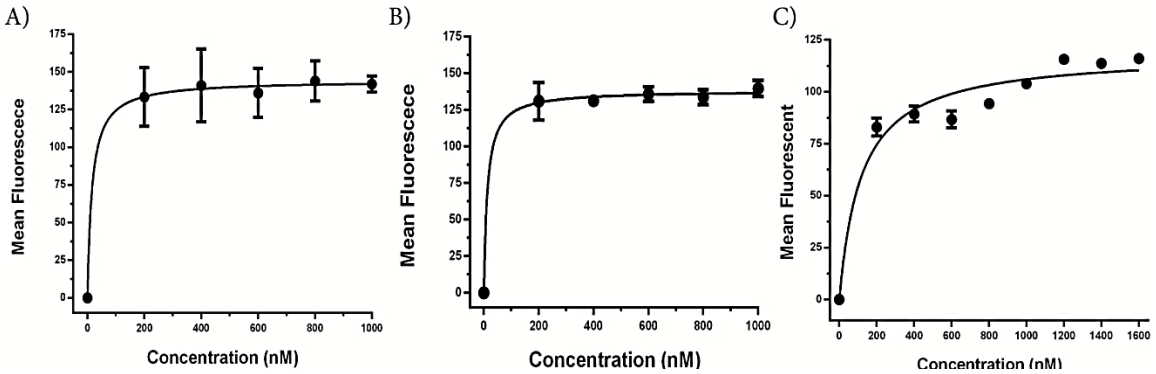

Figure 7: Binding kinetics of ovarian tumor specific aptamers to determine equilibrium dissociation constants (K_d) to ovarian tumor cell lines. To assess target cell and aptamer binding affinities I used flow cytometry to quantify mean Cy5 fluorescence to demonstrate binding and specificity to an ovarian epithelial malignant cell line Caov-3 (●). Data points represent the average mean fluorescence ovbserved (n=3, error bars ±SD) at indicated nM concentrations A) Cy5-RLA01 aptamer conjugates with Caov-3 target cells in increasing nM doses. B) Cy5-RLA02 aptamer conjugates with Caov3 target cells in increasing nM doses. C) Cy5-RLA03 aptamer conjugates with Caov-3 target cells in increasing nM doses. Individual apparent K_d values were calculated by using the equation Y=Bmax*X^h/(K_d^h+X^h) for the three DNA aptamers.

Table 4: Characterization of identified Caov-3 aptamer binding kinetics with target and non-target cells

	Ovarian			Normal		Cervical	Breast		Pancreatic		Murine
	Caov-3	SK-OV-3	SW626	HEK293	HOSE 6-3	HeLa	MDA-MB-231	MCF-7	Suit-2	Hs766t	NIH 3T3
RLA01	+++ 16.02 ± 4.14	+	-	-	-	+	-	-	-	-	-
RLA02	+ 12.73 ± 2.29	-	-	-	-	-	-	-	-	-	-
RLA03	++ 118 ± 7.64	-	-	-	-	-	-	-	-	-	-

K_d= nM

+++: >15% of total cell population showing Cy5 fluorescent events

++: 10%-15% of total cell population showing Cy5 fluorescent events

+: <10% of the total cell population showing Cy5 fluorescent events

-: <1% of total cell population showing Cy5 fluorescent events-K_d undetermined

Imaging by Confocal Microscopy

Aptamer specificity was further demonstrated by comparison of Cy5-aptamer binding to a large panel of cell lines. Incubation with both 400 nM (Figure 8A-blue) and 800 nM (Figure 8A-green) Cy5-RLA01 for 2 hr produced a right shift in the fluorescent Caov3 cell population over untreated cells, consistent with an increase in aptamer-cell interaction. By contrast minimal shift of the population above baseline was observed with either non-transformed HOSE 6-3 cells or kidney epithelial HEK293 cells when incubated with increasing molar concentrations of Cy5-RLA01, Cy5-RLA02, or Cy5-RLA03 (Figure 8A). This was further demonstrated by confocal microscopy as seen in Figure 8C. Cell-aptamer interactions were observed with Cy5-RLA01 when incubated with SK-OV-3 and HeLa cell lines (Figure 8D). Although flow cytometry confirms aptamer-cell binding for both HeLa and SK-OV-3 cell lines, the average fluorescent events observed were significantly less for both when compared to RLA01 binding to Caov-3 cells and showed no interaction with the scrambled aptamer at equal doses (Figure 8D).

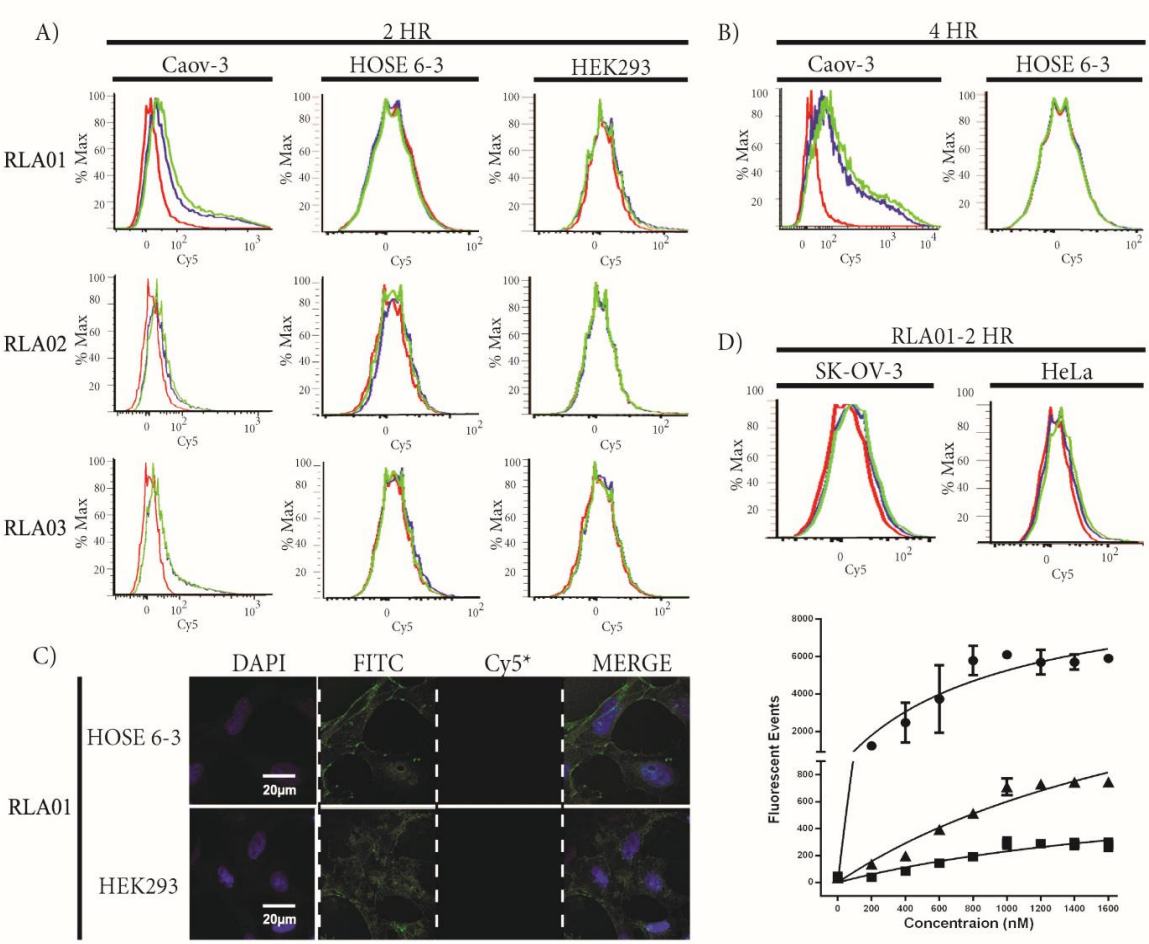

Figure 8: Dose-dependent and time-dependent specificity of aptamer binding to target cells but no interaction with non-malignant epithelial cells by flow cytometry and confocal microscopy. RLA01 aptamers were incubated at increasing concentrations and times to normal and malignant epithelial cell lines. A) Cy5-RLA01, RLA02, and RLA03 incubated with indicated cell lines for 2 hours. Aptamer doses corresponding to colored hisotgrams are control **(■)**, 400nM **(■)**, and 800nM **(■)** concentrations. B) Cy5-RLA01 incubated with indicated cell lines for 4 hours. C) Confocal imaging of indicated cell lines treated with RLA01 imaged at 60X using a nuclear stain (DAPI-blue), a membrane stain (WGA-Alexa Fluor 488-green), and Cy5-aptamers (Cy5 pseudocolored as yellow). D) Binding kinetics of RLA01 when increasing molar conentrations are incubated with Caov-3 **(●)**, SK-OV-3 **(■)**, and HeLa **(▲)**. Data points represent the average fluorescent events ovbserved (n=3, error bars ±SD) at indicated nM concentrations.

Specificity of all three aptamers was further demonstrated with a large panel of immortalized nonmalignant epithelial and multiple malignant epithelial cell lines

including two malignant pancreatic epithelial carcinomas (Suit-2, Hs766t), two mammary epithelial adenocarcinomas (MCF-7, MDA-MB-231), one cervical epithelial adenocarcinoma (HeLa), two ovarian epithelial adenocarcinoma cell lines (SK-OV-3, SW626), as well as kidney epithelial cells (HEK293), and murine fibroblast NIH/3T3 cells. Kidney epithelial tissue was chosen because kidneys play a major role in removal of organic waste from the bloodstream thus would impact potential clinical use by intravenous delivery of aptamers. Aptamer-binding events were minimal or undetectable as shown by flow cytometry when incubated with malignant cell lines in increasing molar concentrations (Table 4). Binding of aptamers was also time dependent (Figure 8B). Increasing incubation time of Cy5-RLA01 with Caov-3 cells from 2 hr to 4 hr produced 275% more fluorescent events while fluorescent events in HOSE 6-3 cells remained similar to baseline controls (Figure 8B).

Specific binding and internalization of RLA01, RLA02, and RLA03 to Caov-3 cells was demonstrated by flow cytometry and confocal imaging (Figure 9). Cell membranes were identified by Wheat Germ Agglutinin conjugates labeled with Alexa Fluor® 488 enabling identification of two key cellular structures: (i) the cell membrane where Cy5-aptamer conjugates are predicted to localize upon initial target recognition, and (ii) the internal endosomal membranes where aptamers are expected to localize to if efficiently internalized into cells. Images of aptamer specific binding and endosomal internalization were assessed as early as 30 min and up to 2 hours post initial treatment of Cy5-aptamer conjugates ranging in dosages of 1 µM to 25 µM. Supporting the flow cytometry data, no internalization at any dose was observed with scrambled aptamer

(Table 3). Aptamers RLA01, RLA02, or RLA03 (pseudo-colored yellow) localized on and around membranes of Caov-3 cells (Figure 9A).

The observed Cy5 fluorescent signals appeared at or near the membranes similarly to that of the Alexa Fluor® WGA stain. All three aptamers localized to the cell membranes (Figure 9A). In addition, all three localized to multiple compartments within the cytoplasm proximal to the membranes suggesting endosomal internalization. Internalization of Cy5-aptamer (500 nM) conjugates was measured by flow cytometry at 30, 60, 90, and 120 minutes post initial treatment with aptamer RLA01 on Caov-3 cells (Figure 9B). Additionally, the percent of internalization events above background over the same range of time is shown in Figure 9C. These data were further confirmed by confocal imaging. I used the endosomal marker pHrodo® Red Transferrin Conjugate to identify co-localization of Cy5-aptamer conjugates (5 µM) and endosomal structures. As seen in Figure 9D pHrodo® Red stained endosomal structures (pseudo-colored red) co-localize with Cy5 fluorescent aptamers (pseudo-colored yellow). These data are highly suggestive that the internalization of aptamers into Caov-3 cells is regulated by endocytic pathways. Moreover, Z-stack imaging (20 stacks, 2 µm range) further demonstrated Cy5 fluorescence within cells consistent with internalization of aptamers (Figure 10). Thus, confocal imaging of all three Cy5-aptamer conjugates demonstrated fluorescent activity consistent with the average max fluorescent events observed by flow cytometry (Figure 7A, B, C and Figure 9).

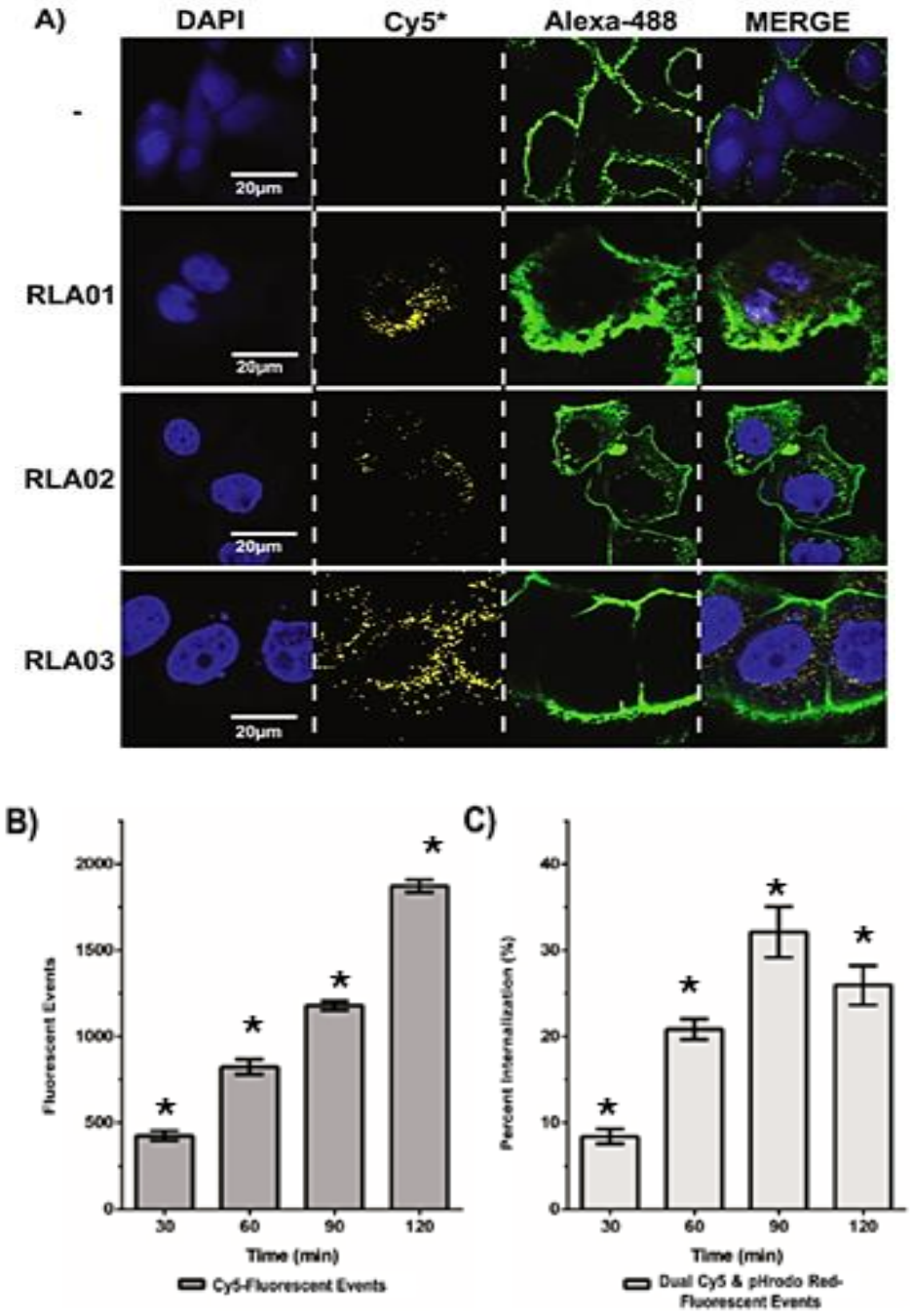

Figure 9: Internalization of aptamers into Caov-3 cell lines occurs through the endocytic pathway. A) Caov-3 cells were treated with Cy5 conjugated aptamers. Untreated (-) and Cy5-aptamer RLA01, RLA02, and RLA03 conjugate treated cells were imaged at 60X using a nuclear stain (DAPI-blue), a membrane stain (WGA-Alexa Fluor 488-green), and Cy5-aptamers (Cy5 pseudo-colored as yellow). B) Graph represents the Cy5 fluorescent events observed after a 500 nM treatment of Cy5-RLA01 conjugates over 2 hr time period. C) Percentage of cells showing positive endocytic internalization of aptamers confirmed using pHrodo Red Transfeffin Conjugate measured above background. Caov-3 cells were treated with 5 µM Cy5 conjugated aptamers.

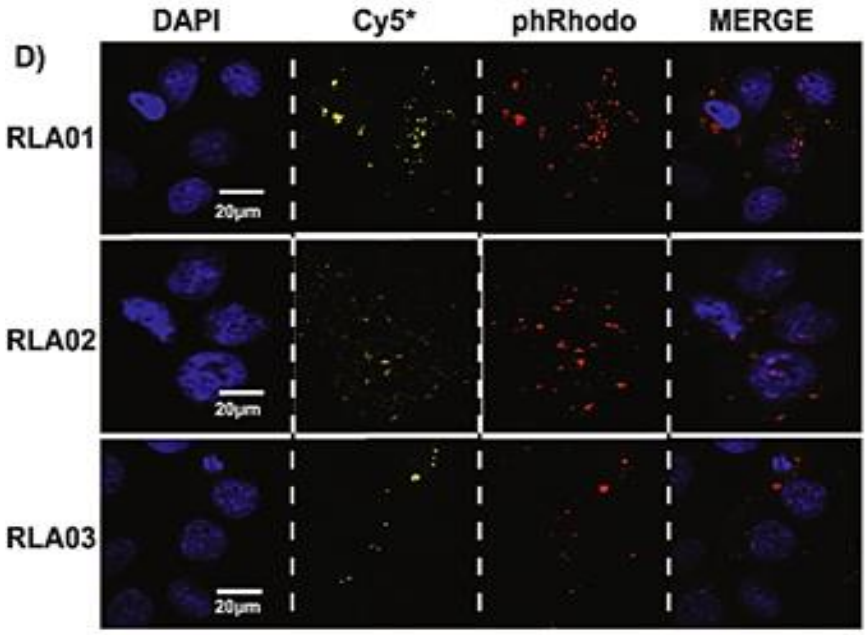

Figure 9: continued: D) Cy5-aptamer RLA01, RLA02, and RLA03 conjugate treated cells were imaged at 60X using a nuclear stain (DAPI-blue), an endosomal specific marker (pHrodo Red pseudo-colored red), and Cy5-aptamers (Cy5 pseudo-colored as yellow). All images at 60X. $P < 0.01$.

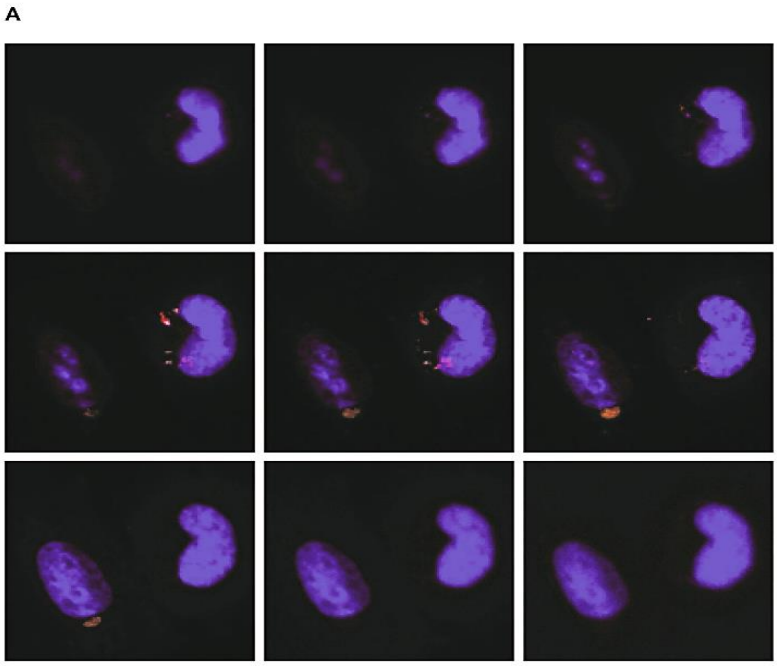

Figure 10: Endosomal internalization of RLA01 as demonstrated by confocal micrscopy z-stack imaging**.**

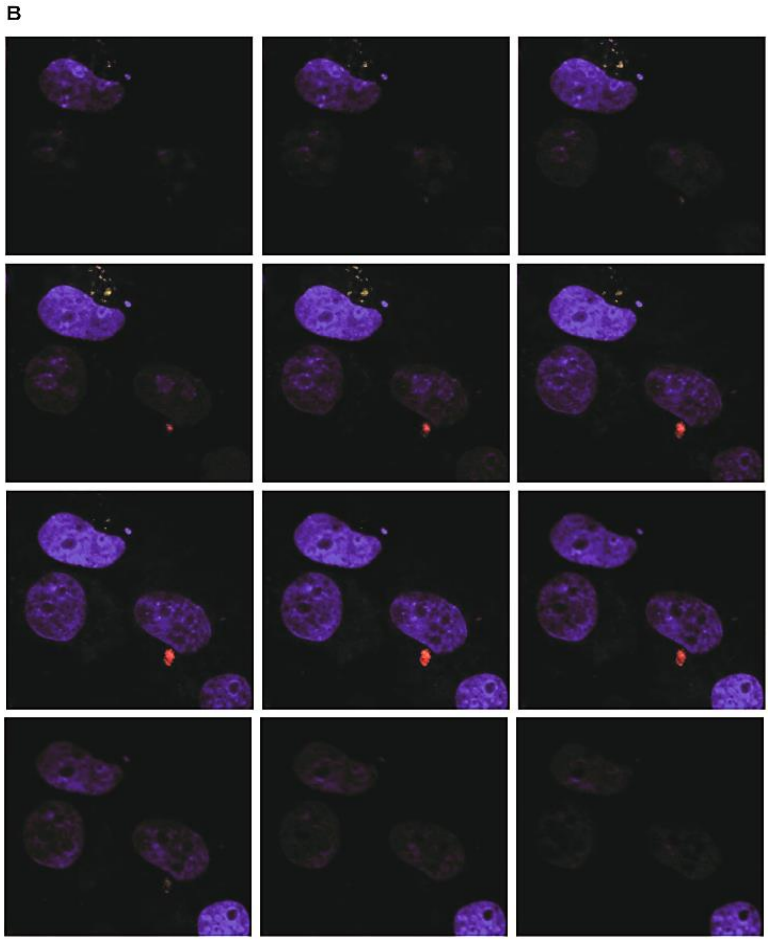

Figure 10 continued: Confocal imaging of Caov-3 cell lines treated with Cy5-RLA01 imaged at 60X using a nuclear stain (DAPI-blue), endosomal specific marker pHrodo Red Transferrin Conjugate (rhodamine psuedo-colored as red), and Cy5-aptamers (Cy5 pseudo-colored as yellow). Figure 10A: 9 image z-stack .35 µm slices. Figure 10: continued 10B: 20 image z-stack .25 µm slices.

Confocal imaging was also employed to further demonstrate aptamer specificity. The three Caov-3 target aptamers were incubated with a panel of selected EOCs, malignant epithelial, and non-malignant immortalized cell lines (Figure 11). Consistent with the flow cytometry histograms shown in Figures 8A and 8B with Cy5-RLA01, fluorescent events were not detected above baseline untreated control levels when increasing molar concentrations of Cy5-RLA03 were administered to non-malignant HOSE 6-3 and HEK293 epithelial cell lines (Figure 11). Additionally, incubation of

Cy5-RLA03 conjugates with malignant epithelial cell lines produced minimal fluorescent events similar to those of untreated control samples. Overall, the full range of Cy5-RLA03 concentrations used for incubation with malignant epithelial cells showed no fluorescent events after a 2 hour incubation period, and this was further supported by confocal imaging (Figure 11). Cy5-RLA02 conjugates produced similar data to the Cy5-RLA03 conjugates. Cy5-RLA02 demonstrated no binding to the panel of malignant and non-malignant cell lines (data not shown). Despite observing detectable fluorescent events when SK-OV-3 and HeLa cell lines were incubated with increasing molar concentrations of RLA01 (Figure 8D), data obtained by flow cytometry against the panel of malignant and non-malignant cell lines showed no total fluorescent events above untreated control baseline levels, also supported by confocal imaging (data not shown).

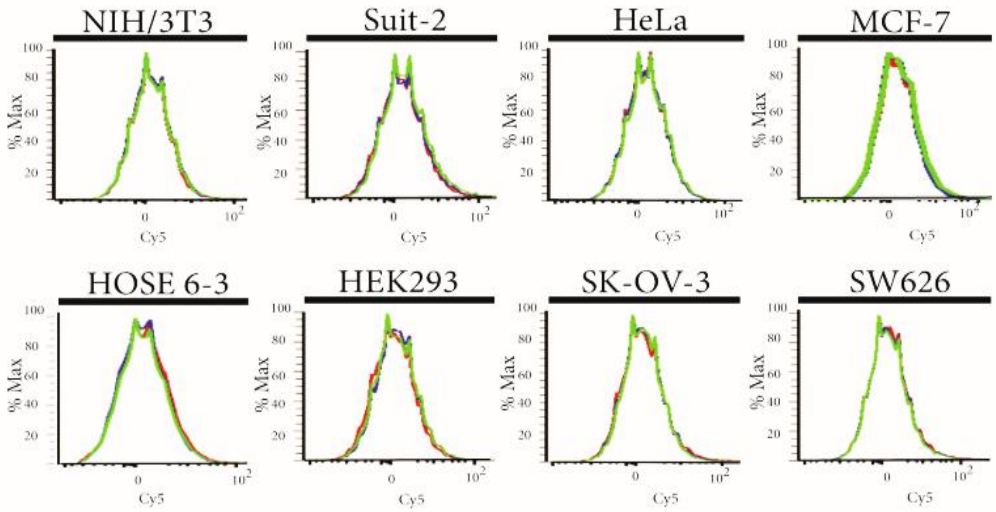

Figure 11: Flow cytometry and confocal imaging to demonstrate specificity of RLA03 to Caov3 cells with no evidence of binding across of a panel of malignant disorders. Epithelial malignancies from breast (MCF-7), pancreatic (Suit-2), cervical (HeLa), and EOC model cell lines SK-OV-3 as well as SW626 were incubated with Cy5-RLA03 aptamer conjugates. Non-malignant immortalized HOSE 6-3 (ovarian epithelial), HEK293 (kidney epithelial), and murine fibroblast (NIH/3T3) were included to demonstrate RLA03 specificity. Flow cytometry histograms (above) and corresponding confocal imaging (below) are shown for Cy5-RLA03 conjugates incubated with indicated cell lines for 2 hours. Cy5-RLA03 doses corresponding to colored hisotgrams are control **(■)**, 400nM **(■)**, and 800nM (■ **)** concentrations.

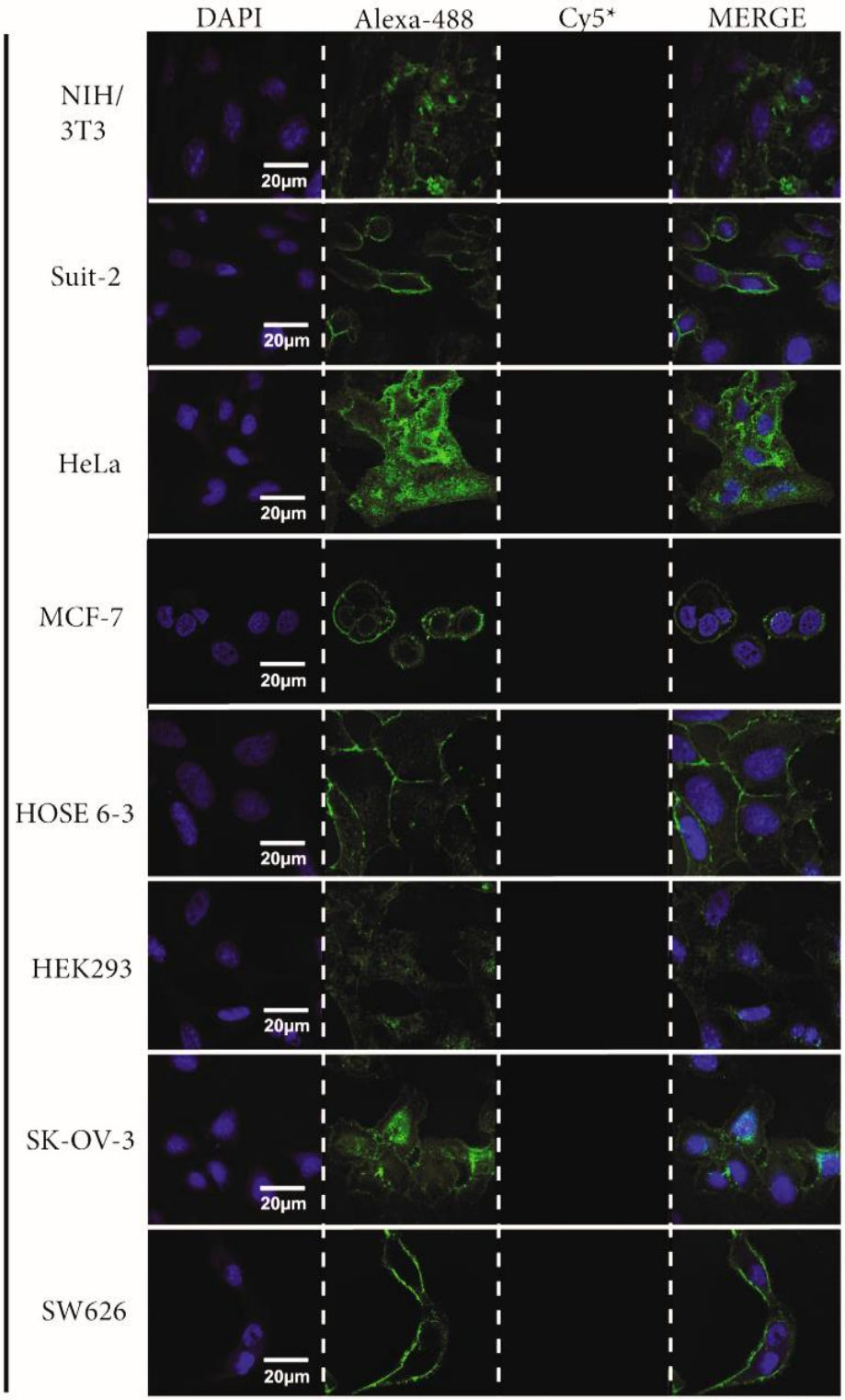

Figure 11: continued For confocal imaging cells were were treated with Cy5 conjugated aptamers and incubated at 37°C for 2 hours. Imaging of cells was done at 60X using a nuclear stain (DAPI-blue), a membrane stain (WGA-Alexa Fluor 488-green), and Cy5-aptamers (Cy5 pseudocolored as yellow). All images at 60X.

2.3 Discussion

Flow cytometry data showed positive enrichment of cell specific aptamer pools through successive rounds of Cell-SELEX. Additionally, utilizing TA TOPO10A cloning kits allowed for the identification and sequencing of individual aptamers within a sampled cell specific pool. However, this approach is limiting since (i) bacterial transformation and subsequent Sanger sequencing of aptamer inserts would not guarantee identification of all unique aptamers within the pool and (ii) this approach would fail to accurately quantify aptamer sub- populations within the pool. Thus, it was determined that a sequencing platform capable of yielding larger quantities of sequence data was necessary to evaluate the aptamer pool at the final round of enrichment. I chose the Ion Torrent sequencing platform due to its compatibility with the Cell-SELEX protocol. Firstly, any of the Illumina platforms, for example MiSeq, will yield significantly more reads than a 314 Ion Torrent chip (~2.5×10^7 versus ~3.0×10^5 respectively). Having prior knowledge of the PCR primer sequences and desired bp length for aptamers within cell specific pools; also it was not expected to a large degree of variability within the sequences. Thus 3.0×10^5 DNA reads was adequate and provided a data set large enough to identify significant sub-populations of aptamers within aptamer pools from the final round of selection. Additionally, I was able to do Ion Torrent sequencing within the research facilities rather than out-sourcing to a commercial facility. This allowed me to work with "in-house" equipment and have the expertise of collaborators within the UNC Charlotte bioinformatics department familiar with both the software and hardware of the Ion Torrent machine. More importantly, it allowed me to alter the current protocol to

parameters that produced the greatest amount of DNA reads *i.e. omission of the Pippin Prep*.

As expected, all three aptamers RLA01, RLA02, and RLA03 bound with high affinity to the target Caov-3 cells used in the initial screen for their identification. Additionally, all three aptamers displayed no obsesrved cytotoxicity at any of the administered concentrations. However, aptamer exposure on cells was limited to 4 hours. High dose apatamer treatments ranging 24 hours and over could promote cytotoxicity through intracellular pH changes due to continued endosomal internalization. RLA02 and RLA03 demonstrated exclusive specificity with minimal to undetectable interaction with any of the malignant or non-malignant epithelial cell lines tested except the target Caov-3 cells. It is interesting to note that RLA01 showed binding interactions with both SK-OV-3 and HeLa cells, as compared to controls. However, the max fluorescent events observed in the other cell lines were lower than the binding kinetics to Caov-3. One possible explanation for these results could be the existence of a commonly shared receptor among the three cell lines expressed at highest levels in Caov-3 cells and moderate or low levels on the other two. A second explanation could be structurally similar or related proteins are present on the membranes of the three cell lines with RLA01 having the highest binding affinity for the one that is expressed on Caov-3 cells. Ovarian surface epithelium and cells in the Müllerian tract are derived from common embryonic coelomic progenitors [3]. Since Caov-3 and SK-OV-3 cells were isolated from ovarian epithelial tissue it is likely that a common receptor is shared between the two cell lines. However, a study comparing EOC cell lines involving karyotyping, surface markers, and drug resistance indicated that Caov-3 cell lines display a unique

genetic lesion on the long arm of chromosome 3 (del(3)(p13:) not seen in SK-OV-3 cell lines [311, 312]. This could result in altered morphology in common surface structures such as dysregulated glycosylation of common receptors on Caov-3 versus SK-OV-3 cells. Additionally, the heterogeneity observed in EOC development could further explain common expression of surface structures seen in ovarian tumor subtypes and cervical carcinomas which are known to originate from squamocolumnar junctions of the cervix [315]. Data suggest that ovarian tumors manifest from cells expressing Müllerian tract differentiation. Although fallopian, ovarian, and pelvic cancers are treated as three distinct neoplastic diseases, data suggests that the majority of them originate from a common Müllerian progenitor and/or distal fimbrae tubes of the ovary [3, 6, 10, 11, 316]. It is possible that these malignant cell lines share a common receptor that is up- or down-regulated depending on particular context, abnormality, or in response to external stimuli such as hormones. SK-OV-3 cells originate from an epithelial adenocarcinoma similar to Caov-3 cells; however they also demonstrate levels of resistance to multiple cytotoxic drugs including platinum taxanes [311, 313] and thus could differ from Caov-3 at a minimum in their expression of ABC multiple drug resistance (MDR) transporters on the cell surface. However, similarity of characteristics of these cell lines is in their origin in the female reproductive tract rather than as epithelial cells per se since no binding events were detected by either flow cytomerty or confocal imaging when RLA01 was incubated with epithelial cells from other tissues.

The three aptamers have apparent K_d values in the nanomolar range which show that they bind with high affinity to target cells. Physiologically relevant apparent equilibrium dissociation values for therapeutic molecules are considered to be in the

nanomolar to picomolar range. Initial dosing of pegaptanib to inhibit $VEGF_{165}$ in HUVEC cells had an IC_{50} value between 0.75-1.4 nM with total inhibition of $VEGF_{165}$ binding observed at 10nM [317]. Current FDA approved treatment protocols administer 0.3 mg IV injections every 6 weeks for 30 weeks to patients suffering from AMD [272]. However it is important to note that pegaptanib is an inhibitory aptamer with a single agonist and was developed in a sequential process similar to that described here but in the presence of a purified target molecule only [318]. Aptamers that have been identified through positive selection with whole cells similar to the methods described here can target Axl (GL21 aptamer apparent K_d 221nM) [134], ovarian cancer Caov3 cell line (DOV-3 apparent K_d 132 ± 32nM) [93], B-cell receptors of Burkitt's lymphoma cell lines (TD05 apparent K_d 74.7 ± 8.7 nM) [152, 319], and liver cancer MEAR cell line (TLS6 apparent K_d 157.0 ± 16.9 nM) [320]. The non-SELEX identified aptamer AS1411, formerly ARGO100, showed initial inhibition of MDA-MD-231 cell proliferation after a 15μM dose [300, 321]. Currently a phase II, single-arm study of AS1411 for treatment of metastatic renal cell carcinoma administers 40 mg/kg/day on a continuous IV infusion on days 1-4 of a 28 day cycle for two cycles [322]. In addition to reporting apparent K_d values in the nanomolar range, reporting of higher total fluorescent events over a range of aptamer doses supports use of these aptamers as attractive candidates to chaperone chemotherapeutic drugs or small molecule vehicles directly to tumor sites. I hypothesize that the number of events observed by flow cytometry directly correlates to effective dose of aptamer-drug conjugates internalized. This could increase the efficacy of current treatment protocols by delivering more cytotoxic drugs to the tumor while reducing systemic cytotoxic side effects typically seen with them.

Further, confocal imaging clearly supports significant internalization of aptamers into specific cell types. Data suggests that aptamers internalize into cells via canonical endosomal pathways [323-325]. My raw confocal images as well as Z-stack generated images support colocalization of Cy5-aptamer signal to internal endosomal membranes.

The three aptamers are similar in their 5' and 3' sequences that were used as anchors for PCR amplification during cell-SELEX. Despite these known identities, the aptamers have different stable predicted structures and hairpin loops that would produce unique surfaces for interactions with target cell membranes. Further support that these aptamers are unique comes from the independent equilibrium binding kinetics of each on Caov-3 cells. The confocal imaging was consistent with the total fluorescent events observed by flow cytometry using Cy5 conjugated aptamers with highest levels of internalized aptamer observed with RLA01, followed by RLA03, and lowest with RLA02. Further, RLA01 was determined to bind to a broader spectrum of cell types, as discussed above. Although others reported identification of ovarian carcinoma specific aptamers, sequence alignment of the three described here shows that they are unique from those previously reported. In order to be most physiologically relevant for future therapeutic uses, aptamers should interact with the target malignant cells and not other non-malignant cells which would be neighboring cells and likely of the same original cell origin. Notably, my cell-SELEX protocol included negative selection against non-malignant ovarian epithelial cells. Flow cytomerty and confocal analysis supported nonreactivity of the aptamers to non-malignant epithelial cells of both ovarian and kidney origin. By contrast to this report, others utilized HeLa cells, a known neoplastic immortalized line for negative selection [93]. That the protocol yielded aptamers unique

from those previously reported highlights that individual Cell-SELEX strategies used will be a key factor in determining what aptamers are identified. Large bioinformatics approaches for comparison of multiple parallel aptamer pools and a large panel of cell types could reveal similar sequence patterns for aptamers that bind to related disorders.

A more comprehensive panel of EOC cell types should be used for comparative studies. Particularly those of different developmental stage or sub-types as tumor cells often up-regulate biomarkers during stages of tumorigenesis and are type specific. All the cells used for this Cell-SELEX protocol were exclusively adenocarcinomas. Although a panel of malignant and non-malignant disorders was used to demonstrate specificity, this fails to elucidate any information about aptamer binding with early tumor or stem cell progenitors from coelomic tissues. Demonstrating binding to these types of tissue would be most important in utilizing RLA01, RLA02, or RLA03 as a diagnostic tool for the early detection of malignant cells.

Notably, it was observed that Caov-3 cells demonstrated morphological changes during incubation with aptamers as seen by confocal imaging and flow cytometry. Fluctuations in front and side scatter channels during flow cytometry suggest morphological instability potentially due to the influx of endosomal structures. Additionally some confocal imaging did show evidence of nonspecific membrane disruption. Due to aptamer binding and eventual internalization, it is yet to be shown how the aptamers described here can disrupt important cell regulatory functions either in pro- or antagonistically. Extracellular receptor binding to aptamers could disrupt intra cellular tyrosine kinase signaling. This could potentially dysregulate important cell signaling such as auto- and endocrine pathways that could increase the potential of

detachment by up-regulating matrix metalloproteinases. Aptamer attachment could also affect the up or down regulation of proliferative or pro angiogenesis cell signaling cascades. Additional analysis comparing aptamers and known post transcriptional gene silencing siRNA species to elucidate any sequence homology. Some aptamers could potentially block translation of mRNA transcripts or bind and inhibit siRNA species.

In conclusion, I used whole Cell-SELEX to identify seven unique DNA-based aptamers specific to Caov-3. Of those seven identified, three were characterized and demonstrated high binding affinity to Caov-3 cells but more importantly not to the nonmalignant epithelial HOSE 6-3 cell line. My study reaffirmed the effectiveness of whole Cell-SELEX as a molecular tool to identify aptamers that specifically target neoplastic diseases. The modified protocol described here is unique in that I identified EOC aptamers specific to Caov-3 following negative selection against a non-transformed epithelial cell line. Specificity of all three aptamers was shown across a panel of tumor types including breast, cervical, and pancreatic malignancies. Additionally the differences in aptamer binding kinetics demonstrated here can be used to infer particular molecular characteristics of the target cells. The identified aptamers can potentially be used to enhance the sensitivity of current clinical diagnostic tools to identify ovarian neoplasms. The lack of interactions observed with non-tumor epithelial cells suggests that aptamer-based therapies can minimalize interaction with non-malignant tissues and improve upon the incidence of false positive results regarding benign versus malignant diagnosis or to potentially deliver cytotoxic drugs to distal tumor sites in the body. Thus, overall, the data suggest these aptamers are attractive candidates for further analysis to

direct and localize chemotherapeutics to tumor sites and potentially aid in the early diagnosis of ovarian malignancies.

CHAPTER 3: LOCALIZATION AND CELLULAR UPTAKE OF RLA01 LABELED PACLITAXEL LOADED NANOPARTICLES

3.1 Introduction

The work described in Chapter 3 demonstrates the potential of aptamer RLA01 as a molecular chaperone when linked to PLGA based polymeric nanoparticles. I have previously described the binding and internalization kinetics of aptamer RLA01 when incubated with target Caov-3 cell lines (Chapter 2). RLA01 demonstrates a high specificity for targeting malignant Caov-3 cells and the ability to internalize by the endocytic pathway. Thus RLA01 could promote internalization of NPs that have been labeled with RLA01 on its surface. Additionally, this would suggest that loading NPs with small molecules, such as cytotoxic drugs, could increase internalization when incubated on target cells. I intend to demonstrate the potential increased uptake of aptamer labeled NPs with both fluorescein diacetate (FDA) and Paclitaxel (Ptx) loaded NPs. Cells incubated with aptamer labeled FDA NPs will demonstrate increased fluorescent events and will be demonstrated qualitatively and by confocal microscopy. Additionally, aptamer labeling the surface of Ptx loaded NPs will increase cell death when compared to Ptx alone when used to treat Caov-3 cells.

3.2 Materials and Methods

Cell Lines

The human ovarian adenocarcinoma cell lines Caov-3 (HTB-75) and SK-OV-3 (HTB-77) obtained from ATCC (Manassas, VA) maintained in tissue culture 37°C 5%

CO_2. Caov-3 cell lines maintained in Dulbecco's minimal essential medium (DMEM, GIBCO) supplemented with 10% fetal bovine serum (FBS, GIBCO) and 1% penicillin−streptomycin (GEMINI). SK-OV-3 cell lines maintained in McCoys5a media (ATCC) supplemented with 10% FBS (heat-inactivated, GIBCO), 1% penicillin−streptomycin (GEMINI). Normal epithelial cell lines HEK-293 (ATCC, CRL-1573) maintained in DMEM supplemented with 10% FBS (heat-inactivated, GIBCO), 1% penicillin−streptomycin (GEMINI). The HPV immortalized human ovarian epithelial (HOSE 6-3) cells [309] maintained in Medium199/MCDB105 media (1:1, Sigma Aldrich) supplemented with 10% FBS (heat-inactivated, GIBCO), 1% penicillin--streptomycin (GEMINI), 1% sodium bicarbonate (7.5% w/v, Cellgro).

Aptamer labeling of nanoparticles

PLGA-PCL-PEG blank, fluorescein diacetate, or Paclitaxel loaded NP suspension (10 mg/mL) in 18Ω H_2O was mixed with 100µL NuLink-BE2 (2 mg/mL) 5 min. at room temperature. Addition of NuLink-BE2 to functionalize the terminal amine groups of protruding hydrophilic PEG molecules is necessary for aptamer attachment. Nanoparticles were spun (21,000 rcf, 4°C), washed (2x, 18Ω H_2O) and resuspended in 1 mL 18Ω H_2O. To the cleaned and functionalized NPs we added .2% (by weight of NPs) 5'-amino-6C-RLA01 conjugated aptamer and incubated overnight under constant agitation 4°C. Aptamer labeled NPs were spun, washed with 18Ω H_2O (5xs) and resuspened at a working concentration (1 mg/mL).

Nanoparticle-RLA01 characterization

To show the attachment of aptamer RLA01 to the NP surface agarose (2%) electrophoresis was used was used. The DNA marker (50BP Marker, New England

Biolabs) and free aptamer (IDT) served as standards for a 60 base pair band on the gel. Nanoparticles were labeled with RLA01 overnight, washed with 18Ω H_2O (5x's), and resuspended at 1 mg/mL. A 50 µL aliquot of NPs was taken from the stock solution and spun down 21,000 rcf 4° 10 minutes. The supernatant was removed and NPs were resuspended in 20 µL H_2O. Samples were run at 150V for 2 hours. Gel stained with 10 µL Ethidium Bromide in TAE (1X).

SEM imaging

For imaging lyophilized NPs were sampled placed on silicon wafers (LVEM5 DeLong America) and placed in a glass vacuum. After complete evacuation of atmospheric gases the chamber was flooded with Argon gas and excited with 10 mA voltage to promote gold sputtering of NPs. Imaging was done a JEOL SEM 6460LV at 10 kV.

Confocal and Light Microscopy

Coav-3 cell lines plated on a 35, 0/10 mm glass bottom culture dish (Greiner bio-one) (seeded at 5.0×10^4 per well/plate 48 hours prior, 37°C 5% CO_2). 5 µL of labeled or unlabeled fluorescein diacetate loaded NPs (100ng-900ng range) were added to 1 mL cell specific media and incubated on target cells 37°C 5% CO_2 2 hours agitated slightly every 30 min. Endosomal internalization was observed at 30, 60, 90, and 120 min post initial treatment. At 30 min prior to desired time points cells were treated with endosomal specific stain pHrodo® Red Transferrin Conjugate according to the manufacturers' protocol (Invitrogen, 25 µg/µL). Cells were washed with PBS (3x) and fixed with 2ml heptane (1:8.25 PBS: 37% Formaldehyde (Sigma Aldrich)) 37°C 10 min. Subsequent staining with DAPI (10 ng/µL, 10 min) was done following standard procedures.

Imaging of the cells was done with an Olympus FluoView 1000 confocal microscope using DAPI (blue), pHrodo® Red (orange), and Cy5 (red) filters. For light microscopy Caov-3 cells were seeded 5.0×10^6 per well/plate on a 6-well plate (BD Falcon) and incubated 37°C 5% CO_2 48 hrs. 25 µL of labeled or unlabeled fluorescein diacetate loaded NPs (100ng-900ng range) were added to 2 mL cell specific media and incubated on target cells 37°C 5% CO_2 2 hours agitated slightly every 30 min. Cells were imaged at 30, 60, 90, and 120 minute time points and continued to incubate. Light microscopy was done on a Zeiss AxioCamMRc microscope using an X-cite-series 120Q laser.

Flow Cytometry

Caov-3 cells were plated on 6-well plates (seeded at 1.0×10^6 48 hours prior, 37°C 5% CO_2). 25 µL of labeled or unlabeled fluorescein diacetate loaded NPs (100ng-900ng range) were added to 2 mL cell specific media and incubated on target cells 37°C 5% CO_2 2 and up to 4 hours agitated slightly every 30. Cells were then washed with PBS (2x), scraped in 1 mL 1X PBS, and filtered through a 35µm nylon mesh cell strainer polystyrene tube (BD Falcon). Cells were subjected to flow cytometric analysis within 1 min and fluorescent events were determined with a Becton Dickinson LSRFortessa Flow Cytometer by counting 50,000 events. Aptamer and non-aptamer directed blank NPs was used as a negative control.

Drug Cytoxicity

Cell proliferation was measured with a Vybrant MTT Cell Proliferation Assay Kit (Invitrogen, Eugene, Oregon) according to the manufacturers' protocol. Cells were seeded into 96-well plates (seeded at 5000 cells/well 48 hours prior, 37°C 5% CO_2). 50 µL of indicated treatments (10µM to .001µM) were added to 150µL cell specific media.

Cells where then washed in PBS (3x), and given fresh media. Cell proliferation was observed at 0, 4, 8, 24, and 48 hours post initial treatment. Cell proliferation activity was evaluated by adding 10μL MTT stock solution incubate 4 hrs 37°C 5% CO_2, then addition of 100μL SDS-HCl solution and allowed to stand for 4-12 hours 37°C 5% CO_2. Resulting solution was pipetted vigorously and the optical density (OD) was measured at 570nm using a Multiskan GO Microplate Reader (Thermo Scientific, Vantaa, Finland). Time points in Figure 3 mark average OD reading (n=3) at indicated concentrations

Western blotting

To assess the up-regulation of pro-apoptotic proteins Caspase-3 and PARP-1 cells were treated with 0.1 μM concentrations of Paclitaxel loaded NPs 4 hours 37°C 5% CO_2. Cells were washed with PBS (3x) and incubated 37°C 5% CO_2. The cells were harvested after 0, 4, 8, 12, 24, and 48 hours post initial treatment. Cell pellets were frozen and stored at -80ºC. Protein extraction from cell lysates was collected by Total Protein Extraction Kit (CHEMICON International). Protein concentrations were analyzed by Bio-Rad D_c Protein Assay (Bio-Rad Laboratories, Hercules, CA). Equal amount (7 mg) of protein was subjected to electrophoresis on NuPAGE 10% Bis-Tris Gel (Life Technologies) and then transferred to positively charged nylon transfer membrane (GE Healthcare). The blotted membranes were immunostained with primary antibodies specific for Caspase-3 antigens (8G10, Cell Signaling Technology) or PARP1 antigens (H-300, Santa Cruz Biotechnology) then 2º antibody (rabbit-IgG, Santa Cruz Biotechnology). PARP-1 and caspase 3 treated membranes were stripped and immunoblotted with anti-β-actin. The signals were developed by Amershem™ ECL Plus

Western Blotting Detection System according to the manufacturer's protocol (GE Healthcare).

3.3 Results

Labeling the surface of nanoparticles with RLA01

To demonstrate the surface labeling of NPs with aptamer RLA01 (PLGA-RLA01) agarose electrophoresis was done (Fig 12). RLA01 alone showed a band at a molecular weight of 60 bp (Fig 12 lane B) when compared to a 50 bp weight marker (Fig 12 lane A). The gel shows that the resulting band from a 60mer RLA01 aptamer stock did appear beyond the expected band size when compared to the 50bp DNA ladder. This is due to the single stranded structure of RLA01. Nanoparticles alone did not show any band (Fig 12 lane C). When NPs are labeled with RLA01 and the labeled NP is denatured by boiling a visible band can be seen consistent with the 60mer aptamer stock (Fig 12 lane E). Furthermore, NPs incubated with RLA01 in the absence of NuLink-BE2 fail to label the surface of NPs. This can be seen by the resulting band in lane D and demonstrates the necessity of NuLink-BE2 to attach RLA01 to the NP surface. These data strongly demonstrate the labeling of the NP surface with aptamer RLA01. Additionally I used a scanning electron microscope (SEM) to image NPs in order to elucidate information concerning physical structure. Dynamic light scattering (DLS) analysis showed NPs to be within the range of 200-250 nm (data not shown). The SEM data provided information about surface characteristics and batch uniformity. The DLS and SEM data both showed spherical NPs, in solution and lyophilized respectively, with a high degree of size uniformity.

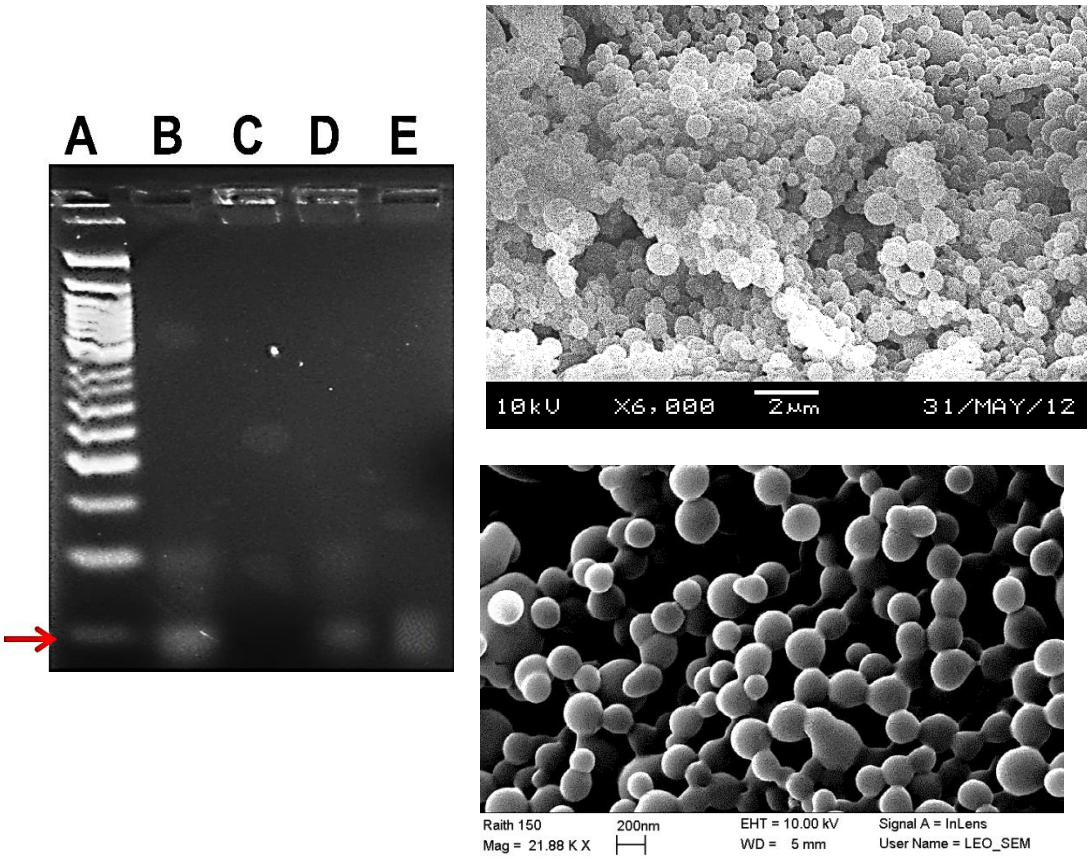

Figure 12: PAGE electrophoresis demonstrating the attachement of RLA01 to nanoparticles and SEM imaging showing nanoparticle size. The labeling of NPs with Caov-3 specific aptamer RLA01 is shown by agarose electrophoresis (Left). Lane A) 50bp weight marker; lane B) RLA01 (60 bp) stock; lane C) PLGA-NP; lane D) NP and aptamer mixed in absence of NuLink-BE2, and lane E) PLGA-RLA01. SEM imaging of loaded NPs at indicated magnification (Right images).

Qualitative Evaluation by Flow Cytometry

One important property of a targeted drug delivery system is internalization of the complex by target cells. I have previously shown that aptamer RLA01 can be internalized into target Caov-3 cells by endocytic mediated pathways (Chapter 2). Here I am examining the ability of RLA01 surface labeled fluorescein diacetate loaded NPs (PLGA-FDA-RLA01) to internalize into target Caov-3 cells. The benefit of using FDA loaded NPs is that positive identification of fluorescent signal is dependent upon

hydrolysis of FDA by an intracellular esterase or acidic conditions which allows the acetoxymethyl-ester to yield fluorescein [326]. Degradation of the NP and hydrolysis of FDA is necessary for generation of fluorescent signal and flow cytometry can quantify live populations of cells known to have positively internalized labeled NPs. I used flow cytometry to analyze cells that have been incubated with FDA loaded NPs. I compared this to the observed fluorescent events with non-aptamer directed NPs (PLGA-FDA) to show any differences in both the rate and overall cellular uptake of NPs when labeled with aptamer RLA01.

The graphical data in Figure 13 show that unlabeled FDA loaded NPs internalized into non-malignant immortalized human ovarian surface epithelial cells (HOSE 6-3 [309]) and human epithelial kidney (HEK293) cell lines in a dose dependent manner after a four hour period. However, observed fluorescent events for malignant ovarian cell lines Caov-3 and analogous SK-OV-3 are 4-fold lower when compared to HOSE 6-3 and HEK293 cell lines (Figure 13). The total fluorescent events observed with HOSE 6-3 and HEK293 cells (48,915 and 34,198 respectively) were significantly higher when compared to detected fluorescent events in Caov-3 and SK-OV-3 cells (14,791 and 8,846 respectively). The neoplastic development of tumor cells causes the up-regulation of surface structures that could alter canonical endocytic pathways like pinocytosis or receptor mediated endocytosis (RME) of NPs. Surface labeled NPs could increase internalization of a drug loaded NP.

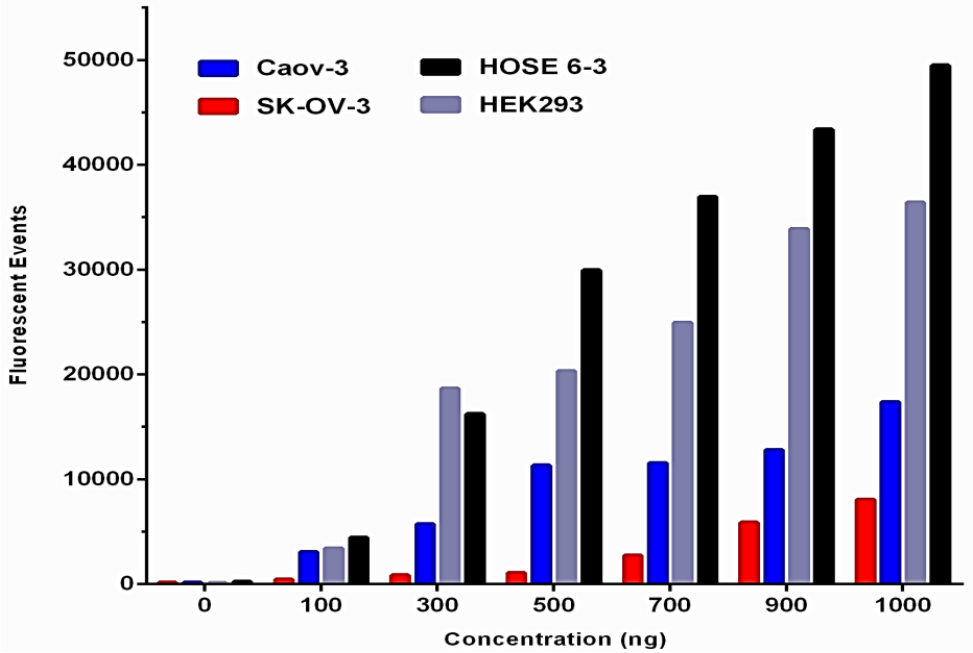

Figure 13: Internalization of fluorescein diacetate loaded nanoparticles after four hours. Caov-3 cells were treated with indicated concentrations of FDA loaded NPs for 4 hours. Data points represent the average total fluorescence (n=3, error bars ±SD).

Target EOC Caov-3 cells were treated with indicated concentrations of aptamer or non-aptamer labeled FDA loaded NPs for 1 and 4 hour periods (Figure 14). To establish baseline fluorescence Caov-3 untreated and Caov-3 treated with aptamer labeled and non-aptamer labeled blank NPs were used (Figure 14A). No appreciable shift was seen in fluorescent cell populations as demonstrated by the histograms in Figure 14A suggesting no background fluorescence caused by NPs or aptamer labeled NPs. Additionally it suggests minimal to no cytotoxicity over the four hour treatment caused by NPs or aptamers. Gating of the background fluorescence was set to 0.01% of the total population analyzed. As expected I observed a dose-dependent increase of FDA positive cells within the total cell population when Caov-3 cells were incubated with aptamer labeled versus non-aptamer labeled NPs (Figure 14B and C). Moreover, both aptamer and non-aptamer labeled NPs internalize into cells in a time dependent manner as seen by

the increase of observed fluorescent events between 1 and 4 hour incubation periods on Caov-3 cells at equal doses (Figure 14B and C, respectively). The increased fluorescent events observed with aptamer labeled NPs compared to non-aptamer labeled NPs at equal doses were significant for all treatment doses in both 1 and 4 hour assays. Data analyzed by two-way ANOVA significant p-values $p < 0.001$.

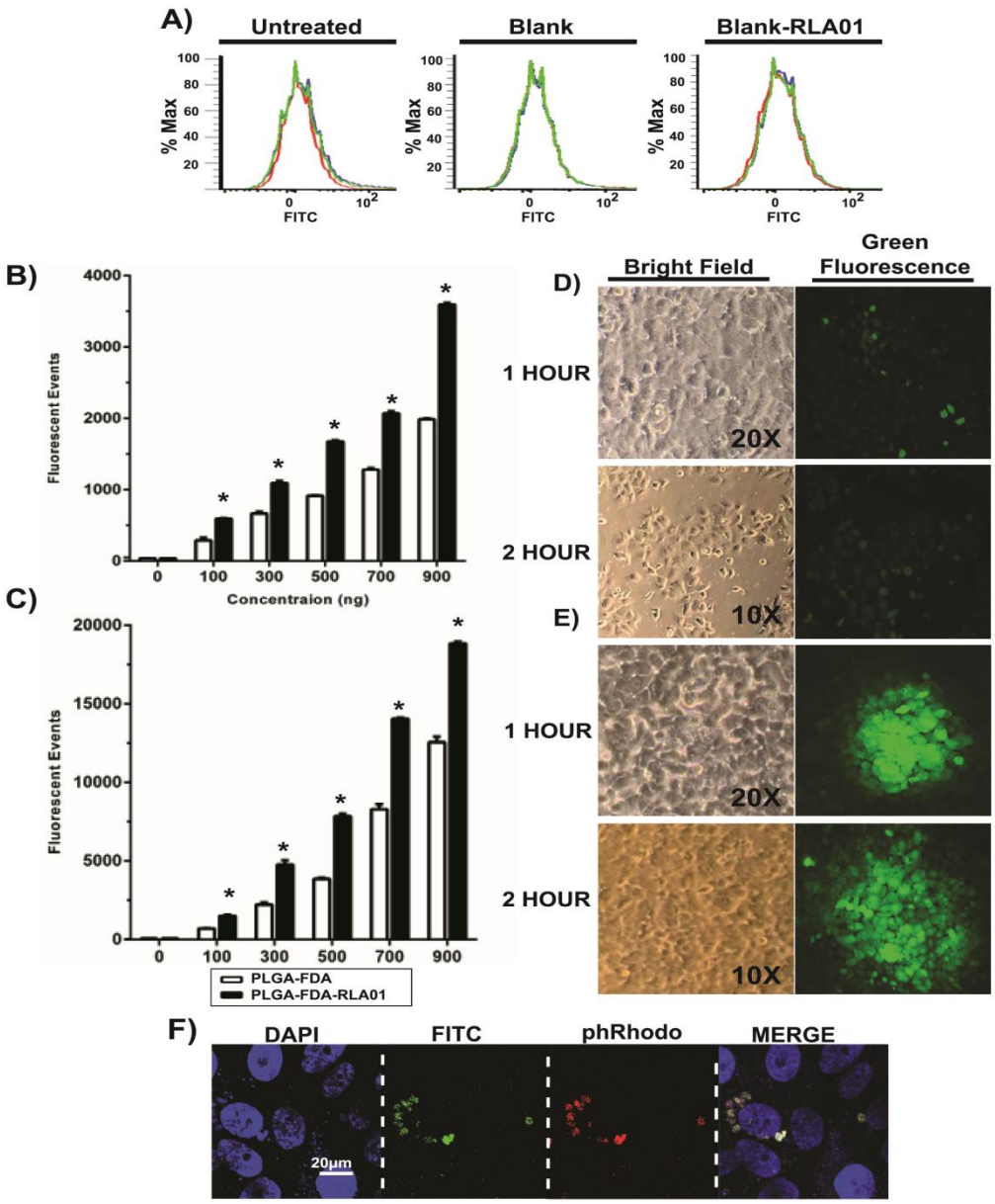

Figure 14: RLA01 directed nanoparticles increase cellular internalization of FDA loaded nanoparticles in Caov-3 cells. A) Flow cytometry was used to quantify Caov-3 cell populations that bind and internalize FDA loaded NPs. Histograms of all negative controls are provided to ensure fluorescent activity is based solely on the cleavage of FDA. B and C) Qualitative analysis of aptamer labeled versus non-aptamer labeled FDA loaded NPs. Caov-3 cells were incubated with NPs for 1 (B) and 4 (C) hours. Data bars represent the average fluorescent events observed (n=3, error bars ±SD). D and E) Caov3 cells were treated with non-aptamer labeled (D) or aptamer labeled (E) FDA NPs. Light field (left) and green fluorescent (right) filters are displayed showing fluorescent cell populations at 1 and 2 hour time points post initial treatment. F) For confocal imaging cells were imaged at 60X after 1 hour using a nuclear stain (DAPI-blue), an endosomal specific marker pHrodo® Red Transferrin Conjugate (pseudo-colored red), and Fluorescein Diacetate (FDA) loaded NPs (green). $P < 0.001$

In addition to the increased cellular uptake seen with aptamer labeled NPs into target Caov-3 cells (Figure 14), the data suggest aptamer labeling can reduce internalization of FDA loaded NPs in non-malignant cell lines (Figure 15). When Caov-3 cells are incubated with equal concentrations of FDA loaded NPs there is a significant difference in the amount of fluorescent events demonstrated over time by flow cytometry (Figures 13 and 15). When equal concentrations of aptamer labeled and non-aptamer labeled NPs are incubated with HOSE 6-3 cells, there is a significant difference in the amount of FDA fluorescent events (Figure 15). The addition of a Caov-3 cell line specific aptamer label to the NP surface reduces fluorescent events by 50% when comparing non-aptamer and aptamer labeled NPs at equal concentrations incubated on HOSE 6-3 cells. These data suggest that the addition of Caov-3 tumor specific aptamers can block the internalization of NPs into non-malignant HOSE 6-3 cells. The labeling of NPs coats the polymeric exterior with target specific aptamers which could lead to decreased levels of internalization due to the absence of targeted receptors. Additionally, aptamer labeling could block or interfere with NP interactions that would otherwise promote internalization into HOSE 6-3 cells. Overall, the data shown in Figures 13, 14, and 15 suggest that the labeling of NPs with RLA01 aptamers can alter internalization kinetics in both the malignant and non-malignant cell lines used here.

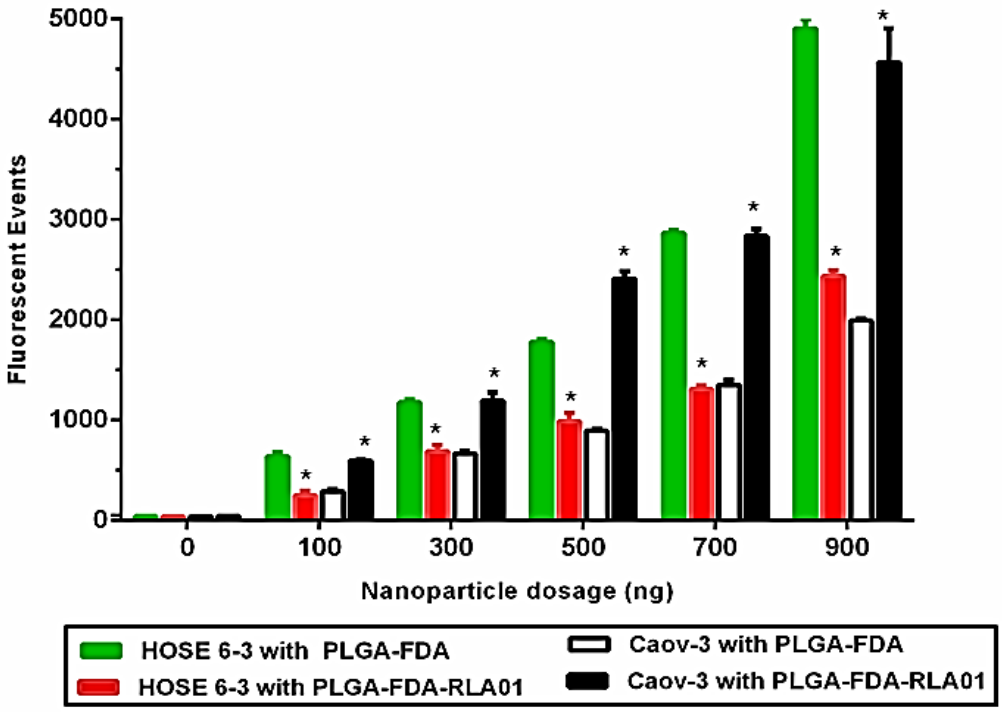

Figure 15: Labeling of nanoparticles with aptamers can inhibit random internalization in non-malignant immortalized epithelial cells. Caov-3 and HOSE 6-3 cells were treated with indicated concentrations of aptamer directed and non-aptamer directed FDA loaded NPs for 2hrs. Data points represent the average total fluorescence (n=3, error bars ±SD).

Fluorescent Microscopy Shows Cellular Uptake of Nanoparticles

To further investigate the *in vitro* uptake of FDA loaded NPs in Caov-3 ovarian tumor cells, confocal imaging and light microscopy was used (Figure 14D, E, and F). As shown in Figure 14B and C, qualitative data indicates that aptamer labeled FDA loaded NPs result in larger cell populations exhibiting green fluorescence over a range of concentrations (100ng to 900ng). To further demonstrate this I used fluorescent light microscopy to observe and image visibly green fluorescent cells over the same concentration range. For Figures 14D and E, fluorescent signals were significantly higher in cells treated with aptamer labeled NPs (bottom set) versus non-aptamer labeled NPs (top set) after 1 and 2 hour time points. Although fluorescent signals were detected

with Caov-3 cells treated with non-aptamer labeled FDA loaded NPs, it is significantly less. In order to elucidate the mechanistic pathway of internalization, I used an endosomal marker to stain live Caov-3 cells over the predetermined time course of the assay. Spherical endosomal structures are co-localizing with the green fluorescence indicative of cleaved FDA suggesting endosomal internalization of labeled NPs. The nuclear stain (DAPI) shows that the loaded NPs accumulate into the cytoplasm of the cell proximal to the nucleus. Both confocal and light microscopy images corroborate with flow cytometry data and suggest that FDA loaded aptamer labeled NPs show a significantly higher rate of internalization over time and produce cell populations with more robust fluorescent activity when compared to the non-aptamer labeled NP treatment.

Cytotoxicity of Paclitaxel loaded nanoparticles

The amount of fluorescent events observed in Figure 14B and C could potentially correlate to drug delivered to the cell surface resulting in an increased efficacy of drug treatments. To further test this Ptx loaded NPs were used (PLGA-Ptx). Aptamer labeled NPs loaded with Ptx (PLGA-Ptx-RLA01) could increase the efficacy of Ptx alone particularly after long treatment periods due to the increased localization at the membrane and internalization mediated by aptamer RLA01. To evaluate any cytotoxic effects Caov-3 cell lines were exposed to increasing molar concentrations (by weight of Ptx) of Ptx loaded NPs. Blank NPs were used to determine any cytotoxic effects caused by the polymeric vehicle. Additionally, blank RLA01 labeled NPs were used to determine if the increased uptake of NPs can have any adverse or cytotoxic effects on Caov-3 cell lines. Additionally, Ptx loaded NPs were labeled with a previously described aptamer (PLGA-

Ptx-DOV3) [93] in order to compare models with an established aptamer identified by similar methods.

Cells were treated for 4 hours and washed in PBS (3x), given fresh media, and allowed to incubate. Cells were analyzed by an MTT Cell Proliferation Assay Kit at 0, 4, 8, 24, and 48 hours post exposure at indicated treatments (Figure 16; .1µM, .01µM, and .001µM doses displayed, left to right respectively). Optical density (OD) values were compared against an untreated population (n=3) of cells to measure any reduced proliferation. At .1µM doses of blank and labeled blank NPs no apparent effect on cell proliferation was seen (Figure 16). This demonstrates that both NPs and labeled NPs fail to promote any increased cytotoxicity to targeted cells. Cells treated with non-labeled NP encapsulated Ptx (70% survival) demonstrated anti-proliferative affects similar to that of Ptx alone (68% survival) at equal concentrations over 48 hours and exhibited a 30% reduction in cell viability when compared to blank NP (99% survival) treatments. This shows the effectiveness of NPs to deliver the cytotoxic drug Ptx which is a hydrophobic molecule. Aptamer labeled NPs (PLGA-Ptx-RLA01) caused a significant decrease in cell proliferation when compared to drug alone and drug loaded NPs after 24 and 48 hours at all reported Ptx concentrations (Figure 16A, B, and C). Decreased cell proliferation was observed for all treatments in a dose-dependent manner. Data analyzed by two-way ANOVA significant p-values $p<0.001$.

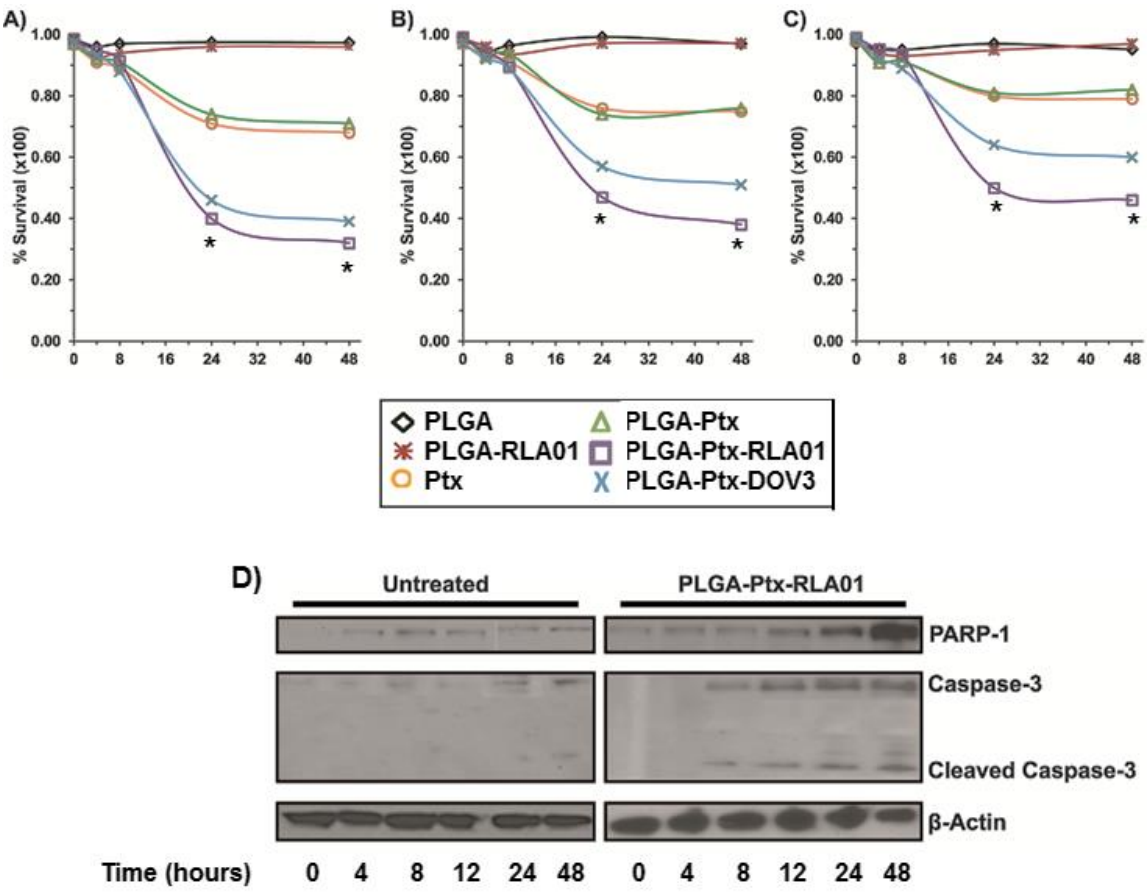

Figure 16: MTT proliferation assay after Paclitaxel loaded nanoparticle treatments on ovarian Caov-3 cell lines. An MTT proliferation kit was used to assess cell viability post treatment at 0, 4, 8, 12, 24, and 48 hours. Graphs represent a complete 48 hour timeline of cell proliferation after treatment with loaded NPs A) .1 µM B), .01 µM, and C) .001 µM concentrations by weight of Paclitaxel. Data points represent the percent average OD reading recored (n=3). PLGA-Ptx-RLA01 (n=4). D): Caov-3 cells were untreated (left) or treated with .1 µM (by weight of Ptx) of aptamer directed Ptx loaded NPs (right). Total protein was collected from cell lysates and a Western blot to demonstrate Ptx induced cell apoptosis was done probing for pro-apoptotic proteins Caspase 3 and PARP-1. After protein transfer membranes were immunoblotted with anti-Caspase 3 antibodies and anti-PARP-1 antibodies as indicated. Membranes were re-probed with anti-β-actin antibody. $P < 0.001$.

Western blotting to demonstrate cellular apoptosis

To investigate the mechanistic signaling pathway responsible for the pro-apoptotic affects observed with aptamer labeled Ptx loaded NPs treatments Western blotting was performed. Two proteins were chosen: (i) Caspase-3 a cysteine protease that

plays a key role in apoptotic signaling cascades induced by extrinsic ligands (i.e Ptx) and (ii) PARP1 (Poly-(ADP-ribose) polymerase) a protein upregulated in response to DNA damage and a downstream effector of cleaved caspase-3 [327, 328]. Caov-3 cells were treated with .1 μM (by weight of Ptx) concentrations of NPs for 4 hours. Untreated cells were also analyzed to determine baseline protein levels. Cells were washed then harvested by trypsinization at 0, 4, 8, 12, 24, and 48 hours post initial treatment to observe the up-regulation of Caspase-3 and PARP-1 by Western blot. Figure 16D shows a time dependent increase of both PARP-1 and Caspase-3 following treatment with RLA01 labeled NPs but not in untreated cells. Upregulated levels of PARP-1 and Caspase-3 appear as early as 8 hours post treatment and are highest at 24 and 48 hour time points consistent with MTT proliferation data seen in Figures 16A, B, and C. In comparison to untreated cells, Caspase-3 and PARP-1 protein levels are significantly lower with no evidence of significant up-regulation of Caspase-3 or PARP-1 throughout the 48 hour time course.

4. Discussion

First I showed that labeling the surface of NPs can increase the cellular uptake of FDA loaded NPs as compared to non-labeled NPs when incubated on Caov-3 cells. Aptamer RLA01 is specific to Caov-3 ovarian tumor cell lines and I have shown NPs labeled with RLA01 can increase the cellular uptake of FDA loaded NPs *in vitro*. Fluorescent events, which correlate to positive internalization of FDA loaded NPs, were quantified by flow cytometry and visualized by confocal microscopy. These data support that the increase in cellular internalization and fluorescent events observed with aptamer labeled NPs are due to the addition of RLA01 to the NP surface. Nanoparticles labeled

with RLA01 promote internalization by receptor-aptamer binding at the surface of Caov-3 cells and localize NPs at the membrane following washing of residual particles. Thus, when cells are no longer exposed to treatment and residual particles are washed away—the high affinity bonds made between aptamer and cell surface moieties continue to localize NPs at the membrane. This can increase the time of exposure despite significant depletion of loaded NPs within the system. Such aptamer based treatments could persistently localize cytotoxic drugs at the tumor site which could overcome tradition multi-drug resistance mechanisms seen in many cancers.

I have shown that RLA01 induces no cytotoxic affects. This would suggest its binding target does not regulate apoptotic signaling pathways. However, the overall affect that aptamer labeled NPs could have on cellular morphology and physiology needs to be further investigated. It is believed that tumors are typically of lower pH [329] which could promote degradation of the NP and increase drug concentration at the tumor. However, the increased endosomal internalization could cause regulatory affects for normal cells if abundantly absorbed that could alter intracellular pH and potentially disrupt organelles. Additionally increased membrane disruption could affect adhesion and tight junction proteins promoting detachment and migration. This could alter the polarity of cells disrupting transcellular transport and exocytosis pathways. It could be beneficial to analyze transcriptomic profiles following NP treatments to elucidate information about potential disruption of regulatory pathways. Such pathways could include those involved with the up-regulation of key metabolic enzymes involved in cellular respiration (Kreb's cycle) due to the high influx of organic metabolites.

Secondly I was able to show internalization through the endocytic pathway using a Transferrin Conjugate. Although NPs can internalize by multiple endocytic pathways [330], data supports that NPs internalize by clathrin-mediated endocytosis [331]. However, it is unclear whether the NPs described here exclusive mechanism of internalization is clathirin mediated or potentially pino- or phagocytic. This could be elucidated by discovering the ligand that RLA01 binds to on the cell surface. The endosomal fate of cytotxic compounds is crucial when delivering effective dosages of NP encapsulated Paclitaxel. The endosomal internalization of FDA loaded NPs was shown using an endosomal specific markers whose fluorescent intensity is dependent upon pH. The mechanism of release could potentially be elucidated from the pH sensitive endosomal marker we have chosen. The fluctuating acidity within the endosome caused by the rupturing NP would alter the acidity levels in the endosome and thus reduce or enhance the fluorescent intensity observed. This allows us to assess the fate of endosomal internalized NPs as it pertains to potential mechanisms of endosome escape.

Release from the endosome is largely dependent upon the physical make-up of the polymeric NP *i.e.* inorganic versus organic subunits and cationic properties [332]. I have postulated what facilitates endosomal release of the NP complex. It has been shown that pH sensitive polymeric NPs, like those made from polyethylenimine (PEI) or polyamidoamines (PAA) can be protonated and degraded to assist endosomal escape [331]. The initially acidic endosomal environment causes hyper protonation of the degrading polymer and an influx of ions and water rupturing the endosome referred to as the “sponge effect” [331, 332]. More analysis must be done to demonstrate endosomal release by apparent “sponge effect” mechanisms. However, PLGA based NPs are

chemically similar to PEI and PAA based NPs thus suggesting NPs escape from the endosome is due to hyper-protonation of the terminal amine located on polyethylene glycol chains protruding from the NP surface.

Third, I was able to demonstrate increased cell death at equitoxic dosages with aptamer labeled Ptx loaded NPs versus Ptx alone as well as non-labeled Ptx NPs *in vitro*. Aptamer directed NPs caused a higher incidence of drug induced cell death as suggested by MTT proliferation assay and further demonstrated by Western blot analysis. Data reported here with regards to cell proliferation following treatment with aptamer labeled drug loaded NPs were consistent with *in vitro* data reported using epirubicin loaded $FeNO_3$ NPs in colon cancer [293], cisplatin loaded PLGA-*b*-PEG NPs in pancreatic cancer [190], doxorubicin loaded gold NPs in breast cancer [191], and vinorelbine loaded PLGA-PEG NPs in breast cancer [296].

The nanoparticles described provide a stable drug vehicle because: (i) they provide an amphipathic structure that can exist in a colloidal suspension, (ii) allow for the encapsulation of lipophilic drugs and other hydrophobic molecules, (iii) the structural formation remains consistent in context of size distribution and zeta potential when analyzing multiple batches of prepared particles, (iv) they degrade and release drug payloads in acidic environments, such as endosomal structures, and (v) can be used for active targeting following labeling of the surface with a cell specific ligand [197, 219, 279]. Moreover the metabolites formed by PLGA hydrolysis are lactic and glycolic acid monomers which are rapidly processed by the body producing little to no systemic toxicity and PLGA is approved by the Food and Drug Administration (FDA) [187, 196]. My studies concluded that the NPs described here showed minimal cytoxicity at high

concentrations. Additionally the labeling of NPs with RLA01 demonstrated no cytotoxic affects.

These data described here are promising when considering translation to clinical models. However, the intrinsic benefit to encapsulation into polymeric NPs is that it promotes solubility of Ptx as seen with nab-Paclitaxel [333]. Paclitaxel stocks (dissolved in a polar aprotic solvent) are generally diluted in 50:50 CremophorEl® (CrEL, a non-ionic surfactant polyoxyethylated castoroil) and ethanol with further 5-to-20 fold dilutions in saline. Castor oil based solvents can limit efficacy by forming large polar micelles in plasma altering drug pharmokinetics [334]. Additionally, CrEL solvent-based formulations can be associated with systemic dose-limiting toxicities. It has been shown that CrEL is biologically and pharmacologically active and leaches plasticizers from standard intravenous tubing [334, 335]. Moreover CrEL has been shown to cause acute hypersensitivity, increase blood viscosity, as well as intercalate into and disrupt the plasma membranes of red blood cells, and can cause neuropathy which may lead to demyelination and axonal degeneration [41, 336-340]. Our *in vitro* model using NP encapsulated Ptx reduced any adverse effects seen with castor oil based solutions of lipophilic drugs.

In conclusion I have shown that labeling of the NP surface with tumor specific aptamers promotes internalization into target Caov-3 cells. This resulted in an increased amount of fluorescent cells when treated with FDA loaded NPs and increased cell death when treated with Ptx loaded NPs. Nanoparticle characterization can be shown by agarose electrophoresis to demonstrate positive labeling of the NP surface. Data described here suggest the feasibility and effectiveness of such aptamer directed drug

therapy models. However the efficacy of aptamer labeled NPs must be tested in an *in vivo* model to assess the feasibility of drug loaded aptamer labeled NPs as a front line therapy. Moreover, such models will truly elucidate the effectiveness of aptamer labeled NPs as a targeted cancer therapy and potentially show evidence of increased aggregation at the tumor site due to the enhanced permeability and retention effect seen in tumors.

CHAPTER 4: *IV VIVO* MOUSE IMAGING DEMONSTRATING ENHANCED RETENTION AND TARGETING CAPABILITIES OF RLA01 LABELED NANOPARTICLES USING XENOGRAFT TUMOR MICE

4.1. Introduction

The goal of this work is to determine if RLA01 labeled NPs can bind and be retained by tumor cells in an *in vivo* mouse model. This will elucidate information about aptamer stability and the ability to maintain specific targeting and binding capabilities in the presence of endogenous nucleases. Firstly, I will demonstrate the circulatory pattern of unlabeled NPs loaded with a fluorescent reporter to track NP kinetics after tail vein injection. Next I will observe the differences in retention capabilities of aptamer labeled and non-aptamer labeled Indocyanine green (ICG) loaded NP treatments. In parallel with retention studies, I will investigate the efficacy of an aptamer labeled Ptx loaded NP complex versus Ptx alone in tumor induced Nu/J mice. Lastly, I will demonstrate the targeting capabilities of an aptamer labeled ICG loaded NP complex in a tumor induced mouse model when treatments are administered through tail vein injections.

4.2 Materials and Methods

Paclitaxel and ICG Loaded PLGA Nanoparticles

Graciously provided by the Ogle lab, Chemistry Department UNCC

Paclitaxel

Paclitaxel was purchased from Ark Pharm Inc (Chicago, Illinois) and diluted in DMSO (Sigma Aldrich) at 50 mg/mL. Additional dilution of Paclitaxel for working

doses was done in a 50:50 solution CremaphorEl and ethanol (Sigma Aldrich) at 1 mg/mL and diluted to working concentrations in PBS (1X).

In vivo Mouse Imaging

Nu/J mice (6 weeks, ~23 g) were purchased from The Jackson Laboratory (Bar Harbor, Maine). All animal experiments were performed in accordance with protocols evaluated and approved by the IACUC committee at UNC-Charlotte. Each mouse was inoculated with 5.0×10^6 Caov-3 cells subcutaneously in the right-rear flank. Eight days post inoculation all mice began the predetermined treatment regimen despite evidence of a tumor mass. For biodistribution one cohort (n=4) of mice received a single dose of either 25, 15, 10, or 5 mg/kg by weight of NP (2% ICG) and imaged at 10 min, 1, 4, 8, 12, 24, 48 hours post treatment. For retention studies two cohorts (n=4, n=5) of mice received weekly subcutaneous injections at the tumor site of either aptamer labeled or non-aptamer labeled 71 mg/kg ICG loaded NPs (.5% ICG) and imaged at 1, 4, 8, 12 24, 48, 72, and 96 hours post treatment. For drug studies one cohorts (n=4) of mice received weekly subcutaneous injections at the tumor site of 71 mg/kg aptamer labeled Paclitaxel loaded NPs (2% Ptx). Additionally one cohort (n=5) received an equal doses of Ptx-CrEL alone. For aptamer targeting two mice received a single dose by tail vein of either aptamer labeled or non aptamer labeled 350 mg/kg ICG loaded NPs (.5% ICG) and imaged at 1, 4, 8, 12 24, 48, 72, and 96 hours post treatment. All mouse imaging was done using an IVIS® Spectrum Pre-clinical In Vivo Imaging System (Perkin Elmer, USA) with appropriate wavelength (745 nm, excitation wavelength and filter; 810 nm, emission wavelength and filter. After 60 days following initial inoculation with Caov-3 cells mice were sacrificed by CO_2 asphyxiation and organs were harvested. Body weight

and tumor size was measured before administering weekly treatment and tumors were measured by digital caliper

4.3 Results

Biodistribution of ICG Loaded Nanoparticles

In order to establish nanoparticle kinetics and biodistribution in an *in vivo* model I treated a single group of mice (n=4) with different doses of ICG loaded NPs (2% ICG). Mice received injections through tail vein and were observed at indicated time points in Figure 17 by an IVIS Spectrum imager to assess NP localization throughout the body. Additionally I was interested in seeing if there were any areas of increased absorption that would not be typical i.e. liver, heart, and kidneys during normal circulation.

Fluorescent signal (10 min):
- Observed in all mouse tails at the injection site except the mouse receiving a 5 mg/kg dose.
- Shows minimal perfusion away from the injection site.

Fluorescent signal (1 hour):
- Shows minimal profusion away from the tumor site as seen at 10 minutes.
- No observed apparent change in the total area of fluorescent signal for all mice.
- No detectable signal for 5 mg/kg dosage

Fluorescent signal (4 hour):
- Observed increase in the total area of fluorescence as well as area of max fluorescent signal suggesting accumulation within the tail of mice receiving 25 or 15 mg/kg dosage but no detectable level of fluorescence throughout the body.
- Mice receiving dosages of 10 and 5 mg/kg showed a fluorescent signal (max ~5000 counts) in the upper thoracic area suggesting movement away from the injection site and accumulation of NPs within the heart.

Fluorescent signal (8 hour):
- Observed decrease in the total area as well as max area of fluorescence within the tail suggesting profusion of NPs away from the injections site in mice receiving 25 or 15 mg/kg dosages but no accumulation of NPs was detected in expected organs.
- Mice receiving 10 and 5 mg/kg dosages showed continued accumulation of NPs in the chest cavity.

- The diffuse pattern of fluorescent intensity (max ~4500 counts) observed in the mouse treated with a 5 mg/kg dosage suggests movement through the lungs and heart of the mouse.

Fluorescent signal (12 hour):

- Circulation to major organ systems observed in all mice.
- Mice receiving 20 and 15 mg/kg dosages show fluorescent counts (max ~4500 counts) in the lower thoracic region suggesting localization in the liver or kidneys.
- Both higher doses resulted in a progressive but slower rate of profusion away from the injection site and accumulation in vital organs when compared to 10 and 5 mg/kg doses.
- A downward shift in the fluorescent area away from the heart within the thoracic cavity can be observed at 12 hour time points of mice receiving 10 and 5 mg/kg doses. This shift downward towards the abdomen suggests an increased accumulation of NPs within the liver and kidneys.

Fluorescent signal (24 hour):

- Observed fluorescent signal within the tail is significantly decreased for all mice. Mouse receiving 25 mg/kg injection shows increased absorption of NPs in the hind legs and tissues surrounding the common and external iliac veins.
- All mice show localization at the liver and lower abdomen.
- The pattern of fluorescence seen in the mouse receiving a 5 mg/kg suggests accumulation of NPs in left kidney (max ~4000 counts).

Fluorescent signal (48 hour):

- Full body fluorescence can be detected in the 25 mg/kg dosed mouse with observed absorption of NPs throughout the body and extremities.
- Residual NPs can be detected at the site of injection in the mice receiving 20 or 15 mg/kg dosage as well as accumulation in the liver.
- Mice receiving 10 and 5 mg/kg dosages show a complete depletion of fluorescent signal within the tail at the injection site but persistent fluorescence in the liver.

No time points were taken after 48 hours but data in Figure 19 suggest that ICG loaded NPs can remain in tissue for up to 96 hours depending on site of injection and dosage.

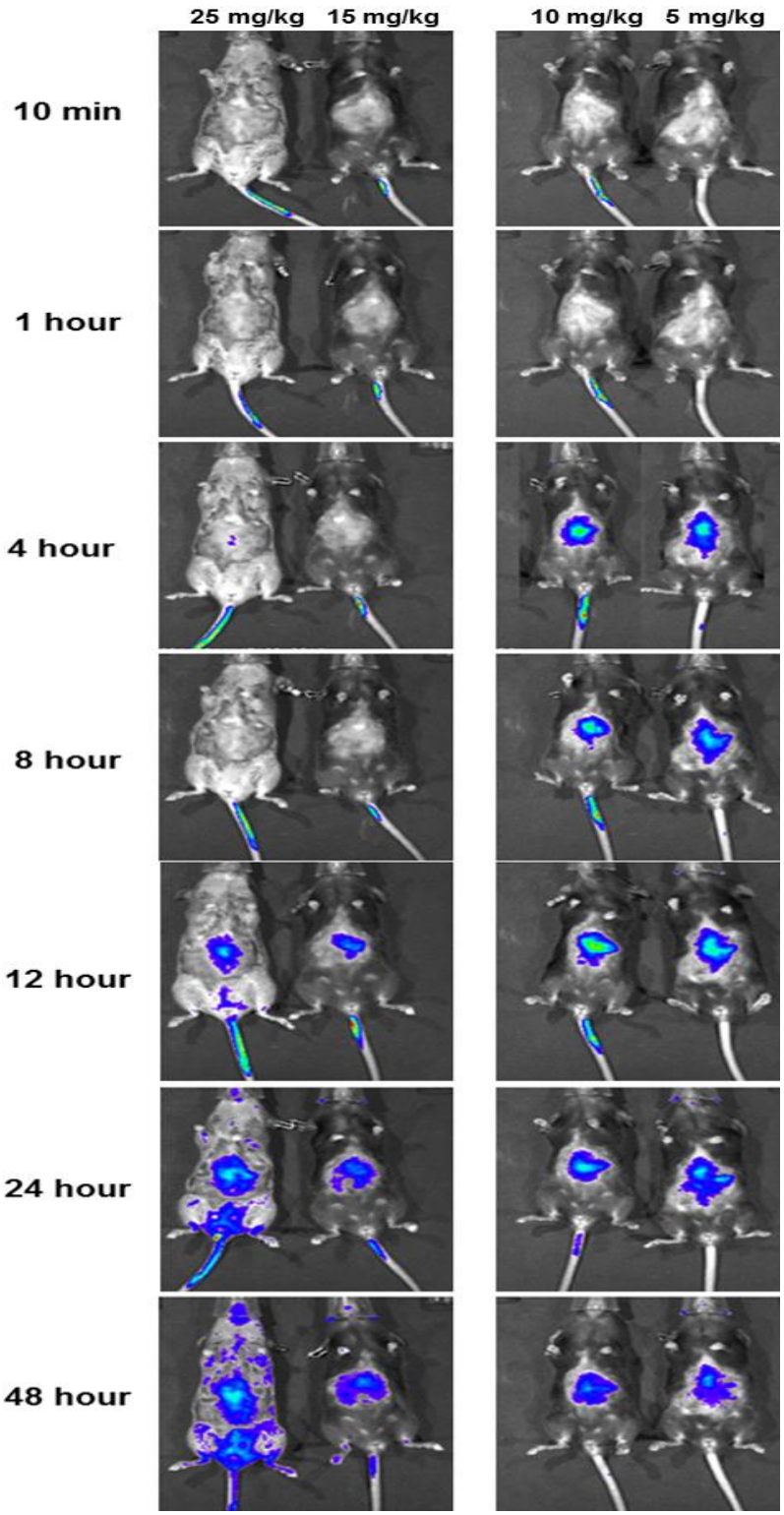

Figure 17: Biodistibution of ICG loaded nanoparticles by tail vein injection in female mice. Mice were treated with 20, 15, 10, or 5 mg/kg doses by weight of nanoparticles (2% ICG). All mice were anesthetized with isofluorene and imaged on an IVIS Spectrum imager using a 745 nm excitation wavelength and 810 nm emission filters.

Aptamer Directed Indocyanine Green Nanoparticles

The goal of this study was to investigate the potential for RLA01 to increase the retention time of labeled NPs at the tumor site following direct injection. I will do this by comparing the radiant efficiency observed after treatment with aptamer labeled ICG loaded NPs (PLGA-ICG-RLA01) versus non-aptamer labeled ICG loaded NPs (PLGA-ICG) in xenograft tumor mice. Mice received weekly injections directly at the tumor site. All mice from both cohorts grew visible tumors over the 8 week study (Table 1). Cohorts I and II were treated with a NP dosage of 71 mg/kg (.5% ICG), anesthetized, and observed (Table 5). Mice were non-sequentially observed at 0, 1, 4, 12, 24, 48, 72, and 96 hour time points throughout the 60 day study following injection to observe ICG fluorescence. Additionally, mice were imaged before weekly ICG treatments to demonstrate metabolism and clearance of ICG NPs from previous treatments.

Table 5: Mouse cohorts for *in vivo* imaging and aptamer labeled nanoparticle encapsulated Paclitaxel drug treatment

Cohort	Nanoparticle dosage	Taxol or ICG equivalent	Number of mice	Number of mice completing study
I Non-labeled ICG NP	71 mg/kg	0.36 mg/kg	4	3^{Δ}
II RLA01 Labeled ICG NP	71 mg/kg	0.36 mg/kg	5	3^{+}
III RLA01 Labeled Ptx NP	71 mg/kg	1.3 mg/kg	4	4
IV Ptx alone	71 mg/kg	Ptx only	5	5

$^{\Delta}$A Mouse from cohort 1 died while anesthetized in week 4 (day 23) during data collection.

$^{+}$Two mice from cohort 2 died while anesthetized in week 6 (day 43) during data collection.

Figure 18 shows a graphical representation of radiant fluorescent signal detected in mice following treatments with either aptamer labeled or non-labeled ICG loaded NPs. In addition, a representative mouse is shown demonstrating the profusion of NPs away from the injection site over 48 hours. Between 1 and up to 8 hours NPs show slow profusion away from the injections site and surrounding tissue following injection with aptamer labeled and non-labeled NPs (Figure 18). The radiant efficiency and total area of detectable fluorescence diminished at 24 hours with non-labeled NP treatments and is demonstrated by both imaging and qualitative data. The slow drainage and clearance of NPs away from the injection site is likely due to the lack of vascularization and slow absorption of NPs into the blood stream. I observed a more persistent fluorescent signal at 24 and 48 hours, measured by radiant efficiency, at the tumor site with an aptamer labeled NP versus a non-aptamer labeled NP (Figure 18). Furthermore, observed area of max fluorescence (yellow coloring) remained higher at 24 and 48 hours when mice were treated with aptamer labeled NPs and appeared to localize on the tumor.

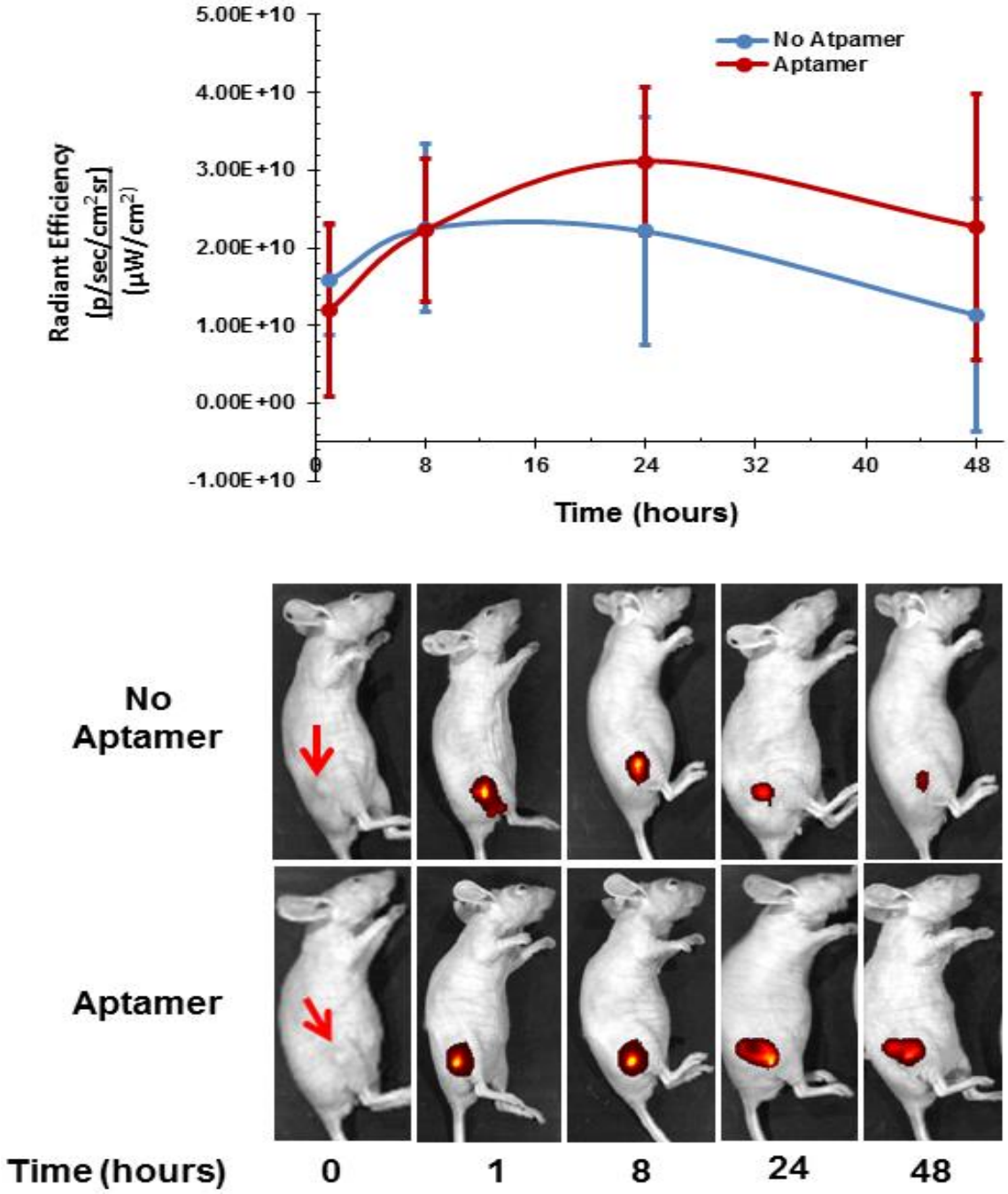

Figure 18: Long-term retention of aptamer directed versus non-aptamer directed ICG loaded nanoparticles in a xenograft mouse model. Graphical representation of radiant efficiency over time (Top). Mice were inoculated with 5.0 x 10^6 Caov-3 cells in the right rear flank (red arrow) of female Nu/J mice and treated with either aptamer labeled or non-aptamer labeled ICG loaded NPs (Bottom).

Table 6: Post-mortem analysis of ICG loaded nanoparticle treated mice

Cohort I PLGA-ICG	Spleen	Liver	Kidneys	Lungs	Heart
Mouse 1	Enlarged	Enlarged		Speckled▲	
Mouse 4	Enlarged				
Cohort II PLGA-ICG-RLA01					
Mouse 2	Enlarged	Enlarged		Speckled▲	
Mouse 3	Enlarged	Enlarged			

▲ Evidence of tumor micrometastasis to the lungs

Paclitaxel Loaded Nanoparticles

The goal of this study was to investigate the potential for RLA01 to increase the retention time of Paclitaxel loaded aptamer labeled NPs at the tumor site in Nu/J mice. This was demonstrated by comparing the reduction in tumor burden between mice receiving weekly injections of aptamer labeled Ptx loaded NPs (PLGA-Ptx-RLA01) versus drug alone (Ptx, Table 5 and 7). In cohort III, 3 of 4 mice grew tumors and 1 mouse from cohort IV grew a tumor. Tumor measurements were taken weekly. Mice received a total of 7 injections over a 60 day period and there was an observed reduction in tumor burden for both cohorts. Aptamer labeled NPs showed to be as effective as Ptx treatments alone, but post hoc analysis showed that this difference was not significant. Additionally, the poor tumor formation seen in cohort IV decreased statistical power. A total of 9 mice survived the 60 day treatment protocol and were euthanized to harvest organs. No abnormalities were seen during post-mortem analysis.

Table 7: Observed reduction in tumor burden in mice treated with aptamer labeled Paclitaxel loaded nanoparticles versus Paclitaxel alone*

					Day				
Cohort III (PLGA-Ptx-RLA01)	**0**	**8**	**15**	**22**	**29**	**36**	**43**	**50**	**57**
Mouse 1	**0**	**3.24**	**3.72**	**4.91**	**1.73**	**5.22**	**9.87**	**6.54**	**4.87**
Mouse 2	**0**	**0**	**0.59**	**0.66**	**0.73**	**3.27**	**4.41**	**3.65**	**2.57**
Mouse 3	**0**	**0**	**0**	**0**	**0**	**0**	**0**	**0**	**0**
Mouse 4	**0**	**1.79**	**2.46**	**3.05**	**2.20**	**1.60**	**5.55**	**4.25**	**3.18**
Cohort IV (Ptx alone)									
Mouse 1	**0**	**0**	**0**	**0**	**0**	**0**	**0**	**0**	**0**
Mouse 2	**0**	**0**	**0**	**0**	**0.8**	**0**	**0**	**0**	**0**
Mouse 3	**0**	**0.67**	**0.78**	**0.93**	**1.30**	**0.74**	**1.56**	**1.16**	**0.68**
Mouse 4	**0**	**0**	**0**	**0**	**0**	**0**	**0**	**0**	**0**
Mouse 5	**0**	**0**	**0**	**0**	**0**	**0**	**0**	**0**	**0**

*Tumor sizes measured in mm^3

Single Dose Tail Vein Injection in Xenograft Tumor Mice
to Assess Targeting Capabilities of Labeled Nanoparticles

Two mice received a single tail vein dose of either labeled or non-labeled ICG loaded NPs (1.75 mg/kg equivalent ICG). Fluorescent ICG was used to monitor the circulatory kinetics of NPs (Figure 19) and any localization that may occur within the mouse. Graphical data is shown that highlights the radiant efficiency in a specific region of interest (ROI) on the mouse (Figure 19, top). Radiance levels were measured directly at the tumor site to determine honing capabilities of RLA01 labeled NPs. The images show a complete 96 hour time course of the observed average radiant efficiency following injection with either ICG aptamer labeled or non-labeled NPs (Figure 19, bottom). No localization of ICG mediated fluorescence was seen at the tumor 1 hour post injection (data not shown)

Single dose tail vein injection with aptamer labeled and non-labeled ICG loaded NPs:

Fluorescent signal (4 hour)

- ICG NPs begin to localize at the tumor site in the mouse treated with aptamer labeled NPs.

Fluorescent signal (8 hour)

- Radiant efficiency rose 25% in the tail of both mice suggesting absorption at the injection site
- The mouse treated with labeled NPs displayed a significantly higher fluorescent signal and larger area of fluorescence suggesting accumulation at the tumor.

Fluorescent signal (24 hour)

- Both mice showed depletion of fluorescent signal within the tail suggesting clearance of NPs away from the injection site.
- Max fluorescent signal localized at the tumor site and the area of total fluorescence was larger for the mouse treated with aptamer labeled NPs suggesting a higher amount of accumulation and increased absorption.

Fluorescent signal (48, 72, and 96 hour)

- The mouse receiving aptamer labeled NPs showed a persistent fluorescent signal at the tumor while the mouse receiving non-labeled NPs displayed no levels of detectable fluorescence as measure by radiant efficiency.

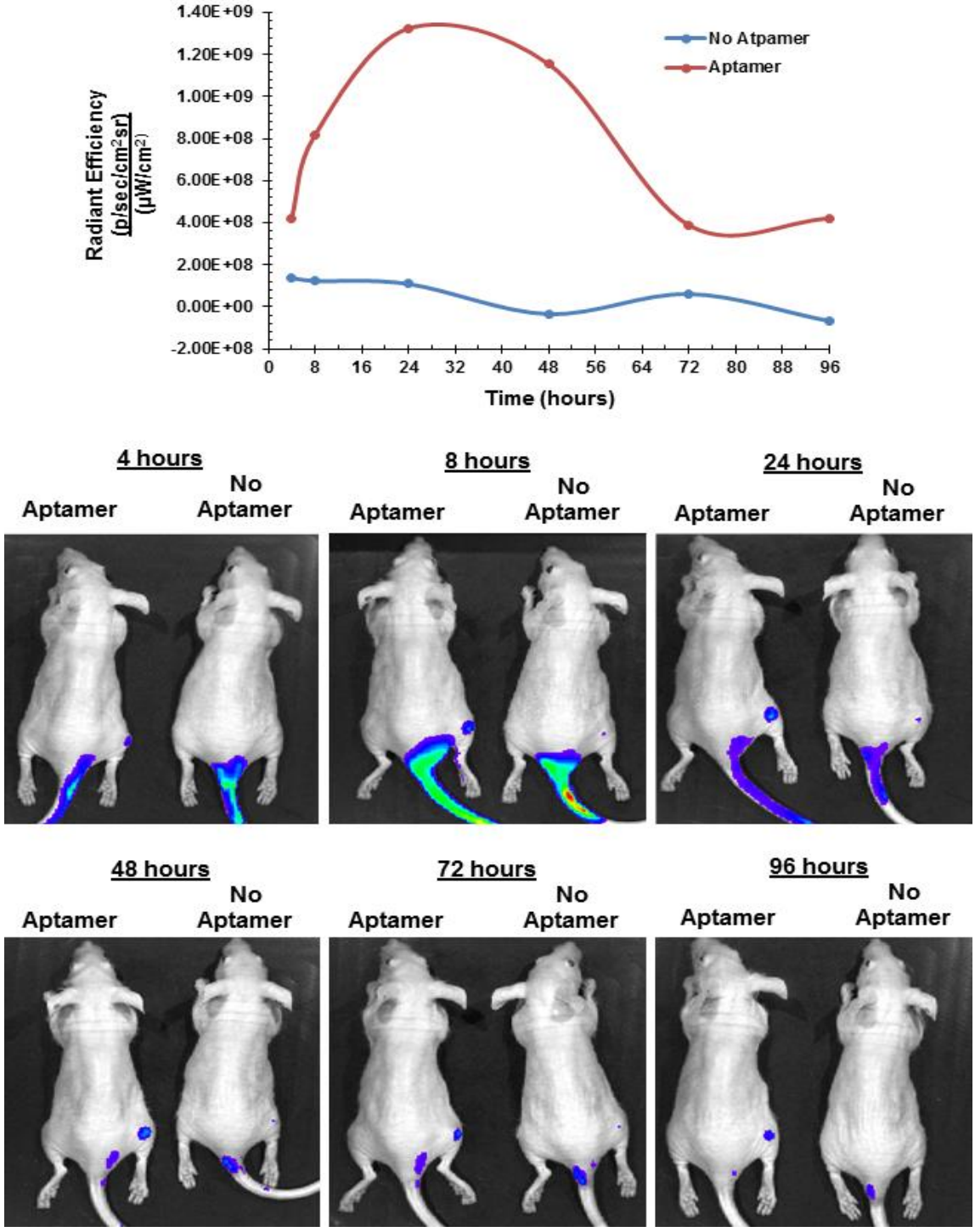

Figure 19: Biodistribution of ICG loaded nanoparticles in an ovarian tumor xeonograft mouse following tail vein injection. Graphical representation of radiant efficiency above background over time (Top). Mice were treated with either aptamer labeled or non-aptamer labeled ICG loaded NPs by tail vein injection (Bottom).

4.4 Discussion

It was my intention to elucidate NP kinetics with regards to overall physiological circulation that include areas of NP accumulation and absorption *in vivo*. Additionally, I wanted to investigate aptamer stability, targeting capabilities, and the potential to promote prolonged retention at the tumor site in the context of an aptamer labeled NP. In the present investigation an efficient strategy to obtain data on the biodistribution of ICG loaded NPs introduced by tail vein injection has been reported. Indocyanine Green is useful for imaging due to its characterization as a near infrared (NIR) fluorescent dye that utilizes wavelengths in the range of 700−900 nm [341]. This is particularly useful in imaging allowing for a high signal-to-background ratio as well as excellent tissue penetration thereby providing a means to detect contrast material at a depth of several millimeters within tissue [341, 342]. ICG infrared frequencies penetrate tissue layers that allows ICG based angiography to image deeper patterns of circulation when compared to fluorescein based angiography [343]. Additionally, imaging is enhanced due to ICG plasma protein interactions that tightly bind one another to promote retention within the vascular system [331, 343, 344]. Moreover, since ICG is approved by the FDA, the clinical translation of ICG based imaging is rapidly advancing as there has been 206 active or concluded clinical trials to date that have used ICG to image colorectal cancer [345], head and neck cancer [346], and breast cancer [343]. More recently, fluorescence-based image guided surgery (IGS) has shown potential to promote clean margins after tumor debulking. Real time NIR imaging during mouse surgeries have been conducted to ensure the complete excision of malignant tissue [342] and a 2014 phase II study

(NCT02027818) assessing the pre- and postoperative analysis of ICG accumulation levels localized at the tumor site following injection in patients with breast cancer.

I was able to track measurable ICG signals and observed accumulation in major organ systems (heart, liver, and kidney). In assessing the feasibility of NPs as a small molecule vehicle, it would seem that the structural integrity of the particles is maintained in the system. The typical half-life of ICG is ~3 minutes and is quickly removed from the circulatory system by the liver [344], thus a potential explanation of the persistent accumulation in mouse livers for all dosages over a 48 hour period. However, the imaging data clearly indicates that ICG loaded NPs administered by tail vein are present within the mouse up to and beyond 48 hours suggesting no apparent increased degradation of NPs in an *in vivo* model. A more rapid reduction of fluorescent signal would have suggested increased degradation of NPs releasing ICG into the blood stream. Although it is likely some NPs were degraded leaking ICG throughout the body, this persistent ICG signal is indicative of structurally intact NPs within the blood plasma and liver. The mice also showed no evidence of overwhelming systemic toxicity with NPs nor NPs conjugated to aptamer RLA01. Even high dosages of NPs were well tolerated by the mice. In addition, no significant sign of toxicity on the major organs was observed in terms of changes in body weight but two mice did present with enlarged livers and spleens that received NP based treatments. Circulatory patterns and organ inflammation were consistent with NP based findings in Wu *et. al.* where by PEG-PAMAM NPs were loaded with a similar NIR dye (Cy3) and introduced by tail vein [347]. This enlargement could be due to the consistent filtering of ICG by these organs and not specifically due to NP accumulation. No mice within cohort III receiving Ptx loaded PLGA NPs showed

any organ abnormalities and it is known that the monomeric units of organic NPs are quickly metabolized by cells (Krebs cycle). It is clear that higher dosages of NPs (25 mg/kg & 15 mg/kg) lead to slower profusion rates away from the injection site, decreased rate of circulation, and increased absorption by tissue surrounding major arteriole networks and within the extremities.

I attempted to determine the potential increased absorption or retention of aptamer labeled NPs versus non-labeled NPs if any. This was also done by NIR imaging where by fluorescent signal was observed in mice receiving subcutaneous injections of NP treatments directly at the tumor site. I chose direct tumor injection of NPs due to the feasibility of this as a clinical option for ovarian tumors. Intraperitoneal therapies have been used for many years that include the use of Paclitaxel and help to diminish residual disease following invasive tumor debulking [348, 349]. Although the location chosen for administering the injection will inherently localize the NPs at the tumor site, the slower rate of clearance away from the tumor site observed with aptamer labeled NPs demonstrates the retention capabilities of RLA01 labeled NPs. Additionally there is a noticeable change in the area of max fluorescence between aptamer directed and non-aptamer directed treatments. I attribute this to an increase of NP localization mediated by aptamer-receptor interactions. This would reduce the rate of NP drainage away from the tumor site with aptamer labeled NPs. Strongest max fluorescent signal for both cohorts appear to be localized directly on the tumor suggesting retention by the EPR effect. Despite all three surviving mice who received non-labeled ICG loaded NP treatments (cohort I) growing palpable tumors, there was significantly less max fluorescent signal after 24 and 48 hours when compared to aptamer labeled NP treatments (cohort II).

These data suggest increased localization and retention at tumors that remain for longer periods of time. Such treatments can minimize cytotoxic effects to neighboring or distal non-malignant tissue with proper dosing and direct administration into malignant tissue.

When investigating the efficacy of Ptx loaded NPs the data suggest that NPs loaded with Ptx can be as effective as drug alone. I did observe a reduction in tumor burden for both cohorts. However, because I was only able to induce a tumor in one mouse from cohort 5 (Ptx alone), the post hoc power analysis indicated a low degree of confidence. Further treatments with tumor induced mice will be needed to determine if aptamer conjugated Ptx loaded NPs are more effective than drug treatments alone. The data does suggest that this type of treatment is clinically feasible and warrants more investigation. Furthermore, the observed increase of retention seen with aptamer labeled ICG loaded NPs could correlate to Ptx loaded NPs as well.

I described earlier the increased cellular uptake of targeted therapies in the context of a Ptx and FDA loaded NP labeled with RLA01 *in vitro* (Chapter 3). To demonstrate the potential targeting capabilities of RLA01 labeled NPs *in vivo*, tumor bearing Nu/J mice were used to investigate the biodistribution of aptamer labeled ICG loaded NPs. The results from IVIS imaging showed that aptamer conjugated NPs administered by tail vein injection promoted the accumulation of NPs at the tumor. The increase of localized fluorescence is due to the addition of the RLA01 aptamer that then enhances the EPR effect often associated with tumor masses. The increased retention of drugs or NPs at the tumor site is dependent on two important factors: (i) circulation time with regards to kidney filtration meaning larger molecules will remain circulating longer, and (ii) development of tumor masses large enough where vascularization is essential for

sustained tumor growth [250, 350]. It has been shown that tumor masses as small as 1.5 mm^3 in total volume require an increase of angiogenesis for survival [351]. Additionally, data suggests that observed accumulation of drug due to the EPR effect are typically seen after 6 hours of circulation [250, 352]. Tumor sizes measured in this study were large enough to promote an increase of vascularization. Furthermore, NPs used for this study will circulate throughout the body for periods of 48 hours or longer as shown by the normal biodistribution of unmodified NPs in non-tumor induced mice (Figure 17). Taking all these data together highly suggests that the increase of fluorescent signal at the tumor for aptamer labeled NP treatments was caused by the EPR effect. Although increased fluorescent signal was seen at the tumor site for non-aptamer labeled NPs, there was significantly less area of fluorescence, lower levels of max fluorescent counts, and higher rates of profusion and lymphatic drainage away from the tumor site over the time course.

I have established that this RLA01 labeled NP model was designed efficiently and that labeled NPs are useful vectors for delivering targeted therapeutics and small molecules to tumor in mouse models. Taken together the results described in the current report demonstrate the following: (i) the use of NP encapsulated ICG provides fluorescent data with little to no background noise often caused by mouse auto-fluorescence providing an accurate assessment of NP kinetics *in vivo*, (ii) data suggests that NPs and labeled NPs do not induce functional impairment to normal tissues and vital organs (iii) PLGA based nano-vehicles clearly enhance the circulatory capabilities of ICG and maintain structural integrity up to 48 hours, (iv) aptamer labeled NPs show an increased retention that could improve the efficacy of current locally administered

therapies, and (v) aptamer directed NPs can localize at the tumor site after long periods of circulation attributed to the EPR effect.

CHAPTER 5: DISSCUSSION AND FUTURE DIRECTION

5.1 Project Summary

- I have identified Caov-3 tumor specific aptamers that bind with apparent K_d values calculated in the nM range. Aptamers RLA01, RLA02, and RLA03 exclusively bind to target Caov-3 cell lines and not to analogous EOC cell lines SW626 and SK-OV-3. More importantly when all three aptamers are conjugated to a Cy5 fluorescent reporter and incubated with non-transformed HOSE 6-3 and HEK293 cells as well as a panel of malignant epithelial disorders no fluorescent events are detected by flow cytometry or confocal microscopy.
- I was able to utilize RLA01 as a molecular chaperone by labeling the surface of nanoparticles. I demonstrated that aptamer labeled NPs carrying Ptx are more effective at limiting cell proliferation when compared to Ptx alone. NP labeling with RLA01 increased internalization mediated by aptamer-receptor interactions.
- I investigated the stability of aptamer RLA01 *in vivo* when used to label ICG loaded NPs. Additionally, I demonstrated the increased retention and targeting capabilities of labeled NPs in xenograft tumor mice.

5.2 Potential Pitfalls of the Cell-SELEX Protocol

I was able to identify unique aptamers that bind to target EOC cancer cells with K_d values that are measured in the nM ranged using Cell-SELEX. The Cell-SELEX protocol can be used to identify aptamers for any chosen cell type. Advances in Cell-SELEX selection and screening have made the number of potential aptamers virtually limitless. However, a major challenge to Cell-SELEX is a scheme to identify aptamers that can distinguish between tumor and highly similar neighboring non-tumor cell populations of that largely share developmental ontogeny. The use of HOSE 6-3 cells improves upon methodology previously described to identify Caov-3 aptamers (DOV3) [93]. Non-malignant transformed ovarian epithelium provided a negative selection

platform that most closely resembles biological normal ovarian tissue. Negative selection using biologically normal cells promotes identification of aptamers that bind exclusively to malignant tissues. More importantly the use of non-malignant epithelial cell lines for negative selection is novel and no other reported ovarian tumor specific aptamer has been identified this way.

A potential modification to the Cell-SELEX protocol in Chapter 2 could be the addition of a single or mulitple cell lines to carry out negative selection. One example could be to add both HEK293 cells as well as a liver cell line such as HepG2. Aptamers identified by this method could demonstrate a decrease in local absorption and retention in kidneys and liver cells, a common place of aptamer retention. Conversely, transformed cells within evolving tumors can be heterogeneous, and how highly specific aptamers can be effective against these tumors remains unclear when aptamers are typically selected against cell lines. It would be interesting to observe any aptamer-cell interactions for the aptamers described here on primary tumor targets to observed potential compatibility of my *in vitro* selection methods with primary tumor explants. Moreover, it would be feasible to apply the methods described here using primary tumor explants as positive selection target cells to generate aptamer pools.

The selection process described utilized serous adenocarcinomas in a late stage of development. As described in Chapter 1, ovarian cancer can originate from multiple types of physiologically similar epithelial progenitors. The aptamers described here were selected against adenocarcinoma serous EOC cells exclusively and the binding kinetics of RLA01, RLA02, and RLA03 showed minimal interaction with analogous SK-OV-3 and SW626 cells. Either aptamer could preferentially bind to other sub-types due to the up-

regulation of similar cell surface markers. A more comprehensive panel of EOC sub-types could be used to determining the specificity of the aptamers described here. Aptamers RLA01, RLA02, and RLA03 bind with high affinity to target cells, but for aptamers to be considered relevant as an early detection diagonstic tool it is important to show binding to pre-staged tumor cells Furthermore it would be interesting to test the binding capabilities of RLA01, RLA02, and RLA03 with a panel of immune specific cells. For future *in vivo* modeling aptamer mediated treatment could disrupt immune response cell signaling by binding and inhibiting interleukins or cause an immune response by activating complement cascades or binding with toll-like receptors.

5.3 Potential Biological Effects of Aptamers

As discussed in Chapter 1 a number of aptamers have been selected against and identified that bind to known cell surface biomarkers *in vitro*. Further analysis to identify any dysregulation within cell signaling or metabolic pathways could be elucidated by identifying the primary target molecule all aptamers identified by this study preferentially bind to. While there are aptamers that show a correlation between binding and the expression of a specific biomarker on the cell surface, many aptamers can simply display a propensity for adherence. This could include one or multiple events that involve binding with lipid rafts, hyper/hypo-glycosylated cell surface markers, upregulated receptors (VEGF, folate, estrogen, Her2), glycoproteins, glycoclipids, or long carbohydrate chains. Identification of the target receptor would be instrumental in determining if identified aptamers demonstrate any inhibitory or antagonistic characteristics within key signaling pathways.

Aptamers could interact with any number of signaling receptors as a first messenger which includes immune receptors, insulin receptors, and G protein-coupled receptors. Specific and non-specific aptamer binding could initiate secondary messenger systems. For example the binding of aptamers to tyrosine kinase receptors could initiate a response within the MAPKK pathway or JAK-STAT pathway promoting cellular processes like proliferation, apoptosis, differentiation, or migration. The aptamers described here showed no apparent cytotoxicity so it would seem that RLA01, RLA02, and RLA03 fail to bind with pro-apoptotic receptors. Alternatively, the aptamers identified here could demonstrate antagonistic effects thus preventing downstream signaling as seen with pegaptanib, potential inhibition of paracrine or endocrine stimulation, or simply bind to the cell surface on lipid moieties or non-functional carbohydrate chains. However, identifying which aptamers demonstrate specific or non-specific binding will help determine what biological assays are feasibly relevant in the future.

It is also not completely understood how aptamer RLA01 could affect the tumor microenvironment and the potential to promote metastasis. Accumulation of aptamers at tumors could inhibit ligands or hormones over time. Such inhibition could promote or inhibit detachment from the tumor mass. Long-term treatments with aptamers on cells *in vitro* could elucidate information about this. I did show an increased incidence of internalization with aptamer labeled NPs *in vitro* (Chapter 2) which correlated with *in vivo* assays described in Chapter 3. This evidence would suggest that aptamer binding and internalization are not significantly altered when comparing *in vitro* and *in vivo* models. Thus *in vitro* aptamer treatments on targets cells followed by genome wide RNA

sequencing transcriptome profiling looking for the up- or down regulation of transcripts that can eventually alter cellular morphology and anchoring would help to identify proteins of interest and determine if aptamers alter such pathways.

I was able to demonstrate the positive internalization of aptamers through the endocytic pathway using an endosomal specific dye. However, no data has been shown that describe the release of aptamers from the endosome, or the subsequent metabolism of aptamers when in the cytosol. Two concerning factors potentially associated with aptamer based diagnostics or therapies and cellular accumulation could include: (i) random integration of DNA aptamers into the genome, and (ii) unintentional mRNA interference. Despite previous knowledge of stable aptamer secondary structures, linearization of the single stranded aptamer due to endosomal pH or cytosolic nucleases could promote non-specific binding with mRNA transcripts and disrupt ribosomal translation. Although the aptamers described in this study are DNA and not RNA based, this mode of disruption seems unlikely and has not been reported to date with DNA aptamers. The potential of prolonged exposure to aptamer based treatments could lead to eventual genomic integration. Despite aptamers existing as single stranded oligonucleotides the potential to bind to complimentary short strands of degraded mRNA could create double stranded molecules. Moreover, some chemotherapeutics molecules will intercalate with DNA and is exploited to build aptamer-drug conjugates. Drug metabolites can shuttle aptamers to the nucleus or aptamers within the cytosol could non-specifically bind to nuclear bound proteins.

Aptamers RLA01, RLA02, and RLA03 do bind to target cells in their native form. The addition of post sequencing modifications could alter the binding kinetics of these

aptamers as well as cause cytotoxic or regulatory affects. For example, aptamer binding can be altered by phosphothioate substitutions that have been shown to increase aptamer binding with plasmid DNA and mRNA *in vitro* (Table 1). However, phospothioate substitutions are also correlated with increase retention in both kidney and liver cells *in vivo*. Since the conjugation of Cy5 dye to RLA01 or RLA01 covalent linkage to NPs does not appear to demonstrate inhibition of binding when incubated with target cells, it would suggest that the tethering of RLA01 to small molecules does not alter binding kinetics.

In addition to looking at the effects caused by sequencing modifications of aptamers *in vitro*, a multi-arm *in vivo* analysis that exposes mice to various concentrations of modified Cy5-aptamer conjugates can provide data on several key physiological barriers seen with aptamer treatments including: (i) general biodistribution and areas of localization or absorption, (ii) ability to resist endogenous plasma nucleases and overall degradation, (iii) circulatory half-life, (iv) overall toxicity of aptamers, and (v) ability of aptamers to localize at tumor sites when administered to tumor models. Non-specific nuclease degradation reduces maximum plasma concentration of circulating aptamers. The high degree of conformational malleability of aptamers, including available post sequencing modifications, could inhibit or enhance binding abilities. While additions of LNAs or 2'-O-methyl substitutions could increase nuclease resistance, post-transcriptional modifiers could increase hepatic toxicity and alter binding kinetics depending on physiological factors such as pH and ion concentrations.

5.4 Aptamer Sequencing

The ability to modify sequencing protocols and utilize machinery within our facility provided a great advantage. The Ion Torrent was an optimal platform knowing we would not see a high degree of variability within the aptamer pool as well as knowing the initial size of the sequence. Because of this a larger scale illumina platform was determined to be unnecessary. Future sequencing utilizing illumina facilities could help to identify potential problems that lead to low yields of aptamer sub-populations. Additional analysis of sequencing data can help to identify all aptamer sub-populations. Superficial searches for PCR priming sequences identified full length aptamers and thus proved to be effective. However, coding to identify sequences showing various degrees of homology are yet to be employed. In addition, sequence analysis of RLA01 through RLA07 could show sequence homology that could prove to be cell line or receptor class specific. For example aptamers whose sequences show a high degree of G·C rich nucleotides could preferentially bind to particular receptors up-regulated on tumor cells. Data mining on aptamers that preferentially bind to up-regulated ovarian tumor markers such as folate or HER2 could elucidate more information showing sequence specific binding. The identification of 7 aptamers that demonstrate biologically unique apparent binding constants suggests I reached the final round of selection. Additionally the process for monitoring aptamer selection with bacterial transformations and by the increase of fluorescent activity when comparing successive aptamer pools by flow cytometry was effective. Additional methods such as gel extraction and purification, column affinity and purification, and streptavidin bead isolation of aptamer sequences could be used to confirm recovery and enrichment.

The current push to improve upon *in silico* modeling when designing single aptamers or aptamer pools could be used to improve upon previously established aptamers like RLA01, RLA02, and RLA03. For example computer modeling would predict changes in binding affinity after modifications like base substitutions. This could improve up the current structures of aptamers which would help with stability and resistance to endogenous nucleases as well as increase binding affinities. However, knowing the preferential binding target of RLA01, RLA02, and RLA03 is necessary to apply this strategy.

5.5 Aptamer-Nanoparticle Conjugates

Because I was able to collaborate on this project with Dr. Craig Ogle from the Chemistry department at UNC-Charlotte, I was able to utilize their already established formulation to make PLGA based NPs. The PLGA polymer allowed me to encapsulate multiple hydrophobic drugs, such as Ptx, because of the amphipathic nature of the particle. The PLGA particle demonstrates no auto-fluorescence and PLGA metabolites are quickly processed and cleared by the body. In addition to being biodegradable and showing high biocompatibility, PLGA is found in a variety of FDA approved therapeutic devices and products. Nanoparticles formulated from other materials like silicon, silver, or gold often possess intrinsic auto-fluorescent profiles that could have altered ICG based visualization for xenograft mouse imaging. In addition there is a well-established safety record with PLGA based NPs. I was also able to visualize NPs for size analysis by SEM imaging which is important for predicting mechanistic modes of internalization. The successful labeling of NPs with aptamers demonstrates the feasibility of using NPs as a labeling platform and could be altered in several ways. One example would be the dual

loading of NPs with both ICG and Ptx for future *in vivo* studies. Such models could help to quantify drug doses localized at tumors. In addition to dual loading the potential for dual targeting could promote additional internalization to what has been observed (Chapter 2). Dual targeting and combinatorial loading of NPs could potentially lead to treatments that circumvent multidrug resistance pathways.

5.6 Biological Significance and Future Challenges

The potential of aptamer development can lead to increased sensitivity of diagnostics including visualization or isolation of malignant cells. Furthermore, generating tumor specific aptamers could help differentiate between various tumor subtypes. Multi-targeted aptamers specific to tumor sub-types could increase the positive identification of malignant tissue with more accuracy that PCR identification of biomarkers in serum. This could increase the general utility of Cell-SELEX identified aptamers by employing them to assess specific information about the cell-surface proteome. Aptamer arrays can give us a better understanding concerning the tumor microenvironment and overall topography [353]. Clearly there is an invading presence of aptamers as drugs for different targets and diseases. Since the initial description of aptamers and aptamer technology in 1990, only one aptamer has been FDA approved and is in use for therapeutics but not directed against cancer. In 2011 there were a total of nine DNA/RNA based antagonistic aptamers undergoing phase I, II, or III clinical trials [79]. Four years later in 2015, twenty-six aptamer related clinical trials have been developed, the majority of which have been completed. In large part this slow move from translational benchtop to market reflects the anti-cancer drug model as a whole; only an estimated 0.5% - 3% of drugs tested in the laboratory eventually lead to FDA

approval. Continued development of Cell-SELEX protocols along with the development of *in silico* modeling will lead to more efficient techniques for developing targeting aptamer pools.

Off-target or unanticipated effects including induction of opposite effects, *e.g.* cell killing versus migration or differences between sexes may prove to be barriers to large-scale therapeutic development without intensive pre-clincial testing. Even despite this testing, a disconnect between promising early studies and less effective clinical trial outcomes has been frustrating to the field. The nucleolin AS1411 aptamer showed excellent efficacy in laboratory studies and phase I clinical trial, yet phase II results were significantly less compelling and the study was terminated.

The power of NP labeling through the combination of nanoparticle and aptamer technologies may be thwarted by the need to bring together multiple entities with potentially competing financial and commercial interests. By contrast, single aptamer therapeutics as well as drug loaded nanoparticles have progressed to clinical trials and may come to market more quickly. Despite these challenges, the financial outlook and continued interest by the biotechnology industries remains highly positive. The achievement of pegaptanib has given the aptamer field a boost, and the aptamer market is poised to grow on par with antibodies in the next 10-15 years at an estimated growth rate of 49% [276]. The global aptamer market was valued at $236 million in 2010 and increased to $287 million in 2013 [79] and is expected to reach $2.1 billion by 2018 [276]. However, it should be noted that previous global growth estimates proved overly positive; in 2010 it was estimated the market in this year would be valued at $1.9 billion [79], but this has been significantly adjusted to under $500 million [276]. As aptamer

screening techniques and efficiency continue to be optimized, they will provide the ability to identify aptamers unique to each individual's tumor and development of personalized medicine.

REFERENCES

1. Siegel, R.L., K.D. Miller, and A. Jemal, *Cancer statistics, 2015.* CA Cancer J Clin, 2015. **65**(1): p. 5-29.

2. Kroep, J.R., *Advances in epithelial ovarian cancer therapy.* Curr Pharm Des, 2012. **18**(25): p. 3735-40.

3. Hennessy, B.T., R.L. Coleman, and M. Markman, *Ovarian cancer.* Lancet, 2009. **374**(9698): p. 1371-82.

4. SEER Cancer Statistics Factsheets: Ovary Cancer. National Cancer Institute. Bethesda, M.

5. Cohen, J.G., et al., *In 2014, can we do better than CA125 in the early detection of ovarian cancer?* World J Biol Chem, 2014. **5**(3): p. 286-300.

6. Saad, A.F., W. Hu, and A.K. Sood, *Microenvironment and pathogenesis of epithelial ovarian cancer.* Horm Cancer, 2010. **1**(6): p. 277-90.

7. Choi, M., et al., *Conditional survival in ovarian cancer: results from the SEER dataset 1988-2001.* Gynecol Oncol, 2008. **109**(2): p. 203-9.

8. Steffensen, K.D., et al., *Prevalence of epithelial ovarian cancer stem cells correlates with recurrence in early-stage ovarian cancer.* J Oncol, 2011. **2011**: p. 620523.

9. Conic, I., et al., *Ovarian epithelial cancer stem cells.* ScientificWorldJournal, 2011. **11**: p. 1243-69.

10. Dubeau, L., *The cell of origin of ovarian epithelial tumours.* Lancet Oncol, 2008. **9**(12): p. 1191-7.

11. Crum, C.P., et al., *Lessons from BRCA: the tubal fimbria emerges as an origin for pelvic serous cancer.* Clin Med Res, 2007. **5**(1): p. 35-44.

12. Lambros, M.B., et al., *Analysis of ovarian cancer cell lines using array-based comparative genomic hybridization.* J Pathol, 2005. **205**(1): p. 29-40.

13. Sonoda, G., et al., *Comparative genomic hybridization detects frequent overrepresentation of chromosomal material from 3q26, 8q24, and 20q13 in human ovarian carcinomas.* Genes Chromosomes Cancer, 1997. **20**(4): p. 320-8.

14. Watanabe, T., et al., *A novel amplification at 17q21-23 in ovarian cancer cell lines detected by comparative genomic hybridization.* Gynecol Oncol, 2001. **81**(2): p. 172-7.

15. Schraml, P., et al., *Combined array comparative genomic hybridization and tissue microarray analysis suggest PAK1 at 11q13.5-q14 as a critical oncogene target in ovarian carcinoma.* Am J Pathol, 2003. **163**(3): p. 985-92.

16. Hauptmann, S., et al., *Genetic alterations in epithelial ovarian tumors analyzed by comparative genomic hybridization.* Hum Pathol, 2002. **33**(6): p. 632-41.

17. Lawrenson, K., et al., *Modelling genetic and clinical heterogeneity in epithelial ovarian cancers.* Carcinogenesis, 2011. **32**(10): p. 1540-9.

18. Gounaris, I., D.S. Charnock-Jones, and J.D. Brenton, *Ovarian clear cell carcinoma--bad endometriosis or bad endometrium?* J Pathol, 2011. **225**(2): p. 157-60.

19. Obata, K., et al., *Frequent PTEN/MMAC mutations in endometrioid but not serous or mucinous epithelial ovarian tumors.* Cancer Res, 1998. **58**(10): p. 2095-7.

20. Meinhold-Heerlein, I., et al., *Molecular and prognostic distinction between serous ovarian carcinomas of varying grade and malignant potential.* Oncogene, 2005. **24**(6): p. 1053-65.

21. Desai, A., et al., *Epithelial ovarian cancer: An overview.* World J Transl Med, 2014. **3**(1): p. 1-8.

22. Singer, G., et al., *Patterns of p53 mutations separate ovarian serous borderline tumors and low- and high-grade carcinomas and provide support for a new model of ovarian carcinogenesis: a mutational analysis with immunohistochemical correlation.* Am J Surg Pathol, 2005. **29**(2): p. 218-24.

23. Willner, J., et al., *Alternate molecular genetic pathways in ovarian carcinomas of common histological types.* Hum Pathol, 2007. **38**(4): p. 607-13.

24. Sieben, N.L., et al., *In ovarian neoplasms, BRAF, but not KRAS, mutations are restricted to low-grade serous tumours.* J Pathol, 2004. **202**(3): p. 336-40.

25. Seidman, J.D., B.M. Ronnett, and R.J. Kurman, *Pathology of borderline (low malignant potential) ovarian tumours.* Best Pract Res Clin Obstet Gynaecol, 2002. **16**(4): p. 499-512.

26. Yip, P., et al., *Comprehensive serum profiling for the discovery of epithelial ovarian cancer biomarkers.* PLoS One, 2011. **6**(12): p. e29533.

27. Gemignani, M.L., et al., *Role of KRAS and BRAF gene mutations in mucinous ovarian carcinoma.* Gynecol Oncol, 2003. **90**(2): p. 378-81.

28. Storey, D.J., et al., *Endometrioid epithelial ovarian cancer : 20 years of prospectively collected data from a single center.* Cancer, 2008. **112**(10): p. 2211-20.

29. Kuo, K.T., et al., *Frequent activating mutations of PIK3CA in ovarian clear cell carcinoma.* Am J Pathol, 2009. **174**(5): p. 1597-601.

30. Duska, L.R., et al., *When 'never-events' occur despite adherence to clinical guidelines: the case of venous thromboembolism in clear cell cancer of the ovary compared with other epithelial histologic subtypes.* Gynecol Oncol, 2010. **116**(3): p. 374-7.

31. Chen, C.H., et al., *Overexpression of cyclin D1 and c-Myc gene products in human primary epithelial ovarian cancer.* Int J Gynecol Cancer, 2005. **15**(5): p. 878-83.

32. Hellstrom, I. and K.E. Hellstrom, *SMRP and HE4 as biomarkers for ovarian carcinoma when used alone and in combination with CA125 and/or each other.* Adv Exp Med Biol, 2008. **622**: p. 15-21.

33. Sorace, J.M. and M. Zhan, *A data review and re-assessment of ovarian cancer serum proteomic profiling.* BMC Bioinformatics, 2003. **4**: p. 24.

34. Jacobs, I., et al., *A risk of malignancy index incorporating CA 125, ultrasound and menopausal status for the accurate preoperative diagnosis of ovarian cancer.* Br J Obstet Gynaecol, 1990. **97**(10): p. 922-9.

35. Moore, R.G., et al., *A novel multiple marker bioassay utilizing HE4 and CA125 for the prediction of ovarian cancer in patients with a pelvic mass.* Gynecol Oncol, 2009. **112**(1): p. 40-6.

36. Zhang, Z., et al., *Three biomarkers identified from serum proteomic analysis for the detection of early stage ovarian cancer.* Cancer Res, 2004. **64**(16): p. 5882-90.

37. McGuire, W.P., 3rd and M. Markman, *Primary ovarian cancer chemotherapy: current standards of care.* Br J Cancer, 2003. **89 Suppl 3**: p. S3-8.

38. du Bois, A., et al., *A randomized clinical trial of cisplatin/paclitaxel versus carboplatin/paclitaxel as first-line treatment of ovarian cancer.* J Natl Cancer Inst, 2003. **95**(17): p. 1320-9.

39. Bicaku, E., et al., *In vitro analysis of ovarian cancer response to cisplatin, carboplatin, and paclitaxel identifies common pathways that are also associated with overall patient survival.* Br J Cancer, 2012. **106**(12): p. 1967-75.

40. Markman, M., *Intraperitoneal antineoplastic drug delivery: rationale and results.* Lancet Oncol, 2003. **4**(5): p. 277-83.

41. Markman, M., *Current status of intraperitoneal antineoplastic drug delivery.* Cancer Treat Res, 2007. **134**: p. 153-69.

42. Piso, P., et al., *Cytoreductive surgery and hyperthermic intraperitoneal chemotherapy in peritoneal carcinomatosis from ovarian cancer.* World J Surg Oncol, 2004. **2**: p. 21.

43. Mantia-Smaldone, G.M., R.P. Edwards, and A.M. Vlad, *Targeted treatment of recurrent platinum-resistant ovarian cancer: current and emerging therapies.* Cancer Manag Res, 2011. **3**: p. 25-38.

44. Monk, B.J., et al., *Trabectedin as a new chemotherapy option in the treatment of relapsed platinum sensitive ovarian cancer.* Curr Pharm Des, 2012. **18**(25): p. 3754-69.

45. Audeh, M.W., et al., *Oral poly(ADP-ribose) polymerase inhibitor olaparib in patients with BRCA1 or BRCA2 mutations and recurrent ovarian cancer: a proof-of-concept trial.* Lancet, 2010. **376**(9737): p. 245-51.

46. Cannistra, S.A., et al., *Phase II study of bevacizumab in patients with platinum-resistant ovarian cancer or peritoneal serous cancer.* J Clin Oncol, 2007. **25**(33): p. 5180-6.

47. Kroep, J.R. and J.W. Nortier, *The role of bevacizumab in advanced epithelial ovarian cancer.* Curr Pharm Des, 2012. **18**(25): p. 3775-83.

48. Konner, J.A., et al., *Farletuzumab, a humanized monoclonal antibody against folate receptor alpha, in epithelial ovarian cancer: a phase I study.* Clin Cancer Res, 2010. **16**(21): p. 5288-95.

49. Markman, M., *Current standards of care for chemotherapy of optimally cytoreduced advanced epithelial ovarian cancer.* Gynecol Oncol, 2013. **131**(1): p. 241-5.

50. Meyer, C., U. Hahn, and A. Rentmeister, *Cell-specific aptamers as emerging therapeutics.* J Nucleic Acids, 2011. **2011**: p. 904750.

51. Dausse, E., S. Da Rocha Gomes, and J.J. Toulme, *Aptamers: a new class of oligonucleotides in the drug discovery pipeline?* Curr Opin Pharmacol, 2009. **9**(5): p. 602-7.

52. Tuerk, C. and L. Gold, *Systematic evolution of ligands by exponential enrichment: RNA ligands to bacteriophage T4 DNA polymerase.* Science, 1990. **249**(4968): p. 505-10.

53. Ellington, A.D. and J.W. Szostak, *In vitro selection of RNA molecules that bind specific ligands.* Nature, 1990. **346**(6287): p. 818-22.

54. Fang, X. and W. Tan, *Aptamers generated from cell-SELEX for molecular medicine: a chemical biology approach.* Acc Chem Res, 2010. **43**(1): p. 48-57.

55. McKeague, M. and M.C. Derosa, *Challenges and opportunities for small molecule aptamer development.* J Nucleic Acids, 2012. **2012**: p. 748913.

56. Bazak, R., et al., *Cancer active targeting by nanoparticles: a comprehensive review of literature.* J Cancer Res Clin Oncol, 2014.

57. Jayasena, S.D., *Aptamers: an emerging class of molecules that rival antibodies in diagnostics.* Clin Chem, 1999. **45**(9): p. 1628-50.

58. Healy, J.M., et al., *Pharmacokinetics and biodistribution of novel aptamer compositions.* Pharm Res, 2004. **21**(12): p. 2234-46.

59. Kanwar, J.R., K. Roy, and R.K. Kanwar, *Chimeric aptamers in cancer cell-targeted drug delivery.* Crit Rev Biochem Mol Biol, 2011. **46**(6): p. 459-77.

60. Zhu, G., et al., *Nucleic acid aptamers: an emerging frontier in cancer therapy.* Chem Commun (Camb), 2012. **48**(85): p. 10472-80.

61. Lee, J.H., et al., *Molecular diagnostic and drug delivery agents based on aptamer-nanomaterial conjugates.* Adv Drug Deliv Rev, 2010. **62**(6): p. 592-605.

62. Tan, W., et al., *Molecular aptamers for drug delivery.* Trends Biotechnol, 2011. **29**(12): p. 634-40.

63. Zhang, Y., H. Hong, and W. Cai, *Tumor-targeted drug delivery with aptamers.* Curr Med Chem, 2011. **18**(27): p. 4185-94.

64. Talekar, M., et al., *Targeting of nanoparticles in cancer: drug delivery and diagnostics.* Anticancer Drugs, 2011. **22**(10): p. 949-62.

65. Cunningham, E.T., Jr., et al., *A phase II randomized double-masked trial of pegaptanib, an anti-vascular endothelial growth factor aptamer, for diabetic macular edema.* Ophthalmology, 2005. **112**(10): p. 1747-57.

66. Ng, E.W., et al., *Pegaptanib, a targeted anti-VEGF aptamer for ocular vascular disease.* Nat Rev Drug Discov, 2006. **5**(2): p. 123-32.

67. Jilma-Stohlawetz, P., et al., *Inhibition of von Willebrand factor by ARC1779 in patients with acute thrombotic thrombocytopenic purpura.* Thromb Haemost, 2011. **105**(3): p. 545-52.

68. Darisipudi, M.N., et al., *Dual blockade of the homeostatic chemokine CXCL12 and the proinflammatory chemokine CCL2 has additive protective effects on diabetic kidney disease.* Am J Pathol, 2011. **179**(1): p. 116-24.

69. Duda, D.G., et al., *CXCL12 (SDF1alpha)-CXCR4/CXCR7 pathway inhibition: an emerging sensitizer for anticancer therapies?* Clin Cancer Res, 2011. **17**(8): p. 2074-80.

70. Ashrafuzzaman, M., *Aptamers as both drugs and drug-carriers.* Biomed Res Int, 2014. **2014**: p. 697923.

71. Brody, E.N. and L. Gold, *Aptamers as therapeutic and diagnostic agents.* J Biotechnol, 2000. **74**(1): p. 5-13.

72. Bouchard, P.R., R.M. Hutabarat, and K.M. Thompson, *Discovery and development of therapeutic aptamers.* Annu Rev Pharmacol Toxicol, 2010. **50**: p. 237-57.

73. Gutsaeva, D.R., et al., *Inhibition of cell adhesion by anti-P-selectin aptamer: a new potential therapeutic agent for sickle cell disease.* Blood, 2011. **117**(2): p. 727-35.

74. Mann, A.P., et al., *Identification of thioaptamer ligand against E-selectin: potential application for inflamed vasculature targeting.* PLoS One, 2010. **5**(9).

75. Chen, C.H., et al., *Inhibition of heregulin signaling by an aptamer that preferentially binds to the oligomeric form of human epidermal growth factor receptor-3.* Proc Natl Acad Sci U S A, 2003. **100**(16): p. 9226-31.

76. Green, L.S., et al., *Inhibitory DNA ligands to platelet-derived growth factor B-chain.* Biochemistry, 1996. **35**(45): p. 14413-24.

77. Shigdar, S., et al., *RNA aptamers targeting cancer stem cell marker CD133.* Cancer Lett, 2013. **330**(1): p. 84-95.

78. Khati, M., et al., *Neutralization of infectivity of diverse R5 clinical isolates of human immunodeficiency virus type 1 by gp120-binding 2'F-RNA aptamers.* J Virol, 2003. **77**(23): p. 12692-8.

79. Esposito, C.L., et al., *New insight into clinical development of nucleic acid aptamers.* Discov Med, 2011. **11**(61): p. 487-96.

80. Zhu, J., et al., *Progress in Aptamer-Mediated Drug Delivery Vehicles for Cancer Targeting and Its Implications in Addressing Chemotherapeutic Challenges.* Theranostics, 2014. **4**(9): p. 931-944.

81. Shum, K.T., J. Zhou, and J.J. Rossi, *Nucleic Acid Aptamers as Potential Therapeutic and Diagnostic Agents for Lymphoma.* J Cancer Ther, 2013. **4**(4): p. 872-890.

82. Kim, N., H.H. Gan, and T. Schlick, *A computational proposal for designing structured RNA pools for in vitro selection of RNAs.* RNA, 2007. **13**(4): p. 478-92.

83. Son, Y.M., J.H. Lee, and D.R. Kim, *Modulation of RAG/DNA complex by HSP70 in V(D)J recombination.* Biochem Biophys Res Commun, 2008. **365**(1): p. 113-7.

84. Chushak, Y. and M.O. Stone, *In silico selection of RNA aptamers.* Nucleic Acids Res, 2009. **37**(12): p. e87.

85. Patzel, V., *In silico selection of functional RNA molecules.* Curr Opin Drug Discov Devel, 2004. **7**(3): p. 360-9.

86. Sanchez-Luque, F.J., et al., *Efficient HIV-1 inhibition by a 16 nt-long RNA aptamer designed by combining in vitro selection and in silico optimisation strategies.* Sci Rep, 2014. **4**: p. 6242.

87. Morris, K.N., et al., *High affinity ligands from in vitro selection: complex targets.* Proc Natl Acad Sci U S A, 1998. **95**(6): p. 2902-7.

88. Homann, M. and H.U. Goringer, *Combinatorial selection of high affinity RNA ligands to live African trypanosomes.* Nucleic Acids Res, 1999. **27**(9): p. 2006-14.

89. Stoltenburg, R., C. Reinemann, and B. Strehlitz, *SELEX--a (r)evolutionary method to generate high-affinity nucleic acid ligands.* Biomol Eng, 2007. **24**(4): p. 381-403.

90. Ara, M.N., et al., *Development of a Novel DNA Aptamer Ligand Targeting to Primary Cultured Tumor Endothelial Cells by a Cell-Based SELEX Method.* PLoS One, 2012. **7**(12): p. e50174.

91. Xiao, Z., et al., *Cell-specific internalization study of an aptamer from whole cell selection.* Chemistry, 2008. **14**(6): p. 1769-75.

92. Xiao, Z., et al., *Engineering of targeted nanoparticles for cancer therapy using internalizing aptamers isolated by cell-uptake selection.* ACS Nano, 2012. **6**(1): p. 696-704.

93. Van Simaeys, D., et al., *Study of the molecular recognition of aptamers selected through ovarian cancer cell-SELEX.* PLoS One, 2010. **5**(11): p. e13770.

94. Daniels, D.A., et al., *A tenascin-C aptamer identified by tumor cell SELEX: systematic evolution of ligands by exponential enrichment.* Proc Natl Acad Sci U S A, 2003. **100**(26): p. 15416-21.

95. Tatarinova, O., et al., *Comparison of the 'chemical' and 'structural' approaches to the optimization of the thrombin-binding aptamer.* PLoS One, 2014. **9**(2): p. e89383.

96. Keefe, A.D. and S.T. Cload, *SELEX with modified nucleotides.* Curr Opin Chem Biol, 2008. **12**(4): p. 448-56.

97. Burmeister, P.E., et al., *Direct in vitro selection of a 2'-O-methyl aptamer to VEGF.* Chem Biol, 2005. **12**(1): p. 25-33.

98. Chelliserrykattil, J. and A.D. Ellington, *Evolution of a T7 RNA polymerase variant that transcribes 2'-O-methyl RNA.* Nat Biotechnol, 2004. **22**(9): p. 1155-60.

99. Fa, M., et al., *Expanding the substrate repertoire of a DNA polymerase by directed evolution.* J Am Chem Soc, 2004. **126**(6): p. 1748-54.

100. Sousa, R. and R. Padilla, *A mutant T7 RNA polymerase as a DNA polymerase.* EMBO J, 1995. **14**(18): p. 4609-21.

101. Jellinek, D., et al., *Potent 2'-amino-2'-deoxypyrimidine RNA inhibitors of basic fibroblast growth factor.* Biochemistry, 1995. **34**(36): p. 11363-72.

102. Lin, Y., et al., *High-affinity and specific recognition of human thyroid stimulating hormone (hTSH) by in vitro-selected 2'-amino-modified RNA.* Nucleic Acids Res, 1996. **24**(17): p. 3407-14.

103. Proske, D., et al., *Prion-protein-specific aptamer reduces PrPSc formation.* Chembiochem, 2002. **3**(8): p. 717-25.

104. Lin, Y., et al., *Modified RNA sequence pools for in vitro selection.* Nucleic Acids Res, 1994. **22**(24): p. 5229-34.

105. Kato, Y., et al., *New NTP analogs: the synthesis of 4'-thioUTP and 4'-thioCTP and their utility for SELEX.* Nucleic Acids Res, 2005. **33**(9): p. 2942-51.

106. Kang, J., et al., *Combinatorial selection of a single stranded DNA thioaptamer targeting TGF-beta1 protein.* Bioorg Med Chem Lett, 2008. **18**(6): p. 1835-9.

107. Weiss, S., et al., *RNA aptamers specifically interact with the prion protein PrP.* J Virol, 1997. **71**(11): p. 8790-7.

108. Porter, K.W., J.D. Briley, and B.R. Shaw, *Direct PCR sequencing with boronated nucleotides.* Nucleic Acids Res, 1997. **25**(8): p. 1611-7.

109. Chakravarthy, U., et al., *Year 2 efficacy results of 2 randomized controlled clinical trials of pegaptanib for neovascular age-related macular degeneration.* Ophthalmology, 2006. **113**(9): p. 1508 e1-25.

110. Obubuafo, A., et al., *Poly(methyl methacrylate) microchip affinity capillary gel electrophoresis of aptamer-protein complexes for the analysis of thrombin in plasma.* Electrophoresis, 2008. **29**(16): p. 3436-3445.

111. Gordon, E.M. and F.L. Hall, *Rexin-G, a targeted genetic medicine for cancer.* Expert Opin Biol Ther, 2010. **10**(5): p. 819-32.

112. He, K., et al., *Synthesis of 5-substituted 2'-deoxycytidine 5'-(alpha-P-borano)triphosphates, their incorporationinto DNA and effects on exonuclease.* Nucleic Acids Res, 1999. **27**(8): p. 1788-94.

113. Masud, M.M., et al., *Sialyllactose-binding modified DNA aptamer bearing additional functionality by SELEX.* Bioorg Med Chem, 2004. **12**(5): p. 1111-20.

114. Kuwahara, M. and N. Sugimoto, *Molecular evolution of functional nucleic acids with chemical modifications.* Molecules, 2010. **15**(8): p. 5423-44.

115. Jensen, T.B., et al., *Synthesis and Structural Characterization of 2 '-Fluoro-alpha-L-RNA-Modified Oligonucleotides.* Chembiochem, 2011. **12**(12): p. 1903-1910.

116. Layzer, J.M., et al., *In vivo activity of nuclease-resistant siRNAs.* RNA, 2004. **10**(5): p. 766-71.

117. Schmidt, K.S., et al., *Application of locked nucleic acids to improve aptamer in vivo stability and targeting function.* Nucleic Acids Res, 2004. **32**(19): p. 5757-65.

118. Kuwahara, M. and S. Obika, *In vitro selection of BNA (LNA) aptamers.* Artif DNA PNA XNA, 2013. **4**(2): p. 39-48.

119. Singh, S.K., R. Kumar, and J. Wengel, *Synthesis of Novel Bicyclo[2.2.1] Ribonucleosides: 2'-Amino- and 2'-Thio-LNA Monomeric Nucleosides.* J Org Chem, 1998. **63**(18): p. 6078-6079.

120. Petersen, M., et al., *Locked nucleic acid (LNA) recognition of RNA: NMR solution structures of LNA : RNA hybrids.* Journal of the American Chemical Society, 2002. **124**(21): p. 5974-5982.

121. Yang, X., et al., *Aptamers containing thymidine 3'-O-phosphorodithioates: synthesis and binding to nuclear factor-kappaB.* Bioorg Med Chem Lett, 1999. **9**(23): p. 3357-62.

122. Sundaram, P., et al., *Therapeutic RNA aptamers in clinical trials.* Eur J Pharm Sci, 2012. **48**(1-2): p. 259-271.

123. Jo, N., et al., *Inhibition of platelet-derived growth factor B signaling enhances the efficacy of anti-vascular endothelial growth factor therapy in multiple models of ocular neovascularization.* Am J Pathol, 2006. **168**(6): p. 2036-53.

124. Huang, Y.F., et al., *Molecular assembly of an aptamer-drug conjugate for targeted drug delivery to tumor cells.* Chembiochem, 2009. **10**(5): p. 862-8.

125. Van Lehn, R.C., Ricci, M., Silva, P.H., Andreozzi, P., Reguera, J., Voitchovsky, K., Stellacci, F., Alexander-Katz, A., *Lipid tail protrusions mediate the intsertion of nanoparticles into model cell membranes.* Nature Comm, 2014. **5**.

126. Buerger, C. and B. Groner, *Bifunctional recombinant proteins in cancer therapy: cell penetrating peptide aptamers as inhibitors of growth factor signaling.* J Cancer Res Clin Oncol, 2003. **129**(12): p. 669-75.

127. Ng, E.W. and A.P. Adamis, *Anti-VEGF aptamer (pegaptanib) therapy for ocular vascular diseases.* Ann N Y Acad Sci, 2006. **1082**: p. 151-71.

128. Aiello, L.P., et al., *Vascular endothelial growth factor in ocular fluid of patients with diabetic retinopathy and other retinal disorders.* N Engl J Med, 1994. **331**(22): p. 1480-7.

129. Linger, R.M., et al., *TAM receptor tyrosine kinases: biologic functions, signaling, and potential therapeutic targeting in human cancer.* Adv Cancer Res, 2008. **100**: p. 35-83.

130. Verma, A., et al., *Targeting Axl and Mer kinases in cancer.* Mol Cancer Ther, 2011. **10**(10): p. 1763-73.

131. Hector, A., et al., *The Axl receptor tyrosine kinase is an adverse prognostic factor and a therapeutic target in esophageal adenocarcinoma.* Cancer Biol Ther, 2010. **10**(10): p. 1009-18.

132. Holland, S.J., et al., *R428, a selective small molecule inhibitor of Axl kinase, blocks tumor spread and prolongs survival in models of metastatic breast cancer.* Cancer Res, 2010. **70**(4): p. 1544-54.

133. Ye, X., et al., *An anti-Axl monoclonal antibody attenuates xenograft tumor growth and enhances the effect of multiple anticancer therapies.* Oncogene, 2010. **29**(38): p. 5254-64.

134. Cerchia, L., et al., *Targeting Axl with an high-affinity inhibitory aptamer.* Mol Ther, 2012. **20**(12): p. 2291-303.

135. Camorani, S., et al., *Inhibition of receptor signaling and of glioblastoma-derived tumor growth by a novel PDGFRbeta aptamer.* Mol Ther, 2014. **22**(4): p. 828-41.

136. Biesecker, G., et al., *Derivation of RNA aptamer inhibitors of human complement C5.* Immunopharmacology, 1999. **42**(1-3): p. 219-30.

137. Sheehan, J.P. and H.C. Lan, *Phosphorothioate oligonucleotides inhibit the intrinsic tenase complex.* Blood, 1998. **92**(5): p. 1617-25.

138. Swayze, E.E., et al., *Antisense oligonucleotides containing locked nucleic acid improve potency but cause significant hepatotoxicity in animals.* Nucleic Acids Res, 2007. **35**(2): p. 687-700.

139. Frazier, K.S., *Antisense Oligonucleotide Therapies: The Promise and the Challenges from a Toxicologic Pathologist's Perspective.* Toxicol Pathol, 2015. **43**(1): p. 78-89.

140. Henry, S.P., et al., *Evaluation of the toxicity of ISIS 2302, a phosphorothioate oligonucleotide, in a four-week study in cynomolgus monkeys.* Toxicology, 1997. **120**(2): p. 145-55.

141. Henry, S.P., et al., *Activation of the alternative pathway of complement by a phosphorothioate oligonucleotide: potential mechanism of action.* J Pharmacol Exp Ther, 1997. **281**(2): p. 810-6.

142. Henry, S.P., D. Monteith, and A.A. Levin, *Antisense oligonucleotide inhibitors for the treatment of cancer: 2. Toxicological properties of phosphorothioate oligodeoxynucleotides.* Anticancer Drug Des, 1997. **12**(5): p. 395-408.

143. Hagedorn, P.H., et al., *Hepatotoxic potential of therapeutic oligonucleotides can be predicted from their sequence and modification pattern.* Nucleic Acid Ther, 2013. **23**(5): p. 302-10.

144. Farman, C.A. and D.J. Kornbrust, *Oligodeoxynucleotide studies in primates: antisense and immune stimulatory indications.* Toxicol Pathol, 2003. **31 Suppl**: p. 119-22.

145. Barchet, W., et al., *Accessing the therapeutic potential of immunostimulatory nucleic acids.* Curr Opin Immunol, 2008. **20**(4): p. 389-95.

146. Ackroyd, R., et al., *Eradication of dysplastic Barrett's oesophagus using photodynamic therapy: long-term follow-up.* Endoscopy, 2003. **35**(6): p. 496-501.

147. Du, K.L., et al., *Preliminary results of interstitial motexafin lutetium-mediated PDT for prostate cancer.* Lasers Surg Med, 2006. **38**(5): p. 427-34.

148. Cuenca, R.E., et al., *Breast cancer with chest wall progression: treatment with photodynamic therapy.* Ann Surg Oncol, 2004. **11**(3): p. 322-7.

149. Moore, C.M., M. Emberton, and S.G. Bown, *Photodynamic therapy for prostate cancer--an emerging approach for organ-confined disease.* Lasers Surg Med, 2011. **43**(7): p. 768-75.

150. Lamberti, M.J., N.B. Vittar, and V.A. Rivarola, *Breast cancer as photodynamic therapy target: Enhanced therapeutic efficiency by overview of tumor complexity.* World J Clin Oncol, 2014. **5**(5): p. 901-7.

151. Yano, T., et al., *Photodynamic therapy for esophageal cancer.* Ann Transl Med, 2014. **2**(3): p. 29.

152. Tang, Z., et al., *Selection of aptamers for molecular recognition and characterization of cancer cells.* Anal Chem, 2007. **79**(13): p. 4900-7.

153. Mallikaratchy, P., Z. Tang, and W. Tan, *Cell specific aptamer-photosensitizer conjugates as a molecular tool in photodynamic therapy.* ChemMedChem, 2008. **3**(3): p. 425-8.

154. Shieh, Y.A., et al., *Aptamer-based tumor-targeted drug delivery for photodynamic therapy.* ACS Nano, 2010. **4**(3): p. 1433-42.

155. Soundararajan, S., et al., *The nucleolin targeting aptamer AS1411 destabilizes Bcl-2 messenger RNA in human breast cancer cells.* Cancer Res, 2008. **68**(7): p. 2358-65.

156. Liu, Q., et al., *Enhanced Photodynamic Efficiency of an Aptamer-Guided Fullerene Photosensitizer toward Tumor Cells.* Chem Asian J, 2013.

157. Ferreira, C.S., et al., *Phototoxic aptamers selectively enter and kill epithelial cancer cells.* Nucleic Acids Res, 2009. **37**(3): p. 866-76.

158. Wang, K., et al., *Self-assembly of a bifunctional DNA carrier for drug delivery.* Angew Chem Int Ed Engl, 2011. **50**(27): p. 6098-101.

159. Han, D., et al., *Engineering a cell-surface aptamer circuit for targeted and amplified photodynamic cancer therapy.* ACS Nano, 2013. **7**(3): p. 2312-9.

160. Gopinath, S.C. and P.K. Kumar, *Aptamers that bind to the hemagglutinin of the recent pandemic influenza virus H1N1 and efficiently inhibit agglutination.* Acta Biomater, 2013. **9**(11): p. 8932-41.

161. Musafia, B., R. Oren-Banaroya, and S. Noiman, *Designing anti-influenza aptamers: novel quantitative structure activity relationship approach gives insights into aptamer-virus interaction.* PLoS One, 2014. **9**(5): p. e97696.

162. Binning, J.M., et al., *Development of RNA aptamers targeting Ebola virus VP35.* Biochemistry, 2013. **52**(47): p. 8406-19.

163. Liang, H.R., et al., *Isolation of ssDNA aptamers that inhibit rabies virus.* Int Immunopharmacol, 2012. **14**(3): p. 341-7.

164. Gourronc, F.A., et al., *Identification of RNA aptamers that internalize into HPV-16 E6/E7 transformed tonsillar epithelial cells.* Virology, 2013. **446**(1-2): p. 325-33.

165. Nicol, C., et al., *An RNA aptamer provides a novel approach for the induction of apoptosis by targeting the HPV16 E7 oncoprotein.* PLoS One, 2013. **8**(5): p. e64781.

166. Toscano-Garibay, J.D., M.L. Benitez-Hess, and L.M. Alvarez-Salas, *Isolation and characterization of an RNA aptamer for the HPV-16 E7 oncoprotein.* Arch Med Res, 2011. **42**(2): p. 88-96.

167. Nicol, C., et al., *Effects of single nucleotide changes on the binding and activity of RNA aptamers to human papillomavirus 16 E7 oncoprotein.* Biochem Biophys Res Commun, 2011. **405**(3): p. 417-21.

168. Zhu, G., et al., *Self-assembled aptamer-based drug carriers for bispecific cytotoxicity to cancer cells.* Chem Asian J, 2012. **7**(7): p. 1630-6.

169. Lupold, S.E., et al., *Identification and characterization of nuclease-stabilized RNA molecules that bind human prostate cancer cells via the prostate-specific membrane antigen.* Cancer Res, 2002. **62**(14): p. 4029-33.

170. Taghdisi, S.M., et al., *Targeted delivery of Epirubicin to cancer cells by PEGylated A10 aptamer.* J Drug Target, 2013.

171. Taghdisi, S.M., et al., *Targeted delivery of daunorubicin to T-cell acute lymphoblastic leukemia by aptamer.* J Drug Target, 2010. **18**(4): p. 277-81.

172. Willner, D., et al., *(6-Maleimidocaproyl)hydrazone of doxorubicin--a new derivative for the preparation of immunoconjugates of doxorubicin.* Bioconjug Chem, 1993. **4**(6): p. 521-7.

173. Meng, L., et al., *Targeted delivery of chemotherapy agents using a liver cancer-specific aptamer.* PLoS One, 2012. **7**(4): p. e33434.

174. Subramanian, N., et al., *Target-specific delivery of doxorubicin to retinoblastoma using epithelial cell adhesion molecule aptamer.* Mol Vis, 2012. **18**: p. 2783-95.

175. Liu, Z., et al., *Novel HER2 aptamer selectively delivers cytotoxic drug to HER2-positive breast cancer cells in vitro.* J Transl Med, 2012. **10**: p. 148.

176. Hu, Y., et al., *Novel MUC1 aptamer selectively delivers cytotoxic agent to cancer cells in vitro.* PLoS One, 2012. **7**(2): p. e31970.

177. Skocaj, M., et al., *Titanium dioxide in our everyday life; is it safe?* Radiol Oncol, 2011. **45**(4): p. 227-47.

178. Li, Z., et al., *Ag nanoparticle-ZnO nanowire hybrid nanostructures as enhanced and robust antimicrobial textiles via a green chemical approach.* Nanotechnology, 2014. **25**(14): p. 145702.

179. Trost, S., et al., *Plasmonically sensitized metal-oxide electron extraction layers for organic solar cells.* Sci Rep, 2015. **5**: p. 7765.

180. Kim, J.S., et al., *In vivo Genotoxicity of Silver Nanoparticles after 90-day Silver Nanoparticle Inhalation Exposure.* Saf Health Work, 2011. **2**(1): p. 34-8.

181. Wang, G. and H. Uludag, *Recent developments in nanoparticle-based drug delivery and targeting systems with emphasis on protein-based nanoparticles.* Expert Opin Drug Deliv, 2008. **5**(5): p. 499-515.

182. D'Addio, S.M. and R.K. Prud'homme, *Controlling drug nanoparticle formation by rapid precipitation.* Adv Drug Deliv Rev, 2011. **63**(6): p. 417-26.

183. Letchford, K. and H. Burt, *A review of the formation and classification of amphiphilic block copolymer nanoparticulate structures: micelles, nanospheres, nanocapsules and polymersomes.* Eur J Pharm Biopharm, 2007. **65**(3): p. 259-69.

184. Zeng, Z., et al., *Fast super-resolution imaging with ultra-high labeling density achieved by joint tagging super-resolution optical fluctuation imaging.* Sci Rep, 2015. **5**: p. 8359.

185. Hartmann, S., et al., *Tailored first- and second-order coherence properties of quantum dot superluminescent diodes via optical feedback.* Opt Lett, 2013. **38**(8): p. 1334-6.

186. Vasir, J.K. and V. Labhasetwar, *Biodegradable nanoparticles for cytosolic delivery of therapeutics.* Adv Drug Deliv Rev, 2007. **59**(8): p. 718-28.

187. Danhier, F., et al., *PLGA-based nanoparticles: an overview of biomedical applications.* J Control Release, 2012. **161**(2): p. 505-22.

188. Huang, Y.F., H.T. Chang, and W. Tan, *Cancer cell targeting using multiple aptamers conjugated on nanorods.* Anal Chem, 2008. **80**(3): p. 567-72.

189. Van de Broek, B., et al., *Specific cell targeting with nanobody conjugated branched gold nanoparticles for photothermal therapy.* ACS Nano, 2011. **5**(6): p. 4319-28.

190. Dhar, S., et al., *Targeted delivery of cisplatin to prostate cancer cells by aptamer functionalized Pt(IV) prodrug-PLGA-PEG nanoparticles.* Proc Natl Acad Sci U S A, 2008. **105**(45): p. 17356-61.

191. Shiao, Y.S., et al., *Aptamer-Functionalized Gold Nanoparticles As Photoresponsive Nanoplatform for Co-Drug Delivery.* ACS Appl Mater Interfaces, 2014.

192. Kwon, S., et al., *Silica-based mesoporous nanoparticles for controlled drug delivery.* J Tissue Eng, 2013. **4**: p. 2041731413503357.

193. Yin, J., et al., *One-step engineering of silver nanoclusters-aptamer assemblies as luminescent labels to target tumor cells.* Nanoscale, 2012. **4**(1): p. 110-2.

194. Dhar, S., et al., *Targeted delivery of a cisplatin prodrug for safer and more effective prostate cancer therapy in vivo.* Proc Natl Acad Sci U S A, 2011. **108**(5): p. 1850-5.

195. Guo, J., et al., *Aptamer-functionalized PEG-PLGA nanoparticles for enhanced anti-glioma drug delivery.* Biomaterials, 2011. **32**(31): p. 8010-20.

196. Acharya, S. and S.K. Sahoo, *PLGA nanoparticles containing various anticancer agents and tumour delivery by EPR effect.* Adv Drug Deliv Rev, 2011. **63**(3): p. 170-83.

197. Markman, J.L., et al., *Nanomedicine therapeutic approaches to overcome cancer drug resistance.* Adv Drug Deliv Rev, 2013. **65**(13-14): p. 1866-79.

198. Smitha, S.L. and K.G. Gopchandran, *Surface enhanced Raman scattering, antibacterial and antifungal active triangular gold nanoparticles.* Spectrochim Acta A Mol Biomol Spectrosc, 2013. **102**: p. 114-9.

199. Kumari, A., S.K. Yadav, and S.C. Yadav, *Biodegradable polymeric nanoparticles based drug delivery systems.* Colloids Surf B Biointerfaces, 2010. **75**(1): p. 1-18.

200. Koziara, J.M., et al., *In-vivo efficacy of novel paclitaxel nanoparticles in paclitaxel-resistant human colorectal tumors.* J Control Release, 2006. **112**(3): p. 312-9.

201. Rouf, M.A., et al., *Development and characterization of liposomal formulations for rapamycin delivery and investigation of their antiproliferative effect on MCF7 cells.* J Liposome Res, 2009. **19**(4): p. 322-31.

202. Gabizon, A., et al., *Prolonged circulation time and enhanced accumulation in malignant exudates of doxorubicin encapsulated in polyethylene-glycol coated liposomes.* Cancer Res, 1994. **54**(4): p. 987-92.

203. Gabizon, A., et al., *Clinical studies of liposome-encapsulated doxorubicin.* Acta Oncol, 1994. **33**(7): p. 779-86.

204. Gabizon, A.A., *Liposomal anthracyclines.* Hematol Oncol Clin North Am, 1994. **8**(2): p. 431-50.

205. Schroeder, A., et al., *Remotely activated protein-producing nanoparticles.* Nano Lett, 2012. **12**(6): p. 2685-9.

206. Yang, L., et al., *Aptamer-conjugated nanomaterials and their applications.* Adv Drug Deliv Rev, 2011. **63**(14-15): p. 1361-70.

207. Rafiyath, S.M., et al., *Comparison of safety and toxicity of liposomal doxorubicin vs. conventional anthracyclines: a meta-analysis.* Exp Hematol Oncol, 2012. **1**(1): p. 10.

208. Harris, L., et al., *Liposome-encapsulated doxorubicin compared with conventional doxorubicin in a randomized multicenter trial as first-line therapy of metastatic breast carcinoma.* Cancer, 2002. **94**(1): p. 25-36.

209. Sajid, M., et al., *Impact of nanoparticles on human and environment: review of toxicity factors, exposures, control strategies, and future prospects.* Environ Sci Pollut Res Int, 2014.

210. Seok, S.H., et al., *Rat pancreatitis produced by 13-week administration of zinc oxide nanoparticles: biopersistence of nanoparticles and possible solutions.* J Appl Toxicol, 2013. **33**(10): p. 1089-96.

211. Teow, Y., et al., *Health impact and safety of engineered nanomaterials.* Chem Commun (Camb), 2011. **47**(25): p. 7025-38.

212. Foldvari, M. and M. Bagonluri, *Carbon nanotubes as functional excipients for nanomedicines: II. Drug delivery and biocompatibility issues.* Nanomedicine, 2008. **4**(3): p. 183-200.

213. Seaton, A., et al., *Nanoparticles, human health hazard and regulation.* J R Soc Interface, 2010. **7 Suppl 1**: p. S119-29.

214. Greco, F., et al., *[Toxicity of nanoparticles on reproduction]*. Gynecol Obstet Fertil, 2015. **43**(1): p. 49-55.

215. Tortiglione, C., *The heritable effects of nanotoxicity.* Nanomedicine (Lond), 2014. **9**(18): p. 2829-41.

216. Qaddoumi, M.G., et al., *The characteristics and mechanisms of uptake of PLGA nanoparticles in rabbit conjunctival epithelial cell layers.* Pharm Res, 2004. **21**(4): p. 641-8.

217. Gref, R., et al., *Biodegradable long-circulating polymeric nanospheres.* Science, 1994. **263**(5153): p. 1600-3.

218. Bege, N., et al., *Biodegradable poly(ethylene carbonate) nanoparticles as a promising drug delivery system with "stealth" potential.* Macromol Biosci, 2011. **11**(7): p. 897-904.

219. Feczko, T., et al., *Influence of process conditions on the mean size of PLGA nanoparticles.* Chemical Engineering and Processing, 2011. **50**(8): p. 846-853.

220. Brem, H., et al., *Placebo-controlled trial of safety and efficacy of intraoperative controlled delivery by biodegradable polymers of chemotherapy for recurrent gliomas. The Polymer-brain Tumor Treatment Group.* Lancet, 1995. **345**(8956): p. 1008-12.

221. Westphal, M., et al., *Gliadel wafer in initial surgery for malignant glioma: long-term follow-up of a multicenter controlled trial.* Acta Neurochir (Wien), 2006. **148**(3): p. 269-75; discussion 275.

222. Jaidev, L.R., U.M. Krishnan, and S. Sethuraman, *Gemcitabine loaded biodegradable PLGA nanospheres for in vitro pancreatic cancer therapy.* Mater Sci Eng C Mater Biol Appl, 2015. **47**: p. 40-7.

223. Sun, Y., et al., *Enhanced antitumor efficacy of vitamin E TPGS-emulsified PLGA nanoparticles for delivery of paclitaxel.* Colloids Surf B Biointerfaces, 2014. **123**: p. 716-23.

224. Soppimath, K.S., et al., *Biodegradable polymeric nanoparticles as drug delivery devices.* J Control Release, 2001. **70**(1-2): p. 1-20.

225. Andrieu, V., et al., *Pharmacokinetic evaluation of indomethacin nanocapsules.* Drug Des Deliv, 1989. **4**(4): p. 295-302.

226. Perche, F. and V.P. Torchilin, *Recent trends in multifunctional liposomal nanocarriers for enhanced tumor targeting.* J Drug Deliv, 2013. **2013**: p. 705265.

227. Vijayakumar, M.R., M.S. Muthu, and S. Singh, *Copolymers of poly(lactic acid) and D-alpha-tocopheryl polyethylene glycol 1000 succinate-based nanomedicines: versatile multifunctional platforms for cancer diagnosis and therapy.* Expert Opin Drug Deliv, 2013. **10**(4): p. 529-43.

228. Ran, Z., et al., *Silica composite nanoparticles containing fluorescent solid core and mesoporous shell with different thickness as drug carrier.* J Colloid Interface Sci, 2013.

229. Li, Z., et al., *Mesoporous silica nanoparticles in biomedical applications.* Chem Soc Rev, 2012. **41**(7): p. 2590-605.

230. Wu, X., M. Wu, and J.X. Zhao, *Recent Development of Silica Nanoparticles as Delivery Vectors for Cancer Imaging and Therapy.* Nanomedicine, 2013.

231. Lee, J.E., et al., *Uniform mesoporous dye-doped silica nanoparticles decorated with multiple magnetite nanocrystals for simultaneous enhanced magnetic resonance imaging, fluorescence imaging, and drug delivery.* J Am Chem Soc, 2010. **132**(2): p. 552-7.

232. Singh, N., et al., *Bioresponsive mesoporous silica nanoparticles for triggered drug release.* J Am Chem Soc, 2011. **133**(49): p. 19582-5.

233. Jia, L., et al., *In vitro and in vivo evaluation of paclitaxel-loaded mesoporous silica nanoparticles with three pore sizes.* Int J Pharm, 2013. **445**(1-2): p. 12-9.

234. Chen, C., et al., *Polyvalent nucleic acid/mesoporous silica nanoparticle conjugates: dual stimuli-responsive vehicles for intracellular drug delivery.* Angew Chem Int Ed Engl, 2011. **50**(4): p. 882-6.

235. Meng, H., et al., *Autonomous in vitro anticancer drug release from mesoporous silica nanoparticles by pH-sensitive nanovalves.* J Am Chem Soc, 2010. **132**(36): p. 12690-7.

236. Wu, C., et al., *Molecule-scale controlled-release system based on light-responsive silica nanoparticles.* Chem Commun (Camb), 2008(23): p. 2662-4.

237. El-Ghannam, A., et al., *A ceramic-based anticancer drug delivery system to treat breast cancer.* J Mater Sci Mater Med, 2010. **21**(9): p. 2701-10.

238. Chen, Z., et al., *Mesoporous silica nanoparticles with manipulated microstructures for drug delivery.* Colloids Surf B Biointerfaces, 2012. **95**: p. 274-8.

239. Park, J.H., et al., *Biodegradable luminescent porous silicon nanoparticles for in vivo applications.* Nat Mater, 2009. **8**(4): p. 331-6.

240. Cai, L., et al., *MUC-1 aptamer-conjugated dye-doped silica nanoparticles for MCF-7 cells detection.* Biomaterials, 2013. **34**(2): p. 371-81.

241. Babu, E., P.M. Mareeswaran, and S. Rajagopal, *Highly sensitive optical biosensor for thrombin based on structure switching aptamer-luminescent silica nanoparticles.* J Fluoresc, 2013. **23**(1): p. 137-46.

242. Hernandez, F.J., et al., *Targeting cancer cells with controlled release nanocapsules based on a single aptamer.* Chem Commun (Camb), 2013. **49**(13): p. 1285-7.

243. Kim, S., et al., *Organically Modified Silica Nanoparticles with Intraparticle Heavy-Atom Effect on the Encapsulated Photosensitizer for Enhanced Efficacy of Photodynamic Therapy.* J Phys Chem C Nanomater Interfaces, 2009. **113**: p. 12641-12644.

244. Peng, J., et al., *Hollow silica nanoparticles loaded with hydrophobic phthalocyanine for near-infrared photodynamic and photothermal combination therapy.* Biomaterials, 2013. **34**(32): p. 7905-12.

245. Zhang, J.Q., et al., *A gold nanoparticles-modified aptamer beacon for urinary adenosine detection based on structure-switching/fluorescence-"turning on" mechanism.* J Pharm Biomed Anal, 2012. **70**: p. 362-8.

246. Wang, P., et al., *Hydroxylamine amplified gold nanoparticle-based aptameric system for the highly selective and sensitive detection of platelet-derived growth factor.* Talanta, 2013. **103**: p. 392-7.

247. Zhu, Y., P. Chandra, and Y.B. Shim, *Ultrasensitive and selective electrochemical diagnosis of breast cancer based on a hydrazine-Au nanoparticle-aptamer bioconjugate.* Anal Chem, 2013. **85**(2): p. 1058-64.

248. Sundaram, P., J. Wower, and M.E. Byrne, *A nanoscale drug delivery carrier using nucleic acid aptamers for extended release of therapeutic.* Nanomedicine, 2012. **8**(7): p. 1143-51.

249. Luo, Y.L., Y.S. Shiao, and Y.F. Huang, *Release of photoactivatable drugs from plasmonic nanoparticles for targeted cancer therapy.* ACS Nano, 2011. **5**(10): p. 7796-804.

250. Maeda, H., *The enhanced permeability and retention (EPR) effect in tumor vasculature: the key role of tumor-selective macromolecular drug targeting.* Adv Enzyme Regul, 2001. **41**: p. 189-207.

251. Etame, A.B., et al., *Design and potential application of PEGylated gold nanoparticles with size-dependent permeation through brain microvasculature.* Nanomedicine, 2011. **7**(6): p. 992-1000.

252. Spivak, M.Y., et al., *Gold nanoparticles - the theranostic challenge for PPPM: nanocardiology application.* EPMA J, 2013. **4**(1): p. 18.

253. Spivak, M.Y., et al., *Development and testing of gold nanoparticles for drug delivery and treatment of heart failure: a theranostic potential for PPP cardiology.* EPMA J, 2013. **4**(1): p. 20.

254. Toikkanen, O., et al., *Synthesis and stability of monolayer-protected Au38 clusters.* J Am Chem Soc, 2008. **130**(33): p. 11049-55.

255. Selvakannan, P.R., et al., *A new method for the synthesis of hydrophobic gold nanotapes.* J Nanosci Nanotechnol, 2003. **3**(5): p. 372-4.

256. Brown, S.D., et al., *Gold nanoparticles for the improved anticancer drug delivery of the active component of oxaliplatin.* J Am Chem Soc, 2010. **132**(13): p. 4678-84.

257. Libutti, S.K., et al., *Phase I and pharmacokinetic studies of CYT-6091, a novel PEGylated colloidal gold-rhTNF nanomedicine.* Clin Cancer Res, 2010. **16**(24): p. 6139-49.

258. Arvizo, R.R., et al., *Mechanism of anti-angiogenic property of gold nanoparticles: role of nanoparticle size and surface charge.* Nanomedicine, 2011. **7**(5): p. 580-7.

259. Gurunathan, S., et al., *Antiangiogenic properties of silver nanoparticles.* Biomaterials, 2009. **30**(31): p. 6341-50.

260. Mukherjee, P., et al., *Antiangiogenic properties of gold nanoparticles.* Clin Cancer Res, 2005. **11**(9): p. 3530-4.

261. Kemp, M.M., et al., *Gold and silver nanoparticles conjugated with heparin derivative possess anti-angiogenesis properties.* Nanotechnology, 2009. **20**(45): p. 455104.

262. Sung, J.H., et al., *Acute inhalation toxicity of silver nanoparticles.* Toxicol Ind Health, 2011. **27**(2): p. 149-54.

263. Sung, J.H., et al., *Subchronic inhalation toxicity of gold nanoparticles.* Part Fibre Toxicol, 2011. **8**: p. 16.

264. Blaser, S.A., et al., *Estimation of cumulative aquatic exposure and risk due to silver: contribution of nano-functionalized plastics and textiles.* Sci Total Environ, 2008. **390**(2-3): p. 396-409.

265. Dreher, K.L., *Health and environmental impact of nanotechnology: toxicological assessment of manufactured nanoparticles.* Toxicol Sci, 2004. **77**(1): p. 3-5.

266. Shukla, R., et al., *Biocompatibility of gold nanoparticles and their endocytotic fate inside the cellular compartment: a microscopic overview*. Langmuir, 2005. **21**(23): p. 10644-54.

267. Du, L., et al., *Mechanism and cellular kinetic studies of the enhancement of antioxidant activity by using surface-functionalized gold nanoparticles.* Chemistry, 2013. **19**(4): p. 1281-7.

268. Chen, J., et al., *Sex differences in the toxicity of polyethylene glycol-coated gold nanoparticles in mice.* Int J Nanomedicine, 2013. **8**: p. 2409-19.

269. Khan, M.S., G.D. Vishakante, and H. Siddaramaiah, *Gold nanoparticles: A paradigm shift in biomedical applications.* Adv Colloid Interface Sci, 2013.

270. Etame, A.B., et al., *Enhanced delivery of gold nanoparticles with therapeutic potential into the brain using MRI-guided focused ultrasound.* Nanomedicine, 2012. **8**(7): p. 1133-42.

271. Liu, Z., et al., *Effects of internalized gold nanoparticles with respect to cytotoxicity and invasion activity in lung cancer cells.* PLoS One, 2014. **9**(6): p. e99175.

272. Gonzalez, V.H., et al., *Intravitreal injection of pegaptanib sodium for proliferative diabetic retinopathy.* Br J Ophthalmol, 2009. **93**(11): p. 1474-8.

273. Cunningham, E.T., Jr., et al., *A phase II randomized double-masked trial of pegaptanib, an anti-vascular endothelial growth factor aptamer, for diabetic macular edema.* Ophthalmology, 2005. **112**(10): p. 1747-57.

274. Bayrac, A.T., et al., *In vitro Selection of DNA Aptamers to Glioblastoma Multiforme.* ACS Chem Neurosci, 2011. **2**(3): p. 175-181.

275. Li, L., et al., *Nucleolin-targeting liposomes guided by aptamer AS1411 for the delivery of siRNA for the treatment of malignant melanomas.* Biomaterials, 2014. **35**(12): p. 3840-50.

276. Research, B. *Aptamers market--technology trend analysis by applications--therapeutics, diagnostics, biosensors, drug discovery, biomarker discovery, research applications with market landscape analysis-- global forecasts to 2018*. 2013.

277. Xiao, Z. and O.C. Farokhzad, *Aptamer-functionalized nanoparticles for medical applications: challenges and opportunities.* ACS Nano, 2012. **6**(5): p. 3670-6.

278. Pramanik, D., et al., *A composite polymer nanoparticle overcomes multidrug resistance and ameliorates doxorubicin-associated cardiomyopathy.* Oncotarget, 2012. **3**(6): p. 640-50.

279. Verma, A. and F. Stellacci, *Effect of surface properties on nanoparticle-cell interactions.* Small, 2010. **6**(1): p. 12-21.

280. Zhang, Z., et al., *Biocatalytic release of an anticancer drug from nucleic-acids-capped mesoporous SiO2 Using DNA or molecular biomarkers as triggering stimuli.* ACS Nano, 2013. **7**(10): p. 8455-68.

281. Li, L.L., et al., *A vitamin-responsive mesoporous nanocarrier with DNA aptamer-mediated cell targeting.* Chem Commun (Camb), 2013. **49**(52): p. 5823-5.

282. Chen, C., et al., *Photosensitizer-incorporated quadruplex DNA-gated nanovechicles for light-triggered, targeted dual drug delivery to cancer cells.* Small, 2013. **9**(16): p. 2793-800, 2653.

283. Hattori, Y. and Y. Maitani, *Folate-linked lipid-based nanoparticle for targeted gene delivery.* Curr Drug Deliv, 2005. **2**(3): p. 243-52.

284. Pan, X. and R.J. Lee, *Tumour-selective drug delivery via folate receptor-targeted liposomes.* Expert Opin Drug Deliv, 2004. **1**(1): p. 7-17.

285. Zhao, X., H. Li, and R.J. Lee, *Targeted drug delivery via folate receptors.* Expert Opin Drug Deliv, 2008. **5**(3): p. 309-19.

286. Zuber, G., C.D. Muller, and J.P. Behr, *Targeted gene delivery to cancer cells with nanometric DNA particles enveloped with folic acid using a polymerisable anchor.* Technol Cancer Res Treat, 2005. **4**(6): p. 637-43.

287. Huang, Z., et al., *SERPINB2 down-regulation contributes to chemoresistance in head and neck cancer.* Mol Carcinog, 2014. **53**(10): p. 777-86.

288. Fassnacht, M., et al., *Combination chemotherapy in advanced adrenocortical carcinoma.* N Engl J Med, 2012. **366**(23): p. 2189-97.

289. Liao, L., et al., *A convergent synthetic platform for single-nanoparticle combination cancer therapy: ratiometric loading and controlled release of cisplatin, doxorubicin, and camptothecin.* J Am Chem Soc, 2014. **136**(16): p. 5896-9.

290. Kim, E., et al., *Prostate cancer cell death produced by the co-delivery of Bcl-xL shRNA and doxorubicin using an aptamer-conjugated polyplex.* Biomaterials, 2010. **31**(16): p. 4592-9.

291. Zhang, K., et al., *A novel aptamer developed for breast cancer cell internalization.* ChemMedChem, 2012. **7**(1): p. 79-84.

292. He, X., et al., *One-pot synthesis of sustained-released doxorubicin silica nanoparticles for aptamer targeted delivery to tumor cells.* Nanoscale, 2011. **3**(7): p. 2936-42.

293. Jalalian, S.H., et al., *Epirubicin loaded super paramagnetic iron oxide nanoparticle-aptamer bioconjugate for combined colon cancer therapy and imaging in vivo.* Eur J Pharm Sci, 2013. **50**(2): p. 191-7.

294. Yu, C., et al., *Novel aptamer-nanoparticle bioconjugates enhances delivery of anticancer drug to MUC1-positive cancer cells in vitro.* PLoS One, 2011. **6**(9): p. e24077.

295. Aravind, A., et al., *AS1411 aptamer tagged PLGA-lecithin-PEG nanoparticles for tumor cell targeting and drug delivery.* Biotechnol Bioeng, 2012. **109**(11): p. 2920-31.

296. Zhou, W., et al., *Aptamer-nanoparticle bioconjugates enhance intracellular delivery of vinorelbine to breast cancer cells.* J Drug Target, 2014. **22**(1): p. 57-66.

297. Lin, Z., et al., *A novel aptamer functionalized CuInS2 quantum dots probe for daunorubicin sensing and near infrared imaging of prostate cancer cells.* Anal Chim Acta, 2014. **818**: p. 54-60.

298. Sayari, E., et al., *MUC1 aptamer conjugated to chitosan nanoparticles, an efficient targeted carrier designed for anticancer SN38 delivery.* Int J Pharm, 2014. **473**(1-2): p. 304-15.

299. Kolishetti, N., et al., *Engineering of self-assembled nanoparticle platform for precisely controlled combination drug therapy.* Proc Natl Acad Sci U S A, 2010. **107**(42): p. 17939-44.

300. Ireson, C.R. and L.R. Kelland, *Discovery and development of anticancer aptamers.* Mol Cancer Ther, 2006. **5**(12): p. 2957-62.

301. Guarneri, V., M.V. Dieci, and P. Conte, *Enhancing intracellular taxane delivery: current role and perspectives of nanoparticle albumin-bound paclitaxel in the treatment of advanced breast cancer.* Expert Opin Pharmacother, 2012. **13**(3): p. 395-406.

302. Hamaguchi, T., et al., *NK105, a paclitaxel-incorporating micellar nanoparticle formulation, can extend in vivo antitumour activity and reduce the neurotoxicity of paclitaxel.* Br J Cancer, 2005. **92**(7): p. 1240-6.

303. Ramanathan, R., Hamburg, S.I., Borad, M., Seetharam, M., Kundranda, M., Lee, P., Frelund, P., Gibert, M., Mast, C., Semple, S., Judge, A., Crowell, A., Vocila, L., MacLachlan, I., Northfeld, D.W., , *A phasi I dose escalation study of TKM-080301, a RNA therapeutic directed aptamer against PLK1, in patients with advanced solid tumors* in *104th Annual Meeting of the American Association of Cancer Research*. 2013, AACR: Cancer Res: Washington, D.C.

304. Zuckerman, J.E., et al., *Correlating animal and human phase Ia/Ib clinical data with CALAA-01, a targeted, polymer-based nanoparticle containing siRNA.* Proc Natl Acad Sci U S A, 2014. **111**(31): p. 11449-54.

305. Pottier, A., E. Borghi, and L. Levy, *New use of metals as nanosized radioenhancers.* Anticancer Res, 2014. **34**(1): p. 443-53.

306. Maggiorella, L., et al., *Nanoscale radiotherapy with hafnium oxide nanoparticles.* Future Oncol, 2012. **8**(9): p. 1167-81.

307. Jaetao, J.E., et al., *Enhanced leukemia cell detection using a novel magnetic needle and nanoparticles.* Cancer Res, 2009. **69**(21): p. 8310-6.

308. Iwamura, T., T. Katsuki, and K. Ide, *Establishment and characterization of a human pancreatic cancer cell line (SUIT-2) producing carcinoembryonic antigen and carbohydrate antigen 19-9.* Jpn J Cancer Res, 1987. **78**(1): p. 54-62.

309. Tsao, S.W., et al., *Characterization of human ovarian surface epithelial cells immortalized by human papilloma viral oncogenes (HPV-E6E7 ORFs).* Exp Cell Res, 1995. **218**(2): p. 499-507.

310. Zhan, S.B. and Y. Zeng, *[Recent progress on SELEX and its applications]*. Bing Du Xue Bao, 2013. **29**(5): p. 573-7.

311. Buick, R.N., R. Pullano, and J.M. Trent, *Comparative properties of five human ovarian adenocarcinoma cell lines.* Cancer Res, 1985. **45**(8): p. 3668-76.

312. Beaufort, C.M., et al., *Ovarian cancer cell line panel (OCCP): clinical importance of in vitro morphological subtypes.* PLoS One, 2014. **9**(9): p. e103988.

313. Abouzeid, A.H., N.R. Patel, and V.P. Torchilin, *Polyethylene glycol-phosphatidylethanolamine (PEG-PE)/vitamin E micelles for co-delivery of paclitaxel and curcumin to overcome multi-drug resistance in ovarian cancer.* Int J Pharm, 2014. **464**(1-2): p. 178-84.

314. Furlong, M.T., et al., *Evidence for the colonic origin of ovarian cancer cell line SW626.* J Natl Cancer Inst, 1999. **91**(15): p. 1327-8.

315. Herfs, M., et al., *A discrete population of squamocolumnar junction cells implicated in the pathogenesis of cervical cancer.* Proc Natl Acad Sci U S A, 2012. **109**(26): p. 10516-21.

316. Masiakos, P.T., et al., *Human ovarian cancer, cell lines, and primary ascites cells express the human Mullerian inhibiting substance (MIS) type II receptor, bind, and are responsive to MIS.* Clin Cancer Res, 1999. **5**(11): p. 3488-99.

317. Bell, C., et al., *Oligonucleotide NX1838 inhibits VEGF165-mediated cellular responses in vitro.* In Vitro Cell Dev Biol Anim, 1999. **35**(9): p. 533-42.

318. Ruckman, J., et al., *2'-Fluoropyrimidine RNA-based aptamers to the 165-amino acid form of vascular endothelial growth factor (VEGF165). Inhibition of receptor binding and VEGF-induced vascular permeability through interactions requiring the exon 7-encoded domain.* J Biol Chem, 1998. **273**(32): p. 20556-67.

319. Mallikaratchy, P.R., et al., *A multivalent DNA aptamer specific for the B-cell receptor on human lymphoma and leukemia.* Nucleic Acids Res, 2011. **39**(6): p. 2458-69.

320. Shangguan, D., et al., *Identification of liver cancer-specific aptamers using whole live cells.* Anal Chem, 2008. **80**(3): p. 721-8.

321. Bates, P.J., et al., *Antiproliferative activity of G-rich oligonucleotides correlates with protein binding.* J Biol Chem, 1999. **274**(37): p. 26369-77.

322. Rosenberg, J.E., et al., *A phase II trial of AS1411 (a novel nucleolin-targeted DNA aptamer) in metastatic renal cell carcinoma.* Invest New Drugs, 2014. **32**(1): p. 178-87.

323. Ming, X., *Cellular delivery of siRNA and antisense oligonucleotides via receptor-mediated endocytosis.* Expert Opin Drug Deliv, 2011. **8**(4): p. 435-49.

324. Hicke, B.J., et al., *Tumor targeting by an aptamer.* J Nucl Med, 2006. **47**(4): p. 668-78.

325. Chou, L.Y., K. Ming, and W.C. Chan, *Strategies for the intracellular delivery of nanoparticles.* Chem Soc Rev, 2011. **40**(1): p. 233-45.

326. Schnurer, J. and T. Rosswall, *Fluorescein diacetate hydrolysis as a measure of total microbial activity in soil and litter.* Appl Environ Microbiol, 1982. **43**(6): p. 1256-61.

327. Ghavami, S., et al., *Apoptosis and cancer: mutations within caspase genes.* J Med Genet, 2009. **46**(8): p. 497-510.

328. Yu, Z., et al., *Nitric oxide-dependent negative feedback of PARP-1 trans-activation of the inducible nitric-oxide synthase gene.* J Biol Chem, 2006. **281**(14): p. 9101-9.

329. Gerweck, L.E. and K. Seetharaman, *Cellular pH gradient in tumor versus normal tissue: potential exploitation for the treatment of cancer.* Cancer Res, 1996. **56**(6): p. 1194-8.

330. Sahay, G., D.Y. Alakhova, and A.V. Kabanov, *Endocytosis of nanomedicines.* J Control Release, 2010. **145**(3): p. 182-95.

331. Sheng, Z., et al., *Smart human serum albumin-indocyanine green nanoparticles generated by programmed assembly for dual-modal imaging-guided cancer synergistic phototherapy.* ACS Nano, 2014. **8**(12): p. 12310-22.

332. Varkouhi, A.K., et al., *Endosomal escape pathways for delivery of biologicals.* J Control Release, 2011. **151**(3): p. 220-8.

333. Montana, M., et al., *Albumin-bound paclitaxel: the benefit of this new formulation in the treatment of various cancers.* J Chemother, 2011. **23**(2): p. 59-66.

334. Miele, E., et al., *Albumin-bound formulation of paclitaxel (Abraxane ABI-007) in the treatment of breast cancer.* Int J Nanomedicine, 2009. **4**: p. 99-105.

335. Rowinsky, E.K. and R.C. Donehower, *Paclitaxel (taxol).* N Engl J Med, 1995. **332**(15): p. 1004-14.

336. Ma, P. and R.J. Mumper, *Paclitaxel Nano-Delivery Systems: A Comprehensive Review.* J Nanomed Nanotechnol, 2013. **4**(2): p. 1000164.

337. Gelderblom, H., et al., *Cremophor EL: the drawbacks and advantages of vehicle selection for drug formulation.* Eur J Cancer, 2001. **37**(13): p. 1590-8.

338. Calhoun, E., et al., *International comparison of the quality of voluntary adverse event reports for cremophor-containing paclitaxel-associated anaphylaxis submitted to regulatory agencies in the United States, Europe, and Japan.* Journal of Clinical Oncology, 2009. **27**(15).

339. Campos, F.C., et al., *Systemic toxicity induced by paclitaxel in vivo is associated with the solvent cremophor EL through oxidative stress-driven mechanisms.* Food Chem Toxicol, 2014. **68**: p. 78-86.

340. Mark, M., et al., *Commercial taxane formulations induce stomatocytosis and increase blood viscosity.* Br J Pharmacol, 2001. **134**(6): p. 1207-14.

341. Frangioni, J.V., *In vivo near-infrared fluorescence imaging.* Curr Opin Chem Biol, 2003. **7**(5): p. 626-34.

342. Hill, T.K., et al., *Indocyanine Green-Loaded Nanoparticles for Image-Guided Tumor Surgery.* Bioconjug Chem, 2015.

343. Verbeek, F.P., et al., *Near-infrared fluorescence sentinel lymph node mapping in breast cancer: a multicenter experience.* Breast Cancer Res Treat, 2014. **143**(2): p. 333-42.

344. Alander, J.T., et al., *A review of indocyanine green fluorescent imaging in surgery.* Int J Biomed Imaging, 2012. **2012**: p. 940585.

345. Hutteman, M., et al., *Clinical translation of ex vivo sentinel lymph node mapping for colorectal cancer using invisible near-infrared fluorescence light.* Ann Surg Oncol, 2011. **18**(4): p. 1006-14.

346. van der Vorst, J.R., et al., *Near-infrared fluorescence sentinel lymph node mapping of the oral cavity in head and neck cancer patients.* Oral Oncol, 2013. **49**(1): p. 15-9.

347. Wu, X., et al., *Study on the prostate cancer-targeting mechanism of aptamer-modified nanoparticles and their potential anticancer effect in vivo.* Int J Nanomedicine, 2014. **9**: p. 5431-40.

348. Bristow, R.E., et al., *Intraperitoneal cisplatin and paclitaxel versus intravenous carboplatin and paclitaxel chemotherapy for Stage III ovarian cancer: a cost-effectiveness analysis.* Gynecol Oncol, 2007. **106**(3): p. 476-81.

349. Markman, M. and J.L. Walker, *Intraperitoneal chemotherapy of ovarian cancer: a review, with a focus on practical aspects of treatment.* J Clin Oncol, 2006. **24**(6): p. 988-94.

350. Iyer, A.K., et al., *Exploiting the enhanced permeability and retention effect for tumor targeting.* Drug Discov Today, 2006. **11**(17-18): p. 812-8.

351. Folkman, J., *Angiogenesis in cancer, vascular, rheumatoid and other disease.* Nat Med, 1995. **1**(1): p. 27-31.

352. Maeda, H., L.W. Seymour, and Y. Miyamoto, *Conjugates of anticancer agents and polymers: advantages of macromolecular therapeutics in vivo.* Bioconjug Chem, 1992. **3**(5): p. 351-62.

353. Li, N., et al., *Technical and biological issues relevant to cell typing with aptamers.* J Proteome Res, 2009. **8**(5): p. 2438-48.

APPENDIX A: AWARDS AND ACHIEVEMENTS

Gordon Research Conference Genetic Recombination, poster presentation, 2011
White, R., Sung, P., Benedetto, G., Richardson, C., **Interchromosomal homologous recombination in vivo.**

UNC Charlotte Graduate Research Symposium, oral presentation, 2011
Benedetto, G., Francis, R., Richardson, C., **The role of pif-1 protein during repair of DNA damage and genomic stability in mouse hematopoietic stem cells (HSCs).**

UNC Charlotte Graduate Research Symposium, oral presentation, 2012
Benedetto, G., **Aptamer linked PLGA Nanoparticle Targeted Drug Delivery in Ovarian Tumor Cell Lines**.

Charlotte Life Sciences Conference, poster presentation 2012 & 2013*^
Benedetto, G., Almeida, A., Kastanis, J., Ogle, C., Richardson, C., **A targeted approach at ovarian cancer therapy: Aptamer directed Paclitaxel loaded PLGA nanoparticles.**

*Selected as graduate student poster competition finalist of submissions from across the state of North Carolina
^Second place overall

UNC Charlotte Graduate Research Symposium, oral presentation, 2013
Benedetto, G., Almeida, A., Kastanis, J., Hamp, T., Brouwer, C., Ogle, C., Richardson, C. **A targeted approach at ovarian cancer therapy: Aptamer directed Paclitaxel loaded PLGA nanoparticles.**

Center for Biomedical Engineering and Science (CBES), poster presentation 2013^ & 2014
Benedetto, G., Almeida, A., Kastanis, C., Ogle, C., Richardson, C., **A targeted approach at ovarian cancer therapy: Aptamer directed Paclitaxel loaded PLGA nanoparticles.**

^First place Medical Therapies & Technology Focus Area

APPENDIX B:
IDENTIFICATION OF EPITHELIAL OVARIAN TUMOR SPECIFIC APTAMERS

Published in *Nucleic Acid Therapeutics*

Gregory Benedetto [1], Timothy J. Hamp [1,2], Peter J. Wesselman [1], Christine Richardson [1,*]

[1] Department of Biological Sciences, UNC Charlotte, 1902 University City Blvd., Woodward Hall, Charlotte NC 28223 USA
[2] College of Computing and Informatics, UNC Charlotte, 1902 University City Blvd., Bioinformatics, Charlotte NC 28223 USA
[*] Corresponding Author—University of North Carolina Charlotte, 9201 University City Blvd, Woodward Hall Room 386B, Charlotte NC, 28223. Telephone (704) 687-8683, FAX (704) 687-3128, Email C.Richardson@uncc.edu

Keywords: aptamer, Cell-SELEX, biomarker, molecular probes, epithelial ovarian cancer, tumor targeting

Abstract

Ovarian cancer is often diagnosed in late stages with few treatment options and poor long-term prognosis. New clinical tools for early detection of ovarian malignancies will significantly help reduce mortality and improve current long-term survival rates. The objective of this work was to identify ovarian tumor specific single-stranded DNA aptamers that bind to malignant ovarian tumor cells and internalize with high affinity and specificity. Aptamers can identify unique tumor biomarkers, can aid in early detection and diagnosis of neoplastic disorders, and can be functionalized by conjugation to small molecules. To identify aptamers from random single-stranded DNA pools (60 bases long), we used whole Cell-SELEX (Systematic Evolution of Ligands by Exponential enrichment) to enrich and isolate tumor specific aptamers that bind to tumor specific receptors in their native state on the cell surface. Next Generation sequencing identified seven novel aptamers, and detailed analysis of three are described. Aptamers bound to, and were internalized by, target Caov-3 cell populations but not non-target non-malignant ovarian epithelial HOSE 6-3 cells or multiple other epithelial tumor cell lines. Further, aptamers showed unique binding affinities with apparent dissociation constants (K_d) measuring in the sub-micromolar range supporting their physiological relevance and potential use in clinical applications.

Introduction

Epithelial ovarian cancer (EOC) is one of the most common and highly malignant diseases affecting women. In 2014 almost 22,000 new cases of EOC will be diagnosed with over 14,000 EOC related deaths in the Unites States alone [1]. Since the majority of EOC are diagnosed at stage II or later, there are fewer treatment options for patients and poor long-term prognosis with a 5-year mean survival rate of 44%. Moreover, the relative survival rate decreases to 27% when EOC is diagnosed at stage III which constitutes almost 62% of all new cases each year [1]. Current treatment regimens include surgical

resection of malignant tissue followed by adjuvant platinum-taxane combination therapy giving a high rate of initial response, but 60% to 75% of patients demonstrate local recurrence [2,3].

There remains limited understanding of the pathogenesis of ovarian tumors due to the heterogeneous nature of the disease. Subtypes include serous, endometrioid, mucinous, clear cell, transitional cell, squamous cell, mixed epithelial, and undifferentiated [4]. Further, the origin of tumors is difficult to understand since the physical development of cyst-like structures within the ovary is uncharacteristic of normal epithelial ovarian tissue [5], and at least a portion of serous ovarian tumors likely originate within the fallopian tube [5].

Genome wide studies on the proteome and transcriptome abnormalities of EOC generated a large number of potential tumor biomarkers, including CA-125 and WFDC2 (HE4) proteins [6-8]. A widely accepted Risk of Malignancy Index (RMI) is used to differentiate between a malignant and benign abdominal mass [9]. The criteria used include a woman's age, ultrasound score, menopausal status, a clinical impression score, and serum CA-125 count. The Risk of Malignancy Algorithm (RMA) improved upon RMI by including an additional biomarker HE4 [10], and the OVA1 blood tests includes a panel of five biomarkers which include CA125, HE4, transferrin, prealbumin, and β2 microglobulin [11]; however, comprehensive serum studies evaluating the effectiveness of RMI, ROMA, and OVA1 blood tests have given conflicting results and still fail to promote early detection of EOC [6,12].

Alternative approaches to generate more sensitive diagnostic tools to aid in early detection of EOC include recognition of novel or existing tumor markers and membrane structures in their native state on the cell surface of EOC cells. Aptamers are single-stranded (ss) DNA/RNA oligonucleotides that fold into complex secondary and tertiary structures that enable them to bind with antibody-like properties to multiple targets. Aptamers have been used as probes for diagnostic identification of tumors *in vivo*, as single molecule antagonists, and as directed therapy agents when conjugated to chemotherapeutics or small molecule vehicles both *in vitro* and *in vivo* [13-19]. The potential clinical significance of aptamers has grown significantly [20] with reports of several clinical trials including Macugen (pegaptanib) to inhibit VEGF-165 mediated ocular neovascularization in age related macular degeneration (AMD) [21,22], and Fovista, the anti-PDGF-β aptamer to treat wet AMD [23]. Additional antagonistic aptamers disrupt complement component 5 (ARC1905) [24], bind tumor specific antigens such as B-cell receptors on human lymphoma and leukemia [25], as well as a pro-apoptotic AS1411 aptamer that targets nucleolin and inhibits nuclear factor-κB and Bcl-2 [26,27]. Since biomarkers on the surface of specific tumor subtypes is not always known, protocols such as whole Cell-SELEX (Systematic Evolution of Ligands by Exponential enrichment) can be used to screen for unique aptamers based on their ability to bind to the target tumor cells. Notably, aptamers have been identified by whole Cell-SELEX that can bind to the HGC-27 gastric cancer cell line and to paraffin-embedded primary gastric tumor sections [28].

To identify epithelial ovarian cancer cell-specific aptamers we adopted and modified whole Cell-SELEX and identified aptamers that distinguish between neoplastic epithelial cells and non-transformed epithelial cells. We identified novel target-specific DNA aptamers recognizing human epithelial ovarian adenocarcinoma cells with no prior

knowledge of target molecules. These aptamers specifically recognize target cells with an apparent equilibrium dissociation constant (K_d) measured in the nanomolar range but show minimal interaction with physiologically similar epithelial tumor cells and non-transformed cell lines. Further, that aptamers internalize into target cells thus have the potential to be utilized clinically as a diagnostic tool for detection, visualization including metastasis, or for direct delivery of chemotherapeutics for treatment.

Materials and Methods

Cell Lines. The human ovarian adenocarcinoma cell lines Caov-3 (HTB-75), SK-OV-3 (HTB-77), and SW626 (HTB-78) were obtained from ATCC (Manassas, VA) and maintained in tissue culture 37°C 5% CO_2. Caov-3 cell lines were maintained in Dulbecco's minimal essential medium (DMEM, GIBCO) supplemented with 10% fetal bovine serum (FBS, GIBCO) and 1% penicillin−streptomycin (GEMINI). SK-OV-3 cell lines were maintained in McCoys5a media (ATCC) supplemented with 10% FBS (heat-inactivated, GIBCO), 1% penicillin−streptomycin (GEMINI). SW626 cell lines were maintained in Leibovitz media (ATCC) supplemented with 10% FBS (heat-inactivated, GIBCO), 1% penicillin−streptomycin (GEMINI), and 1% sodium bicarbonate (7.5% *w/v*, Cellgro). The pancreatic carcinoma cell line Hs766T (ATCC, HTB-134) and Suit-2 [29], human cervical adenocarcinoma HeLA (ATCC, CCL-2), breast adenocarcinoma cell lines MCF-7 (ATCC, HTB-22) and MDA-MB-231 (ATCC, CRM-HTB-26), murine embryonic fibroblast NIH/3T3 (ATCC, CRL-1658) were all maintained in DMEM supplemented with 10% FBS (heat-inactivated, GIBCO), 1% penicillin−streptomycin (GEMINI). Normal epithelial cell lines HEK-293 (ATCC, CRL-1573) maintained in DMEM supplemented with 10% FBS (heat-inactivated, GIBCO), 1% penicillin−streptomycin (GEMINI). The HPV immortalized human ovarian epithelial (HOSE 6-3) cells [30] maintained in Medium199/MCDB105 media (1:1, Sigma Aldrich) supplemented with 10% FBS (heat-inactivated, GIBCO), 1% penicillin-- streptomycin (GEMINI), 1% sodium bicarbonate (7.5% *w/v*, Cellgro).

*Whole Cell-SELEX***.** An HPLC-purified ssDNA aptamer library (Integrated DNA Technologies (IDT)) contained a centralized random sequence of 20 nucleotides flanked by fixed 5' and 3' 20 nucleotide sequences for PCR enrichment (5'-CTCCTCTGACTGTAACCACG-N_{20}-GCATAGGTAGTCCAGAAGCCA-3'). 2 μL of the aptamer library (100 μM) in TE was added to 8 μL H_2O with target Caov-3 cells. Samples were denatured 95°C 5 min and cooled on ice for 5 min before treating target cells. Cooled suspension were added to 980 μL binding buffer (BB, PBS (GIBCO) supplemented with 1% *w/v* Bovine Serum Albumin (BSA, Cellgro), 4.5 g/L glucose (Sigma Aldrich), 5mM $MgCl_2$ (Sigma Aldrich). Aptamers were incubated on a monolayer of Caov-3 cells (seeded at 2.0×10^6 48 hrs prior, 37ºC 5% CO_2) in T25 flask 4°C 30 min under constant agitation in the absence of competitor. After washing with PBS (3X) for 1 min, adhesive cells were collected. Cells with aptamers were centrifuged 12,000 rpm 2 min in microcentrifurge. The supernatant was discarded and bound aptamers were eluted 95°C 5 min in 50 μL 1X PBS. Eluted aptamers were collected, resuspended in 950 μL BB and used for negative selection against HOSE 6-3 cells (seeded at 2.0×10^6 48 hrs prior, 37º 5% CO_2) in T25 flask 4°C 30 min under constant agitation in the absence of competitor. 1 mL of BB was collected and aptamers eluted by ethanol precipitation resuspended in 20 μL TE. The collected aptamers were amplified by

PCR (GE HEALTHCARE illustra PuReTaq Ready-To-Go PCR beads): Primer A: 5'-gaggagactgacattggtgc, Primer B: cgtatccatcaggtcttcgga-5', Cycle: 94°C 5 min, (35 cycles) 94°C 30 sec, 62°C 30 sec, and 72°C 45 sec, followed by elongation 72°C 10 min. PCR product was concentrated using DNA Clean & Concentrator™-5 (Zymo Research) and the total volumes of recovered aptamers were used for proceeding rounds of selection. Concentrations, as detected by NanoDrop, were significantly less than initial starting concentration at the conclusion of round 1. Subsequent treatment concentration of aptamers was maintained (~100 ng) following elution of aptamers and PCR enrichment. The first and second rounds of SELEX did not utilize the counter selection step, but were introduced during the 3^{rd}, 5^{th}, 7^{th} and subsequent odd rounds of selection. A total of 15 rounds of whole-cell SELEX were performed on the target cell line. Wash strength was enhanced gradually from 1 to 2 min and flask sizes increased from T25 to T75 following and including round 10 of positive selection. To monitor the presence of aptamers through rounds of selection, aptamers from rounds 5, 8, and 12 were cloned into *Escherichia coli* by manufacturers' recommendations using a One Shot TOPO10A cloning kit (Invitrogen) then analyzed by Sequetech DNA Sequencing Service (Mountain View, California). Global sequence panels were obtained after 15 rounds of selection by Ion Torrent Next Generation Sequencing (University of North Carolina-Charlotte).

Next Generation Ion Torrent Sequencing. 100 ng dsDNA PCR products was confirmed by Quant-iT™ PicoGreen® dsDNA Assay Kit (Invitrogen) and were used as template in the Ion Xpress Plus Fragment Library Kit (Invitrogen) following the protocol for short amplicons. Amplification of the prepared library was required; therefore the protocol to amplify and purify the library was followed. The amplified library was quantified using the Kapa Biosystems Library Quantification Kit for the Ion Torrent platform on a Bio-Rad MyIQ iCycler to determine the Template Dilution Factor (TDF) to be used with the Ion PGM Template OT2 200 Kit and the OneTouch 2 instrument. After emulsion PCR, the clonally amplified sample was run on the Ion Torrent PGM instrument using the Ion PGM Sequencing 200 Kit v2 and a 314 chip. Run conditions included 260 flows on the PGM instrument for sample 1 and 500 flows for sample 2.

Flow Cytometry (Binding Kinetics). To test the binding capacity of selected ovarian aptamers-RLA01, RLA02, and RLA03 were obtained from IDT labeled with a Cy5 fluorescent dye. The binding affinity of aptamers was determined by incubating cell lines on 6-well plates (seeded at 1.0×10^6, incubated 48 hours) with varying concentrations of Cy5 labeled aptamer. 25µL aptamer pool in TE was added to 1 mL of cell line specific media and incubated at 37°C 5% CO_2 2 hours agitating slightly every 30 min. Cells were then washed twice with 2 mL 1X PBS, scraped in 1 mL 1X PBS, and filtered through a 35µm nylon mesh cell strainer polystyrene tube (BD Falcon). Cells were subjected to flow cytometric analysis within 1 min and fluorescent events were determined with a Becton Dickinson LSRFortessa Flow Cytometer by counting 50,000 events. A Cy5 labeled randomized unselected 60mer oligo was used as negative control. Mean fluorescent events (n=3) were recorded and used to calculate an apparent dissociation constant (K_d) for specific binding. The K_d of the fluorescent aptamers were obtained by fitting the dependence of fluorescence intensity of specific binding on the concentration of the ligands to the equation $Y = B_{max*}X\text{^}h/(K_d\text{^}h + X\text{^}h)$ using GraphPad Prism software (2236 Avenida de la Playa, La Jolla, CA 92037). When calculating respective K_d values baseline fluorescence for untreated cells was not pre-subtracted off since detected initial

auto fluorescence made no significant impact on the calculated K_d values. Concentrations of Cy5-aptamer conjugates were brought to 1600 nM to saturate the system and obtain sigmoidal curves giving the most accurate K_d values for post hoc analysis.

Flow Cytometry (Endosomal internalization). To determine the percent internalization of Cy5-aptamer conjugates pHrodo® Red Transferrin Conjugate was used (Invitrogen). Aptamers (500 nM) were added to 1 mL cell specific media and incubated on Caov-3 cells (6-well plates seeded at 1.0×10^6 48 hrs prior, 37º 5% CO_2) and observed at 30, 60, 90, and 120 min post treatment. 30 min before pre-determined time points staining with endosomal specific marker pHrodo® Transferrin Conjugate was done by the manufacturers' recommended protocol (25 µg/mL). Cells were then washed twice with 2 mL 1X PBS, scraped in 1 mL 1X PBS, and filtered through a 35µm nylon mesh cell strainer polystyrene tube (BD Falcon). Cells were subjected to flow cytometric analysis within 1 min and fluorescent events were determined with a Becton Dickinson LSRFortessa Flow Cytometer by counting 100,000 events. Percent internalization was calculated by the following equation: (# of dual Cy5 pHrodo Red events - # of pHrodo Red untreated background)/ # of Cy5 events.

Confocal Imaging. Cells were seeded at 5.0×10^4 per well/plate and incubated 37°C 5% CO_2 48 hrs. 2µL Cy5-aptamer conjugates at concentration ranges of 1 µM to 25 µM was added to 1 mL cell specific media and incubated on target cells 37°C 5% CO_2 2 hours agitating slightly every 30 min on a 35, 0/10 mm glass bottom culture dish and 35, 0/10 mm glass bottom 24 well plate (Greiner bio-one). Cells were washed with PBS (3x) and fixed with 2ml heptane (1:8.25 PBS: 37% Formaldehyde (Sigma Aldrich)) 37°C 10 min. For endosomal internalization specific microscopy, cells were treated with pHrodo® Red Transferrin Conjugates by the manufacturers' recommended protocol 30 min before fixing. Endosomal internalization was observed at 30, 60, 90, and 120 min time points post initial treatment with Cy5-aptamer conjugates. Cells were washed with PBS (3x) and fixed with 2ml heptane (1:8.25 PBS: 37% Formaldehyde (Sigma Aldrich)) 37°C 10 min. Subsequent staining of fixed cells was performed with DAPI (10 ng/µL, 10 min), or cell membrane stain Wheat Germ Agglutinin Alexa 488 conjugate (1µg/µL, 10 min, Invitrogen) using standard procedures. Imaging of the cells was done with an Olympus FluoView 1000 confocal microscope using DAPI (blue), Alexa448 (green), pHrodo® Red (orange), and Cy5 (red) filters.

Results

Identification of Caov3 specific aptamers

Whole Cell-SELEX was utilized to identify aptamers that bind and internalize into Caov-3 ovarian epithelial adenocarcinoma cells [31,32]. The Caov-3 adenocarcinoma cell line corresponds to late stage ovarian epithelial cancer and has been shown to express upregulated tumor biomarkers such as NB/70K, Ca-1, CEA, and Ba-2 [33]. To ensure aptamer target cell specificity, rounds of negative selection were carried out on human papilloma virus (HPV) immortalized human ovarian surface epithelial cells (HOSE 6-3) [30]. Morphologically HOSE 6-3 cells exhibited structurally identical cytoskeleton filaments with that of normal ovarian epithelial cells and show no up-regulation of known ovarian tumor specific markers such as CA-125 after immortalization [30]. The non-transformed immortalized HOSE 6-3 cell line has

demonstrated to be non-tumorigenic when inoculated into nude mice after 20 passages [30]. The use of HOSE 6-3 cells for negative selection was deemed significant for potential *in vivo* therapeutic applications in which aptamers would need to bind to malignant cells but not to neighboring non-tumor cells of otherwise similar cell type or origin. Potential aptamers were identified from an initial randomly generated ssDNA 60bp oligonucleotide library in a dual positive and negative selection process consisting of selection rounds followed with PCR enrichment prior to the subsequent round. Negative selection was performed at rounds 3, 5, 7, 9, 11, and 13 which promoted identification of aptamers highly specific to malignant cells.

Monitoring aptamer selection and identification of ovarian tumor-specific aptamers

In order to confirm that full-length aptamers were being selected for and enriched through consecutive rounds, we used TOPO cloning. Complete 60mer aptamer sequences were identified after rounds 3, 8, and 12 of whole Cell-SELEX. Clones analyzed from round 3 showed 11 distinct aptamer species with one subgroup representing 67% of the population. Sequencing of clones from round 12 of selection provided 10 distinct aptamer species with one of these aptamer species representing 33% of the sequenced population. Additionally, the enrichment process was also monitored by way of flow cytometry with Cy5 labeled aptamers. Aptamers were amplified from indicated rounds of Cell-SELEX (Figure 1) by PCR using a 5'-Cy5 labeled primer and a anti-sense 5'-biotin labeled primer. The removal of the 60mer aptamer anti-sense strands was done by denaturing the double stranded PCR product (95°C 5 min) and isolating biotin labeled strands with streptavidin with subsequent exposure to a magnetic field. This ensured that the remaining supernatant was rich with Cy5 labeled aptamers. The Cy5 labeled aptamers (100 ng) were incubated with target Caov-3 cells, collected by scraping, and analyzed by flow cytometry. Baseline fluorescent values were determined using a Cy5 labeled initial random library (red). A right shift in the fluorescent cell population can be seen when fluorescently labeled aptamers from rounds 3, 8, and 12 of Cell-SELEX were incubated with Caov-3 cells (Figure 1). This shift in fluorescent populations indicates enrichment of cell specific aptamers that bind and internalize into cells. Moreover, the observed difference in Cy5 fluorescently labeled Caov-3 cell populations significantly increases when comparing aptamer pools from round 3 (blue) to round 8 (orange) of Cell-SELEX (Figure 1). The observed shift in fluorescently labeled Caov-3 cell populations seen between round 8 and round 12 (green) aptamer pools is significantly less which suggests that aptamer pools are nearing the threshold of potential aptamer enrichment. In order to characterize the complete aptamer population we used Next-Generation Ion Torrent (NGIT) sequencing. We obtained 53% loading efficiency resulting in over 293,000 ssDNA reads. From an initial random pool of approximately 4^{20} sequences, NGIT sequencing identified 7 full-length aptamers (Table 1) within the aptamer pool, and here we report on three of these aptamers RLA01, RLA02, and RLA03. Given the flow cytometry data and the identification of 7 unique aptamers in sequencing data from our initial randomized pool, we terminated our Cell-SELEX protocol after 15 rounds.

Specificity of aptamer binding and internalization to target cells

Flow cytometry was used to quantify aptamer binding activity. RLA01, RLA02, and, RLA03 were evaluated to determine the binding kinetics of each and calculate apparent equilibrium dissociation constants (K_d). The aptamers were conjugated to

cyanine dye Cy5 on the 5' end to enable detection by flow cytometry and quantify the number of cells that bind to the target aptamer. Additionally, a random scrambled aptamer also conjugated to Cy5 was used as a negative control to demonstrate specificity (Table 1). Target EOC Caov-3 cells as well as EOC cell lines SK-OV-3 and SW626 were treated with increasing molar concentrations of Cy5-aptamers for 2 hr. Following washing of excess unbound aptamer, cells were analyzed by flow cytometry to quantify Cy5 fluorescence. To establish baseline fluorescence, untreated Caov-3 cells were also analyzed and gating of the background fluorescence was set to 0.01% of the total population analyzed (data not shown). As expected, no fluorescent events above the background gate were observed when Caov-3 cells were incubated with the random scrambled aptamer at concentrations (1 nM to 1.6 μM; data not shown). RLA01, RLA02, and RLA03 all demonstrated a dose-dependent increase (1 nM to 1.6 μM) in binding to target Caov-3 cells as demonstrated by the increased number of fluorescent events (Figure 2A, B, C, closed circles, respectively). Binding of each of the aptamers to Coav-3 cells was highly specific since minimal binding events were detectable by flow cytometry when any were incubated with either of the analogous epithelial ovarian tumor cell lines SK-OV-3 or SW626 (Figure 2). Similar to Caov-3, SK-OV-3 cells are derived from epithelial ovarian adenocarcinoma, but also characterized as resistant to multiple cytotoxic drugs [34]. Although SW626 was isolated as an ovarian adenocarcinoma, genome expression evidence recently indicated it likely originated as a colorectal tumor metastasized to the ovary [35]. From the flow cytometry data (Figure 2), respective apparent K_d values for RLA01, RLA02, and RLA03 to Caov-3 cells were calculated in the nanomolar range as 365.3 ± 24.14 nM, 225.5 ± 48.29 nM, and 505 ± 70.64 nM, respectively (Table 2).

Aptamer specificity was further demonstrated by comparison of Cy5-aptamer binding to a large panel of cell lines. Incubation with both 400 nM (Figure 3A-blue) and 800 nM (Figure 3A-green) Cy5-RLA01 for 2 hr produced a right shift in the fluorescent Caov3 cell population over untreated cells, consistent with an increase in aptamer-cell interaction. By contrast minimal shift of the population above baseline was observed with either non-transformed HOSE 6-3 cells or kidney epithelial HEK293 cells when incubated with increasing molar concentrations of Cy5-RLA01, Cy5-RLA02, or Cy5-RLA03 (Figure 3A). This was further demonstrated by confocal microscopy as seen in Figure 3C. Aptamer-cell interactions were observed with Cy5-RLA01 when incubated with SK-OV-3 and HeLa cell lines (Figure 3D), and apparent K_d values of 627.1± 65.67 nM and 645.3 ± 60.91 nM were determined (Table 2). Although flow cytometry confirms aptamer-cell binding for both HeLa and SK-OV-3 cell lines, the average fluorescent events observed were significantly less for both when compared to RLA01 binding to Caov-3 cells and showed no interaction with the scrambled aptamer at equal doses (Figure 3D).

Specificity of all three aptamers was further demonstrated with a large panel of immortalized non-malignant epithelial and multiple malignant epithelial cell lines including two malignant pancreatic epithelial carcinomas (Suit-2, Hs766t), two mammary epithelial adenocarcinomas (MCF-7, MDA-MB-231), one cervical epithelial adenocarcinoma (HeLa), two ovarian epithelial adenocarcinoma cell lines (SK-OV-3, SW626), as well as kidney epithelial cells (HEK293), and murine fibroblast NIH/3T3 cells. Kidney epithelial tissue was chosen because kidneys play a major role in removal

of organic waste from the bloodstream thus would impact potential clinical use by intravenous delivery of aptamers. Aptamer-binding events were minimal or undetectable as shown by flow cytometry when incubated with malignant cell lines in increasing molar concentrations (Table 2). Binding of aptamers was also time dependent (Figure 3B). Increasing incubation time of Cy5-RLA01 with Caov-3 cells from 2 hr to 4 hr produced 275% more fluorescent events while fluorescent events in HOSE 6-3 cells remained similar to baseline controls (Figure 3B).

Specific binding and internalization of RLA01, RLA02, and RLA03 to Caov-3 cells was demonstrated by flow cytometry and confocal imaging (Figure 4). Cell membranes were identified by Wheat Germ Agglutinin conjugates labeled with Alexa Fluor® 488 enabling identification of two key cellular structures: (i) the cell membrane where Cy5-aptamer conjugates are predicted to localize upon initial target recognition, and (ii) the internal endosomal membranes where aptamers are expected to localize to if efficiently internalized into cells. Images of aptamer specific binding and endosomal internalization were assessed as early as 30 min and up to 2 hours post initial treatment of Cy5-aptamer conjugates ranging in dosages of 1 µM to 25 µM. Supporting the flow cytometry data, no internalization at any dose was observed with scrambled aptamer (Table 1). Aptamers RLA01, RLA02, or RLA03 (pseudo-colored yellow) localized on and around membranes of Caov-3 cells (Figure 4A). The observed Cy5 fluorescent signals appeared at or near the membranes similarly to that of the Alexa Fluor® WGA stain. All three aptamers localized to the cell membranes (Figure 4A). In addition, all three localized to multiple compartments within the cytoplasm proximal to the membranes suggesting endosomal internalization. Internalization of Cy5-aptamer (500 nM) conjugates was measured by flow cytometry at 30, 60, 90, and 120 minutes post initial treatment with aptamer RLA01 on Caov-3 cells (Figure 4B). Additionally, the percent of internalization events over the same range of time is shown in Figure 4C. These data were further confirmed by confocal imaging. We used the endosomal marker pHrodo® Red Transferrin Conjugate to identify co-localization of Cy5-aptamer conjugates (5 µM) and endosomal structures. As seen in Figure 4D pHrodo® Red stained endosomal structures (pseudo-colored red) co-localize with Cy5 fluorescent aptamers (pseudo-colored yellow). These data are highly suggestive that the internalization of aptamers into Caov-3 cells is regulated by endocytic pathways. Moreover, Z-stack imaging (20 stacks, 2 µm range) further demonstrated Cy5 fluorescence within cells consistent with internalization of aptamers (Supplemental Figure 1A and B). Thus, confocal imaging of all three Cy5-aptamer conjugates demonstrated fluorescent activity consistent with the average max fluorescent events observed by flow cytometry (Figure 2A, B, C and Figure 4).

Confocal imaging was also employed to further demonstrate aptamer specificity. The three Caov-3 target aptamers were incubated with a panel of selected EOCs, malignant epithelial, and non-malignant immortalized cell lines (Supplemental Figure 2). Consistent with the flow cytometry histograms shown in Figures 3A Cy5-RLA01, fluorescent events were not detected above baseline untreated control levels when increasing molar concentrations of Cy5-RLA03 were administered to non-malignant HOSE 6-3 and HEK293 epithelial cell lines (Supplemental Figure 2). Additionally, incubation of Cy5-RLA03 conjugates with malignant epithelial cell lines produced minimal fluorescent events similar to those of untreated control samples. Overall, the full

range of Cy5-RLA03 concentrations used for incubation with malignant epithelial cells showed no fluorescent events after a 2 hour incubation period, and this was further supported by confocal imaging (Supplemental Figure 2). Cy5-RLA02 conjugates produced similar data to the Cy5-RLA03 conjugates. Cy5-RLA02 demonstrated no binding to the panel of malignant and non-malignant cell lines (data not shown). Despite observing detectable fluorescent events when SK-OV-3 and HeLa cell lines were incubated with increasing molar concentrations of RLA01 (Figure 3D), data obtained by flow cytometry against the panel of malignant and non-malignant cell lines showed no total fluorescent events above untreated control baseline levels, also supported by confocal imaging (data not shown).

Predicting tertiary structures of aptamers

In order to predict the most stable structure for RLA01, RLA02, and RLA03, we used UNAfold (Rensselaer Polytechnic Institute). Ranking of the stability for aptamers RLA01, RLA02, and RLA03 is based on Gibbs free energy and yielded ΔG values of -2.4, -4.91, -4.24 kcal/mol respectively. RLA01 and RLA02 exhibit a large central loop with small hairpin structures radiating from the main loop. RLA03 will form a longer structure consisting of a double hairpin with a central loop. Figures detailing the top energetically stable secondary structures of aptamers RLA01, RLA02, and RLA03 are available in supplemental data (Supplemental Figure 3).

Discussion

As expected, all three aptamers RLA01, RLA02, and RLA03 bound with high affinity to the target Caov-3 cells used in the initial screen for their identification. RLA02 and RLA03 demonstrated exclusive specificity with minimal to undetectable interaction with any of the malignant or non-malignant epithelial cell lines tested except the target Caov-3 cells. It is interesting to note that RLA01 showed binding interactions with both SK-OV-3 and HeLa cells, as compared to controls. However, the max fluorescent events observed in the other cell lines were lower than the binding kinetics to Caov-3. One possible explanation for these results could be the existence of a commonly shared receptor among the three cell lines expressed at highest levels in Caov-3 cells and moderate or low levels on the other two. A second explanation could be structurally similar or related proteins are present on the membranes of the three cell lines with RLA01 having the highest binding affinity for the one that is expressed on Caov-3 cells. Ovarian surface epithelium and cells in the Müllerian tract are derived from common embryonic coelomic progenitors [36]. Since Caov-3 and SK-OV-3 cells were isolated from ovarian epithelial tissue it is likely that a common receptor is shared between the two cell lines. However, a study comparing EOC cell lines involving karyotyping, surface markers, and drug resistance indicated that Caov-3 cell lines display a unique genetic lesion on the long arm of chromosome 3 (del(3)(p13:) not seen in SK-OV-3 cell lines [33,37]. This could result in altered morphology in common surface structures such as dysregulated glycosylation of common receptors on Caov-3 versus SK-OV-3 cells. Additionally, the heterogeneity observed in EOC development could further explain common expression of surface structures seen in ovarian tumor subtypes and cervical carcinomas which are known to originate from squamocolumnar junctions of the cervix [38]. Data suggest that ovarian tumors manifest from cells expressing Müllerian tract differentiation. Although fallopian, ovarian, and pelvic cancers are treated as three

distinct neoplastic diseases, it is believed that the majority of them originate from a common Müllerian progenitor and/or distal fimbrae tubes of the ovary [5,36,39-41]. It is possible that these malignant cell lines share a common receptor that is up- or down-regulated depending on particular context, abnormality, or in response to external stimuli such as hormones. SK-OV-3 cells originate from an epithelial adenocarcinoma similar to Caov-3 cells; however they also demonstrate levels of resistance to multiple cytotoxic drugs including platinum-taxanes [33,34] and thus could differ from Caov-3 at a minimum in their expression of ABC multiple drug resistance (MDR) transporters on the cell surface. However, similarity of characteristics of these cell lines is in their origin in the female reproductive tract rather than as epithelial cells *per se* since no binding events were detected by either flow cytometry or confocal imaging when RLA01 was incubated with epithelial cells from other tissues.

The three aptamers have apparent K_d values in the nanomolar range which show that they bind with high affinity to target cells. Physiologically relevant apparent equilibrium dissociation values for therapeutic molecules are considered to be in the nanomolar to picomolar range. Initial dosing of pegaptanib (Macugen) to inhibit $VEGF_{165}$ in HUVEC cells had an IC_{50} value between 0.75-1.4 nM with total inhibition of $VEGF_{165}$ binding observed at 10nM [42]. However it is important to note that pegaptanib is an inhibitory aptamer with a single agonist and was developed in a sequential process in the presence of a purified target molecule only [43]. Another non-SELEX identified aptamer AS1411, formerly ARGO100, showed initial inhibition of MDA-MD-231 cell proliferation after a 15μM dose [44,45]. Several aptamers have been identified through positive and negative whole Cell-SELEX. The reported DOV-3 aptamer with an apparent K_d 132 ± 32nM [46] identified as binding to Caov3 cells, similar to this study, was counter-selected against malignant cervical HeLa cells which may not be as relevant for identification of ovarian tumor specific aptamers. Additional whole Cell-SELEX aptamers with nanomolar K_d values target Axl (GL21 aptamer apparent K_d 221nM) [47], B-cell receptors of Burkitt's lymphoma cell lines (TD05 apparent K_d 74.7 ± 8.7 nM) [25,48], and liver cancer MEAR cell line (TLS6 apparent K_d 157.0 ± 16.9 nM) [49]. In addition to reporting apparent K_d values in the nanomolar range, our reporting of higher total fluorescent events over a range of aptamer doses supports use of these aptamers as attractive candidates to chaperone chemotherapeutic drugs or small molecule vehicles directly to tumor sites. We hypothesize that the number of events observed by flow cytometry directly correlates to effective dose of aptamer-drug conjugates internalized. This could increase the efficacy of current treatment protocols by delivering more cytotoxic drugs to the tumor while reducing systemic cytotoxic side effects typically seen with them.

Further, confocal imaging clearly supports significant internalization of aptamers into specific cell types. Typically it is believed that aptamers internalize into cells via canonical endosomal pathways. Our raw confocal images utilizing an endosomal specific marker, as well as Z-stack, generated images support colocalization of Cy5-aptamer signal to internal endosomal membranes.

The three aptamers are similar in their 5' and 3' sequences that were used as anchors for PCR amplification during Cell-SELEX. Despite these known identities, the aptamers have different stable predicted structures and hairpin loops that would produce unique surfaces for interactions with target cell membranes. Further support that these

aptamers are unique comes from the independent equilibrium binding kinetics of each on Caov-3 cells. The confocal imaging was consistent with the total fluorescent events observed by flow cytometry using Cy5 conjugated aptamers with highest levels of internalized aptamer observed with RLA01, followed by RLA03, and lowest with RLA02. Further, RLA01 was determined to bind to a broader spectrum of cell types, as discussed above. Although others reported identification of ovarian carcinoma specific aptamers, sequence alignment of the three described here shows that they are unique from those previously reported. In order to be most physiologically relevant for future therapeutic uses, it is believed that aptamers should interact with the target malignant cells and not other non-malignant cells which would be neighboring cells and likely of the same original cell origin. Notably, our adapted Cell-SELEX protocol included negative selection against non-malignant ovarian epithelial cells. Flow cytometry and confocal analysis supported non-reactivity of the aptamers to non-malignant epithelial cells of both ovarian and kidney origin. By contrast to this report, others utilized HeLa cells, a known neoplastic immortalized line for negative selection [46]. That our protocol yielded aptamers unique from those previously reported highlights that individual Cell-SELEX strategies used will be a key factor in determining what aptamers are identified. Large bioinformatics approaches for comparison of multiple parallel aptamer pools and a large panel of cell types could reveal similar sequence patterns for aptamers that bind to related disorders.

In conclusion, we modified whole Cell-SELEX to identify three DNA-based aptamers that bind with high affinity to the EOC cell line Caov-3 but importantly not to the non-malignant epithelial HOSE 6-3 cell line. The modified protocol described here is unique in that we identified EOC aptamers specific to Caov-3 following negative selection against a non-transformed epithelial cell line. Specificity of all three aptamers was shown across a panel of tumor types including breast, cervical, and pancreatic malignancies. Additionally the differences in aptamer binding kinetics demonstrated here can be used to infer particular molecular characteristics of the target cells. The identified aptamers can potentially be used to enhance the sensitivity of current clinical diagnostic tools to identify ovarian neoplasms. The lack of interactions observed with non-tumor epithelial cells suggests that aptamer-based therapies can minimalize interaction with non-malignant tissues and improve upon the incidence of false positive results regarding benign versus malignant diagnosis or to potentially deliver cytotoxic drugs to distal tumor sites in the body. Thus, overall, our data suggest these aptamers are attractive candidates for further analysis to direct and localize chemotherapeutics to tumor sites and potentially aid in the early diagnosis of ovarian malignancies.

Acknowledgements

Christine Richardson and this report was funded through a Faculty Research Grant, UNC Charlotte, the Charlotte Research Institute, UNC Charlotte, and the Center for Biomedical Engineering and Science, UNC Charlotte. We gratefully acknowledge Cory Brouwer (College of Computing and Informatics, UNC Charlotte) for providing Ion Torrent Sequencing reagents, George S. W. Tsao for HOSE 6-3 cells, David Gray for confocal imaging and flow cytometry expertise and technical assistance, and Deborah Nwafor and Noelle Cornelio for technical assistance.

References

1. Choi M, Fuller CD, Thomas CR, Jr., Wang SJ (2008) Conditional survival in ovarian cancer: results from the SEER dataset 1988-2001. Gynecol Oncol 109: 203-209.
2. Kroep JR (2012) Advances in epithelial ovarian cancer therapy. Curr Pharm Des 18: 3735-3740.
3. Bicaku E, Xiong Y, Marchion DC, Chon HS, Stickles XB, et al. (2012) In vitro analysis of ovarian cancer response to cisplatin, carboplatin, and paclitaxel identifies common pathways that are also associated with overall patient survival. Br J Cancer 106: 1967-1975.
4. Conic I, Dimov I, Tasic-Dimov D, Djordjevic B, Stefanovic V (2011) Ovarian epithelial cancer stem cells. ScientificWorldJournal 11: 1243-1269.
5. Dubeau L (2008) The cell of origin of ovarian epithelial tumours. Lancet Oncol 9: 1191-1197.
6. Cohen JG, White M, Cruz A, Farias-Eisner R (2014) In 2014, can we do better than CA125 in the early detection of ovarian cancer? World J Biol Chem 5: 286-300.
7. Hellstrom I, Hellstrom KE (2008) SMRP and HE4 as biomarkers for ovarian carcinoma when used alone and in combination with CA125 and/or each other. Adv Exp Med Biol 622: 15-21.
8. Sorace JM, Zhan M (2003) A data review and re-assessment of ovarian cancer serum proteomic profiling. BMC Bioinformatics 4: 24.
9. Jacobs I, Oram D, Fairbanks J, Turner J, Frost C, et al. (1990) A risk of malignancy index incorporating CA 125, ultrasound and menopausal status for the accurate preoperative diagnosis of ovarian cancer. Br J Obstet Gynaecol 97: 922-929.
10. Moore RG, McMeekin DS, Brown AK, DiSilvestro P, Miller MC, et al. (2009) A novel multiple marker bioassay utilizing HE4 and CA125 for the prediction of ovarian cancer in patients with a pelvic mass. Gynecol Oncol 112: 40-46.
11. Zhang Z, Bast RC, Jr., Yu Y, Li J, Sokoll LJ, et al. (2004) Three biomarkers identified from serum proteomic analysis for the detection of early stage ovarian cancer. Cancer Res 64: 5882-5890.
12. Yip P, Chen TH, Seshaiah P, Stephen LL, Michael-Ballard KL, et al. (2011) Comprehensive serum profiling for the discovery of epithelial ovarian cancer biomarkers. PLoS One 6: e29533.
13. Kruspe S, Meyer C, Hahn U (2014) Chlorin e6 Conjugated Interleukin-6 Receptor Aptamers Selectively Kill Target Cells Upon Irradiation. Mol Ther Nucleic Acids 3: e143.
14. Zhu J, Huang H, Dong S, Ge L, Zhang Y (2014) Progress in Aptamer-Mediated Drug Delivery Vehicles for Cancer Targeting and Its Implications in Addressing Chemotherapeutic Challenges. Theranostics 4: 931-944.
15. Brody EN, Gold L (2000) Aptamers as therapeutic and diagnostic agents. J Biotechnol 74: 5-13.
16. Zhou W, Huang PJ, Ding J, Liu J (2014) Aptamer-based biosensors for biomedical diagnostics. Analyst 139: 2627-2640.
17. Shum KT, Zhou J, Rossi JJ (2013) Nucleic Acid Aptamers as Potential Therapeutic and Diagnostic Agents for Lymphoma. J Cancer Ther 4: 872-890.
18. Jalalian SH, Taghdisi SM, Shahidi Hamedani N, Kalat SA, Lavaee P, et al. (2013) Epirubicin loaded super paramagnetic iron oxide nanoparticle-aptamer

bioconjugate for combined colon cancer therapy and imaging in vivo. Eur J Pharm Sci 50: 191-197.
19. Cunningham ET, Jr., Adamis AP, Altaweel M, Aiello LP, Bressler NM, et al. (2005) A phase II randomized double-masked trial of pegaptanib, an anti-vascular endothelial growth factor aptamer, for diabetic macular edema. Ophthalmology 112: 1747-1757.
20. Research B (2013) Aptamers market--technology trend analysis by applications--therapeutics, diagnostics, biosensors, drug discovery, biomarker discovery, research applications with market landscape analysis-- global forecasts to 2018. marketsandmarkets.com.
21. Ng EW, Adamis AP (2006) Anti-VEGF aptamer (pegaptanib) therapy for ocular vascular diseases. Ann N Y Acad Sci 1082: 151-171.
22. Ng EW, Shima DT, Calias P, Cunningham ET, Jr., Guyer DR, et al. (2006) Pegaptanib, a targeted anti-VEGF aptamer for ocular vascular disease. Nat Rev Drug Discov 5: 123-132.
23. Tolentino MJ, Dennrick A, John E, Tolentino MS (2014) Drugs in Phase II clinical trials for the treatment of age-related macular degeneration. Expert Opin Investig Drugs: 1-17.
24. Biesecker G, Dihel L, Enney K, Bendele RA (1999) Derivation of RNA aptamer inhibitors of human complement C5. Immunopharmacology 42: 219-230.
25. Mallikaratchy PR, Ruggiero A, Gardner JR, Kuryavyi V, Maguire WF, et al. (2011) A multivalent DNA aptamer specific for the B-cell receptor on human lymphoma and leukemia. Nucleic Acids Res 39: 2458-2469.
26. Soundararajan S, Chen W, Spicer EK, Courtenay-Luck N, Fernandes DJ (2008) The nucleolin targeting aptamer AS1411 destabilizes Bcl-2 messenger RNA in human breast cancer cells. Cancer Res 68: 2358-2365.
27. Girvan AC, Teng Y, Casson LK, Thomas SD, Juliger S, et al. (2006) AGRO100 inhibits activation of nuclear factor-kappaB (NF-kappaB) by forming a complex with NF-kappaB essential modulator (NEMO) and nucleolin. Mol Cancer Ther 5: 1790-1799.
28. Zhang X, Zhang J, Ma Y, Pei X, Liu Q, et al. (2014) A cell-based single-stranded DNA aptamer specifically targetsgastric cancer. Int J Biochem Cell Biol 46: 1-8.
29. Iwamura T, Katsuki T, Ide K (1987) Establishment and characterization of a human pancreatic cancer cell line (SUIT-2) producing carcinoembryonic antigen and carbohydrate antigen 19-9. Jpn J Cancer Res 78: 54-62.
30. Tsao SW, Mok SC, Fey EG, Fletcher JA, Wan TS, et al. (1995) Characterization of human ovarian surface epithelial cells immortalized by human papilloma viral oncogenes (HPV-E6E7 ORFs). Exp Cell Res 218: 499-507.
31. Zhan SB, Zeng Y (2013) [Recent progress on SELEX and its applications]. Bing Du Xue Bao 29: 573-577.
32. Daniels DA, Chen H, Hicke BJ, Swiderek KM, Gold L (2003) A tenascin-C aptamer identified by tumor cell SELEX: systematic evolution of ligands by exponential enrichment. Proc Natl Acad Sci U S A 100: 15416-15421.
33. Buick RN, Pullano R, Trent JM (1985) Comparative properties of five human ovarian adenocarcinoma cell lines. Cancer Res 45: 3668-3676.

34. Abouzeid AH, Patel NR, Torchilin VP (2014) Polyethylene glycol-phosphatidylethanolamine (PEG-PE)/vitamin E micelles for co-delivery of paclitaxel and curcumin to overcome multi-drug resistance in ovarian cancer. Int J Pharm 464: 178-184.
35. Furlong MT, Hough CD, Sherman-Baust CA, Pizer ES, Morin PJ (1999) Evidence for the colonic origin of ovarian cancer cell line SW626. J Natl Cancer Inst 91: 1327-1328.
36. Hennessy BT, Coleman RL, Markman M (2009) Ovarian cancer. Lancet 374: 1371-1382.
37. Beaufort CM, Helmijr JC, Piskorz AM, Hoogstraat M, Ruigrok-Ritstier K, et al. (2014) Ovarian cancer cell line panel (OCCP): clinical importance of in vitro morphological subtypes. PLoS One 9: e103988.
38. Herfs M, Yamamoto Y, Laury A, Wang X, Nucci MR, et al. (2012) A discrete population of squamocolumnar junction cells implicated in the pathogenesis of cervical cancer. Proc Natl Acad Sci U S A 109: 10516-10521.
39. Masiakos PT, MacLaughlin DT, Maheswaran S, Teixeira J, Fuller AF, Jr., et al. (1999) Human ovarian cancer, cell lines, and primary ascites cells express the human Mullerian inhibiting substance (MIS) type II receptor, bind, and are responsive to MIS. Clin Cancer Res 5: 3488-3499.
40. Saad AF, Hu W, Sood AK (2010) Microenvironment and pathogenesis of epithelial ovarian cancer. Horm Cancer 1: 277-290.
41. Crum CP, Drapkin R, Kindelberger D, Medeiros F, Miron A, et al. (2007) Lessons from BRCA: the tubal fimbria emerges as an origin for pelvic serous cancer. Clin Med Res 5: 35-44.
42. Bell C, Lynam E, Landfair DJ, Janjic N, Wiles ME (1999) Oligonucleotide NX1838 inhibits VEGF165-mediated cellular responses in vitro. In Vitro Cell Dev Biol Anim 35: 533-542.
43. Ruckman J, Green LS, Beeson J, Waugh S, Gillette WL, et al. (1998) 2'-Fluoropyrimidine RNA-based aptamers to the 165-amino acid form of vascular endothelial growth factor (VEGF165). Inhibition of receptor binding and VEGF-induced vascular permeability through interactions requiring the exon 7-encoded domain. J Biol Chem 273: 20556-20567.
44. Bates PJ, Kahlon JB, Thomas SD, Trent JO, Miller DM (1999) Antiproliferative activity of G-rich oligonucleotides correlates with protein binding. J Biol Chem 274: 26369-26377.
45. Ireson CR, Kelland LR (2006) Discovery and development of anticancer aptamers. Mol Cancer Ther 5: 2957-2962.
46. Van Simaeys D, Lopez-Colon D, Sefah K, Sutphen R, Jimenez E, et al. (2010) Study of the molecular recognition of aptamers selected through ovarian cancer cell-SELEX. PLoS One 5: e13770.
47. Cerchia L, Esposito CL, Camorani S, Rienzo A, Stasio L, et al. (2012) Targeting Axl with an high-affinity inhibitory aptamer. Mol Ther 20: 2291-2303.
48. Tang Z, Shangguan D, Wang K, Shi H, Sefah K, et al. (2007) Selection of aptamers for molecular recognition and characterization of cancer cells. Anal Chem 79: 4900-4907.

49. Shangguan D, Meng L, Cao ZC, Xiao Z, Fang X, et al. (2008) Identification of liver cancer-specific aptamers using whole live cells. Anal Chem 80: 721-728.

APPENDIX C:
APTAMER-FUNCTIONALIZED NANOPARTICLES AS "SMART BOMBS": THE UNREALIZED POTENTIAL FOR PERSONALIZED MEDICINE AND TARGETED CANCER TREATMENT

Being reviewed by *Targeted Oncology*

Gregory Benedetto[a], C. Greer Vestal[b], and Christine Richardson[c,*]

[a] Department of Biological Sciences, UNC Charlotte, 1902 University City Blvd., Woodward Hall Room 386B, Charlotte NC 28223 USA; gbenedet@uncc.edu
[b] Department of Biological Sciences, UNC Charlotte, 1902 University City Blvd., Woodward Hall Room 386B, Charlotte NC 28223 USA; cvestal1@uncc.edu
[c] Department of Biological Sciences, UNC Charlotte, 1902 University City Blvd., Woodward Hall Room 386B, Charlotte NC 28223 USA; C.Richardson@uncc.edu

[*] to whom correspondence should be addressed: C.Richardson@uncc.edu; 01 704-687-8683

Potential conflict of interest:
CR is funded through NIH/NCI and has grant pending with NIH/NCI and patent pending.
GB has patent pending.
CV has no conflict of interest.

Abstract

Conventional delivery of chemotherapeutic agents leads to multiple systemic side effects and toxicity, limiting the doses that can be used. Development of targeted therapies to selectively deliver anti-cancer agents to tumor cells without damaging neighboring unaffected cells would lead to higher effective local doses and improved response rates. Aptamers are single-stranded oligonucleotides that bind to target molecules with both high affinity and high specificity. The high specificity exhibited by aptamers promotes localization and uptake by specific cell populations such as tumor cells, and their conjugation to anti-cancer drugs have been explored for targeted therapy. Advancements in the development of polymeric nanoparticles allow anti-cancer drugs to be encapsulated in protective nonreactive shells for controlled drug delivery with reduced toxicity. Nanoparticles themselves of various formulations have been used extensively in industrial, commercial, and biomedical applications. Conjugation of aptamers to nanoparticle-based therapeutics may further enhance direct targeting and personalized medicine. Here we present how the combinatorial use of aptamer and nanoparticle technologies has the potential to develop "smart bombs", highlighting recent studies demonstrating efficacy for the direct targeting of particular tumor cell populations to synergistically improve outcomes of conventional anti-cancer treatment.

Keywords: aptamers; nanomaterials; targeted delivery; targeted therapeutics; multidrug resistance; drug-loaded nanocarriers

I. Introduction

Recent statistics project a total of 1,658,370 new cancer cases and 589,430 cancer deaths to occur in the United States in 2015 [1]. The majority of primary solid tumors are treated by invasive surgery to remove accessible malignant tissue, followed by adjuvant nonselective chemotherapy and/or radiation therapy with high dose-limiting toxicities [2, 3]. The development of personalized or targeted therapeutic strategies may minimalized the adverse side-effects seen with systemic treatments. Distinct expression of surface receptors or biomarkers give individual cancer subtypes unique molecular signatures that may be identified and bound by antibodies, antigen-binding fragments, small molecules, or aptamers [4-6].

Aptamers are short single-stranded DNA or RNA oligonucleotides that bind to target molecules with high affinity and specificity. Aptamers have more generally been used as reagents for identifying cell surface proteins and for cell typing [7] The emergence of multiple library screening protocols to identify aptamers with therapeutic potential has led to an abundance of both agonistic and antagonistic aptamer-based therapies[8]. Rapidly, aptamers are being investigated as a valid alternative to antibodies *in vivo* as targeted therapeutics alone or as targeted delivery agents for chemotherapeutics, small interfering RNAs, and molecular imaging probes [9]. Additionally, nanocarriers are emerging as a fundamental means for transporting small molecules systemically while increasing bioavailability [10]. Delivery of therapeutic-loaded nanocarriers is enhanced when the surface is functionalized, *i.e.* conjugated to cell specific targeting ligands such as aptamers [11, 12]. Such "smart bombs" may overcome the challenges of conventional systemic anti-cancer treatment regimens and lead to higher local doses, more effective tumor cell death, reduction of subsequent treatment rounds, and reduced relapse rates [13]. This review presents current data that explores the development of biomarker-based aptamer therapies, particularly those utilizing nanoparticle vehicles for customized drug delivery in anti-cancer approaches.

II. Aptamers as anti-cancer therapeutic agents

A. Identification of Clinically Relevant Aptamers

Aptamers have an average length of 40-80 nucleotides that bind with high affinity and specificity to specific protein or non-protein targets by folding into complex secondary and tertiary structures. Commercially available aptamers can be engineered to a desired length and offer a variety of post sequencing modifications that allow for aptamer design flexibility. Post sequencing modifications can increase stability to promote bioavailability or conjugate a fluorescent reporter to terminal ends that could be used for *in vitro* tracking. Aptamers display a conventional binding behavior similar to that of antibodies with dissociation constants (Kd) measuring on the order of μM to pM ranges [14, 15]. The initial descriptions of aptamers as ligands that bind to specific targets or cells were reported more than 20 years ago [16, 17]. In contrast to early aptamers engineered against known specific ligands, a major advantage of aptamers for biomedical applications is that they may be identified through random library screens without knowledge of their direct ligand on the cell membrane surface. Systematic evolution of exponential enrichment (SELEX) was initially described as *in vitro* identification scheme to enrich of a small pool of cell-specific aptamers from randomly

generated libraries identified through binding to specific cell types and counter-selected against negative cell types. SELEX protocols have been continually modified and improved to *in vivo* screens and localization and internalization-specific screens [7, 15, 18-21]. Aptamers identified by SELEX can bind to small molecules or proteins in their native structure on the cell surface [15, 22, 23]. Information on the structural interface between target and the tertiary structure of aptamers can provide information regarding catalytic binding moieties and lead to modifications that improve design and delivery [24] [25] [26]. While SELEX screening is based on binding interactions to the cell surface, other positive and negative screening approaches have been based on cell internalization into target cell populations as shown effectively in a prostate cancer cell model [21]. To date a number of aptamers have been reported and are in various stages of preclinical and clinical development (reviewed in [27-30]).

Aptamers possess several advantages over antibodies or small molecules (reviewed in [27]) for their therapeutic targeting potential [9]. Biologically, aptamers are (1) smaller in size promoting greater tissue penetration, (2) generally considered non-immunogenic, and (3) demonstrate rapid renal clearance [8, 26, 31, 32]. Commercially, aptamers are chemically synthesized; thus they (1) can be readily modified to alter targeting kinetics, (2) are readily and cheaply produced with low batch variability, (3) can be transported at ambient temperatures, and (4) remain stable for long periods even under adverse conditions [26, 27, 33-36].

Despite the advantages of aptamer-based treatments and promising results *in vitro*, it is still debated if their efficacy will be reduced *in vivo* due to lack of bioavailability, unstable circulation time, minimal cellular internalization, or susceptibility to nuclease attack [5, 15, 31]. Post-sequencing modifications can increase structural integrity to promote bioavailability within the blood stream such as conjugation of larger molecules such as cholesterol or polyethylene glycol (PEG; PEGylation) to the aptamer [37]. It has been shown that 40 kDa PEGylated aptamers have a higher circulatory half-life than non-PEGylated aptamers, and the extended systemic exposure appears to facilitate distribution of aptamers to distal tissues and highly perfused organs [31]. Additionally, structural substitutions on DNA or RNA purine or pyrimidine moieties decrease susceptibility to nuclease attack and chemical degradation as well as improve pharmacokinetics [38]. **Table 1** describes the effective uses of nucleic acid base modifications to aptamers. However, a key drawback for the synthesis of integrated modifications is the requirement of a polymerase capable of adding bulky groups rather than standard wild-type T7 RNA and *Taq* polymerases with high specificity [37]. Multivariate T7 RNA polymerase can synthesize 2'-modified nucleotide triphosphate nucleic acid aptamers that include 2'-azido, 2'-*O*-methyl (A, C, and U), and 2'-fluoro pyrimidines [37, 39, 40]. Many reported modifications (see Table 1) utilize a combination of wild-type T7 polymerase and Taq polymerase. The T7 polymerase variant Y639F and the multivariate Y639F/H784A polymerase can be used in a combinatorial manner to add bulky groups that increase an aptamer's half-life *in vivo* of up to 23 hours [38, 39, 41].

B. Potential Aptamer Toxicity

Aptamer toxicity can vary in species and be altered by post sequencing modifications (Table 1). Physiologically high doses of oligonucleotides (>100μg/mL) have triggered adverse immunogenic effects in non-human rodent and primate models

[65-68]. When antisense oligonucleotides are dosed systemically in rodents, injury to the liver and kidneys is often seen as this is a major site of oligonucleotide accumulation [68, 69]. Swayze *et. al.* showed that antisense oligonucleotides (ASOs) accumulate in the liver confirmed by post-mortem liver necropsy with subsequent histopathological microscopy as well as increased serum levels of aminotransferases ALT and AST. Moreover they looked at ASOs containing either 2'-O-methyl or linked nucleic acid (LNA) modifications and found that LNA modified aptamers showed increased levels of hepatotoxicity for multiple sequences targeting three different biological targets (*Mus Amuscus* PTEN, TNFRSF1A, and apo-lipoprotein B) in additional to a mismatch control ASO with no target [69]. Multiple adverse effects have been seen with phosphorothioate modifications as well. Further continued chronic exposure to phosphorothioate modified ASOs resulted in plasma accumulation which could affect coagulation of the blood [65]. Both high and low concentrations of ASOs in the liver can cause adverse hepatic function, but individual ASOs can exhibit unique hepatotoxic potential [68, 69]. Hagedorn *et. al.* developed computer based software to evaluate and distinguishing between locked nucleic acid modified oligonucleotides with low or high potential for hepatotoxicity [70]. Slow intravenous infusions are likely to lower circulatory plasma levels decreasing accumulation versus direct injection and to reduce these effects [66]. Additionally, RNA and DNA based oligonucleotides have promoted immune-stimulatory effects through toll-like receptors 3, 7, 8, and 9 signaling [71]. Such immunological responses could result in hyperplasia in the lymph nodes, mononuclear cell infiltration, and accumulation of basophilic granules. At least with phosphorothioate modifications, granule formation is seen in kidney and liver epithelial cells that are responsible for filtration and clearance of antisense oligonucleotides and their metabolite species [67, 72-74]. However these studies utilized naked aptamers and conjugation to therapeutics or nanoparticle delivery vehicles has altered both bioavailability and toxicity profiles.

C. Aptamers as single antagonists

Aptamers alone have been shown to bind to target molecules on cell surface membranes and typically internalize into cells via canonical endocytosis pathways [20, 75]. Similar to canonical protein-protein interactions, aptamer-target molecule recognition and interaction can lead to inhibition of target molecule activity or function. Aptamer-target interactions have been shown to be sufficient to block signaling pathways important in cell proliferation, and thus identification of molecules with this property has been long recognized for their therapeutic potential [76]. It has been well established that the aptamer pegaptinib will inhibit the $VEGF_{165}$ isoform without effecting similar isoforms necessary for physiological vascularization [77]. Pegaptinib has been used to target the retina in cases of age related macular degeneration where $VEGF_{165}$ is elevated under hypoxic conditions [77, 78]. Given the high prevalence of VEGF activation in multiple tumor types, this approach could be explored in combination with current front-line chemotherapeutics for cancer treatment [79].

Similar paradigms have been used to study aptamers that target additional signal transduction pathways. The Axl tyrosine kinase receptor has been recognized as a potential anti-tumor therapeutic target for the last decade [80, 81]; several small molecule and protein inhibitors and an anti-Axl monoclonal antibody have been described [82-84]. The aptamer GL21.T binds to Axl and inhibits phosphorylation of Erk and Akt downstream targets, inhibits cell migration and invasion, and reduces tumor growth in an

in vivo xenograft lung tumor model [85]. PDGFR□ tyrosine kinase receptor is overexpressed in multiple tumor types including glioma [86, 87]. The same group that identified GL21.T now reports an aptamer Gint4.T selectively binds to PDGFR□ but not other tyrosine kinases. Aptamer Gint4.T inhibits dimerization and ligand dependent signaling, inhibits cell migration and proliferation, induces differentiation, and reduces tumor growth in an *in vivo* xenograft glioblastoma tumor model [88]. The anti-C5 aptamer ARC1905 is a potent inhibitor of factor C5 of the complement cascade, and inhibition of this signaling pathway prevents the formation of pro-inflammatory fragments inhibiting the release of angiogenic stimulating molecules [89].

D. Aptamer-based Photodynamic Therapy

Photodynamic therapy (PDT) uses a photosensitizer or photosensitizing agent that, after injection, is exposed to a specific wavelength of light to produce a form of oxygen that kills nearby cells. PDT is currently available for prostate, breast, and esophageal cancers [77, 90-94]. Newer models linking PDT to aptamers for targeting are being explored in translational studies. Aptamer TD05 was identified using SELEX targeting the Burkitt's lymphoma Ramos cell line [95] then conjugated to the photosensitizer reagent chlorin e_6 (Ce_6) to create an aptamer-photosensitizer conjugate (APS) [96]. When this APS was incubated with target Ramos cells and followed by light irradiation, >70% of cells exhibited cell death as determined by propidium iodide incorporation, and overall 50-60% more cell death in target cells was observed when compared to four control cell lines (CEM, T-cell leukemia; K562, human bone marrow; NB4, human acute promyelocytic leukemia; HL60, promyelocytic leukemia). Randomly generated aptamers conjugated to Ce_6 photosensitizer exhibited little to no cell death in target cells showing both the efficacy and the high specificity of the complex [96]. Similarly, the nucleolin targeting guanine-rich aptamer AS1411 has been conjugated to six molecules of the cationic porphyrin TmPyP4 that intercalates into the G-quadruplex structures of AS1411 [97, 98]. When MCF7 breast cancer cells were incubated with AS1411-TmPyP4 complexes, an average of 30% more cell death was observed as compared to incubation with TmPyP4 alone. Similar results have been obtained with systems that utilize MUC-1 aptamers for targeting of epithelial cancer cells, aptamer R13 for targeting lung carcinoma, and protein kinase 7 (PTK7) aptamer sgc8 for targeting T-ALL [97, 99-101]. Also, Han et al. have developed a novel aptamer-based DNA nanocircuit which not only targets Ramos cells but demonstrates an amplified photodynamic therapeutic effect [102].

E. Aptamer-based anti-viral therapies

Aptamer-target molecule recognition and inhibition of target activity has been exploited in anti-viral therapies [103-105]. In at least one model system, aptamer-virus interactions act at the initial infection step and potentially inhibit mechanisms necessary for virus internalization [106]. Human papillomavirus (HPV) is linked to high incidence of cervical cancer worldwide as well as multiple other neoplastic diseases [107]. More aggressive types of HPV, such as HPV-16, express the E6 and E7 oncoproteins that degrade the tumor suppressor p53 and disrupt cell cycle checkpoints by destabilizing phosphorylated Rb [108]. Several other groupsm have isolated aptamers that internalize into cells and bind to the E7 oncoprotein as well [107-110]. 2'-fluoro modified aptamer A2 showed affinity for the N-terminal residues of E7, a reduction in E7 and pRb interactions, and increased cell mediated apoptosis of human epithelial cells [108, 110].

Additionally, Gourronc *et. al.* isolated aptamers that demonstrated variable rates of internalization when incubated with E6/E7 HPV-16 transformed human tonsillar epithelial cells (HTECs) as compared to internalization into primary HTECs [107].

F. Aptamer-drug conjugates

Not all aptamer-target molecule interactions are inhibitory. Direct conjugation of aptamers to chemotherapeutic compounds through chemically labile linkers or self-assembly DNA drug nano-structures facilitate internalization into specific tumor cells [20, 75, 111]. Aptamer A10 recognizing prostate-specific membrane antigen (PMSA) conjugated to epirubicin [112, 113] led to increased cellular internalization and cell toxicity when administered *in vitro* to LNCaP ($PMSA^+$) cells as compared to PC3 ($PMSA^-$) cells [113]. The PTK7 T-ALL (T-cell acute lymphoblastic leukemia) aptamer sgc8c has been covalently conjugated to doxorubicin or daunorubicin via a functional thiol group at the 5' terminus [75, 114]. The bond between aptamer and drug is mediated by a hydrazone linker that has a nucleophilic attraction for the terminal carbonyl on the doxorubicin molecule [75], and the hydrazone linker promotes release of the drug in the acidic conditions of an internalized vesicle [115]. Aptamer sgc8c-doxorubicin conjugates were as effective as doxorubicin alone demonstrating approximately 80% cell death in CCRF-CEM T-ALL cell line within 48 hours post-exposure. Moreover, incubation with a randomly synthesized aptamer-doxorubicin complex prevented internalization and demonstrated less than 25% toxicity [75]. Similarly, doxorubicin has been conjugated to aptamers HB5 for breast cancer, EpCAM for retinoblastoma, TSL11 for liver cancer, and MA3 against MUC-1 for lung and breast cancers [116-119]. However, it should be noted that thus far all of these have only been tested in cell lines.

IV. Nanoparticles as targeted delivery modalities for cancer

A. Nanoparticle formulation

Nanoparticles can be manufactured from organic or inorganic materials with sizes ranging from 10-200 nm in length and/or diameter. The relatively small size of nanoparticles makes them optimal delivery vehicles as they can be phagocytosed by the cell through clathirin-mediated endocytosis and fluid phase pinocytosis [120, 121]. Nanoparticles are formulated from a variety of materials into a wide range of structures including lipid-based liposomes, polymer-based particles or micelles, poly-amido-amine dendrimers, silica-based particles, carbon-based nanotubes, protein based nanoparticles, and metallic nanoparticles or nanotubes[122, 123]. (We will hereafter refer to all collectively as nanoparticles.) Nanoparticles are produced either by a process that involve the breakdown of larger particles through milling, or by the assembly and precipitation that allow for incorporation of multiple molecules within their cores or tailored surface functionalities [124, 125]. The use of poly (lactic-co-glycolic acid) (PLGA) polymer-based nanoparticle vehicles offers an FDA-approved biodegradable drug carrier that is metabolized by the body into monomeric subunits [121]. By contrast, carbon-, copper-, and manganese-based nanoparticles have limited solubility and have shown accumulation and toxicity *in vivo* in multiple organs.

Molecules such as chemotherapeutics, vaccines, proteins, miRNAs, anti-fungals, and inhibitors can be encapsulated within nanoparticles and delivered to target cells [120, 121, 126, 127]. Advancements have been made using nanoparticles as a means of delivering chemotherapeutics such as Paclitaxel, docetaxel, cisplatin, doxorubicin, or

radiotherapeutics to specific cell populations [101, 128, 129]. Nanoparticles that contain chemotherapeutics demonstrate consistently increased accumulation within tumors over free drug [15, 130-135] and also increase biodistribution to both primary tumors and distant metastatic sites, increase bioavailability of hydrophobic agents and maximum tolerated doses [99, 124, 136]. Depending on the type of monomeric subunits used to form the nanoparticle, polymer encapsulation of chemotherapeutics can help to (1) solubilize otherwise insoluble compounds, (2) minimize physiological drug degradation, (3) increase blood circulation half-life, (4) prolong systemic activity by reducing physiological secretion by the kidneys, and (5) prevent recognition of therapeutic hydrophobic compounds by the reticulo-endothelial system [121, 137-139].

B. Polymeric nanoparticles

Nanoparticles derived from organic-based compounds can be used in a variety of biomedical and clinical settings for both imaging and delivery of molecular payloads. Polymeric nanoparticles can be constructed from a wide range of monomeric organic molecules or commercially available synthetic compounds [121] including block polymer constituents like PLGA, polystyrene (PS), and poly-ethelene-glycol (PEG) to form three dimensional amphipathic structures. Polymer and copolymers are hydrolyzed into metabolite monomers that are easily consumed by cells through normal respiratory mechanisms such as the Krebs cycle [130]. PEGylation to nanoparticle formulations further increases circulation time and bioavailability in the blood stream, and reduces renal clearance and has a well-established safety record in both clinical and commercial settings [140].

Polymer-based nanoparticles are spherical structures that range in size and can exist in a colloidal suspension [141]. Their three-dimensional amphipathic cage-like structure promotes encapsulation of most drugs and small molecules as well as solubility of hydrophobic compounds [142, 143]. Structure and size can alter pharmaceutical properties such as half-life, cellular uptake, and drug release kinetics [144]. Polymeric drug encapsulation has been used for effective treatment for malignant gliomas for almost 20 years with intraparietal placement of carmustine wafers or carmustine-loaded polymers for effective controlled drug release over time without adverse systemic effects [145, 146].

C. Silica nanoparticles

Silica is found ubiquitously in nature in both single- and multi-cellular organisms. The abundance of silanol groups within the silica matrix provides biocompatibility and promotes affinity towards phospholipids facilitating uptake by endocytosis [147-149]. Mesoporous silica and core-shell silica-based nanoparticles can be easily produced and modified to manipulate structural characteristics such as fluorescence, magnetism, surface area, controlled drug delivery, and pore size [147, 150, 151]. Uniquely, silica nanoparticles can promote slow or modulated release from their cores [152]. Modulation of pore size altered the kinetics of paclitaxel release *in vitro* that correlated with early and late (sustained) levels of apoptosis of MCF-7 (breast adenocarcinoma) cells in culture [153]. Kinetics of drug release is governed foremost by the electrostatic interactions between the drug and the silica surface while drug loading is dictated by pore and particle size [148]. Secondary stimuli such as pH, heat, light, or hydrolysis of structural scaffolding can be used to promote delayed or sustained release of bioactive materials or chemotherapeutics such as doxorubicin [152, 154-156]. Variation of material

composition within the particles can also modulate release activity; hybrid porous silica-calcium phosphate nano-composite particles were developed to demonstrate an initial burst release of 5-FU followed by sustained release of a therapeutically relevant dose (up to 32 days) and decreased tumor growth *in vivo* using a subcutaneous 4T1 breast cancer xenograft mouse model [157].

Similar to polymer-based nanoparticles, silica-based nanoparticles allow functionalization through covalent linkage of targeting molecules on their surface. Functionalization promotes solubility, prevents degradation, and increases delivery of encapsulated compounds [154, 158]. Dextran coating is associated with increased biocompatibility in mice and increased sensitivity for tumor imaging [159]. Conjugation of MUC-1 specific RNA aptamers to the surface of silica nanoparticles has been used to identify MCF-7 breast cancer cells *in vitro* [160]. A red salt crystalline reporter (RuBPY) incorporated in silica nanoparticles allows for quantification of the amount of aptamer species available on the nanoparticle surface as well as the amount of internalization into MCF-7 cells [160]. They also demonstrated a reduction in photobleaching likely due to electrostatic interactions when organic dyes are absorbed between the porous landscape of the silica core and shell [160]. Additional detection assays have utilized α-thrombin aptamers and a nucleolin aptamer conjugated to fluorescein-loaded mesoporous silica nanoparticles in MDA-MB-231 (breast adenocarcinomal) cell lines [161, 162]. In combinatory photodynamic and photothermal therapy [163, 164] a dual phototherapeutic effect was observed by near infrared irradiation of phthalocyanine, as well as 5-fold decrease in KB cell (cervical carcinoma) viability in a dose dependent manner, and a reduction in tumor burden with a 100% survival ratio in an *in vivo S180* sarcoma xenograft mouse model [164].

D. Inert metallic nanoparticles

Inert metals (gold Au, silver Ag) are used in multiple diagnostic modalities for basic biological and biomedical research including imaging, oligonucleotide delivery, detection, photodynamic therapies, biosensors, and drug encapsulation and release [165-167]. Additionally, both Au and Ag nanoparticles have been evaluated for imaging and drug delivery modalities [168-171]. Both Au and Ag nanoparticles demonstrate high permeability often showing retention at tumor sites due to the permissive and incomplete vascularization of tumors [172]. The permeability of these particles has been demonstrated *in vitro* with a model micro-vasculature membrane analogous to the blood-brain barrier. A linear progression and size dependence of Au nanoparticle permeability was demonstrated over 20 hours that could be most beneficial to patients with malignant brain tumors unable to undergo surgical tumor excision [173]. Au and Ag nanoparticles are readily linked to biomaterials, amino acids, proteins, aptamers, and short oligonucleotides through thiol and amine group linker mediators to promote both cellular internalization and potentially higher tolerated doses of therapeutics [174].

Both Au and Ag nanomaterials exhibit intrinsic anti-angiogenic properties that may be exploited in anti-tumor therapeutics [175, 176]. Au nanoparticles inhibited the heparin-binding domain of $VEGF_{165}$ in human umbilical vascular endothelial cells (HUVECs) as well as $VEGF_{165}$-induced migration and RhoA activity [177]. Similar results were obtained with Ag nanoparticles on bovine retinal endothelial cells (BRECs) and *in vivo* studies using mice and rat models implanted with VEGF+/VEGF- matrigel plugs [176]. C57BL/6 mice administered Ag nanoparticles (500nM) in matrigel plugs for

7 days exhibited no significant vascularization and demonstrated results similar to those mice administered anti-angiogenic pigment epithelium-derived factor. BRECs treated with the angiogenic stimulating compound Streptozotocin and Ag nanoparticles showed reduced AKT phosphorylation, and little to no angiogenic response when compared to Streptozotocin treatments alone. These results suggest that Ag nanoparticles themselves may mitigate multiple angiogenic and proliferative cellular pathways characteristic of malignant cells [176]. In support of this, reduction of fibroblast growth factor (FGF-2)-mediated angiogenesis has been shown in both chick chorioallontoic membrane models and in mouse matrigel models. Further, an increase in toxicity with cisplatin-loaded Au nanoparticles in both lung epithelial and colon cancer cell lines was reported [178, 179]. Recently one group has demonstrated a unique internalization mechanism whereby gold Au nanoparticles coated with an amphiphilic organic monolayer can spontaneously insert into lipid bilayers on the cell surface through hydrophobic–hydrophobic contact between the core of the bilayer and the monolayer of the Au nanoparticle dependent on the stochastic protrusion of an aliphatic lipid tail into solution [180].

Because of the increase in the commercial use of Ag, cytotoxicity of Ag exposure has been studied extensively. Ag nanomaterials exhibit many of the same properties observed with Au nanomaterials and produce minimal cytotoxicity and accumulation in respiratory and systemic organs [169, 181-184] as well as some antioxidant properties by interacting and depleting reactive oxygen species and peroxidase metabolites at the cellular level [185-187]. However, in one study, Sprague-Dawley rats highly dosed with Ag nanoparticles (~20μg/m^3) showed both respiratory and renal accumulation while rats receiving 0.04μg/m^3 showed no adverse effects [182]. Results may be governed by specific preparation, particle surface modulations, and even sex differences [173, 188-190]. Sub-chronic inhalation of Au nanoparticles in Sprague-Dawley rats showed that both females and males accumulated NPs (diameter 4-5nm) in lungs in a dose dependent manner, accompanied by tissue histological changes, macrophage infiltrate, and inflammatory response, but accumulation in the kidneys only in females [182]. Au nanoparticles, at least, demonstrate a size-dependence on physiochemical properties. In lung cancer tumor cell lines A549 and 95D cells, incubation with 10nm Au nanoparticles promoted endocytosis and growth inhibition. However, despite the growth inhibition, cell invasion increased and correlated with increased expression of matrix metalloprotease-9 and intercellular adhesion molecule-1 [191]. By contrast, larger particles of 20nm and 40nm did not promote invasion pointing to the need for intensive pre-clinical testing [191].

V. Aptamer-Nanoparticle Conjugates: "Smart Bombs" and Translation to Bedside

A. Aptamer-nanoparticle conjugates show preclinical promise

By themselves, internalization of nanoparticles into target tumor cells depends largely on passive targeting that is based on the enhanced permeability and retention effect that is dependent on leaky vasculature or dysfunctional lymphatic drainage characteristic of tumors [101, 192]. Similar to small molecules, antibodies, and antigen-binding fragments (reviewed in [27]), aptamers have been used to functionalize nanoparticle surfaces and promote active targeting to tumor cells through multiple endocytosis mechanisms. The generation of such dual-functional "smart bomb" complexes that are both loaded with anti-tumor drugs and also conjugated to aptamers

have multiple clinical advantages and their development by both basic research teams and biotechnology industry has increased in the past several years (**Table 2**) [28, 29, 193, 194]. First, such a design will preferentially, or even exclusively, target tumor cell populations. Second, such a design facilitates active rather than passive targeting with both target cell recognition and endocytosis of the complex. Third, such recognition and internalization may circumvent multidrug resistance (MDR)-based chemoresistance mechanisms [195-197]. Although density of aptamer coating on nanoparticles is central to the kinetics of cell binding and internalization, ratios need to be optimized for each model system. It has been demonstrated in at least one report that with a polymer-based system, excessive linkage of aptamers to the nanoparticle surface may mask PEG composition, thus altering surface charge and decreasing tumor cell uptake [194, 198].

Several groups have reported using aptamers to target nanoparticles to cells while also controlling release kinetics of therapeutics through "gating" whereby short ssDNA that forms hairpin structures prevent the release of the encapsulated biomolecule, and presence of complementary ssDNA sequences or binding molecules present inside target cells remove the hairpin structure and permit biomolecule release. In one such study, treatment with camptothecin-loaded nanoparticles gated by an ATP-specific aptamer showed a 40% higher incidence of cell death in MDA-MB-231 (breast adenocarcinoma) cell lines as compared to a fibrocystic normal MCF-10a cell line [207]. The higher incidence of cell death was attributrf to the higher metabolic synthesis of ATP in the cancerous cells [207]. Porous nanoparticles may be gated by strongly-bound biomolecules within the pores. One group gated mesoporous silica nanoparticle pores with desthiobiotin-avidin molecules. While T-ALL (T-cell acute lymphoblastic leukemia) aptamer sgc8c conjugated to their surface promoted interaction and internalization into PTK7 expressing CEM cells (acute lymphoblastic leukemia), the subsequent cytosolic interaction of desthiobiotin-avidin with vitamin H, a hallmark of some tumor types, ungated the pores to allow release of encapsulated doxorubicin [202]. In a similar approach to controlled release, folic acid-conjugated mesoporous silica nanoparticles containing the photosensitizing agent TmPyP4, "capped" the TmPyP4 molecules through interactions with a G-quadruplex DNA species [216]. The folic acid promoted tumor targeting to folate receptors that are commonly overexpressed on the surface of multiple tumor cell types [217-220]. After internalization, light irradiation generated reactive oxygen species that caused cleavage of the DNA cap and release and activation of TmPyP4 to facilitate cell killing in HepG2 liver cancer cell line as compared to folate receptor-deficient murine 3T3 cells [216]. Other groups using temperature and affinity modifications have demonstrated *in vitro* controlled release of neomycin from multiple aptamer-conjugated Au nanoparticles, suggesting that these too could be utilized in therapeutic strategies [170]. Due to the plasmonic resonance and low quantum yield of Au, optical illumination will promote highly efficient conversion of photon energy into heat. Exploiting this property, Au nanoparticles conjugated to both the T-ALL (T-cell acute lymphoblastic leukemia) PTK7 aptamer sgc8c and doxorubicin demonstrated efficient internalization into the CCRF-CEM T-ALL (T-cell acute lymphoblastic leukemia) cell line [171]. Further treatment with a continuous 532 nm wave laser stimulated release of doxorubicin into cells and increased cell killing [171].

Similar to the traditional combination therapies using chemotherapeutics, combinatorial approaches with nanoparticle delivery have shown to be more effective

particularly against late stage or chemoresistant tumors [221-223]. Given that standard cancer treatment regimens include combination therapy, an advantage of nanoparticles as delivery vehicles is that individual cores can encapsulate multiple therapeutic compounds for ensured simultaneous delivery to an individual target cell [213]. One group reported synthesis of polymer nanoparticles that carry precise molar ratios of doxorubicin, camptothecin, and cisplatin. Additionally, the design of the nanoparticle allowed for the photo-triggered release of all three drugs from the polymer vehicle [224]. These particles showed effective internalization into OVCAR3 (ovarian adenocarcinoma) tumor cells and significantly increased cytotoxicity following 365 nm UV light exposure [224]. In a second study, PSMA specific aptamers were conjugated to polyethyeneimine-PEG nanoparticles to deliver both doxorubicin and Bcl-xL shRNA to an LNCaP (prostate adenocarcinoma) PSMA upregulated cell line [215]. Combination therapy with nanoparticles loaded with both doxorubicin and Bcl-xL shRNA was 60% more cytotoxic than either treatment with doxorubicin alone or with nanoparticles with encapsulated Bcl-xL shRNA alone [215]. In addition the co-delivery of both compounds had a synergistic cytotoxic effect when compared to LNCaP cells treated with a mixture of doxorubicin and shRNA polyethyeneimine -PEG nanoparticles simultaneously [215]. Additionally, Au nanoparticles have been used to show potential for gene regulation when their surface is labeled with anti-sense oligonucleotides show to knockdown endogenous EGFP in C166 (murine endothelial) cells [225], [226]. Similar methodology was used to inhibit luciferase activity in HeLa (cervical adenocarcinoma) cells [227] and there is a continued effort to develop DNA based nano-structures to regulated gene expression [228, 229]

B. Clinical Trials: Aptamers as Agents but No "Smart Bomb" Testing Yet

Despite the large amount of promising initial data (see Table 2), the move from benchtop to bedside with aptamer-directed anti-cancer therapies has been slow. Aptamer-nanoparticle conjugates either alone or as "smart bombs" loaded with chemotherapeutics have not yet reached phased clinical trial stages of development [194]. However aptamers as single antagonists and various chemotherapeutic-loaded nanoparticle formulations have been clinically tested.

To date there have been 27 clinical trials that utilize aptamers as single antagonists, although the majority of these do not target cancer but rather utilize pegaptanib and E10030 to inhibit $VEGF_{165}$ in age related macular degeneration and related diseases [63, 230, 231]. Four studies determining the efficacy of single aptamer therapies for cancer-related malignancies were completed in the last eight years, one with EYE001and three with AS1411. PEGylated aptamer EYE001 has high affinity toward isoforms of VEGF, and the genetic mutation found in Hippel-Lindau (VHL) disease up-regulates the production of VEGF. An open label phase I study concluded in 2008 piloted the use of anti-VEGF therapy (EYE001) in 5 patients as a treatment for retinal angioma associated with late stage VHL (NCT00056199). The nucleolin AS1411 aptamer [232] readily internalizes into cells, and is believed to have intrinsic pro-apoptotic properties at least in part through disruption of Bcl-2 mRNA transcripts, as demonstrated in breast cancer cell lines MCF-7 & MDA-MB-231 [98]. A phase I trial (NCT00881244) of patients with nonspecific advanced solid tumors determined tolerable dosage profiles and pharmacokinetics followed by a single arm phase II trial (NCT00740441) as a neoadjuvant therapy in patients suffering from metastatic renal cell carcinoma (MRCC), as well as an open-label randomized controlled dose escalating

phase II trial (NCT00512083) as an adjuvant therapy in combination with cytarabine in patients with primary refractory or relapsed AML (acute myeloid leukemia). Subsequent additional arms of the trial were granted concerning patients with AML between the years 2009 to 2011 but were terminated (NCT01034410). Unfortunately no study results have been posted for any of the completed trials but the continued progression of aptamer development and the push toward aptamers as primary treatments is encouraging.

C. Clinical Trials: Nanoparticles as Delivery Agents for Anti-Cancer Therapy

Currently nearly 300 clinical trials deliver chemotherapeutic or alternative cytotoxic payload encapsulated by nanoparticles to patients with solid tumors and recurring malignancies (*clinicaltrials.gov*). The majority of ongoing trials utilize paclitaxel-loaded micelles (nab-paclitaxel, ABI-007) composed of a negatively charged albumin shell which creates both an amphipathic surface to promote cell interaction as well as a hydrophobic core which promotes solubility of lipophilic paclitaxel and reduces cytotoxic allergic reactions [233]. Adjuvant nab-paclitaxel has been investigated as a treatment for pancreatic, breast, ovarian, melanoma, peritoneal, lung, bladder, gastric, and esophageal cancers.

Other formulations include: (i) paclitaxel-loaded PEG-polyaspartate copolymers (NK105) [234] that are currently in a multi-national phase III clinical study comparing NK105 versus Paclitaxel in patients with metastatic or recurrent breast cancer malignancies (NCT01644890); (ii) Rapamycin-loaded albumin-based micelles (nab-rapamycin) structurally identical to nab-paclitaxel were used in a phase I trial for advanced non-hematologic malignancies (NCT00635284); (iii) an active phase II trial with docetaxel-loaded polystyrene nanoparticles (BIND-014) used in patients with non-small cell lung carcinoma (NSCLC, NCT02283320); (iv) campothecin loaded cyclodextrin polymeric nanoparticles (CRLX101, C-VISA BikDD) were used in a completed phase II trial in patients with advanced metastatic NSCLC (NCT01380769), and two currently recruiting phase I/II trials in combination with Bevacizumab for recurrent ovarian and peritoneal cancer (NCT01652079) or in combination with Capecitabine for rectal cancer (NCT02010567); (v) campothecin semisynthetic analogue irinotecan hydrochloride has been loaded into nanoliposomes (nl cpt-11) and albumin nanoparticle (FOLFIRABAX) used in phase I (NCT00734682) or I/II trials (NCT02333188) respectively in patients with multiple malignant disorders; and finally (iv) an alternative approach using direct linkage of Au nanoparticles to platinum-based oxaliplatin and PEGylated-TNF allowed higher tolerated doses and possibly treatment efficacy in a phase I trial [235].

The incorporation of gene therapy plasmids or small interfering RNA (siRNA) into lipid-based nanoparticles for anti-tumor targeting has become one of the more promising areas of translational development. The anti-cyclin G1 gene construct (Rexin-G) in a stable lipid particle suspension had promising results in both phase I and phase II trials for breast (NCT00505271), soft tissue sarcoma (NCT00505713), osteosarcoma (NCT00572130), and pancreatic cancer (NCT00504998) but no results have been reported. Despite this success, anti-cyclin G1 Rexin-G is a paradigm in the length of time to bring new therapeutics to bedside. Cyclin G1 was identified more than a decade ago, followed by laboratory mouse studies, Phillipine FDA approval (2007) [52]. A similar gene therapy approach with FUS1 tumor suppressor gene expression plasmid-loaded nanoparticles for lung cancer has also reached phase I trials (NCT01455389).

Incorporation of siRNA into lipid-based nanoparticles include: (i) anti-myc DCR-MYC currently in two phase I/II trials for patients with advanced solid tumors, multiple myeloma, lymphoma, hepatocellular carcinoma non-Hodgkins lymphoma (NCT02110563 & NCT02314052); (ii) anti-PLK1 TKM-080301 currently in phase I trials for liver tumors [236], and anti-ribonucleotide reductase CALAA-01 previously in a phase 1a/1b trial for non-specific solid malignancies that initially gave promising results with similar pharmacokinetic profiles to treatments in rat, mice, and primate models but which was subsequently terminated prematurely [209].

New experimental treatment approaches synergize the advantages between nanoparticle technology and ionizing radiation for anti-cancer therapy. Hafnium oxide nanoparticles (NBTXR3) have a high electron density enable the transfer of high dose energy to target cells following ionizing radiation treatments. The increased radio-enhancement could increase the efficacy of current radiation therapies while maintaining low exposure levels in neighboring tissues[237], [238]. A NBTXR3 intra-tumor implantation phase I trials was recently concluded in patients with soft tissue sarcomas (NCT01433068) as well as phase II trials in progress for patients with soft tissue sarcomas (NCT02379845) will ascertain the efficacy of nanoparticle-based ionizing radiation therapy.

Several nanoparticle-based technologies are in clinical trials for imaging of tumors that aid not only in early detection and diagnosis but also in direct surgical removal of malignant tissue or cells. MagProbe is a clinical tool for detection of multiple hematopoietic malignancies including acute leukemia. Phase I trials began in 2011 with an estimated enrollment of 60 patients and was concluded in December 2013 but no results have been disclosed (NCT01411904). The system utilizes ultra-small superparamagnetic iron oxide nanoparticles conjugated to a CD34 antibody [239]. The inherent magnetic property enables both a more sensitive assay for detecting minimal residual disease as well as the isolation of CD34+ malignant cells from relatively small bone marrow samples. In theory this method can be used to clear these tumor cells from patients.

VI. Future Challenges and Outlook

Since the initial description of aptamers and aptamer technology in 1990, only one aptamer has been FDA approved and is in use for therapeutics but not directed against cancer. In 2011 there were a total of nine DNA/RNA based antagonistic aptamers undergoing phase I, II, or III clinical trials [28]. Three years later in 2014, twenty-seven aptamer related clinical trials have been developed, the majority of which have been completed. In large part this slow move from translational benchtop to market reflects the anti-cancer drug model as a whole; only an estimated 0.5% - 3% of drugs tested in the laboratory eventually lead to FDA approval.

Advances in SELEX selection and screening have made the number of potential aptamers virtually limitless. However, a major challenge to SELEX is a scheme to identify aptamers that can distinguish between tumor and highly similar neighboring non-tumor cell populations of that largely share developmental ontogeny. Conversely, transformed cells within evolving tumors can be heterogeneous, and how highly specific aptamers can be effective against these tumors remains unclear. Off-target or unanticipated effects including induction of opposite effects, *e.g.* cell killing versus

migration or differences between sexes may prove to be barriers to large-scale therapeutic development without intensive pre-clincial testing. Even despite this testing, a disconnect between promising early studies and less effective clinical trial outcomes has been frustrating to the field. The nucleolin AS1411 aptamer showed excellent efficacy in laboratory studies [98, 211] and phase I clinical trial, yet phase II results were less compelling and the study was terminated.

The power of "smart bomb" delivery through the combination of nanoparticle and aptamer technologies may be thwarted by the need to bring together multiple entities with potentially competing financial and commercial interests. By contrast, single aptamer therapeutics as well as drug loaded nanoparticles have progressed to clinical trials and may come to market more quickly. Despite these challenges, the financial outlook and continued interest by the biotechnology industries remains highly positive. The achievement of pegaptanib has given the aptamer field a boost, and the aptamer market is poised to grow on par with antibodies in the next 10-15 years at an estimated growth rate of 49% [193]. The global aptamer market was valued at $236 million in 2010 and increased to $287 million in 2013 [28] and is expected to reach $2.1 billion by 2018 [193]. However, it should be noted that previous global growth estimates proved overly positive; in 2010 it was estimated the market in this year would be valued at $1.9 billion [28], but this has been adjusted to under $500 million [193]. As aptamer screening techniques and efficiency continue to be optimized, they will provide the ability to identify aptamers unique to each individual's tumor and development of personalized medicine.

Acknowledgements

We gratefully acknowledge support to C.R. from the Charlotte Research Institute, the Center for Biomedical Engineering and Sciences (University of North Carolina at Charlotte), and a Faculty Research grant (University of North Carolina at Charlotte).

References

1. Siegel, R.L., K.D. Miller, and A. Jemal, *Cancer statistics, 2015.* CA Cancer J Clin, 2015. **65**(1): p. 5-29.
2. Kroep, J.R., *Advances in epithelial ovarian cancer therapy.* Curr Pharm Des, 2012. **18**(25): p. 3735-40.
3. Hennessy, B.T., R.L. Coleman, and M. Markman, *Ovarian cancer.* Lancet, 2009. **374**(9698): p. 1371-82.
4. Chen, A.C., et al., *Upregulation of mucin4 in ER-positive/HER2-overexpressing breast cancer xenografts with acquired resistance to endocrine and HER2-targeted therapies.* Breast Cancer Res Treat, 2012. **134**(2): p. 583-93.
5. Brody, E.N. and L. Gold, *Aptamers as therapeutic and diagnostic agents.* J Biotechnol, 2000. **74**(1): p. 5-13.
6. Datta, J., et al., *CD4+ T-helper Type 1 Cytokines and Trastuzumab Facilitate CD8+ T-cell Targeting of HER-2/neu-expressing Cancers.* Cancer Immunol Res, 2015.
7. Meyer, C., U. Hahn, and A. Rentmeister, *Cell-specific aptamers as emerging therapeutics.* J Nucleic Acids, 2011. **2011**: p. 904750.

8. Dausse, E., S. Da Rocha Gomes, and J.J. Toulme, *Aptamers: a new class of oligonucleotides in the drug discovery pipeline?* Curr Opin Pharmacol, 2009. **9**(5): p. 602-7.
9. Jayasena, S.D., *Aptamers: an emerging class of molecules that rival antibodies in diagnostics.* Clin Chem, 1999. **45**(9): p. 1628-50.
10. Sharma, A., N. Jain, and R. Sareen, *Nanocarriers for diagnosis and targeting of breast cancer.* Biomed Res Int, 2013. **2013**: p. 960821.
11. Hu, M. and K. Zhang, *The application of aptamers in cancer research: an up-to-date review.* Future Oncol, 2013. **9**(3): p. 369-76.
12. Petros, R.A. and J.M. DeSimone, *Strategies in the design of nanoparticles for therapeutic applications.* Nat Rev Drug Discov, 2010. **9**(8): p. 615-27.
13. Muthu, M.S., et al., *Nanotheranostics - application and further development of nanomedicine strategies for advanced theranostics.* Theranostics, 2014. **4**(6): p. 660-77.
14. Fang, X. and W. Tan, *Aptamers generated from cell-SELEX for molecular medicine: a chemical biology approach.* Acc Chem Res, 2010. **43**(1): p. 48-57.
15. McKeague, M. and M.C. Derosa, *Challenges and opportunities for small molecule aptamer development.* J Nucleic Acids, 2012. **2012**: p. 748913.
16. Tuerk, C. and L. Gold, *Systematic evolution of ligands by exponential enrichment: RNA ligands to bacteriophage T4 DNA polymerase.* Science, 1990. **249**(4968): p. 505-10.
17. Ellington, A.D. and J.W. Szostak, *In vitro selection of RNA molecules that bind specific ligands.* Nature, 1990. **346**(6287): p. 818-22.
18. Stoltenburg, R., C. Reinemann, and B. Strehlitz, *SELEX--a (r)evolutionary method to generate high-affinity nucleic acid ligands.* Biomol Eng, 2007. **24**(4): p. 381-403.
19. Ara, M.N., et al., *Development of a Novel DNA Aptamer Ligand Targeting to Primary Cultured Tumor Endothelial Cells by a Cell-Based SELEX Method.* PLoS One, 2012. **7**(12): p. e50174.
20. Xiao, Z., et al., *Cell-specific internalization study of an aptamer from whole cell selection.* Chemistry, 2008. **14**(6): p. 1769-75.
21. Xiao, Z., et al., *Engineering of targeted nanoparticles for cancer therapy using internalizing aptamers isolated by cell-uptake selection.* ACS Nano, 2012. **6**(1): p. 696-704.
22. Van Simaeys, D., et al., *Study of the molecular recognition of aptamers selected through ovarian cancer cell-SELEX.* PLoS One, 2010. **5**(11): p. e13770.
23. Daniels, D.A., et al., *A tenascin-C aptamer identified by tumor cell SELEX: systematic evolution of ligands by exponential enrichment.* Proc Natl Acad Sci U S A, 2003. **100**(26): p. 15416-21.
24. Tatarinova, O., et al., *Comparison of the 'chemical' and 'structural' approaches to the optimization of the thrombin-binding aptamer.* PLoS One, 2014. **9**(2): p. e89383.
25. Chushak, Y. and M.O. Stone, *In silico selection of RNA aptamers.* Nucleic Acids Res, 2009. **37**(12): p. e87.
26. Zhu, G., et al., *Nucleic acid aptamers: an emerging frontier in cancer therapy.* Chem Commun (Camb), 2012. **48**(85): p. 10472-80.

27. Bazak, R., et al., *Cancer active targeting by nanoparticles: a comprehensive review of literature.* J Cancer Res Clin Oncol, 2014.
28. Esposito, C.L., et al., *New insight into clinical development of nucleic acid aptamers.* Discov Med, 2011. **11**(61): p. 487-96.
29. Zhu, J., et al., *Progress in Aptamer-Mediated Drug Delivery Vehicles for Cancer Targeting and Its Implications in Addressing Chemotherapeutic Challenges.* Theranostics, 2014. **4**(9): p. 931-944.
30. Shum, K.T., J. Zhou, and J.J. Rossi, *Nucleic Acid Aptamers as Potential Therapeutic and Diagnostic Agents for Lymphoma.* J Cancer Ther, 2013. **4**(4): p. 872-890.
31. Healy, J.M., et al., *Pharmacokinetics and biodistribution of novel aptamer compositions.* Pharm Res, 2004. **21**(12): p. 2234-46.
32. Kanwar, J.R., K. Roy, and R.K. Kanwar, *Chimeric aptamers in cancer cell-targeted drug delivery.* Crit Rev Biochem Mol Biol, 2011. **46**(6): p. 459-77.
33. Lee, J.H., et al., *Molecular diagnostic and drug delivery agents based on aptamer-nanomaterial conjugates.* Adv Drug Deliv Rev, 2010. **62**(6): p. 592-605.
34. Tan, W., et al., *Molecular aptamers for drug delivery.* Trends Biotechnol, 2011. **29**(12): p. 634-40.
35. Zhang, Y., H. Hong, and W. Cai, *Tumor-targeted drug delivery with aptamers.* Curr Med Chem, 2011. **18**(27): p. 4185-94.
36. Talekar, M., et al., *Targeting of nanoparticles in cancer: drug delivery and diagnostics.* Anticancer Drugs, 2011. **22**(10): p. 949-62.
37. Keefe, A.D. and S.T. Cload, *SELEX with modified nucleotides.* Curr Opin Chem Biol, 2008. **12**(4): p. 448-56.
38. Burmeister, P.E., et al., *Direct in vitro selection of a 2'-O-methyl aptamer to VEGF.* Chem Biol, 2005. **12**(1): p. 25-33.
39. Chelliserrykattil, J. and A.D. Ellington, *Evolution of a T7 RNA polymerase variant that transcribes 2'-O-methyl RNA.* Nat Biotechnol, 2004. **22**(9): p. 1155-60.
40. Fa, M., et al., *Expanding the substrate repertoire of a DNA polymerase by directed evolution.* J Am Chem Soc, 2004. **126**(6): p. 1748-54.
41. Sousa, R. and R. Padilla, *A mutant T7 RNA polymerase as a DNA polymerase.* EMBO J, 1995. **14**(18): p. 4609-21.
42. Jellinek, D., et al., *Potent 2'-amino-2'-deoxypyrimidine RNA inhibitors of basic fibroblast growth factor.* Biochemistry, 1995. **34**(36): p. 11363-72.
43. Lin, Y., et al., *High-affinity and specific recognition of human thyroid stimulating hormone (hTSH) by in vitro-selected 2'-amino-modified RNA.* Nucleic Acids Res, 1996. **24**(17): p. 3407-14.
44. Proske, D., et al., *Prion-protein-specific aptamer reduces PrPSc formation.* Chembiochem, 2002. **3**(8): p. 717-25.
45. Lin, Y., et al., *Modified RNA sequence pools for in vitro selection.* Nucleic Acids Res, 1994. **22**(24): p. 5229-34.
46. Kato, Y., et al., *New NTP analogs: the synthesis of 4'-thioUTP and 4'-thioCTP and their utility for SELEX.* Nucleic Acids Res, 2005. **33**(9): p. 2942-51.
47. Kang, J., et al., *Combinatorial selection of a single stranded DNA thioaptamer targeting TGF-beta1 protein.* Bioorg Med Chem Lett, 2008. **18**(6): p. 1835-9.

48. Weiss, S., et al., *RNA aptamers specifically interact with the prion protein PrP.* J Virol, 1997. **71**(11): p. 8790-7.
49. Porter, K.W., J.D. Briley, and B.R. Shaw, *Direct PCR sequencing with boronated nucleotides.* Nucleic Acids Res, 1997. **25**(8): p. 1611-7.
50. Chakravarthy, U., et al., *Year 2 efficacy results of 2 randomized controlled clinical trials of pegaptanib for neovascular age-related macular degeneration.* Ophthalmology, 2006. **113**(9): p. 1508 e1-25.
51. Obubuafo, A., et al., *Poly(methyl methacrylate) microchip affinity capillary gel electrophoresis of aptamer-protein complexes for the analysis of thrombin in plasma.* Electrophoresis, 2008. **29**(16): p. 3436-3445.
52. Gordon, E.M. and F.L. Hall, *Rexin-G, a targeted genetic medicine for cancer.* Expert Opin Biol Ther, 2010. **10**(5): p. 819-32.
53. He, K., et al., *Synthesis of 5-substituted 2'-deoxycytidine 5'-(alpha-P-borano)triphosphates, their incorporationinto DNA and effects on exonuclease.* Nucleic Acids Res, 1999. **27**(8): p. 1788-94.
54. Masud, M.M., et al., *Sialyllactose-binding modified DNA aptamer bearing additional functionality by SELEX.* Bioorg Med Chem, 2004. **12**(5): p. 1111-20.
55. Kuwahara, M. and N. Sugimoto, *Molecular evolution of functional nucleic acids with chemical modifications.* Molecules, 2010. **15**(8): p. 5423-44.
56. Jensen, T.B., et al., *Synthesis and Structural Characterization of 2 '-Fluoro-alpha-L-RNA-Modified Oligonucleotides.* Chembiochem, 2011. **12**(12): p. 1903-1910.
57. Layzer, J.M., et al., *In vivo activity of nuclease-resistant siRNAs.* RNA, 2004. **10**(5): p. 766-71.
58. Schmidt, K.S., et al., *Application of locked nucleic acids to improve aptamer in vivo stability and targeting function.* Nucleic Acids Res, 2004. **32**(19): p. 5757-65.
59. Kuwahara, M. and S. Obika, *In vitro selection of BNA (LNA) aptamers.* Artif DNA PNA XNA, 2013. **4**(2): p. 39-48.
60. Singh, S.K., R. Kumar, and J. Wengel, *Synthesis of Novel Bicyclo[2.2.1] Ribonucleosides: 2'-Amino- and 2'-Thio-LNA Monomeric Nucleosides.* J Org Chem, 1998. **63**(18): p. 6078-6079.
61. Petersen, M., et al., *Locked nucleic acid (LNA) recognition of RNA: NMR solution structures of LNA : RNA hybrids.* Journal of the American Chemical Society, 2002. **124**(21): p. 5974-5982.
62. Yang, X., et al., *Aptamers containing thymidine 3'-O-phosphorodithioates: synthesis and binding to nuclear factor-kappaB.* Bioorg Med Chem Lett, 1999. **9**(23): p. 3357-62.
63. Sundaram, P., et al., *Therapeutic RNA aptamers in clinical trials.* Eur J Pharm Sci, 2012. **48**(1-2): p. 259-271.
64. Jo, N., et al., *Inhibition of platelet-derived growth factor B signaling enhances the efficacy of anti-vascular endothelial growth factor therapy in multiple models of ocular neovascularization.* Am J Pathol, 2006. **168**(6): p. 2036-53.
65. Sheehan, J.P. and H.C. Lan, *Phosphorothioate oligonucleotides inhibit the intrinsic tenase complex.* Blood, 1998. **92**(5): p. 1617-25.

66. Farman, C.A. and D.J. Kornbrust, *Oligodeoxynucleotide studies in primates: antisense and immune stimulatory indications.* Toxicol Pathol, 2003. **31 Suppl**: p. 119-22.
67. Henry, S.P., et al., *Evaluation of the toxicity of ISIS 2302, a phosphorothioate oligonucleotide, in a four-week study in cynomolgus monkeys.* Toxicology, 1997. **120**(2): p. 145-55.
68. Frazier, K.S., *Antisense Oligonucleotide Therapies: The Promise and the Challenges from a Toxicologic Pathologist's Perspective.* Toxicol Pathol, 2015. **43**(1): p. 78-89.
69. Swayze, E.E., et al., *Antisense oligonucleotides containing locked nucleic acid improve potency but cause significant hepatotoxicity in animals.* Nucleic Acids Res, 2007. **35**(2): p. 687-700.
70. Hagedorn, P.H., et al., *Hepatotoxic potential of therapeutic oligonucleotides can be predicted from their sequence and modification pattern.* Nucleic Acid Ther, 2013. **23**(5): p. 302-10.
71. Barchet, W., et al., *Accessing the therapeutic potential of immunostimulatory nucleic acids.* Curr Opin Immunol, 2008. **20**(4): p. 389-95.
72. Bouchard, P.R., R.M. Hutabarat, and K.M. Thompson, *Discovery and development of therapeutic aptamers.* Annu Rev Pharmacol Toxicol, 2010. **50**: p. 237-57.
73. Henry, S.P., et al., *Activation of the alternative pathway of complement by a phosphorothioate oligonucleotide: potential mechanism of action.* J Pharmacol Exp Ther, 1997. **281**(2): p. 810-6.
74. Henry, S.P., D. Monteith, and A.A. Levin, *Antisense oligonucleotide inhibitors for the treatment of cancer: 2. Toxicological properties of phosphorothioate oligodeoxynucleotides.* Anticancer Drug Des, 1997. **12**(5): p. 395-408.
75. Huang, Y.F., et al., *Molecular assembly of an aptamer-drug conjugate for targeted drug delivery to tumor cells.* Chembiochem, 2009. **10**(5): p. 862-8.
76. Buerger, C. and B. Groner, *Bifunctional recombinant proteins in cancer therapy: cell penetrating peptide aptamers as inhibitors of growth factor signaling.* J Cancer Res Clin Oncol, 2003. **129**(12): p. 669-75.
77. Du, K.L., et al., *Preliminary results of interstitial motexafin lutetium-mediated PDT for prostate cancer.* Lasers Surg Med, 2006. **38**(5): p. 427-34.
78. Aiello, L.P., et al., *Vascular endothelial growth factor in ocular fluid of patients with diabetic retinopathy and other retinal disorders.* N Engl J Med, 1994. **331**(22): p. 1480-7.
79. Kieran, M.W., R. Kalluri, and Y.J. Cho, *The VEGF pathway in cancer and disease: responses, resistance, and the path forward.* Cold Spring Harb Perspect Med, 2012. **2**(12): p. a006593.
80. Linger, R.M., et al., *TAM receptor tyrosine kinases: biologic functions, signaling, and potential therapeutic targeting in human cancer.* Adv Cancer Res, 2008. **100**: p. 35-83.
81. Verma, A., et al., *Targeting Axl and Mer kinases in cancer.* Mol Cancer Ther, 2011. **10**(10): p. 1763-73.

82. Hector, A., et al., *The Axl receptor tyrosine kinase is an adverse prognostic factor and a therapeutic target in esophageal adenocarcinoma.* Cancer Biol Ther, 2010. **10**(10): p. 1009-18.
83. Holland, S.J., et al., *R428, a selective small molecule inhibitor of Axl kinase, blocks tumor spread and prolongs survival in models of metastatic breast cancer.* Cancer Res, 2010. **70**(4): p. 1544-54.
84. Ye, X., et al., *An anti-Axl monoclonal antibody attenuates xenograft tumor growth and enhances the effect of multiple anticancer therapies.* Oncogene, 2010. **29**(38): p. 5254-64.
85. Cerchia, L., et al., *Targeting Axl with an high-affinity inhibitory aptamer.* Mol Ther, 2012. **20**(12): p. 2291-303.
86. Jones, A.V. and N.C. Cross, *Oncogenic derivatives of platelet-derived growth factor receptors.* Cell Mol Life Sci, 2004. **61**(23): p. 2912-23.
87. Strand, J., et al., *Gallium-68-labeled affibody molecule for PET imaging of PDGFRbeta expression in vivo.* Mol Pharm, 2014. **11**(11): p. 3957-64.
88. Camorani, S., et al., *Inhibition of receptor signaling and of glioblastoma-derived tumor growth by a novel PDGFRbeta aptamer.* Mol Ther, 2014. **22**(4): p. 828-41.
89. Biesecker, G., et al., *Derivation of RNA aptamer inhibitors of human complement C5.* Immunopharmacology, 1999. **42**(1-3): p. 219-30.
90. Ackroyd, R., et al., *Eradication of dysplastic Barrett's oesophagus using photodynamic therapy: long-term follow-up.* Endoscopy, 2003. **35**(6): p. 496-501.
91. Cuenca, R.E., et al., *Breast cancer with chest wall progression: treatment with photodynamic therapy.* Ann Surg Oncol, 2004. **11**(3): p. 322-7.
92. Moore, C.M., M. Emberton, and S.G. Bown, *Photodynamic therapy for prostate cancer--an emerging approach for organ-confined disease.* Lasers Surg Med, 2011. **43**(7): p. 768-75.
93. Lamberti, M.J., N.B. Vittar, and V.A. Rivarola, *Breast cancer as photodynamic therapy target: Enhanced therapeutic efficiency by overview of tumor complexity.* World J Clin Oncol, 2014. **5**(5): p. 901-7.
94. Yano, T., et al., *Photodynamic therapy for esophageal cancer.* Ann Transl Med, 2014. **2**(3): p. 29.
95. Tang, Z., et al., *Selection of aptamers for molecular recognition and characterization of cancer cells.* Anal Chem, 2007. **79**(13): p. 4900-7.
96. Mallikaratchy, P., Z. Tang, and W. Tan, *Cell specific aptamer-photosensitizer conjugates as a molecular tool in photodynamic therapy.* ChemMedChem, 2008. **3**(3): p. 425-8.
97. Shieh, Y.A., et al., *Aptamer-based tumor-targeted drug delivery for photodynamic therapy.* ACS Nano, 2010. **4**(3): p. 1433-42.
98. Soundararajan, S., et al., *The nucleolin targeting aptamer AS1411 destabilizes Bcl-2 messenger RNA in human breast cancer cells.* Cancer Res, 2008. **68**(7): p. 2358-65.
99. Liu, Q., et al., *Enhanced Photodynamic Efficiency of an Aptamer-Guided Fullerene Photosensitizer toward Tumor Cells.* Chem Asian J, 2013.
100. Ferreira, C.S., et al., *Phototoxic aptamers selectively enter and kill epithelial cancer cells.* Nucleic Acids Res, 2009. **37**(3): p. 866-76.

101. Wang, K., et al., *Self-assembly of a bifunctional DNA carrier for drug delivery.* Angew Chem Int Ed Engl, 2011. **50**(27): p. 6098-101.
102. Han, D., et al., *Engineering a cell-surface aptamer circuit for targeted and amplified photodynamic cancer therapy.* ACS Nano, 2013. **7**(3): p. 2312-9.
103. Gopinath, S.C. and P.K. Kumar, *Aptamers that bind to the hemagglutinin of the recent pandemic influenza virus H1N1 and efficiently inhibit agglutination.* Acta Biomater, 2013. **9**(11): p. 8932-41.
104. Musafia, B., R. Oren-Banaroya, and S. Noiman, *Designing anti-influenza aptamers: novel quantitative structure activity relationship approach gives insights into aptamer-virus interaction.* PLoS One, 2014. **9**(5): p. e97696.
105. Binning, J.M., et al., *Development of RNA aptamers targeting Ebola virus VP35.* Biochemistry, 2013. **52**(47): p. 8406-19.
106. Liang, H.R., et al., *Isolation of ssDNA aptamers that inhibit rabies virus.* Int Immunopharmacol, 2012. **14**(3): p. 341-7.
107. Gourronc, F.A., et al., *Identification of RNA aptamers that internalize into HPV-16 E6/E7 transformed tonsillar epithelial cells.* Virology, 2013. **446**(1-2): p. 325-33.
108. Nicol, C., et al., *An RNA aptamer provides a novel approach for the induction of apoptosis by targeting the HPV16 E7 oncoprotein.* PLoS One, 2013. **8**(5): p. e64781.
109. Toscano-Garibay, J.D., M.L. Benitez-Hess, and L.M. Alvarez-Salas, *Isolation and characterization of an RNA aptamer for the HPV-16 E7 oncoprotein.* Arch Med Res, 2011. **42**(2): p. 88-96.
110. Nicol, C., et al., *Effects of single nucleotide changes on the binding and activity of RNA aptamers to human papillomavirus 16 E7 oncoprotein.* Biochem Biophys Res Commun, 2011. **405**(3): p. 417-21.
111. Zhu, G., et al., *Self-assembled aptamer-based drug carriers for bispecific cytotoxicity to cancer cells.* Chem Asian J, 2012. **7**(7): p. 1630-6.
112. Lupold, S.E., et al., *Identification and characterization of nuclease-stabilized RNA molecules that bind human prostate cancer cells via the prostate-specific membrane antigen.* Cancer Res, 2002. **62**(14): p. 4029-33.
113. Taghdisi, S.M., et al., *Targeted delivery of Epirubicin to cancer cells by PEGylated A10 aptamer.* J Drug Target, 2013.
114. Taghdisi, S.M., et al., *Targeted delivery of daunorubicin to T-cell acute lymphoblastic leukemia by aptamer.* J Drug Target, 2010. **18**(4): p. 277-81.
115. Willner, D., et al., *(6-Maleimidocaproyl)hydrazone of doxorubicin--a new derivative for the preparation of immunoconjugates of doxorubicin.* Bioconjug Chem, 1993. **4**(6): p. 521-7.
116. Meng, L., et al., *Targeted delivery of chemotherapy agents using a liver cancer-specific aptamer.* PLoS One, 2012. **7**(4): p. e33434.
117. Subramanian, N., et al., *Target-specific delivery of doxorubicin to retinoblastoma using epithelial cell adhesion molecule aptamer.* Mol Vis, 2012. **18**: p. 2783-95.
118. Liu, Z., et al., *Novel HER2 aptamer selectively delivers cytotoxic drug to HER2-positive breast cancer cells in vitro.* J Transl Med, 2012. **10**: p. 148.
119. Hu, Y., et al., *Novel MUC1 aptamer selectively delivers cytotoxic agent to cancer cells in vitro.* PLoS One, 2012. **7**(2): p. e31970.

120. Vasir, J.K. and V. Labhasetwar, *Biodegradable nanoparticles for cytosolic delivery of therapeutics.* Adv Drug Deliv Rev, 2007. **59**(8): p. 718-28.
121. Danhier, F., et al., *PLGA-based nanoparticles: an overview of biomedical applications.* J Control Release, 2012. **161**(2): p. 505-22.
122. Lee, I.H., et al., *Targeted chemoimmunotherapy using drug-loaded aptamer-dendrimer bioconjugates.* J Control Release, 2011. **155**(3): p. 435-41.
123. Wang, G. and H. Uludag, *Recent developments in nanoparticle-based drug delivery and targeting systems with emphasis on protein-based nanoparticles.* Expert Opin Drug Deliv, 2008. **5**(5): p. 499-515.
124. D'Addio, S.M. and R.K. Prud'homme, *Controlling drug nanoparticle formation by rapid precipitation.* Adv Drug Deliv Rev, 2011. **63**(6): p. 417-26.
125. Letchford, K. and H. Burt, *A review of the formation and classification of amphiphilic block copolymer nanoparticulate structures: micelles, nanospheres, nanocapsules and polymersomes.* Eur J Pharm Biopharm, 2007. **65**(3): p. 259-69.
126. Smitha, S.L. and K.G. Gopchandran, *Surface enhanced Raman scattering, antibacterial and antifungal active triangular gold nanoparticles.* Spectrochim Acta A Mol Biomol Spectrosc, 2013. **102**: p. 114-9.
127. Chong, C.S., et al., *Enhancement of T helper type 1 immune responses against hepatitis B virus core antigen by PLGA nanoparticle vaccine delivery.* J Control Release, 2005. **102**(1): p. 85-99.
128. Werner, M.E., et al., *Folate-targeted nanoparticle delivery of chemo- and radiotherapeutics for the treatment of ovarian cancer peritoneal metastasis.* Biomaterials, 2011. **32**(33): p. 8548-54.
129. Dhar, S., et al., *Targeted delivery of cisplatin to prostate cancer cells by aptamer functionalized Pt(IV) prodrug-PLGA-PEG nanoparticles.* Proc Natl Acad Sci U S A, 2008. **105**(45): p. 17356-61.
130. Kumari, A., S.K. Yadav, and S.C. Yadav, *Biodegradable polymeric nanoparticles based drug delivery systems.* Colloids Surf B Biointerfaces, 2010. **75**(1): p. 1-18.
131. Koziara, J.M., et al., *In-vivo efficacy of novel paclitaxel nanoparticles in paclitaxel-resistant human colorectal tumors.* J Control Release, 2006. **112**(3): p. 312-9.
132. Rouf, M.A., et al., *Development and characterization of liposomal formulations for rapamycin delivery and investigation of their antiproliferative effect on MCF7 cells.* J Liposome Res, 2009. **19**(4): p. 322-31.
133. Gabizon, A., et al., *Prolonged circulation time and enhanced accumulation in malignant exudates of doxorubicin encapsulated in polyethylene-glycol coated liposomes.* Cancer Res, 1994. **54**(4): p. 987-92.
134. Gabizon, A., et al., *Clinical studies of liposome-encapsulated doxorubicin.* Acta Oncol, 1994. **33**(7): p. 779-86.
135. Gabizon, A.A., *Liposomal anthracyclines.* Hematol Oncol Clin North Am, 1994. **8**(2): p. 431-50.
136. Schroeder, A., et al., *Remotely activated protein-producing nanoparticles.* Nano Lett, 2012. **12**(6): p. 2685-9.
137. Yang, L., et al., *Aptamer-conjugated nanomaterials and their applications.* Adv Drug Deliv Rev, 2011. **63**(14-15): p. 1361-70.

138. Rafiyath, S.M., et al., *Comparison of safety and toxicity of liposomal doxorubicin vs. conventional anthracyclines: a meta-analysis.* Exp Hematol Oncol, 2012. **1**(1): p. 10.
139. Harris, L., et al., *Liposome-encapsulated doxorubicin compared with conventional doxorubicin in a randomized multicenter trial as first-line therapy of metastatic breast carcinoma.* Cancer, 2002. **94**(1): p. 25-36.
140. Hatakeyama, H., H. Akita, and H. Harashima, *The polyethyleneglycol dilemma: advantage and disadvantage of PEGylation of liposomes for systemic genes and nucleic acids delivery to tumors.* Biol Pharm Bull, 2013. **36**(6): p. 892-9.
141. Qaddoumi, M.G., et al., *The characteristics and mechanisms of uptake of PLGA nanoparticles in rabbit conjunctival epithelial cell layers.* Pharm Res, 2004. **21**(4): p. 641-8.
142. Gref, R., et al., *Biodegradable long-circulating polymeric nanospheres.* Science, 1994. **263**(5153): p. 1600-3.
143. Bege, N., et al., *Biodegradable poly(ethylene carbonate) nanoparticles as a promising drug delivery system with "stealth" potential.* Macromol Biosci, 2011. **11**(7): p. 897-904.
144. Feczko, T., et al., *Influence of process conditions on the mean size of PLGA nanoparticles.* Chemical Engineering and Processing, 2011. **50**(8): p. 846-853.
145. Brem, H., et al., *Placebo-controlled trial of safety and efficacy of intraoperative controlled delivery by biodegradable polymers of chemotherapy for recurrent gliomas. The Polymer-brain Tumor Treatment Group.* Lancet, 1995. **345**(8956): p. 1008-12.
146. Westphal, M., et al., *Gliadel wafer in initial surgery for malignant glioma: long-term follow-up of a multicenter controlled trial.* Acta Neurochir (Wien), 2006. **148**(3): p. 269-75; discussion 275.
147. Ran, Z., et al., *Silica composite nanoparticles containing fluorescent solid core and mesoporous shell with different thickness as drug carrier.* J Colloid Interface Sci, 2013.
148. Li, Z., et al., *Mesoporous silica nanoparticles in biomedical applications.* Chem Soc Rev, 2012. **41**(7): p. 2590-605.
149. Wu, X., M. Wu, and J.X. Zhao, *Recent Development of Silica Nanoparticles as Delivery Vectors for Cancer Imaging and Therapy.* Nanomedicine, 2013.
150. Kwon, S., et al., *Silica-based mesoporous nanoparticles for controlled drug delivery.* J Tissue Eng, 2013. **4**: p. 2041731413503357.
151. Lee, J.E., et al., *Uniform mesoporous dye-doped silica nanoparticles decorated with multiple magnetite nanocrystals for simultaneous enhanced magnetic resonance imaging, fluorescence imaging, and drug delivery.* J Am Chem Soc, 2010. **132**(2): p. 552-7.
152. Singh, N., et al., *Bioresponsive mesoporous silica nanoparticles for triggered drug release.* J Am Chem Soc, 2011. **133**(49): p. 19582-5.
153. Jia, L., et al., *In vitro and in vivo evaluation of paclitaxel-loaded mesoporous silica nanoparticles with three pore sizes.* Int J Pharm, 2013. **445**(1-2): p. 12-9.
154. Chen, C., et al., *Polyvalent nucleic acid/mesoporous silica nanoparticle conjugates: dual stimuli-responsive vehicles for intracellular drug delivery.* Angew Chem Int Ed Engl, 2011. **50**(4): p. 882-6.

155. Meng, H., et al., *Autonomous in vitro anticancer drug release from mesoporous silica nanoparticles by pH-sensitive nanovalves.* J Am Chem Soc, 2010. **132**(36): p. 12690-7.
156. Wu, C., et al., *Molecule-scale controlled-release system based on light-responsive silica nanoparticles.* Chem Commun (Camb), 2008(23): p. 2662-4.
157. El-Ghannam, A., et al., *A ceramic-based anticancer drug delivery system to treat breast cancer.* J Mater Sci Mater Med, 2010. **21**(9): p. 2701-10.
158. Chen, Z., et al., *Mesoporous silica nanoparticles with manipulated microstructures for drug delivery.* Colloids Surf B Biointerfaces, 2012. **95**: p. 274-8.
159. Park, J.H., et al., *Biodegradable luminescent porous silicon nanoparticles for in vivo applications.* Nat Mater, 2009. **8**(4): p. 331-6.
160. Cai, L., et al., *MUC-1 aptamer-conjugated dye-doped silica nanoparticles for MCF-7 cells detection.* Biomaterials, 2013. **34**(2): p. 371-81.
161. Babu, E., P.M. Mareeswaran, and S. Rajagopal, *Highly sensitive optical biosensor for thrombin based on structure switching aptamer-luminescent silica nanoparticles.* J Fluoresc, 2013. **23**(1): p. 137-46.
162. Hernandez, F.J., et al., *Targeting cancer cells with controlled release nanocapsules based on a single aptamer.* Chem Commun (Camb), 2013. **49**(13): p. 1285-7.
163. Kim, S., et al., *Organically Modified Silica Nanoparticles with Intraparticle Heavy-Atom Effect on the Encapsulated Photosensitizer for Enhanced Efficacy of Photodynamic Therapy.* J Phys Chem C Nanomater Interfaces, 2009. **113**: p. 12641-12644.
164. Peng, J., et al., *Hollow silica nanoparticles loaded with hydrophobic phthalocyanine for near-infrared photodynamic and photothermal combination therapy.* Biomaterials, 2013. **34**(32): p. 7905-12.
165. Yin, J., et al., *One-step engineering of silver nanoclusters-aptamer assemblies as luminescent labels to target tumor cells.* Nanoscale, 2012. **4**(1): p. 110-2.
166. Zhang, J.Q., et al., *A gold nanoparticles-modified aptamer beacon for urinary adenosine detection based on structure-switching/fluorescence-"turning on" mechanism.* J Pharm Biomed Anal, 2012. **70**: p. 362-8.
167. Wang, P., et al., *Hydroxylamine amplified gold nanoparticle-based aptameric system for the highly selective and sensitive detection of platelet-derived growth factor.* Talanta, 2013. **103**: p. 392-7.
168. Zhu, Y., P. Chandra, and Y.B. Shim, *Ultrasensitive and selective electrochemical diagnosis of breast cancer based on a hydrazine-Au nanoparticle-aptamer bioconjugate.* Anal Chem, 2013. **85**(2): p. 1058-64.
169. Kim, J.S., et al., *In vivo Genotoxicity of Silver Nanoparticles after 90-day Silver Nanoparticle Inhalation Exposure.* Saf Health Work, 2011. **2**(1): p. 34-8.
170. Sundaram, P., J. Wower, and M.E. Byrne, *A nanoscale drug delivery carrier using nucleic acid aptamers for extended release of therapeutic.* Nanomedicine, 2012. **8**(7): p. 1143-51.
171. Luo, Y.L., Y.S. Shiao, and Y.F. Huang, *Release of photoactivatable drugs from plasmonic nanoparticles for targeted cancer therapy.* ACS Nano, 2011. **5**(10): p. 7796-804.

172. Maeda, H., *The enhanced permeability and retention (EPR) effect in tumor vasculature: the key role of tumor-selective macromolecular drug targeting.* Adv Enzyme Regul, 2001. **41**: p. 189-207.
173. Etame, A.B., et al., *Design and potential application of PEGylated gold nanoparticles with size-dependent permeation through brain microvasculature.* Nanomedicine, 2011. **7**(6): p. 992-1000.
174. Zhou, C., et al., *Aptamer CaCO3 nanostructures: a facile, pH-responsive, specific platform for targeted anticancer theranostics.* Chem Asian J, 2015. **10**(1): p. 166-71.
175. Arvizo, R.R., et al., *Mechanism of anti-angiogenic property of gold nanoparticles: role of nanoparticle size and surface charge.* Nanomedicine, 2011. **7**(5): p. 580-7.
176. Gurunathan, S., et al., *Antiangiogenic properties of silver nanoparticles.* Biomaterials, 2009. **30**(31): p. 6341-50.
177. Mukherjee, P., et al., *Antiangiogenic properties of gold nanoparticles.* Clin Cancer Res, 2005. **11**(9): p. 3530-4.
178. Brown, S.D., et al., *Gold nanoparticles for the improved anticancer drug delivery of the active component of oxaliplatin.* J Am Chem Soc, 2010. **132**(13): p. 4678-84.
179. Kemp, M.M., et al., *Gold and silver nanoparticles conjugated with heparin derivative possess anti-angiogenesis properties.* Nanotechnology, 2009. **20**(45): p. 455104.
180. Van Lehn, R.C., Ricci, M., Silva, P.H., Andreozzi, P., Reguera, J., Voitchovsky, K., Stellacci, F., Alexander-Katz, A., *Lipid tail protrusions mediate the intsertion of nanoparticles into model cell membranes.* Nature Comm, 2014. **5**.
181. Sung, J.H., et al., *Acute inhalation toxicity of silver nanoparticles.* Toxicol Ind Health, 2011. **27**(2): p. 149-54.
182. Sung, J.H., et al., *Subchronic inhalation toxicity of gold nanoparticles.* Part Fibre Toxicol, 2011. **8**: p. 16.
183. Blaser, S.A., et al., *Estimation of cumulative aquatic exposure and risk due to silver: contribution of nano-functionalized plastics and textiles.* Sci Total Environ, 2008. **390**(2-3): p. 396-409.
184. Dreher, K.L., *Health and environmental impact of nanotechnology: toxicological assessment of manufactured nanoparticles.* Toxicol Sci, 2004. **77**(1): p. 3-5.
185. Seaton, A., et al., *Nanoparticles, human health hazard and regulation.* J R Soc Interface, 2010. **7 Suppl 1**: p. S119-29.
186. Shukla, R., et al., *Biocompatibility of gold nanoparticles and their endocytotic fate inside the cellular compartment: a microscopic overview.* Langmuir, 2005. **21**(23): p. 10644-54.
187. Du, L., et al., *Mechanism and cellular kinetic studies of the enhancement of antioxidant activity by using surface-functionalized gold nanoparticles.* Chemistry, 2013. **19**(4): p. 1281-7.
188. Chen, J., et al., *Sex differences in the toxicity of polyethylene glycol-coated gold nanoparticles in mice.* Int J Nanomedicine, 2013. **8**: p. 2409-19.
189. Khan, M.S., G.D. Vishakante, and H. Siddaramaiah, *Gold nanoparticles: A paradigm shift in biomedical applications.* Adv Colloid Interface Sci, 2013.

190. Etame, A.B., et al., *Enhanced delivery of gold nanoparticles with therapeutic potential into the brain using MRI-guided focused ultrasound.* Nanomedicine, 2012. **8**(7): p. 1133-42.
191. Liu, Z., et al., *Effects of internalized gold nanoparticles with respect to cytotoxicity and invasion activity in lung cancer cells.* PLoS One, 2014. **9**(6): p. e99175.
192. Perche, F. and V.P. Torchilin, *Recent trends in multifunctional liposomal nanocarriers for enhanced tumor targeting.* J Drug Deliv, 2013. **2013**: p. 705265.
193. Research, B. *Aptamers market--technology trend analysis by applications--therapeutics, diagnostics, biosensors, drug discovery, biomarker discovery, research applications with market landscape analysis-- global forecasts to 2018*. 2013.
194. Xiao, Z. and O.C. Farokhzad, *Aptamer-functionalized nanoparticles for medical applications: challenges and opportunities.* ACS Nano, 2012. **6**(5): p. 3670-6.
195. Prasad, P., et al., *A novel nanoparticle formulation overcomes multiple types of membrane efflux pumps in human breast cancer cells.* Drug Deliv Transl Res, 2012. **2**(2): p. 95-105.
196. Liu, M., et al., *Intracellular target delivery of 10-hydroxycamptothecin with solid lipid nanoparticles against multidrug resistance.* J Drug Target, 2015: p. 1-6.
197. Qiu, L., et al., *A cell-targeted, size-photocontrollable, nuclear-uptake nanodrug delivery system for drug-resistant cancer therapy.* Nano Lett, 2015. **15**(1): p. 457-63.
198. Verma, A. and F. Stellacci, *Effect of surface properties on nanoparticle-cell interactions.* Small, 2010. **6**(1): p. 12-21.
199. Dhar, S., et al., *Targeted delivery of a cisplatin prodrug for safer and more effective prostate cancer therapy in vivo.* Proc Natl Acad Sci U S A, 2011. **108**(5): p. 1850-5.
200. Zhang, K., et al., *A novel aptamer developed for breast cancer cell internalization.* ChemMedChem, 2012. **7**(1): p. 79-84.
201. He, X., et al., *One-pot synthesis of sustained-released doxorubicin silica nanoparticles for aptamer targeted delivery to tumor cells.* Nanoscale, 2011. **3**(7): p. 2936-42.
202. Li, L.L., et al., *A vitamin-responsive mesoporous nanocarrier with DNA aptamer-mediated cell targeting.* Chem Commun (Camb), 2013. **49**(52): p. 5823-5.
203. Jalalian, S.H., et al., *Epirubicin loaded super paramagnetic iron oxide nanoparticle-aptamer bioconjugate for combined colon cancer therapy and imaging in vivo.* Eur J Pharm Sci, 2013. **50**(2): p. 191-7.
204. Yu, C., et al., *Novel aptamer-nanoparticle bioconjugates enhances delivery of anticancer drug to MUC1-positive cancer cells in vitro.* PLoS One, 2011. **6**(9): p. e24077.
205. Guo, J., et al., *Aptamer-functionalized PEG-PLGA nanoparticles for enhanced anti-glioma drug delivery.* Biomaterials, 2011. **32**(31): p. 8010-20.
206. Aravind, A., et al., *AS1411 aptamer tagged PLGA-lecithin-PEG nanoparticles for tumor cell targeting and drug delivery.* Biotechnol Bioeng, 2012. **109**(11): p. 2920-31.

207. Zhang, Z., et al., *Biocatalytic release of an anticancer drug from nucleic-acids-capped mesoporous SiO2 Using DNA or molecular biomarkers as triggering stimuli.* ACS Nano, 2013. **7**(10): p. 8455-68.
208. Zhou, W., et al., *Aptamer-nanoparticle bioconjugates enhance intracellular delivery of vinorelbine to breast cancer cells.* J Drug Target, 2014. **22**(1): p. 57-66.
209. Zuckerman, J.E., et al., *Correlating animal and human phase Ia/Ib clinical data with CALAA-01, a targeted, polymer-based nanoparticle containing siRNA.* Proc Natl Acad Sci U S A, 2014. **111**(31): p. 11449-54.
210. Lin, Z., et al., *A novel aptamer functionalized CuInS2 quantum dots probe for daunorubicin sensing and near infrared imaging of prostate cancer cells.* Anal Chim Acta, 2014. **818**: p. 54-60.
211. Li, L., et al., *Nucleolin-targeting liposomes guided by aptamer AS1411 for the delivery of siRNA for the treatment of malignant melanomas.* Biomaterials, 2014. **35**(12): p. 3840-50.
212. Sayari, E., et al., *MUC1 aptamer conjugated to chitosan nanoparticles, an efficient targeted carrier designed for anticancer SN38 delivery.* Int J Pharm, 2014. **473**(1-2): p. 304-15.
213. Shiao, Y.S., et al., *Aptamer-Functionalized Gold Nanoparticles As Photoresponsive Nanoplatform for Co-Drug Delivery.* ACS Appl Mater Interfaces, 2014.
214. Kolishetti, N., et al., *Engineering of self-assembled nanoparticle platform for precisely controlled combination drug therapy.* Proc Natl Acad Sci U S A, 2010. **107**(42): p. 17939-44.
215. Kim, E., et al., *Prostate cancer cell death produced by the co-delivery of Bcl-xL shRNA and doxorubicin using an aptamer-conjugated polyplex.* Biomaterials, 2010. **31**(16): p. 4592-9.
216. Chen, C., et al., *Photosensitizer-incorporated quadruplex DNA-gated nanovechicles for light-triggered, targeted dual drug delivery to cancer cells.* Small, 2013. **9**(16): p. 2793-800, 2653.
217. Hattori, Y. and Y. Maitani, *Folate-linked lipid-based nanoparticle for targeted gene delivery.* Curr Drug Deliv, 2005. **2**(3): p. 243-52.
218. Pan, X. and R.J. Lee, *Tumour-selective drug delivery via folate receptor-targeted liposomes.* Expert Opin Drug Deliv, 2004. **1**(1): p. 7-17.
219. Zhao, X., H. Li, and R.J. Lee, *Targeted drug delivery via folate receptors.* Expert Opin Drug Deliv, 2008. **5**(3): p. 309-19.
220. Zuber, G., C.D. Muller, and J.P. Behr, *Targeted gene delivery to cancer cells with nanometric DNA particles enveloped with folic acid using a polymerisable anchor.* Technol Cancer Res Treat, 2005. **4**(6): p. 637-43.
221. Huang, Z., et al., *SERPINB2 down-regulation contributes to chemoresistance in head and neck cancer.* Mol Carcinog, 2014. **53**(10): p. 777-86.
222. Fassnacht, M., et al., *Combination chemotherapy in advanced adrenocortical carcinoma.* N Engl J Med, 2012. **366**(23): p. 2189-97.
223. von Mehren, M., et al., *Phase I study of the safety and pharmacokinetics of trabectedin with docetaxel in patients with advanced malignancies.* Cancer Chemother Pharmacol, 2015.

224. Liao, L., et al., *A convergent synthetic platform for single-nanoparticle combination cancer therapy: ratiometric loading and controlled release of cisplatin, doxorubicin, and camptothecin.* J Am Chem Soc, 2014. **136**(16): p. 5896-9.
225. Rosi, N.L., et al., *Oligonucleotide-modified gold nanoparticles for intracellular gene regulation.* Science, 2006. **312**(5776): p. 1027-30.
226. Young, K.L., et al., *Hollow spherical nucleic acids for intracellular gene regulation based upon biocompatible silica shells.* Nano Lett, 2012. **12**(7): p. 3867-71.
227. Giljohann, D.A., et al., *Gene regulation with polyvalent siRNA-nanoparticle conjugates.* J Am Chem Soc, 2009. **131**(6): p. 2072-3.
228. Li, J., et al., *Self-assembly of DNA nanohydrogels with controllable size and stimuli-responsive property for targeted gene regulation therapy.* J Am Chem Soc, 2015. **137**(4): p. 1412-5.
229. Peterson, A.M. and J.M. Heemstra, *Controlling self-assembly of DNA-polymer conjugates for applications in imaging and drug delivery.* Wiley Interdiscip Rev Nanomed Nanobiotechnol, 2014.
230. Gonzalez, V.H., et al., *Intravitreal injection of pegaptanib sodium for proliferative diabetic retinopathy.* Br J Ophthalmol, 2009. **93**(11): p. 1474-8.
231. Cunningham, E.T., Jr., et al., *A phase II randomized double-masked trial of pegaptanib, an anti-vascular endothelial growth factor aptamer, for diabetic macular edema.* Ophthalmology, 2005. **112**(10): p. 1747-57.
232. Ireson, C.R. and L.R. Kelland, *Discovery and development of anticancer aptamers.* Mol Cancer Ther, 2006. **5**(12): p. 2957-62.
233. Guarneri, V., M.V. Dieci, and P. Conte, *Enhancing intracellular taxane delivery: current role and perspectives of nanoparticle albumin-bound paclitaxel in the treatment of advanced breast cancer.* Expert Opin Pharmacother, 2012. **13**(3): p. 395-406.
234. Hamaguchi, T., et al., *NK105, a paclitaxel-incorporating micellar nanoparticle formulation, can extend in vivo antitumour activity and reduce the neurotoxicity of paclitaxel.* Br J Cancer, 2005. **92**(7): p. 1240-6.
235. Libutti, S.K., et al., *Phase I and pharmacokinetic studies of CYT-6091, a novel PEGylated colloidal gold-rhTNF nanomedicine.* Clin Cancer Res, 2010. **16**(24): p. 6139-49.
236. Ramanathan, R., Hamburg, S.I., Borad, M., Seetharam, M., Kundranda, M., Lee, P., Frelund, P., Gibert, M., Mast, C., Semple, S., Judge, A., Crowell, A., Vocila, L., MacLachlan, I., Northfeld, D.W., , *A phasi I dose escalation study of TKM-080301, a RNA therapeutic directed aptamer against PLK1, in patients with advanced solid tumors* in *104th Annual Meeting of the American Association of Cancer Research*. 2013, AACR: Cancer Res: Washington, D.C.
237. Pottier, A., E. Borghi, and L. Levy, *New use of metals as nanosized radioenhancers.* Anticancer Res, 2014. **34**(1): p. 443-53.
238. Maggiorella, L., et al., *Nanoscale radiotherapy with hafnium oxide nanoparticles.* Future Oncol, 2012. **8**(9): p. 1167-81.
239. Jaetao, J.E., et al., *Enhanced leukemia cell detection using a novel magnetic needle and nanoparticles.* Cancer Res, 2009. **69**(21): p. 8310-6.

APPENDIX D:
PATENT FILING RECEIPT

UNITED STATES PATENT AND TRADEMARK OFFICE

UNITED STATES DEPARTMENT OF COMMERCE
United States Patent and Trademark Office
Address: COMMISSIONER FOR PATENTS
P.O. Box 1450
Alexandria, Virginia 22313-1450
www.uspto.gov

APPLICATION NUMBER	FILING or 371(c) DATE	GRP ART UNIT	FIL FEE REC'D	ATTY.DOCKET.NO	TOT CLAIMS	IND CLAIMS
62/067,727	10/23/2014		130	2015-009PRO1		

CONFIRMATION NO. 5021

FILING RECEIPT

74923
The University of North Carolina at Charlotte
Office of Technology Transfer - 269 Grigg Hall
9201 University City Blvd.
Charlotte, NC 28223-0001

OC00000071711021

Date Mailed: 11/05/2014

Receipt is acknowledged of this provisional patent application. It will not be examined for patentability and will become abandoned not later than twelve months after its filing date. Any correspondence concerning the application must include the following identification information: the U.S. APPLICATION NUMBER, FILING DATE, NAME OF APPLICANT, and TITLE OF INVENTION. Fees transmitted by check or draft are subject to collection. Please verify the accuracy of the data presented on this receipt. **If an error is noted on this Filing Receipt, please submit a written request for a Filing Receipt Correction. Please provide a copy of this Filing Receipt with the changes noted thereon. If you received a "Notice to File Missing Parts" for this application, please submit any corrections to this Filing Receipt with your reply to the Notice. When the USPTO processes the reply to the Notice, the USPTO will generate another Filing Receipt incorporating the requested corrections**

Inventor(s)

Christine Richardson, Charlotte, NC;
Gregory Benedetto, Charlotte, NC;

Applicant(s)

Christine Richardson, Charlotte, NC;
Gregory Benedetto, Charlotte, NC;

Power of Attorney:
Bradley Fach--53855

If Required, Foreign Filing License Granted: 11/05/2014

The country code and number of your priority application, to be used for filing abroad under the Paris Convention, is **US 62/067,727**

Projected Publication Date: None, application is not eligible for pre-grant publication

Non-Publication Request: No

Early Publication Request: No
**** SMALL ENTITY ****
Title

DNA APTAMERS AGAINST CANCER AND THE USES THEREOF IN DELIVERY OF THERAPY AND DIAGNOSIS OF CANCER

Statement under 37 CFR 1.55 or 1.78 for AIA (First Inventor to File) Transition Applications: No

PROTECTING YOUR INVENTION OUTSIDE THE UNITED STATES

Since the rights granted by a U.S. patent extend only throughout the territory of the United States and have no effect in a foreign country, an inventor who wishes patent protection in another country must apply for a patent in a specific country or in regional patent offices. Applicants may wish to consider the filing of an international application under the Patent Cooperation Treaty (PCT). An international (PCT) application generally has the same effect as a regular national patent application in each PCT-member country. The PCT process **simplifies** the filing of patent applications on the same invention in member countries, but **does not result** in a grant of "an international patent" and does not eliminate the need of applicants to file additional documents and fees in countries where patent protection is desired.

Almost every country has its own patent law, and a person desiring a patent in a particular country must make an application for patent in that country in accordance with its particular laws. Since the laws of many countries differ in various respects from the patent law of the United States, applicants are advised to seek guidance from specific foreign countries to ensure that patent rights are not lost prematurely.

Applicants also are advised that in the case of inventions made in the United States, the Director of the USPTO must issue a license before applicants can apply for a patent in a foreign country. The filing of a U.S. patent application serves as a request for a foreign filing license. The application's filing receipt contains further information and guidance as to the status of applicant's license for foreign filing.

Applicants may wish to consult the USPTO booklet, "General Information Concerning Patents" (specifically, the section entitled "Treaties and Foreign Patents") for more information on timeframes and deadlines for filing foreign patent applications. The guide is available either by contacting the USPTO Contact Center at 800-786-9199, or it can be viewed on the USPTO website at http://www.uspto.gov/web/offices/pac/doc/general/index.html.

For information on preventing theft of your intellectual property (patents, trademarks and copyrights), you may wish to consult the U.S. Government website, http://www.stopfakes.gov. Part of a Department of Commerce initiative, this website includes self-help "toolkits" giving innovators guidance on how to protect intellectual property in specific countries such as China, Korea and Mexico. For questions regarding patent enforcement issues, applicants may call the U.S. Government hotline at 1-866-999-HALT (1-866-999-4258).

LICENSE FOR FOREIGN FILING UNDER

Title 35, United States Code, Section 184

Title 37, Code of Federal Regulations, 5.11 & 5.15

GRANTED

The applicant has been granted a license under 35 U.S.C. 184, if the phrase "IF REQUIRED, FOREIGN FILING LICENSE GRANTED" followed by a date appears on this form. Such licenses are issued in all applications where the conditions for issuance of a license have been met, regardless of whether or not a license may be required as set forth in 37 CFR 5.15. The scope and limitations of this license are set forth in 37 CFR 5.15(a) unless an earlier license has been issued under 37 CFR 5.15(b). The license is subject to revocation upon written notification. The date indicated is the effective date of the license, unless an earlier license of similar scope has been granted under 37 CFR 5.13 or 5.14.

This license is to be retained by the licensee and may be used at any time on or after the effective date thereof unless it is revoked. This license is automatically transferred to any related applications(s) filed under 37 CFR 1.53(d). This license is not retroactive.

The grant of a license does not in any way lessen the responsibility of a licensee for the security of the subject matter as imposed by any Government contract or the provisions of existing laws relating to espionage and the national security or the export of technical data. Licensees should apprise themselves of current regulations especially with respect to certain countries, of other agencies, particularly the Office of Defense Trade Controls, Department of State (with respect to Arms, Munitions and Implements of War (22 CFR 121-128)); the Bureau of Industry and Security, Department of Commerce (15 CFR parts 730-774); the Office of Foreign AssetsControl, Department of Treasury (31 CFR Parts 500+) and the Department of Energy.

NOT GRANTED

No license under 35 U.S.C. 184 has been granted at this time, if the phrase "IF REQUIRED, FOREIGN FILING LICENSE GRANTED" DOES NOT appear on this form. Applicant may still petition for a license under 37 CFR 5.12, if a license is desired before the expiration of 6 months from the filing date of the application. If 6 months has lapsed from the filing date of this application and the licensee has not received any indication of a secrecy order under 35 U.S.C. 181, the licensee may foreign file the application pursuant to 37 CFR 5.15(b).

SelectUSA

The United States represents the largest, most dynamic marketplace in the world and is an unparalleled location for business investment, innovation, and commercialization of new technologies. The U.S. offers tremendous resources and advantages for those who invest and manufacture goods here. Through SelectUSA, our nation works to promote and facilitate business investment. SelectUSA provides information assistance to the international investor community; serves as an ombudsman for existing and potential investors; advocates on behalf of U.S. cities, states, and regions competing for global investment; and counsels U.S. economic development organizations on investment attraction best practices. To learn more about why the United States is the best country in the world to develop technology, manufacture products, deliver services, and grow your business, visit http://www.SelectUSA.gov or call +1-202-482-6800.

APPENDIX E:
TRANSCRIPTIONAL AND PHOSPHO-PROTEOMIC SCREENS REVEAL STEM CELL ACTIVATION OF INSULIN-RESISTANCE AND TRANSFORMATION PATHWAYS FOLLOWING A SINGLE MINIMALLY TOXIC EPISODE OF ROS

Published in final edited form as:
Int J Genomics Proteomics. 2011 ; 2(1): 34–49.

TRANSCRIPTIONAL AND PHOSPHO-PROTEOMIC SCREENS REVEAL STEM CELL ACTIVATION OF INSULIN-RESISTANCE AND TRANSFORMATION PATHWAYS FOLLOWING A SINGLE MINIMALLY TOXIC EPISODE OF ROS

R. MOUZANNAR[1], **J. MCCAFFERTY**[2], **G. BENEDETTO**[1], and **C. RICHARDSON**[*,1]

[1] UNC-Charlotte, Department of Biology and Bioinformatics Research Center, Charlotte, NC 28223

[2] UNC-Charlotte, Department of Bioinformatics and Genomics, Charlotte, NC 28223

Abstract

Elevated reactive oxidative species (ROS) are cytotoxic, and chronic elevated levels of ROS have been implicated in multiple diseases as well as cellular transformation and tumor progression. However, the potential for a transient and minimally toxic episode of ROS exposure, or a minimal threshold dose of ROS, to initiate disease or cellular transformation is unclear. We examined both transcriptional and phospho-proteomic responses of murine embryonic stem (ES) cells to a single brief exposure of minimally toxic hydrogen peroxide (H_2O_2). The cellular response was distinct from those induced by either an acute exposure to H_2O_2 or the topoisomerase II poison etoposide. Analysis of tumorigenesis-related transcripts revealed a significant up-regulation of oncogenes and down-regulation of tumor suppressors. Analysis of the phospho-proteomic response demonstrated insulin-signaling induction, including insulin receptor Y972 hypophosphorylation, similar to insulin-resistance mouse models and observed in diabetic patients. In addition, ES cells were more resistant to ROS than differentiated cells, and retained their transcriptional self-renewal signature, suggesting stem cells have a higher potential for ROS-mediated mutagenesis and proliferation *in vivo*. These results are a direct demonstration that even brief and non-toxic exposures to ROS may induce transduction of insulin resistance and transformation signaling in stem cells leading to diabetes and cancer.

Keywords

reactive oxygen species; oxidative stress; DNA damage; stem cells; gene expression; microarray; proteomics; insulin; diabetes; cancer

Introduction

Reactive oxygen species (ROS) are produced by metabolizing molecular oxygen to produce hydroxyl free radicals (OH), superoxide anions ($O_2^{-\bullet}$), singlet oxygens ($^1O_2$), and hydrogen peroxide (H_2O_2). ROS are generated by endogenous reduction of oxygen, by the mitochondrial respiratory pathway, as well as by exogenous exposure to UV or environmental damaging agents [1]. Superoxides produced by NADPH oxidase activity are

[*]Corresponding author: UNC-Charlotte, 9201 University City Blvd. Woodward Bldg. Room 386B, Charlotte NC 28223, phone: (704) 687-8683, FAX: (704) 687-3128, caricha2@uncc.edu.

quickly dismutated by superoxide dismutases (SODs) to the more stable H_2O_2. ROS levels in cells are highly regulated. Increases in ROS above basal cellular concentrations lead to oxidative stress (OS) [2]. OS is thought to damage 20,000 bases per day per human cell and be one of the major causes of DNA damage and mutation [3,4].

At submicromolar concentrations, ROS act as proliferation and growth signaling molecules. Elevated levels of ROS induced by mutations of metabolic enzyme genes, ischemia/reperfusion, chemotherapy, or chronic exposure to 10–100μM H_2O_2 induce multiple effects ranging from cell cycle arrest to death, depending on the cell type [5,6]. High levels of ROS have been implicated in human diseases including cancer, diabetes, cardiac disease, neurodegeneration, and aging [4,7,8]. In support of this, high levels of OS induced by metabolic enzyme deficiency are associated with head and neck cancers as well as child T-cell leukemia [9,10]. High concentrations of H_2O_2 (3mM) can induce multiple insulin-like effects in rat adipose tissue including phosphorylation of the insulin receptor (INSR) subunit at E80 and Y20 [11]. However, the potential for a transient and minimally toxic episode of ROS exposure or what minimal threshold dose of ROS to initiate disease or cellular transformation is unclear.

Upon differentiation of embryonic stem (ES) cells, superoxide production, cellular levels of intracellular ROS, and DNA damage levels increase. At the same time, expression of major antioxidant genes and genes involved in multiple DNA repair pathways is downregulated [12], and DNA repair by homologous recombination is reduced [13]. Thus, elevated ROS may promote tumorigenesis in more differentiated somatic cells indirectly through increased illegitimate repair of the ensuing DNA damage. It is not clear how susceptible stem cells are to a single brief exposure of ROS, particularly at minimally toxic doses not expected to induce apoptosis.

A significant body of literature exists on the transcriptional response of multiple cell types to high toxic or low chronic doses of ROS [14–23] but not the impact of a single minimally toxic ROS episode. In addition, the immediate coordination of both transcriptional and post-translational responses in response to ROS is not understood. In this study we measured the immediate cellular response of mouse ES cells to a single minimally toxic episode of hydrogen peroxide (H_2O_2). The cellular response was distinct from those induced by either an acute exposure to H_2O_2 or by the topoisomerase II poison etoposide. Parallel examination of transcriptional profiles with the post-translational modifications of a significant though limited number of signaling molecules demonstrated that a single minimally toxic exposure to ROS is sufficient to induce significant increases in oncogenic and metastatic pathways and specifically induce insulin signaling, similar to insulin-resistance mouse models and observed in diabetic patients. Despite the significant signaling changes induced by ROS, cells maintained their stem cell signatures suggesting a mechanism for maintenance, survival, and transformation in early stem cell pools.

Results

Growth arrest, cytotoxicity, and DNA fragmentation

ES cells were exposed to a minimally toxic 100 M hydrogen peroxide (H_2O_2) for 15 min. Dose was chosen as H_2O_2 concentrations up to 50μM have been reported in human plasma and 100 M H_2O_2 induces ROS levels similar to those observed in ischemia/reperfusion or respiratory burst conditions [24]. Alternatively, cells were exposed to 5mM hydrogen peroxide (H_2O_2) or 20 M etoposide for 30 min. 5mM H_2O_2 induces ROS levels similar to those observed *in vivo* during acute inflammatory reactions. Etoposide is an inhibitor of the topoisomerase II religation reaction and a known inducer of DNA double-strand breaks

(DSBs). 20 M etoposide is in close agreement with pharmacokinetic studies demonstrating peak patient plasma levels [25].

As expected, ROS and DSBs induced a dose-dependent response of cell cycle arrest and cell death. Cell cycle profiles by BrdU analysis of cells exposed to all three conditions demonstrated G2 cell cycle arrest through 6 hrs post-exposure and release by 24 hrs post-exposure (data not shown). Cells exposed to etoposide demonstrated an intra-S phase arrest at early times and release by 24 hrs post-exposure. The lack of a significant G1/S arrest was expected since ES cells have a defective p53-mediated stress response [26–28]. 100μM H_2O_2 induced minimal cell death; however, doses beyond 200μM induced significant cell death by 24 hrs post-exposure (IC_{50}=5mM), relative to controls, Fig. (1A).

Pulse field gel electrophoresis along with S1 nuclease digestion confirmed ES cells had a dose-dependent ssDNA digestion of chromatin DNA that led to 0.3–1 Mb fragments, capable of inefficient religation and cell survival [29]. There was minimal ssDNA fragmentation following 100 M H_2O_2 and more significant fragmentation at higher toxic exposures, Fig. (1B). 50 kb DNA fragments were not detectable following acute 30 min exposure up to 10mM of H_2O_2. Only when ES cells were exposed to 100 M of H_2O_2 continuously for 24 hrs were 50kb DNA fragments produced, but without oligonucleosomal fragmentation, Fig. (1C).

Transcriptional response

Immediate cellular transcriptional response following a transient minimally toxic exposure to ROS was determined using Affymetrix MG-U74VerA chips and MS 5.0 and GeneSpring software comparing four samples exposed to the minimally toxic H_2O_2, five samples exposed to acute H_2O_2, and three replicate control samples. Among all conditions, 2742 transcripts were found significantly altered ($p \leq 0.05$), and, of these, 501 (433 known, 68 unknown) transcripts had a two-fold or greater change. Real-time RT-PCR results of 19 selected transcripts were concordant with microarray results. Correlation coefficient values for 16 of 19 transcripts were $r_{(100)}$=0.71 and $r_{(5)}$=0.78 for the two exposures to ROS, Table (1).

Transient exposure to a minimally toxic dose of H_2O_2 was sufficient to induce down-regulation of 185 transcripts and up-regulation of 175 transcripts. The response signature was distinct from a transient exposure to an acute dose that induced down-regulation of 114 transcripts and up-regulation of 62 transcripts. Overall, only 19 transcripts were commonly down-regulated and 12 transcripts commonly up-regulated by the two exposures (31 total; Table (2), Fig. (2B)) suggesting major differences, rather than common mechanisms, of immediate cellular response between minimally toxic and acute ROS exposure. A distinct cellular response to ROS exposures was further supported by an inverse dose effect in 11 transcripts, similar to studies in mammalian cells and yeast exposed to low or acute doses of irradiation [30,31] (Out of 360 transcripts altered following minimally toxic ROS and 176 following acute ROS, the expected false discovery rate would be 0.25%, or 2 transcripts). Four transcripts (*calml4*, *cdkn1c*, *S100a6*, *gap43*) were significantly decreased after minimally toxic ROS but increased after acute ROS, as compared to untreated samples. Conversely, seven transcripts (*phtr1*, *dab2*, *bhmt2*, *prg1*, *sox17*, *gata6* and *col4a1*) were significantly increased after the minimally toxic ROS but decreased after acute ROS, as compared to untreated samples.

Maintenance of stem cell markers

Transient minimally toxic exposure to ROS revealed no significant change in 14 of 19 common transcripts associated with stem cell populations and pluripotency including

signature transcripts *oct3/4*, *nanog* and *sox2*, Table (3) [32]. Markers specific for differentiation of ES cells upon LIF withdrawal were unchanged [33]. Three stem cell transcripts with known roles in DNA or stress response (*Mdr1/abcb1* and *ercc5* and *gpx3*) were up-regulated following a minimally toxic dose of H_2O_2, Table (3) [12,34]. Increases in SOD activity can reduce growth and malignant phenotypes of tumor cells in culture although its mechanism of action is not well understood and can be inconsistent [23,35,36]. However, in this study, ROS led to down-regulation of *sod2*, a stem cell marker identified by Sartzki *et al* [12], suggesting the promotion of growth and survival of mouse ES cells following a single minimally toxic exposure. Two transcripts (*gbx2* [37], *c-myc* [38]) were down-regulated. *Gbx2* is within the wnt pathway and not a known myc target gene ([39]; http://www.myccancergene.org/index.asp). Overall, these results suggest that pluripotent stem cell populations have the capacity to respond to ROS while retaining their major self-renewal signatures.

Oncogenic immediate transcriptional signature response

Transcriptional profiles were assessed by GO, Entrez, Locuslink, and Ingenuity Pathway Analysis (IPA) (Ingenuity® Systems, www.ingenuity.com). Pathway analysis demonstrated the minimally toxic and acute ROS stratified top significantly altered biological functions, Table (4). IPA functionally classified all altered transcripts according to tumorigenesis, DNA repair, cell growth/maintenance, development, cell cycle, and pro- or anti-apoptosis (Table 3). IPA noted a significant number of altered transcripts classified in tumorigenesis (139/360; 39%) following the single minimally toxic dose of H_2O_2, specifically a significant up-regulation of oncogenes and down-regulation of tumor suppressors, Table (4), Fig. (3). Consistent with this, IPA noted a significant up-regulation of anti-apoptotic transcripts, Fig. (3). The additional IPA classifications did not reveal significant clustering. These data indicate a nonlinear relationship and strong association between ROS dose and oncogene activation or tumor suppressor silencing, along with cell survival.

Oncogenic immediate post-translational signature response

To more completely assess the signaling pathways induced in stem cells by a transient and minimally toxic exposure to ROS, we used Kinexus® phospho-proteomic screening technology to analyze 92 phosphorylation sites covering 53 proteins in p53, Rb, p38/MAPK/ERK, NFκB, PI3K/Akt and insulin-signaling pathways, Table (5). Reproducibility was validated by detecting concordant normalized CPM values for common epitopes (Mapk1-T185+Y187, Mapk3-T202+Y204, p38Mapk-T180+Y182). Samples were exposed to 100 M H_2O_2 for 15 min, recovered in normal media for 1 hr, then harvested for analysis. Specificity of the response was determined by comparison against a 15 min exposure to 5mM H_2O_2 or 30 min exposure to 20 M etoposide. Based on an absolute cut-off of 300 normalized CPM, nearly two-thirds (52 of 92) of the epitopes had no detectable phosphorylation in either control samples or following ROS or etoposide exposure. The remaining third of epitopes (34 of 92) had a detectable baseline phosphorylation in control samples. We focused on sites that were found differentially phosphorylated by at least 25% with respect to controls. 85% (29 of 34) of these were altered one hour following exposure to either ROS or etoposide, Table (5).

Overall, stem cell response to ROS was distinct from etoposide exposure and could be stratified by dose, with a specific phosphorylation pattern induced by each. Only 5 of the 34 epitopes (15%) with baseline phosphorylation were post-translationally altered by both H_2O_2 and etoposide treatment--activating phoshorylation of CDC2 (CDK1) at T160/161 and of p38a MAPK at T180+Y182, activating dephosphorylation of the catalytic subunit of protein phosphatase 1 (PPP1CA) at T320 and of MAP2K1 (MEK1) at T291, and inhibitory phosphorylation of eIF2B5 at S539. Decreased phosphorylation of eIF2B5 would be

expected as a consequence of slowed translation in response to DNA damage and stress. These results suggest that the immediate response to DNA damage involves changes to homeostatically phosphorylated proteins in ES cells rather than phosphorylation of new ones, at least within the signaling pathways examined.

Eight epitopes were hypophosphorylated and 7 epitopes were hyperphosphorylated in response to 100 M H_2O_2. Consistent with the IPA analysis of transcriptional response, exposure to 100 M H_2O_2 uniquely induced hypophosphorylation of protein kinase C related kinase (Prk1) at T778 associated with cell migration and tumor metastasis and hyperphosphorylation of Npm1 at S4 associated with cell survival and growth, Table (5).

Transient exposure to minimally toxic 100 M H_2O_2 uniquely led to dysregulated insulin signaling activation observed by hypophosphorylation of insulin receptor (INSR) at Y972, Table (5). This response was supported by increased phosphorylation of GSK3 at S21 and increased phosphorylation of FAK/Ptk2 at S910, Table (5). The INSR juxtamembrane autophosphorylation site Y972 promotes interaction and stability between INSR and intracellular substrates [40] while FAK1 acts as an intracellular positive downstream regulator of signaling. Hypophosphorylation of INSR at Y972, phosphorylation of FAK1, and inhibitory phosphorylation of GSK3 at S21 have all been associated with insulin-resistant signaling. Further, protein kinase B/Akt1 plays a role in multiple signaling pathways including insulin-stimulated GLUT4 membrane localization[41]. Partial activation of Akt by S473 phosphorylation, essential for Akt activation, was observed in a dose-dependent manner.

Discussion

Defining the cellular response of stem cells to ROS is critical to understanding the unique sensitivity of stem cells to minimally toxic episodes of ROS exposure, or a minimal threshold dose of ROS, to initiate disease or cellular transformation. In this study we directly examined the response of ES cells to a single transient and minimally toxic exposure of ROS and correlated the immediate transcriptional and post-translational modifications that resulted.

ES cells demonstrated a high resistance to ROS consistent with previous work showing ES cells withstanding extreme hyperoxic conditions (40% 0_2) compared with cells grown under normoxic culture conditions [12]. ES cells were more resistant to OS-induced high molecular weight DNA fragmentation than differentiated cell types [29,42]. ES cells may have an increased DNA repair capacity or endonuclease-protected higher order chromatin similar to some cancer cell lines [43,44]. Consistent with this, the dose-dependent resistance of ES cells to ROS-mediated cell death was similar to Caco2 colon cancer cells and elevated compared to terminally differentiated primary glial cells [44,45]. Low and high dose ROS-inducing therapies have different cytotoxicities and short- and long-term efficacies [46,47] that are likely defined by the immediate cell-specific response to these treatments, similar to the observations made here. Consistent with increased resistance of ES cells to ROS, transcripts of the majority of canonical self-renewing genes were similarly unaffected by 100 M H_2O_2. Following this minimally toxic episode of ROS, we did not observe a significant change in transcripts known to be affected following LIF withdrawal-induced differentiation of ES cells [33]. However, a mild transcriptional signal of differentiation could be discerned following acute levels.

Binning of significant biological functions determined that a minimally toxic ROS exposure primarily affected transcription of tumorigenesis-related genes. We curated oncogenes and tumor suppressors and found a significant proportion of oncogenes were up-regulated and

tumor suppressors were down-regulated uniquely following 100 M H_2O_2. This is direct evidence of an oncogenic transcriptional signature induced specifically following a transient and minimally toxic ROS exposure. We did not observe any significant up-regulation in transcripts of classical antioxidant or DNA repair genes following either minimally toxic or acute dose, similar to studies in yeast models [14].

Results showed that early post-translational response to ROS affects mainly homeostatically phosphorylated proteins rather than phosphorylation of new moieties. Focusing on regulated resting state phosphorylated sites, we discerned no apparent paradigm of stem cell response to multiple genotoxic exposures indicating that unique responses might be specific to each compound. Consistent with the transcriptional data, transient exposure to a minimally toxic dose of of H_2O_2 specifically increased oncogenic (*e.g*. hypophosphosphorylation of RAF1 at S259, hyperphosphosphorylation of NPM1 at S4) and metastatic (hypophosphosphorylation of PTK2 at S910) signals common to pathways leading to survival, growth and proliferation, G2/M transition and migration.

We previously demonstrated that etoposide induces similar cytotoxic and genotoxic effects as the minimally toxic ROS used here [48]; however, post-translational response to the two agents was distinct. Early signaling induced by etoposide could be distinguished from that of ROS through activation of β-catenin survival pathway and reduction of integrin and migration signaling as well as an inhibition of the 47kD isoform of JNK. These data provide evidence that a single exposure to mild ROS is sufficient to promote a distinct cellular response marked by significant oncogenic signals that may intitiate cell transformation in a surviving stem cell population.

We were surprised to observe activating marks of survival (*e.g*. hyperphosphorylated Akt at S473), growth (e.g. hypophosphorylated 70kD RAF1 isoform at S910), and proliferation (e.g. hyperphosphorylated Prkcm at S916 and hypophosphorylation of Ptk2 at S722) in ES cells one hour following a transient exposure to ROS suggesting that ES cells' initial response to stress is to maintain a rapid growth rate and bypass DNA repair. This initial rapid growth is then temporally followed by the well characterized induction of cell cycle checkpoints and reduced E2F-dependent transcription, manifested by almost complete dephosphorylation of Rb at S773, hyperphosphorylation of cdc2 at Y15, and supported by transcriptional microarray data showing down-regulation of E2F targets such as *foxd3*.

This study demonstrated that a single minimally toxic exposure to ROS uniquely led to dysregulated insulin signaling. The tyrosine kinase insulin receptor (INSR) is required to mediate insulin signaling, and the early steps of INSR activation are well understood. INSR is a heterotetrameric membrane glycoprotein composed of two and two subunits, linked together by disulfide bonds with activation cascade initiated by binding of insulin to the receptor's extracellular β-subunit [49,50]. The INSR tyrosine kinase is activated upon binding of insulin binds to the receptor's extracellular β-subunit, initiating subunit colocalization, conformational changes, autophoshorylation, and activation of the receptor's kinase activity on intracellular protein substrates [49,50]. Mutations in the INSR gene can reduce receptor autophosphorylation and tyrosine kinase activity toward an exogenous substrate, resulting in both *in vivo* and *in vitro* insulin resistance and diabetes mellitus [51–56]. In our study, a transient minimally toxic exposure to ROS mediated by H_2O_2 was sufficient to induce immediate hypophosphorylation of Y972 providing a direct link between ROS and insulin resistance. Y972F mutation has been shown to cause severe impairment of downstream effector IRS-1 adaptor tyrosine phosphorylation and, thus, downstream signaling of the insulin pathway [57]. Further, Y972 hypophosphorylation in HEK cells was shown to be dependent on Grb14 which is over-expressed in insulin resistance mouse models and human Type II diabetic patients [58]. In support of the

suggestion that appropriate insulin signaling is altered by ROS, we also observed an almost 2-fold increase in the inhibitory S21 phosphorylation of GSK3. GSK3 is active in a cell's resting state and inhibited by insulin, and complete inhibition of GSK3 by acute insulin exposure occurs through phosphorylation of Ser21. It has been shown that over-expression of GSK3 impairs insulin responsiveness while knockdown of GSK3 improves insulin action [59]. GSK3 is elevated in patients with poorly controlled type 2 diabetes and animal models of insulin resistance [60,61]. Taken together, our data shed new light on the possible mechanism of even transient mild ROS exposure on hypophosphorylation of INSR and insulin resistance [58,62,63].

Overall, this screen demonstrated that ES cell early response to ROS is dose dependent and a single transient minimally toxic exposure is sufficient to promote an early post-translational response with significant oncogenic signals supporting the transcriptional data. In addition to new data related to stem cell signaling, this work supports the hypothesis that cancer emanates from a transformed stem cell and underscores the potential role of even a single exposure to ROS to promote this transformation. These data underscore the importance of deciphering methods to either spare wild type stem cells from transformation after ischemia/reperfusion or chemotherapy approaches or to target cancer stem cells.

Materials and Methods

DNA damage and oxidative stress

E14TG2a-derived mouse embryonic stem (ES) cells were cultured as previously described [64,65]. 2×10^7 cells in suspension were exposed to one of the following: 2 ml PBS containing 100μM or 5mM hydrogen peroxide for 15 and 30 min, 20μM etoposide (Sigma-Aldrich; 20mM stock solution prepared in dimethylosulphoxide (DMSO)) for 30 min, or PBS alone. Cells were replated and recovered for 1 hr at 37°C in 5% CO2 before harvest.

Cell cycle analysis and growth arrest

5×10^6 cells were plated in 10 cm dishes and allowed to recover for 24 hr. Adherent cells were harvested and viable cells determined by hemocytometer and trypan blue exclusion or by BrdU labeling.

Pulse Field Gel Electrophoresis

Treated cells were suspended in embedding buffer (15mM Tris—HCl, pH 7.4, 1mM EGTA, 60mM KCl, 15mM NaCl, 2mM EDTA, 0.5mM spermidine, 0.15mM spermine), embedded in 0.8% low melting agarose at 40°C, casted in BioRad plugs (cat# 170-3622) (3×10^5 cells per 50μl) then cooled for 1 min at −20°C. Lipid and protein extraction was performed by two overnight incubations in extraction buffer (10mM Tris-HCl, pH 9.5, 10mM NaCl, 25mM EDTA, 1mM EGTA, 1.5% SDS, 0.1% mercaptoethanol) at room temperature and gentle rocking. Plugs were washed three times in TE pH 7.6 for two hours each followed by RNA digestion with RNase for one hr at 37°C. Proteinase K digestion for 6 hours at 50°C was followed by washing in TE pH 7.6 three times for two hours each. For single strand break analysis, DNA plugs were digested with 3 units S1 nuclease for one hour at 37°C in 200 μl S1 nuclease buffer (30mM NaAc pH 4.6,100mM NaCl, 0.5mM $ZnCl_2$). DNA breaks were analyzed by field inversion gel electrophoresis (FIGE). Plugs containing purified DNA were inserted in wells of 1% 0.5X TBE pulse field-certified agarose gel and resolved by BioRad CHEF Mapper (cat# 170-3670) at 14°C 0.5X TBE buffer circulated by a pump, 20 min of forward voltage (6 v/cm) without field reversion. Resolution of DNA was programmed as: forward voltage: 5 V/cm, forward initial switch time: 0.3s, forward final switch time: 30s, reverse voltage: 5 V/cm, reverse initial switch time: 0.1s, reverse final

switch time: 10s, A= linear, Run time: 16 hours. Following electrophoresis, gel was stained with ethidium bromide and DNA visualized by UV.

Microarray hybridization and analysis

Samples were exposed to H_2O_2 for 15 min, recovered for 1 hr, then harvested for analysis. cRNA derived from 10 μg of total RNA from treated cell samples was prepared and hybridized to MG_U74Av2 oligonucleotide chip according to Affymetrix's protocol. Prior to filtering, unsupervised hierarchical clustering using standard correlation as a similarity measure algorithm confirmed the relatedness of samples within treatment groups (Supplemental Fig. S1A). "Absent" calls in at least 10 out of 12 samples were filtered, leaving 6970 transcripts (out of 12,488) and consistent with previous data that ES cells express approximately 30% of potential transcripts [66]. Analysis of variance in gene expression between control group of replicates and one of the treated groups was performed using the Welch t-test with a 2 fold or greater change and a p-value of 0.05 or lower. Per gene and chip normalization was used as well as the Cross Gene Error Model. Gene expression normalized values were analyzed using GeneSpring GX software (Agilent Technologies). Data is available at http://www.ncbi.nlm.nih.gov/geo/ Accession number #GSE18708 and http://biology.uncc.edu/Faculty/Richardson/index.htm. SYBR® green and LightCycler® real-time RT-PCR was used to validate data.

Phosphoprotein Analysis

Samples were exposed to H_2O_2 for 15 min, recovered for 1 hr, then harvested for analysis. Cells were washed in ice cold PBS, lysed in 500 μl lysis buffer (150 mM NaCl, 20 mM Tris pH 8.0, 0.5% (w/v) Nonidet P-40, 1 mM dithiothreitol (DTT), 20 mM (β-glycerophosphate, 1 mM Na_3VO_4, 1 mM phenylmethylsulfonyl fluoride, 10 μg/ml aprotinin, 10 μg/ml leupeptin and 1 μg/ml pepstatin A) and sonicated for 30 sec pulsing 1 sec ON 1 sec OFF. Cell debris was removed by centrifugation at 13,000 rpm for 15 min at 4°C. Protein concentration was determined by the Bradford assay. Samples were performed in triplicates. For phosphoscreening the Kinetworks™ platform was used (Kinexus--KPSS-2 and KPSS-4). Images available at http://biology.uncc.edu/Faculty/Richardson/index.htm. 300 μg of total protein were resolved on a 13% single lane SDS-polyacrylamide gel and transferred to nitrocellulose membrane. The membrane was incubated with mixtures of up to three antibodies per lane that react with a distinct subset of at least 95 known phosphorylated sites on 53 cell signaling proteins of distinct molecular masses, then horseradish peroxidase-conjugated secondary antibodies (Santa Cruz Biotechnology). Blots were developed using ECL Plus reagent (Amersham Biosciences) and signals were quantified using Quantity One software (Bio-Rad). The overall early response to OS or etoposide is similar with a Spearman correlation value of 0.94 between etoposide and low OS dose, 0.89 between etoposide and high dose, and 0.90 between low dose and high dose. However, the correlation of response with respect to treatment drops significantly to 0.3–0.4 when only the affected epitopes are analyzed indicating that each treatment can be correlated with a unique identifier.

Acknowledgments

We gratefully acknowledge the assistance of Vladin M. of the Columbia University Microarray Core Facility in microarray sample preparation. CR is supported by NCI/NIH (2R01-CA100159).

References

1. Jackson AL, Loeb LA. Mutation Res. 2001; 477:7–21. [PubMed: 11376682]

2. Davies KJ. Biochem Soc Symp. 1995; 61:1–31. [PubMed: 8660387]

3. Beckman KB, Ames BN. J Biol Chem. 1997; 272:19633–6. [PubMed: 9289489]
4. Waris G, Ahsan H. J Carcinog. 2006; 5:14. [PubMed: 16689993]
5. Burdon RH. Free Radio Biol Med. 1995; 18:775–94.
6. Burdon RH, Alliangana D, Gill V. Free Radio Res. 1995; 23:471–86.
7. Olinski R, Gackowski D, Foksinski M, Rozalski R, Roszkowski K, Jaruga P. Free Radio Biol Med. 2002; 33:192–200.
8. Wang MC, Bohmann D, Jasper H. Dev Cell. 2003; 5:811–6. [PubMed: 14602080]
9. Baysal BE. Trends Endocrinol Metab. 2003; 14:453–9. [PubMed: 14643060]
10. Baysal BE. PLoS ONE. 2007; 2:e436. [PubMed: 17487275]
11. Hayes GR, Lockwood DH. Proc Natl Acad Sci U S A. 1987; 84:8115–9. [PubMed: 3317401]
12. Saretzki G, Armstrong L, Leake A, Lako M, von Zglinicki T. Stem Cells. 2004; 22:962–71. [PubMed: 15536187]
13. Francis R, Richardson C. Genes Dev. 2007; 21:1064–74. [PubMed: 17473170]
14. Birrell GW, Brown JA, Wu HI, Giaever G, Chu AM, Davis RW, Brown JM. Proc Natl Acad Sci USA. 2002; 99:8778–83. [PubMed: 12077312]
15. Weigel AL, Handa JT, Hjelmeland LM. Free Radio Biol Med. 2002; 33:1419–32.
16. Anantharam V, Lehrmann E, Kanthasamy A, Yang Y, Banerjee P, Becker KG, Freed WJ, Kanthasamy AG. Neurochem Int. 2007; 50:834–47. [PubMed: 17397968]
17. Purdom-Dickinson SE, Lin Y, Dedek M, Morrissy S, Johnson J, Chen QM. J Mol Cell Cardiol. 2007; 42:159–76. [PubMed: 17081560]
18. Chuang YY, et al. Cancer Res. 2002; 62:6246–54. [PubMed: 12414654]
19. Yu Q, He M, Lee NH, Liu ET. J Biol Chem. 2002; 277:13059–66. [PubMed: 11821411]
20. Amundson SA, Do KT, Vinikoor L, Koch-Paiz CA, Bittner ML, Trent JM, Meltzer P, Fornace AJ Jr. Oncogene. 2005; 24:4572–9. [PubMed: 15824734]
21. Zhang Y, Fong CC, Wong MS, Tzang CH, Lai WP, Fong WF, Sui SF, Yang M. Apoptosis. 2005; 10:545–56. [PubMed: 15909117]
22. Islaih M, et al. Mutation Res. 2005; 578:100–16. [PubMed: 16109433]
23. Allen RG, Tresini M. Free Radio Biol Med. 2000; 28:463–99.
24. Halliwell B, Clement MV, Long LH. FEBS Letters. 2000; 486:10–3. [PubMed: 11108833]
25. Hardman, J.; Limbird, L.; Goodman Gilman, A. A pharmacological basis of therapeutbs. Mc-Graw Hill; New York: 2001.
26. Aladjem MI, Spike BT, Rodewald LW, Hope TJ, Klemm M, Jaenisch R, Wahl GM. Curr Biol. 1998; 8:145–55. [PubMed: 9443911]
27. Corbet SW, Clarke AR, Gledhill S, Wyllie AH. Oncogene. 1999; 18:1537–44. [PubMed: 10102623]
28. Sabapathy K, Klemm M, Jaenisch R, Wagner EF. EMBO J. 1997; 16:6217–29. [PubMed: 9321401]
29. Mouzannar R, Miric SJ, Wiggins RC, Konat GW. Neurochem Int. 2001; 38:9–15. [PubMed: 10913683]
30. Furuno-Fukushi I, Tatsumi K, Takahagi M, Tachibana A. Int J Radiat Biol. 1996; 70:209–17. [PubMed: 8794850]
31. Vilenchik MM, Knudson AG. Proc Natl Acad Sci U S A. 2003; 100:12871–6. [PubMed: 14566050]
32. Eckfeldt CE, Mendenhall EM, Verfaillie CM. Nat Rev Mol Cell Biol. 2005; 6:726–37. [PubMed: 16103873]
33. Duval D, et al. Cell Death Differ. 2006; 13:564–75. [PubMed: 16311515]
34. Ramalho-Santos M, Yoon S, Matsuzaki Y, Mulligan RC, Melton DA. Science. 2002; 298:597–600. [PubMed: 12228720]
35. Yan T, Oberley LW, Zhong W, St Clair DK. Cancer Res. 1996; 56:2864–71. [PubMed: 8665527]
36. Zhong W, Oberley LW, Oberley TD, St Clair DK. Oncogene. 1997; 14:481–90. [PubMed: 9053845]

37. Rathjen J, Lake JA, Bettess MD, Washington JM, Chapman G, Rathjen PD. J Cell Sci. 1999; 112 (Pt 5):601–12. [PubMed: 9973595]
38. Cartwright P, McLean C, Sheppard A, Rivett D, Jones K, Dalton S. Development. 2005; 132:885–96. [PubMed: 15673569]
39. Katoh Y, Katoh M. Int J Oncol. 2005; 27:581–5. [PubMed: 16010442]
40. Kido Y, Nakae J, Accili D. J Clin Endocrinol Metab. 2001; 86:972–9. [PubMed: 11238471]
41. Coffer PJ, Jin J, Woodgett JR. Biochem, J. 1998; 335 (Pt 1):1–13. [PubMed: 9742206]
42. Kaneko S, et al. J Pharmacol Sci. 2006; 101:66–76. [PubMed: 16651700]
43. Bai H, Konat GW. Neurochem Int. 2003; 42:123–9. [PubMed: 12421592]
44. Wijeratne SS, Cuppett SI, Schlegel V. J Agric Food Chem. 2005; 53:8768–74. [PubMed: 16248583]
45. Konat GW, Mouzannar R, Bai H. Neurochem Int. 2001; 39:179–86. [PubMed: 11434975]
46. Han W, Takano T, He J, Ding J, Gao S, Noda C, Yanagi S, Yamamura H. Antioxid Redox Signal. 2001; 3:1065–73. [PubMed: 11813980]
47. Raffaghello L, Lee C, Safdie FM, Wei M, Madia F, Bianchi G, Longo VD. Proc Natl Acad Sci USA. 2008; 105:8215–20. [PubMed: 18378900]
48. Libura J, Slater DJ, Felix CA, Richardson C. Blood. 2005; 105:2124–31. [PubMed: 15528316]
49. Hubbard SR. EMBO J. 1997; 16:5572–81. [PubMed: 9312016]
50. Hubbard SR, Wei L, Ellis L, Hendrickson WA. Nature. 1994; 372:746–54. [PubMed: 7997262]
51. Moller DE, Flier JS. N Engl J Med. 1988; 319:1526–9. [PubMed: 2460770]
52. Odawara M, et al. Science. 1989; 245:66–8. [PubMed: 2544998]
53. Taira M, et al. Science. 1989; 245:63–6. [PubMed: 2544997]
54. Grunberger G, Zick Y, Gorden P. Science. 1984; 223:932–4. [PubMed: 6141638]
55. Le Marchand-Brustel Y, Gremeaux T, Ballotti R, Van Obberghen E. Nature. 1985; 315:676–9. [PubMed: 3892304]
56. Freidenberg GR, Henry RR, Klein HH, Reichart DR, Olefsky JM. J Clin Invest. 1987; 79:240–50. [PubMed: 3540010]
57. Kaburagi Y, et al. J Biol Chem. 1993; 268:16610–22. [PubMed: 8393870]
58. Nouaille S, Blanquart C, Zilberfarb V, Boute N, Perdereau D, Burnol AF, Issad T. Biochem Pharmacol. 2006; 72:1355–66. [PubMed: 16934761]
59. Ciaraldi TP, Nikoulina SE, Bandukwala RA, Carter L, Henry RR. Endocrinology. 2007; 148:4393–9. [PubMed: 17569761]
60. Eldar-Finkelman H, Schreyer SA, Shinohara MM, LeBoeuf RC, Krebs EG. Diabetes. 1999; 48:1662–6. [PubMed: 10426388]
61. Nikoulina SE, Ciaraldi TP, Mudaliar S, Mohideen P, Carter L, Henry RR. Diabetes. 2000; 49:263–71. [PubMed: 10868943]
62. Dokken BB, Saengsirisuwan V, Kim JS, Teachey MK, Henriksen EJ. Endocrinol Metab. 2008; 294:E615–21.
63. Goldstein BJ, Mahadev K, Wu X, Zhu L, Motoshima H. Antioxid Redox Signal. 2005; 7:1021–31. [PubMed: 15998257]
64. Hooper M, Hardy K, Handyside A, Hunter S, Monk M. Nature. 1987; 326:292–5. [PubMed: 3821905]
65. Richardson C, Jasin M. Nature. 2000; 405:697–700. [PubMed: 10864328]
66. Eckfeldt CE, Mendenhall EM, Flynn CM, Wang TF, Pickart MA, Grindle SM, Ekker SC, Verfaillie CM. PLoS Biol. 2005; 3:e254. [PubMed: 16089502]

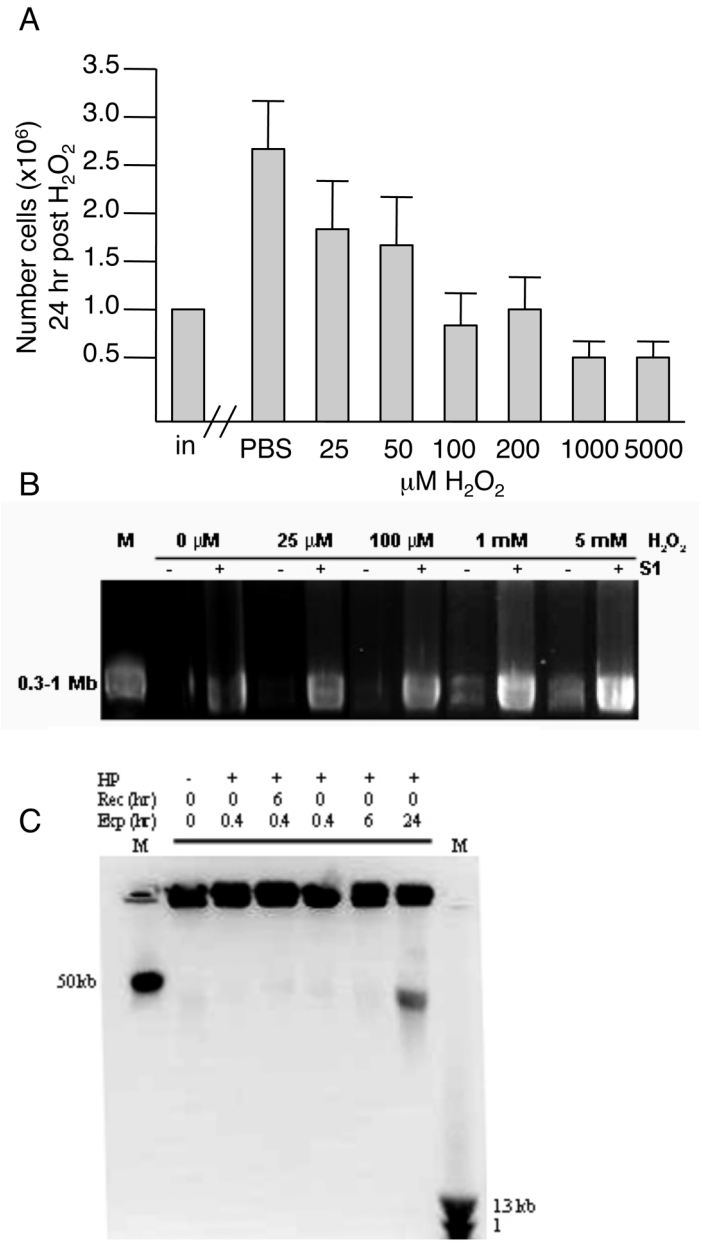

Fig. 1.

Response of ES cells in culture 24 hrs following exposure to minimally toxic ROS. **A.** Cells were exposed to H_2O_2 for 15 min, recovered in normal medium for 20 hrs, then the number of viable cells in culture scored (dead cells were excluded by trypan blue). Data are the average and standard deviation of at least 4 independent experiments. **B.** Dose-dependent accumulation of single-strand breaks (SSBs) following exposure to H_2O_2 for 15 min. Pulse field gel electrophoresis of agarose embedded DNA without (−; DSB) or with (+; SSB and DSB) S1 nuclease digestion. DNA fragmentation was not evident in samples exposed to H_2O_2 at lower doses. Fragmentation was observed at higher doses (1mM and 5mM). As expected, visible fragmentation was detected in all samples, including untreated, following S1 nuclease digestion. Visible fragments were within the 0.3-1 Mb range. **C.** Time-dependent accumulation of 50 kb fragments following exposure (Exp) to 100 M H_2O_2 with

or without recovery (Rec). 50 kb fragments observed only after chronic 24 hour continuous exposure and no recovery. M -- size standard marker.

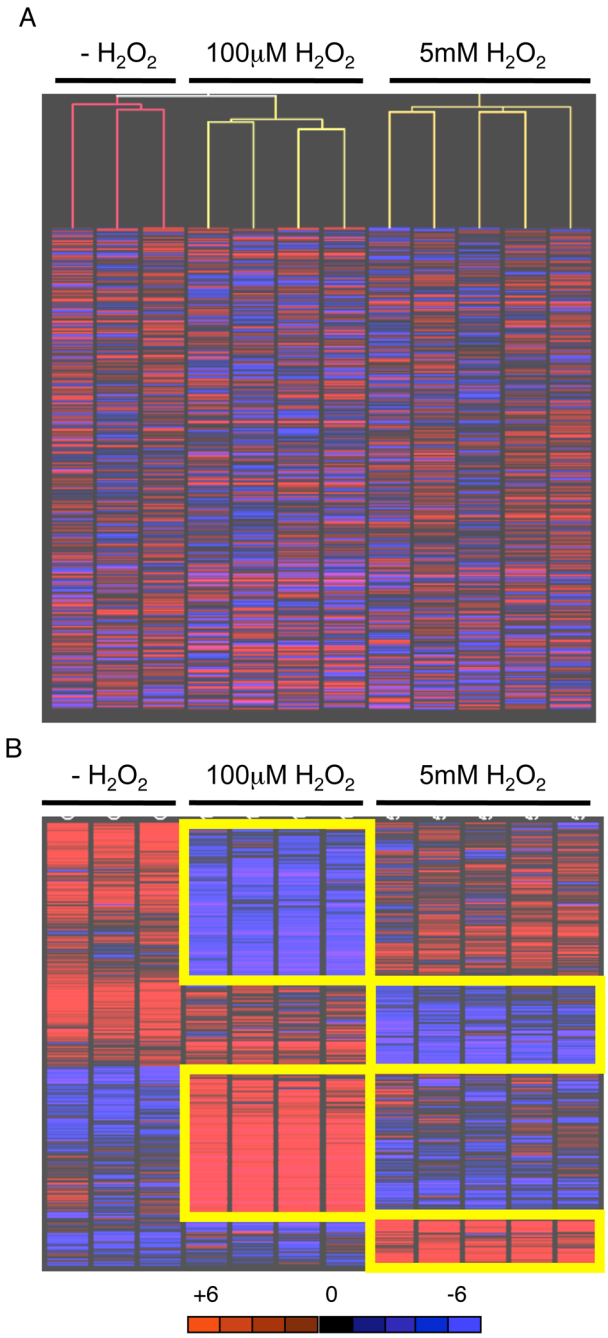

Fig. 2.

A. Relatedness of sample groups confirmed by unsupervised Pearson correlation clustering of transcripts deregulated by two-fold between controls and replicate samples. Analysis performed by GeneSpring data analysis software. **B.** Distinct gene expression signatures induced by low and high doses of H_2O_2. Parametric t-test with unequal variance (Welch t-test) analysis was performed by GeneSpring data analysis software.

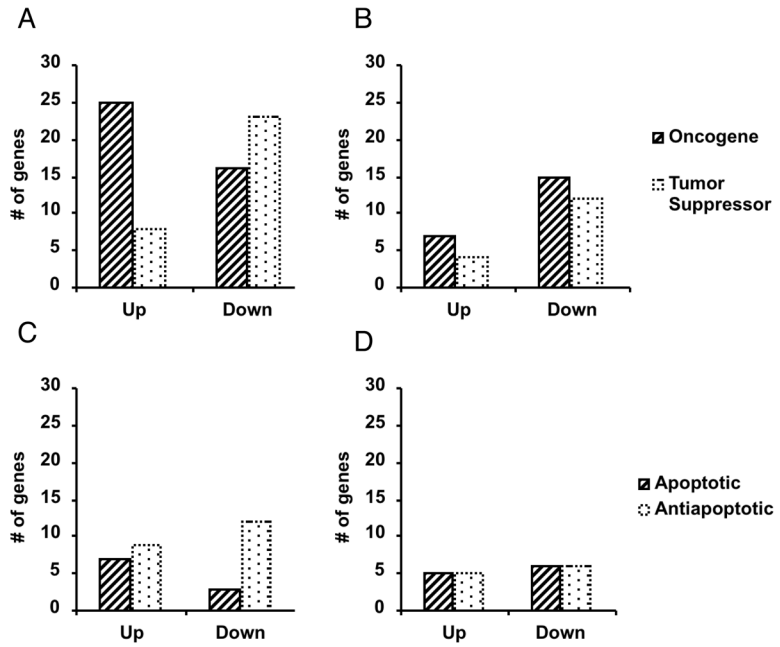

Fig. 3.

IPA clustering shows distinct response of ES cells to minimally toxic ROS. IPA clustering was performed on statistically significant altered transcripts from four samples exposed to 100uM H_2O_2, five samples exposed to 5mM H_2O_2, and three replicate control samples analyzed by Affymetrix MG-U74VerA chips and GeneSpring software. **A.** Altered oncogene and tumor suppressor transcripts following 100 M H_2O_2. **B.** Altered oncogene and tumor suppressor transcripts following 5mM H_2O_2. **C.** Altered apoptotic and anti-apoptotic transcripts following 100 M H_2O_2. **D.** Altered apoptotic and anti-apoptotic transcripts following 5mM H_2O_2.

Table 1

Real-time qPCR validation of transcriptional mbroarray results

	Microarray		Real Time qPCR		
	100 µM-15 min	**5 mM-30 min**	**100 µM-15 min**	**5 mM-30 min**	
Mito (EST)	2.1 ± 0.3	2.5 ± 0.3	1.7 ± 0.3	1.9 ± 0.2	
Ysg2	2 ± 0.2	2.1 ± 0.5	1.8 ± 0.4	2.3 ± 0.5	
Zfp143	3.7 ± 0.5	3.5 ±0.8	2.7 ± 0.7	2.7 ±1.1	
Sgpp1	2 ± 0.8	2 ± 0.7	2.2 ± 0.6	1.5 ±0.4	
Phldb2	**12.6 ± 3**	2.2 ± 1.3	4.8 ± 1.4	1.4 ± 0.5	**Upregulated**
Slc23a3	2.7 ± 0.7	2.1 ± 1	**13.5 ± 4.5**	2.4 ± 1.1	
Ub-Lig (EST)	3 ± 0.6	4.7 ± 1.4	4.7 ± 1.4	6.3 ± 0.8	
Id2	1.9 ± 0.3	1 ± 0.2	3.5 ± 0.9	1.7 ± 0.6	
Id4	2.7 ± 0.3	0.7 ± 0.2	4 ± 1.2	1.1 ± 0.1	
nab1	2 ± 0.6	3 ± 0.3	2.1 ± 0.5	2.8 ± 0.9	
nab2	2.4 ± 0.7	2.7 ± 0.6	2.3 ± 0.4	3.7 ± 0.8	
Gbx2	**10.5 ± 1.6**	3.4 ± 0.7	6.2 ± 0.7	3.2 ± 0.5	
Bmp4	5.3 ± 0.6	2.8 ± 0.4	4.9 ± 0.7	2.1 ± 0.2	
c-myc	5.44 ± 0.9	2.2 ± 0.5	2.7 ± 0.5	1.9 ± 0.2	
Atp11a	2.2 ± 0.2	2 ± 0.4	2.6 ± 1	1.9 ± 0.6	**Upregulated**
Gtl2	4.6 ± 4	3 ± 5	2.5 ± 0.5	1.2 ± 0.3	
Trp53	1.8 ± 0.5	1 ± 0.1	1 ± 0.3	1 ± 0.2	
fgfbp1	3.6 ± 1.5	13.4 ± 8	1.8 ± 0.4	4.1 ± 0.8	
Id1	2.5 ± 0.3	1 ± 0.4	1.9 ± 0.7	1.5 ± 0.6	
	n=4	n=5	n=8	n=10	

Correlation without 3 outliers highlighted in bold: r(100)=0.71; r(5)=0.78. Correlation with outliers: r(100)=0.28; r(5)=0.57

Int J Genomics Proteomics. Author manuscript; available in PMC 2011 July 7.

Table 2

Commonly regulated transcripts following minimally toxic and acute exposures to H_2O_2

Gene Name	Symbol	GenBank	Fold change relative to no treatment	
			100 μM 15 min	5 mM 30 min
upregulated				
fibroblast growth factor binding protein 1	Fgfbpl	AF065441	3.6	13.4
sarco(endo)plasmic reticulum calcium ATPase	Atp2a2; SERCA2	AF029982	2	6.3
Taglin; SM22	Tagln; Sm22a	Z68618	2.8	3.5
gastrulation brain homeobox 2	Gbx2	Z48800	10.5	3.4
Ngfi-A binding protein 1	Nab1	U47008	2	3
GTL2, imprinted maternally expressed untranslated mRNA	Gtl2	Y13832	4.6	3
BMP-4 gene	Bmp4	L47480	5.3	2.8
Ngfi-A binding protein 2	Nab2	U47543	2.4	2.7
EST00652		AA407332	2.3	2.7
solute carrier family 25 (adenine nucleotide translocator), member 5	Slc25a5	U10404	2.8	2.6
Dusp6	Dusp6	AI845584	2.8	2.4
cytochrome c oxidase, subunit VIIc	Cox7c	AI648091	3.2	2.4
myeloid-associated differentiation marker	Myadm	AJ001616	2.1	2.3
c-myc exon 3	c-myc	L00039	5.44	2.2
stratifin	Sfn	AF058798	2.9	2.1
urokinase plasminogen activator receptor	Plaur	X62700	2.6	2.1
CCR4 carbon catabolite repression 4-like	Ccrn4l	AW047630	3.3	2
Nes	Nes	AW061260	3	2
ATPase, class VI, type 11A	Atp11a	AA690863	2.2	2
downregulated				
pleckstrin homology-like domain, family B, member 2	Phldb2	AW125043	12.6	2.2
receptor (calcitonin) modifying protein 2	Ramp2	AJ250490	6	2.7
zinc finger protein 143	Zfp143	U29513	3.7	3.5
protein kinase, lysine deficient 1	Prkwnk1	AV319920	3.2	2.2
RIKEN cDNA 2310014L17, ubiquitin ligase	2310014L17Rik	AA794189	3	4.7
solute carrier family 23 (nucleobase transporters), member 3	Slc23a3	AV222871	2.7	2.1
(clone lambda-MG5.3) acid phosphatase type 5 gene	Acp5; TRAP	M99054	2.4	2.1
DnaJ (Hsp40) homolog, subfamily C, member 3	Dnajc3; hsp40	U28423	2.3	2
FBJ osteosarcoma oncogene B	Fosb	X14897	2.3	2.1
RIKEN cDNA 2310005014 gene, mitochondrion	2310005014Rik	AW124582	2.1	2.5
sphingosine-1-phosphate phosphatase 1	Sgpp1	AI835784	2	2
sialic acid acetylesterase; yolk sac gene 2	Ysg2	U61183	2	2.1

Table 3

Transcriptional state of pluripotency genes following minimally toxic and acute exposures to H_2O_2

Description	Symbol	Effect of OS does on Transcription
Embryonic stem cell specific gene 1	esgl	No change
Octamer binding transcription factor	oct3/4	No change
Zinc finger protein 42	zfp42 (rexl)	No change
Fibroblast growth factor 4	fgf4	No change
SRY-box 2	sox2	No change
Nanog homeobox	nanog	No change
X-ray repair complementing 5	xrcc5	No change
Radiation repair 23 homolog	rad23b	No change
MutS homolog 2 (*E. coli*)	msh2	No change
Zinc finger protein 42	zfp42	No change
Teratocarcinoma derived growth factor, CRIPTO	tdgf1	No change
Integrin alpha 6	itga6	No change
Signal transducer and activator of transcription 3	stat3	No change
Multidrug resistance /ATP binding cassette	Mdr1/abcb1	2× up low dose (2 isoforms)
Excision repair complementing 5	ercc5	2× up low dose
Gastrulation Brain Homeobox 2	gbx2	10× down low dose; 3.4× down high dose
Forkhead homeobox D3	foxod3	5× down high dose
Undifferentiated embryonic transcription factor	utf1	2× down low dose
myelocytomatosis viral oncogene homolog	c-myc	5.4 down low dose; 2.2 down high dose

Table 4

Top significant functions and pathways affected by minimally toxic and acute exposures to H_2O_2.

Low Dose Regulated Genes		
Biological Function.	**# transcripts**	**p-value[a]**
Tumorigenesis	139	4.7×10^{-9}-3.8×10^{-2}
Cell Death	102	1.0×10^{-4} – 3.8×10^{-2}
Cellular Development	81	1.0×10^{-6} – 3.8×10^{-2}
Gene Expression	74	2.3×10^{-5} – 3.8×10^{-2}
Gastrointestinal Disease	55	1.8×10^{-5} – 3.8×10^{-2}
Canonical Pathway		
Wnt/ -Catenin Signaling	11	7.1×10^{-3}
Biosynthesis of Steroids	6	7.5×10^{-5}
High Dose Regulated Genes		
Biological Function	# transcripts	p-value
Tumorigenesis	49	1.9×10^{-4} – 3.2×10^{-2}
Cellular Development	39	1.7×10^{-5} – 3.3×10^{-2}
Cell Cycle	36	2.6×10^{-5} – 3.4×10^{-2}
Embryonic Development	19	1.7×10^{-5} – 2.7×10^{-2}
Respiratory Disease	7	1.9×10^{-4} – 2.9×10^{-2}
Canonical Pathway		
Coagulation system	6	2.2×10^{-2}
VEGF Signaling	5	4.9×10^{-2}
Riboflavin Metabolism	4	1.8×10^{-2}
Cell Cycle: G1/S Checkpoint	3	3.9×10^{-2}
Commonly Regulated Genes		
Biological Function	# transcripts	p-value
Tumorigenesis	13	1.7×10^{-5} – 3.3×10^{-2}
Cellular Development	7	1.9×10^{-5} – 3.2×10^{-2}
Neurological Development	7	1.9×10^{-5} – 2.9×10^{-2}
Cell Cycle	4	1.7×10^{-5} – 2.7×10^{-2}
Neurological Disease	2	2.6×10^{-5} – 3.4×10^{-2}
Canonical Pathway		
Coagulation	6	2.2×10^{-2}
VEGF Signaling	5	4.9×10^{-2}
Riboflavin Metabolism	4	1.8×10^{-2}
Cell Cycle: G1/S Checkpoint	3	3.9×10^{-2}

[a] Fisher's exact test

Table 5

Phosphorylation alterations in response to minimally toxb and acute exposures to H_2O_2 and etoposide

Phosphorylation detected in control and significantly altered following stress.					
			fold phos. relative to control		
Mouse (epitope)	**Human (epitope)**	**Control[a]**	**Etoposide**	**100 μM**	**5mM**
INSR (Y972)	INSR (Y972)	**500**	**1**	**0.45**	**1**
PKN1 (PRK1)(T778)	PRK1 (T774)	**435**	**1**	**0.6**	**1**
PRKCD (T505)	Prkcd (T505)	**544**	**0.6**	**0.6**	**1**
RAF1 (S259) (60 kD)	RAF1 (S259)	**471**	**1**	**0.6**	**1**
PKN2 (N/A)	PRK2 (T816)	**397**	**0.7**	**0.6**	**1**
PPP1CA (T320)	PP1a (T320)	**422**	**0.56**	**0.61**	**0.5**
RAF1 (S259) (70 kD)	RAF1 (S259)	**999**	**1**	**0.63**	**0.68**
MAP2K1 (T292)	MEK1 (T291)	**1700**	**0.75**	**0.67**	**0.49**
MAP2K1 (T386)	MEK1 (T385)	**475**	**1**	**1**	**0**
RB1 (S773)[b]	Rb1 (S780)	**296**	**1**	**1**	**0**
SRC (Y423)	SRC (Y418)	**400**	**0.33**	**1**	**0.17**
PTK2 (S722)	FAK (S722)	**700**	**1**	**1**	**0.27**
PRKCZ (T40/T402)[c]	Prkcz/I(T40/T403)	**498**	**1**	**1**	**0.6**
SRC (Y534)	SRC (Y529)	**2800**	**1**	**1**	**1.3**
MAP2K1 (S298)	MEK1 (S297)	**400**	**1**	**1**	**1.5**
CDC2 (Y15)	CDK1 (Y15)	**2530**	**1**	**1**	**1.6**
MAPK8 (JNK/SAPK) (T183/Y185) (47kD)	JNK (SAPK) (T183/Y185)	**800**	**0.7**	**1**	**1**
PTK2 (S910)	FAK (S910)	**700**	**0.47**	**1.25**	**1**
NPM1 (S4)	NPM1 (S4)	**2719**	**1**	**1.3**	**1**
PRKCM (S916)	Prkcm (S910)	**305**	**1**	**1.3**	**1.3**
AKT1 (S473)	PKBa (Akt1)(S473)	**400**	**0.65**	**1.3**	**3.76**
EIF2B5 (S539)	eIF2Be (S540)	**300**	**1.43**	**1.34**	**1.48**
CDC2 (T161/T160)	CDK1 (T161/T160)	**386**	**1.65**	**1.74**	**2.6**
MAPK14 (T180+Y182)	p38aMAPK (T180/Y182)	**450**	**3.92**	**1.9**	**3.66**

Phosphorylation detected in control and significantly altered following stress.					
			fold phos. relative to control		
Mouse (epitope)	**Human (epitope)**	**Control[a]**	**Etoposide**	**100 μM**	**5mM**
Phosphorylation detected in control and not altered following stress.					
			fold phos. relative to control		
LYN (Y507) (50kD)	Lyn (Y507) (50kD)	**721**	**1**	**1**	**1**
LYN (Y507) (47kD)	Lyn (Y507) (47kD)	**895**	**1**	**1**	**1**
PDPK1 (S241)	PDK1 (S244)	**1066**	**1**	**1**	**1**
MAP2K6 (S207)	MKK6 (S207)	**1306**	**1**	**1**	**1**
CDC2 (T14+Y15)	CDK1 (T14/Y15)	**3500**	**1**	**1**	**1**
phorylation below 300 (normalized intensities) in control and significantly altered to near 300 following stress.					
		normalized intensities			
MAPK1 (T185+Y187)	ERK2 (T185/Y187)	**36**	**52**	**53**	**376**
MAP2K1 (S217/S221)	MEK1 (S217/S221)	**91**	**104**	**175**	**380**
AKT1 (T308)	PKBa/Akt1 (T308)	**99**	**64**	**49**	**296**
GSK3a (S21)	GSK3a (S21)	**144**	**255**	**206**	**166**

[a] Green shading in control column indicates that the normal effect of protein phosphorylation is activation. Red shading in control indicates that the normal effect of protein phosphorylation is inhibition.

[b] PRKCZ was significantly up-regulated following 5 mM H_2O_2 in parallel transcriptional microarray analysis.

[c] Rb1 was significantly down-regulated following 5 mM H_2O_2 in parallel transcriptional microarray analysis.

APPENDIX F:
DOUBLE-STRAND BREAK REPAIR BY INTERCHROMOSOMAL RECOMBINATION: AN *IN* VITRO REPAIR MECHANISM UTILIZED BY MULTIPLE SOMATIC TISSUES IN MAMMALS

OPEN ACCESS Freely available online

PLOS ONE

Double-Strand Break Repair by Interchromosomal Recombination: An *In Vivo* Repair Mechanism Utilized by Multiple Somatic Tissues in Mammals

Ryan R. White[1¤], Patricia Sung[2], C. Greer Vestal[1], Gregory Benedetto[1], Noelle Cornelio[1], Christine Richardson[1*]

1 Department of Biology, University of North Carolina-Charlotte, Charlotte, North Carolina, United States of America, **2** Developmental Biology, Sloan-Kettering Institute, Memorial Sloan-Kettering Cancer Center, New York, New York, United States of America

Abstract

Homologous recombination (HR) is essential for accurate genome duplication and maintenance of genome stability. In eukaryotes, chromosomal double strand breaks (DSBs) are central to HR during specialized developmental programs of meiosis and antigen receptor gene rearrangements, and form at unusual DNA structures and stalled replication forks. DSBs also result from exposure to ionizing radiation, reactive oxygen species, some anti-cancer agents, or inhibitors of topoisomerase II. Literature predicts that repair of such breaks normally will occur by non-homologous end-joining (in G1), intrachromosomal HR (all phases), or sister chromatid HR (in S/G^2). However, no *in vivo* model is in place to directly determine the potential for DSB repair in somatic cells of mammals to occur by HR between repeated sequences on heterologs (i.e., interchromosomal HR). To test this, we developed a mouse model with three transgenes—two nonfunctional green fluorescent protein (GFP) transgenes each containing a recognition site for the I-*Sce*I endonuclease, and a tetracycline-inducible I-*Sce*I endonuclease transgene. If interchromosomal HR can be utilized for DSB repair in somatic cells, then I-*Sce*I expression and induction of DSBs within the GFP reporters may result in a functional GFP+ gene. Strikingly, GFP+ recombinant cells were observed in multiple organs with highest numbers in thymus, kidney, and lung. Additionally, bone marrow cultures demonstrated interchromosomal HR within multiple hematopoietic subpopulations including multi-lineage colony forming unit–granulocyte-erythrocyte-monocyte-megakaryocte (CFU-GEMM) colonies. This is a direct demonstration that somatic cells *in vivo* search genome-wide for homologous sequences suitable for DSB repair, and this type of repair can occur within early developmental populations capable of multi-lineage differentiation.

Citation: White RR, Sung P, Vestal CG, Benedetto G, Cornelio N, et al. (2013) Double-Strand Break Repair by Interchromosomal Recombination: An *In Vivo* Repair Mechanism Utilized by Multiple Somatic Tissues in Mammals. PLoS ONE 8(12): e84379. doi:10.1371/journal.pone.0084379

Editor: Michael Lichten, National Cancer Institute, United States of America

Received April 3, 2012; **Accepted** November 22, 2013; **Published** December 13, 2013

Funding: RW was a recipient of the North Carolina Biotechnology Center Undergraduate Biotechnology Research Fellowship. This work was supported in part by funds provided to CR by the Concern Foundation, National Institutes of Health/National Cancer Institute CA100159, the Alexander and Margaret Stewart Trust, Columbia University, and University of North Carolina-Charlotte. The funders had no role in study design, data collection and analysis, decision to publish, or preparation of the manuscript.

Competing interests: The authors have declared that no competing interests exist.

* E-mail: caricha2@uncc.edu

¤ Current address: Department of Genetics, Albert Einstein College of Medicine, Bronx, New York, United States of America

Introduction

Faithful repair of DNA damage, including double-strand breaks (DSBs), is crucial to genome stability and normal cell survival and proliferation [1]. Chromosomal breaks can occur in a programmed manner through meiosis, immunoglobulin class-switch recombination, and V(D)J recombination [2–4]. In addition, reactive oxidative species may promote 10,000-20,000 DNA damaged sites per cell per day [5–7], and DNA replication errors or stalls may promote another 10-50 DSBs per cell [8,9]. Exposure to ionizing radiation (IR), alkylating agents, and chemotherapeutic drugs such as topoisomerase II inhibitors also promote chromosomal breaks [10–14]. Some environmental and/or dietary compounds may promote DSBs, and the recent observations that bioflavonoids can stabilize DNA DSBs and lead to illegitimate repair and genome rearrangements in cultured cells underscores the importance of understanding DSB repair processes *in vivo* [15–18].

DSBs are potent inducers of recombination and increase both homologous recombination (HR) and non-homologous end-joining (EJ) events by several orders of magnitude [19,20]. These two major DSB repair pathways differ based on their requirement for a donor DNA template with significant

sequence homology; thus, their relative activity changes with each stage of the cell cycle. Studies in multiple organisms have demonstrated that EJ is most efficient in G1 and in noncycling somatic cells while homology-directed DSB repair is favored in both S/G^2 utilizing a sister chromatid and intrachromosomal HR [19,21–26]. *In vivo* systems have been developed to detect EJ, sister chromatid, and intrachromosomal HR that arise both spontaneously and in response to induced DSBs [27–30]. Homologs are utilized for HR-directed DSB repair with lower efficiency although this is increased in organisms that exhibit a high degree of mitotic pairing, supporting the hypothesis that proximity of homologous sequences is an important factor in determining template choice [31–33]. While repair of specific DSBs by more distant homologous repeat sequences on heterologous chromosomes (i.e. interchromosomal HR) has been examined *in vivo* using mitotic yeast and tobacco [34,35], studies in mammalian cells have been limited to cultured cell assays [36–39]. Whether repair of DSBs *in vivo* in mammals occurs by interchromosomal HR at significant and detectable frequencies has not been demonstrated.

If cells are exposed to irradiation, chemotherapeutic agents, or even environmental factors and metabolites, multiple DSBs at unlinked loci will occur in the same cell at the same time. Repair of multiple breaks using interchromosomal HR *in vivo* has the potential to result in reciprocal exchanges that may be viable, inherited by daughter cells in the next cell division, or inherited through the germ line. Genome analysis of plants suggests that translocations are a regular mechanism of plant evolution [40,41]. In mammals, one third of the genome is composed of repetitive elements [42]. The presence of Alu elements elevates recombination rates [43], and Alu-Alu mediated recombination has been associated with founder mutations and evolution [44–49]. In somatic cells, translocations can be tumorigenic, and are a hallmark of human hematopoietic malignancies and some soft-tissue sarcomas [36,50–56]. Thus, such events would likely be suppressed in somatic cells *in vivo* where a selective pressure exists to maintain genome stability and avoid immortalization. Specialized cell types within mammals may preferentially utilize different pathways of repair, particularly as more differentiated cells spend less time in S phase of the cell cycle [57–60] or as proliferation rates change with age [61,62].

To directly test the potential for multiple DSBs to promote interchromosomal HR *in vivo* in mammals, we developed a mouse model with three transgenes--two nonfunctional green fluorescent protein (GFP) reporter transgenes each containing a recognition site for the I-*Sce*I endonuclease, and a tetracycline-inducible I-*Sce*I endonuclease transgene. Induced expression of I-*Sce*I and the resulting induction of DSBs within the GFP reporters may produce a functional GFP gene if interchromosomal HR is utilized for repair. In this system, GFP + recombinant cells were observed in all seven organs examined--pancreas, liver, spleen, kidney, thymus, heart, and lung--with highest numbers in thymus, kidney, and lung. Bone marrow cultures demonstrated interchromosomal HR within multiple colony types including early progenitor CFU-GEMM. This is a direct demonstration that somatic cells *in vivo* maintain the potential to search genome-wide for homologous sequences suitable for DSB repair, and this type of repair can occur within progenitor populations capable of proliferation and multi-lineage differentiation.

Results

In vivo mouse model

Constructs were designed to introduce two defective green fluorescent protein (GFP) genes and a tetracycline-responsive (TET-ON) inducible I-*Sce*I endonuclease gene construct onto heterologous chromosomes in the mouse genome. 1S-GFP and 2S-GFP reporter constructs each contain a unique 18bp restriction site for the endonuclease I-*Sce*I [63,64] in the 5' and 3' ORF regions, respectively, with 460bp homology to each other between the two restriction sites (Figure 1A). The TET-ON I-*Sce*I endonuclease gene is on a single auto-regulated bi-directional expression vector with the tet operator regulating both a TK-rtTAN repressor of the transactivator gene (vector kindly provided by Craig Strathdee) [65] and an I-*Sce*I gene (Figure 2A) [64,66]. Presence of the transgenes within mice was shown by both Southern Blotting and PCR of DNA isolated from tail tips. Founder mice containing each transgene were crossed with wild type, and those that inherited single insertion sites at Mendelian ratios and with the lowest copy number as estimated by both Southern blotting and Q-PCR as compared against a standard (Figure 1B and Methods) were maintained for further breeding. Taken together these analyses estimated 4-5 copies of 1S-GFP and 2-4 copies of 2S-GFP. Mice were screened for an intact I-*Sce*I site at both the 1S-GFP and the 2S-GFP reporters using PCR primers that flank each I-*Sce*I site and digestion of the PCR product with I-*Sce*I endonuclease (Figure 1A, 1C). Individually 1S-GFP and 2S-GFP positive lines were crossed to each other, and then crossed to the I-*Sce*I transgenic line over generations, and inheritance of the three transgenes in expected Mendelian ratios supports unlinked loci. Breeding resulted in triply positive transgenic GS lines for analysis.

DSB-induced interchromosomal HR occurs in mouse embryonic fibroblasts

Mouse embryonic fibroblasts (MEFs) were harvested at day E13.5. MEFs from each GS mouse were divided and cultured in one of 3 conditions: (1) cultured in media without DSB induction, (2) cultured in the presence of tetracycline (2 μg/mL) to induce DSBs through I-*Sce*I expression, or (3) transfected with 30μg I-*Sce*I expression vector CBAS [20] to induce DSBs through I-*Sce*I expression. I-*Sce*I RNA transcripts and protein were detectable by RT-PCR and Western blotting, respectively, following addition of tetracycline to culture media of MEFs (Figure 2B) or to H_2O provided transgenic mice in subsequent experiments (see below).

Individual GFP+ MEFs were detectable by inverted fluorescent microscopy as early as 4 days following the addition of tetracycline (Figure 3A). Cells were analyzed by fluorescent activated cell sorting (FACS) 6-10 days post-tetracycline. Untreated MEFs had an undetectable number of GFP+ cells. By contrast, intermediate/bright GFP+ cells were greater than 12% of the treated cells (compared against

Figure 1

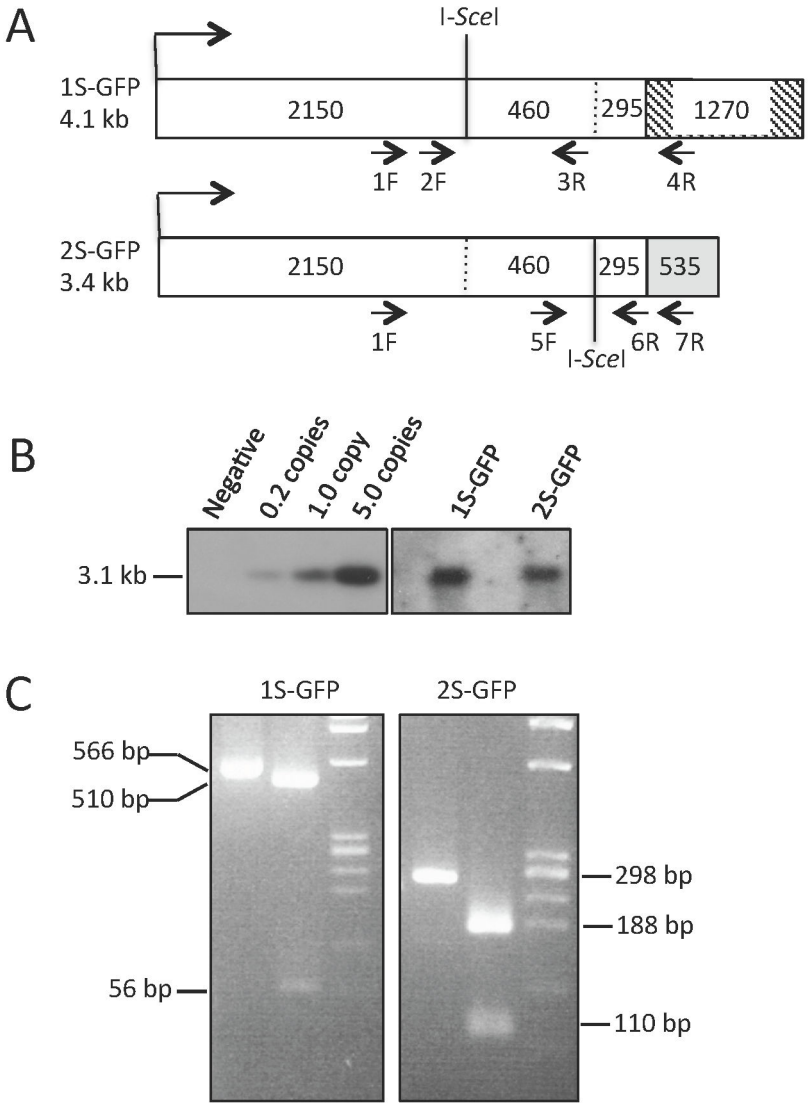

Figure 1. Structure and confirmation of the 1S and 2S GFP transgenes. (**A**) For each construct schematic, the numbers of bases are indicated to show the lengths of homology between the two as well as the relative positions of the engineered I-*Sce*I restriction sites. The 3'UTR sequences of the two constructs do not share homology and are indicated as a hatched box of 1270 bp for 1S-GFP and a grey box of 535 bp for 2S-GFP; these non-homologous sequences allow for PCR amplification specific to each transgene. Nested PCR primer pairs used for verification of intact construct sequences and for analysis of GFP+ hematopoietic colonies are indicated. Primers 1F-4R followed by 2F-3R amplify sequence flanking the I-*Sce*I site in 1S-GFP. Primers 1F-7R followed by 5F-6R amplify sequence flanking the I-*Sce*I site in 2S-GFP. (**B**) Southern blotting to estimate copy number utilized a GFP ORF DNA fragment of 3.1 kb and diluted to pg amounts that approximated 0, 0.2, 1.0, and 5.0 copies per genome spiked into 10µg non-transgenic mouse DNA. Genomic DNA from single transgenic mice (either 1S-GFP or 2S-GFP) was digested with restriction endonucleases within the GFP promoter and ORF of both transgenes to yield a 3.1 kb fragment. Band intensities are consistent with 4-5 copies of 1S-GFP and 2-4 copies of 2S-GFP, and were confirmed with Q-PCR data on the same samples (data not shown). (**C**) PCR reactions flanking each DSB site in the two GFP constructs confirm intact I-SceI recognition sites. Nested PCR as described in Materials amplified each transgene shown in the left side lane of each image. Digestion with I-*Sce*I endonuclease produced the expected sizes indicated in the middle lane of each image. Right side Marker lane PhiX.

doi: 10.1371/journal.pone.0084379.g001

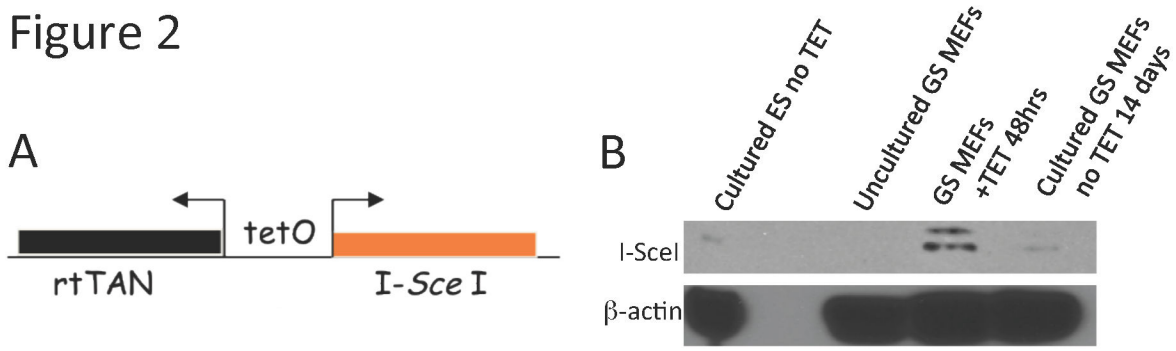

Figure 2. Structure and confirmation of the tetracycline inducible I-*Sce*I transgene. (**A**) For details of the bicistronic I-*Sce*I transgene construct refer to [65]. (**B**) MEFs derived from GS mice were cultured in media supplemented with TET at 2μg/mL for 48 hours. Total protein extracts were harvested and analyzed by Western blotting. By 48 hours post-TET, detectable quantities of I-*Sce*I endonuclease can be observed. As a negative controls, total protein extracts were harvested from cultured E14 ES cells or uncultured MEFs from GS mice. Loading control: Western blotting for β-actin.

doi: 10.1371/journal.pone.0084379.g002

untreated cells with a gate set at 0.1%; n=12) (Figure 3B). Individual GFP+ cells were FACS sorted and confirmed to be GFP+ by inverted fluorescent microscopy (Figure 3C).

DSB-induced interchromosomal HR occurs *in vivo* in multiple somatic cell types

GS mice at least 3 months of age (n=47) were administered tetracycline through H_20 for 21d to allow an extended period of I-*Sce*I expression and subsequent induction of DSBs. Mice were then taken off tetracycline for 7d-21d prior to analysis. This waiting period would restrict analysis to viable GFP+ cells after cells with unstable repair structures would be cleared from the *in vivo* tissues. A total of seven organs--pancreas, liver, spleen, kidney, thymus, heart, and lung--were analyzed for GFP+ recombinants by FACS (Figure 4). Mice were analyzed in batches, and each batch included an age-matched non-transgenic mouse (n=8). Gates for determination of GFP+ cells were set such that negative controls had ≤3 events per million, and then the same gates were used to score GFP+ cells from GS tetracycline-treated mice. This analysis directly demonstrated that GFP+ cells, as determined by >3 GFP+ cells per million by FACS, were readily detectable in multiple tissues from 40 of the 47 mice treated and analyzed (Figures 4,5; Table S1). Despite variance in GFP+ numbers detected between mice, all organs had significantly increased GFP+ cells as compared to the age-matched negative controls (Figure 5). For comparison, constitutively expressing EGFP mice consistently contained >45% GFP+ cells in all tissues examined (data not shown) [67]. These data demonstrate that somatic cell types *in vivo* retain the potential to repair DSBs with a homologous sequence on a heterologous chromosome. Furthermore, the potential for interaction between sequences on heterologous chromosomes in wild-type cells has not been eliminated by epigenetic factors or chromatin remodeling associated with differentiation programs.

Additionally, age-matched GS mice that were not administered tetracycline were analyzed (n=15). 13 of 15 of these mice had undetectable levels of GFP+ cells in all organs examined, similar to the non-transgenic controls. However, two of the 15 mice contained GFP+ populations of cells in multiple tissues (data not shown). In these mice, it is possible that the I-*Sce*I transgene became activated. Alternatively, it is possible that an early progenitor cell *in utero* underwent spontaneous interchromosomal HR giving rise to a GFP+ progenitor cell that contributed to multiple tissues, or was a cell type that gave rise to cells capable of infiltrating multiple organs, e.g. circulating hematopoietic cells.

Impact of aging on DSB-induced interchromosomal HR in multiple somatic cell types

Close examination of the variance of numbers of GFP+ cells detected in tetracycline-treated GS mice indicated that 7 of the 47 mice contained no detectable GFP+ cells in any organs analyzed, similar to non-transgenic controls. All 7 mice were older. Thus, we separated analysis of the 47 mice GS mice into two age cohorts, young (≤ 5months old, n=16) and old (≥ 8 months, n=31) (Figures 6A and 6B, respectively). Regardless of age, statistically significant numbers of GFP+ cells were in most organs examined, as compared to negative control mice. Comparison of GFP+ cell numbers by age (Figure 6C) indicated that in 5 of the 7 organs examined (pancreas, kidney, spleen, lung, and thymus), overall numbers of detectable GFP+ cells were lower in the cohort of older mice (Figure 6C). The decrease in detectable number of GFP+ cells was significant in 3 of these (pancreas, lung, thymus). However, two organs (heart and liver) appeared to have an overall slight increase in numbers GFP+ cells in older mice, although the trend did not reach statistical significance. Decreases in transgene expression levels with age has been observed in multiple other models. A similar mechanism of transgene shutdown may be involved in this model, but only occur in a subset of tissue types. It is possible that certain organs contain specific cell types or progenitor cells capable of DSB-induced interchromosomal HR, even within older mice. Further

Figure 3

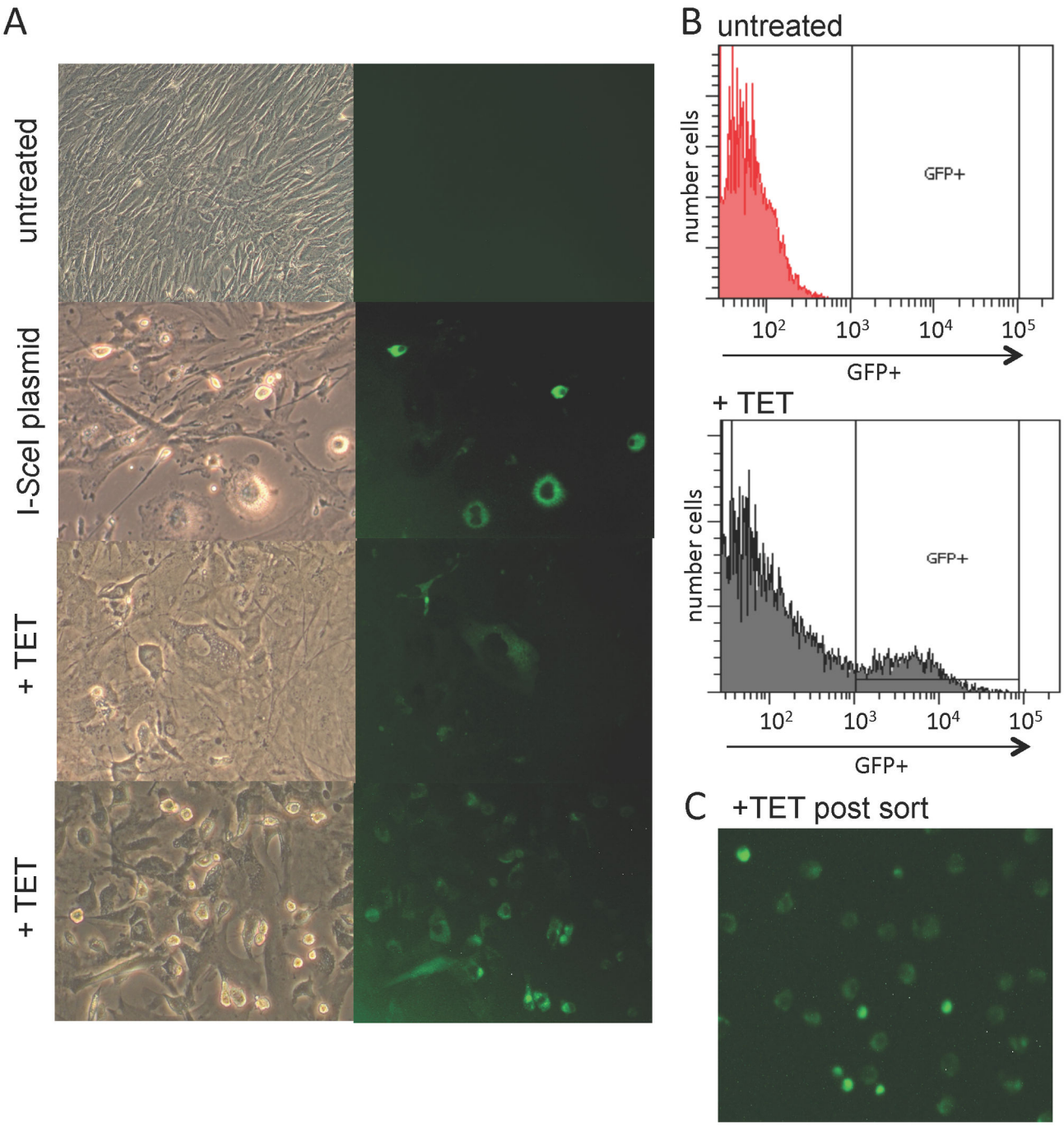

Figure 3. Analysis of GFP+ MEFs post-TET. (**A**) Phase contrast and matched fluorescent microscopy images of MEFs in culture —magnification 400X. Top row-untreated MEFs. Second row-96 hrs post-electroporation with I-*Sce*I expression plasmid. Third and fourth rows-96 hrs after addition of tetracycline to the culture medium (+TET). (**B**) Representative FACS plot of MEFs with GFP positivity in log scale on the x axis plotted against number of cells on the y axis. Upper plot--untreated MEFs. Lower plot-- +TET treated MEFs. In this sample, the GFP+ population is 12.4%. (**C**) Confirmation of GFP+ cells after FACS single cell sorting for GFP+ MEFs. Cells within the GFP+ gate indicated in B lower panel were sorted and then viewed by fluorescent microscopy—magnification 400X.

doi: 10.1371/journal.pone.0084379.g003

Figure 4

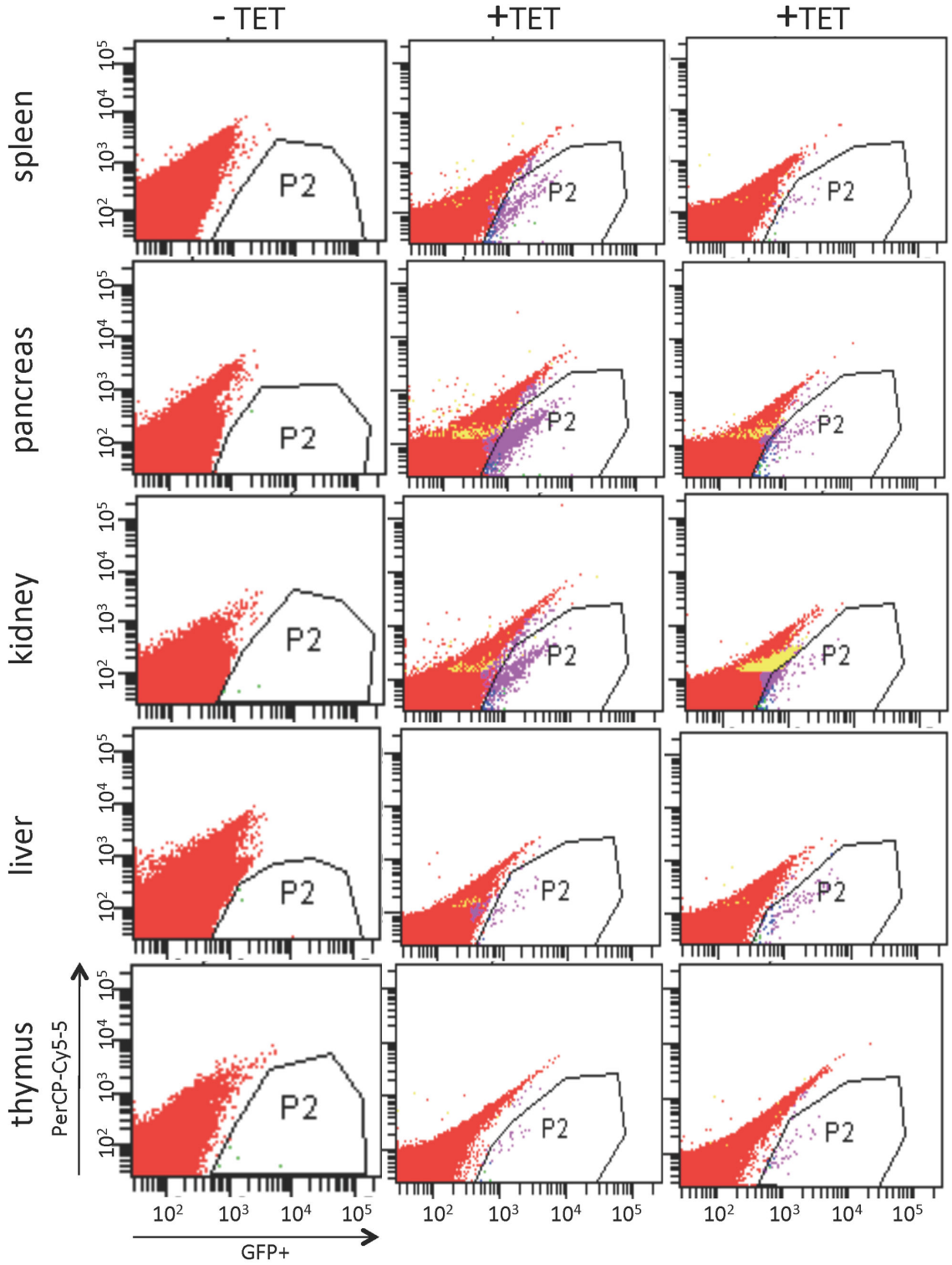

Figure 4. Representative FACS analysis plots of three GS mice for spleen, pancreas, kidney, liver, and thymus. GFP positivity is shown on log scale on the X axis plotted against nonspecific PerCP-Cy5-5 on the Y axis to visualize individual cells. Age-matched negative control mice were not provided TET (-TET). Two representative age-matched mice contain all 3 transgenes and were provided TET as described in text (+TET). Establishment of gates is described in text.

doi: 10.1371/journal.pone.0084379.g004

Figure 5

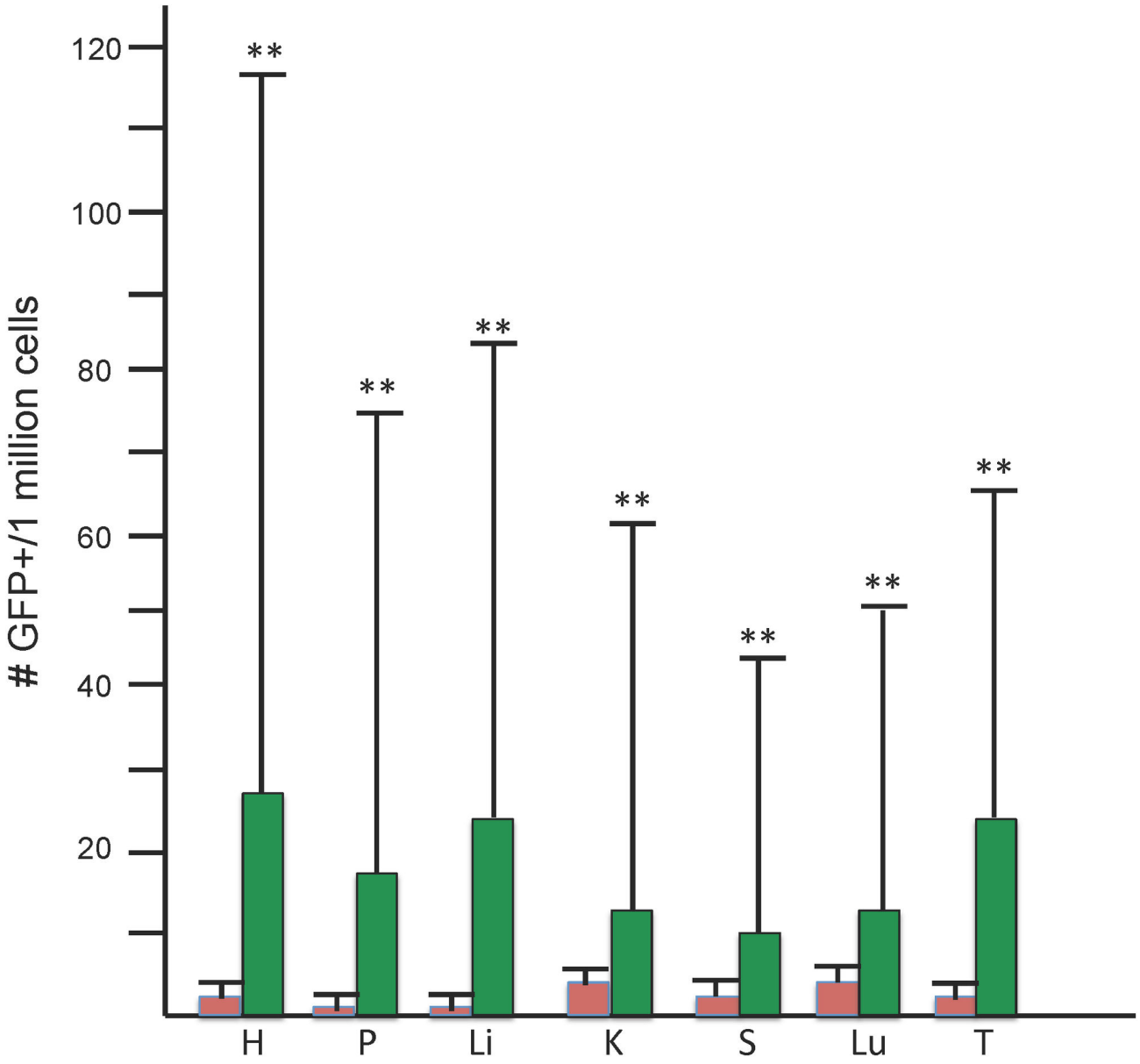

Figure 5. Quantitative analysis of GFP+ cells in all mice analyzed. The number of GFP+ cells in each organ of analyzed mice was determined. Establishment of gates is described in text. From FACS analysis, the average number of GFP+ recombinant cells per million cells and the standard deviation of each was calculated for seven organs and represented in bar graph form. Negative controls are shown in red bars (n=8), and +TET are shown in green bars (n=47). H=heart, P=pancreas, Li=liver, K=kidney, S=spleen, Lu=lung, T=thymus. Organs with statistically significant increased numbers of GFP+ cells groups are indicated by ** above the error bars.

doi: 10.1371/journal.pone.0084379.g005

determination of the specific cell types that are GFP+ within each of the mice could provide this information.

Given the variance in GFP+ numbers detected between mice (Figures 5, 6; Table S1), statistical significance of the probabilities associated with covariance among the traits was calculated for each pair of traits separately in the young and old cohorts (Table S2). In the young cohort, only a single strong positive correlation of covariance between spleen and kidney

Figure 6

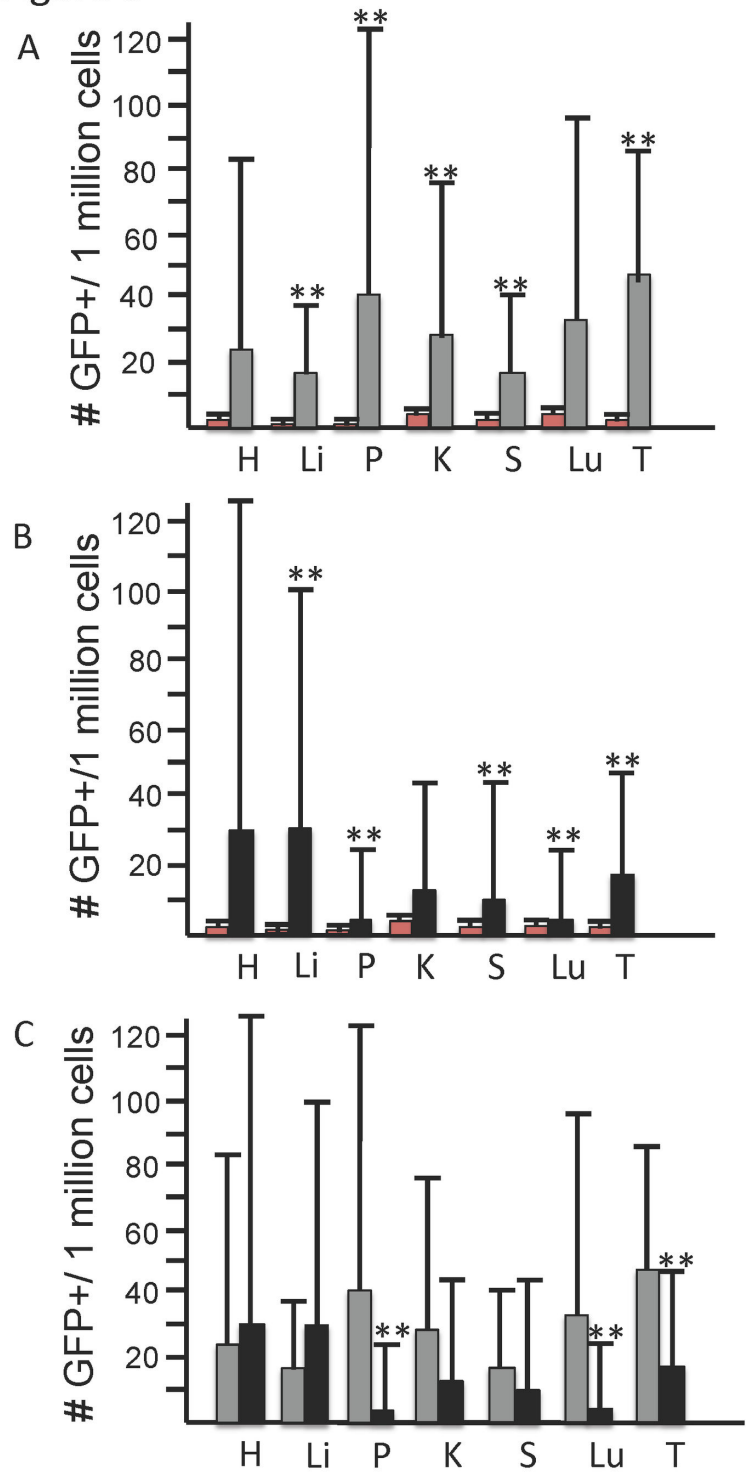

Figure 6. Quantitative analysis of GFP+ cells by age. (**A**) In the young mouse cohort (age<5.5 months), negative controls are shown in red bars (n=5), and +TET are shown in grey bars (n=16). Organs with statistically significant increased numbers of GFP+ cells groups are indicated by ** above the error bars. (**B**) In the older mouse cohort (age>8 months), negative controls are shown in red bars (n=11) and +TET are shown in black bars (n=31). (**C**) Comparison of +TET young mice (grey bars) versus +TET old mice (black bars) from A and B. Organs with statistically significant different numbers of GFP+ cells by age are indicated by ** above the error bars. For all panels, H=heart, P=pancreas, Li=liver, K=kidney, S=spleen, Lu=lung, T=thymus.

doi: 10.1371/journal.pone.0084379.g006

(p=0.002) was noted. In the old cohort, a larger number, although weaker, of positive correlations of covariance were noted; these were between heart and pancreas (p=0.021) or thymus (0.021), as well as between spleen and kidney (0.021) or thymus (p=0.021).

DSB-induced interchromosomal HR occurs *in vivo* in hematopoietic multi-lineage progenitor cell types

Hematopoiesis is characterized by a hierarchy of cells, with hematopoietic stem cells (HSC) possessing the highest proliferative potential and thought to be the targets of aberrant interchromosomal DSB repair events leading to mutagenic chromosomal rearrangements. Our previous *in vitro* studies demonstrated that early stem and progenitor cells are more proficient than terminally differentiated myeloid cells in repairing DSBs by interchromosomal HR [68]. Here, we determined the potential for hematopoietic multi-lineage progenitor cells to utilize this mechanism of repair *in vivo*. GS mice (ages 3-5 months) were administered tetracycline, then bone marrow cells harvested, and subsequently seeded into methylcellulose colony forming assays that support proliferation of myeloid, erythroid, or B-cell progenitors [68–70]. Total numbers of hematopoietic CFUs were scored and classified based on their morphology, and individual GFP+ CFUs determined by inverted fluorescent microscopy (Figure 7). Mature colonies derived from individual precursors included the colony forming unit- granulocyte-erythrocyte-monocyte-megakaryocte (CFU-GEMM), granulocyte-monocyte (CFU-GM), granulocyte (CFU-G), monocyte (CFU-M), erythrocyte (CFU-E), and pre-B (CFU-pre-B). Colonies that contain mixed cell populations are presumed to derive from immature progenitor cells capable of differentiation into multiple cell types. Colonies that contain a single cell population are presumed to derive from more differentiated progenitors that only have the capacity to expand a single cell type.

Following DSBs, GFP+ recombinants were readily obtained from all sub-populations assayed. Strikingly, the results parallel observations previously made in studies of DSB-induced interchromosomal HR using genetically engineered murine ES cells differentiated *in vitro* into hematopoietic colonies [68]. The highest average number of GFP+ recombinant colonies (32 ± 15) was observed in the multi-potent CFU-GEMM cells scored by this assay (Table 1). Observed numbers of GFP+ recombinants decreased with increased differentiation status with the lowest average number of GFP+ recombinant colonies (5 ± 5) observed in the terminally differentiated but actively proliferating monocytic cells (p value = 0.02) (Table 1). The average frequency of recombination in this *in vivo* system was estimated to be 8.0 x 10^{-5} in CFU-GEMM cells, 5.5 x 10^{-5} in CFU-GM cells, 6.5 x 10^{-5} in CFU-G cells, and decreasing to 1.25 x 10^{-5} in CFU-M cells. Overall these data demonstrate that both multipotent and terminally differentiated cell types retain the potential to repair DSBs with a homologous sequence on a heterologous chromosome *in vivo*.

Because CFU represent clonal populations, the recombinant HR repair products could be verified at the sequence level. DNA was extracted from individual BM colonies, and nested PCR used to amplify across the two I-*Sce*I endonuclease DSB repair sites (Figure 1A). Because the 3' UTR ends of the transgene sequences are unique, primers could selectively amplify each of the two transgenes (Figure 1A). A total of 22 individual BM colony PCR products were cloned and sequenced. Because each transgene is inserted in multiple copies, PCR will amplify both GFP+ recombinant and parental non-recombinant copies of the transgenes. These were distinguishable following TA cloning and sequencing of multiple TA clones from each BM colony PCR. This analysis verified that all 22 BM colonies contained a repaired GFP+ wild-type sequence on at least one allele. In 6 of 22 colonies this analysis detected HR repair at only one allele (4 at 1S-GFP and 2 at 2S-GFP). In 16 of 22 colonies this analysis detected HR repair at both alleles; however given the multiple copy inserts, these likely represented independent events.

Discussion

This study presents an *in vivo* model that directly demonstrates that DSB-induced interchromosomal HR occurs at readily detectable rates. GFP+ recombinant cells were readily detectable in a broad range of somatic cell types. Variability in numbers of GFP+ recombinant cells was observed between the multiple somatic cell types and mice in all cohorts examined. Such variability could be due to differences in GFP expression, recombination rates, clonal expansion of individual GFP+ recombinants, or I-*Sce*I transgene induction, expression, or stability. This mouse model initiates I-*Sce*I expression *in vivo* using a single bicistronic TET-ON system [65]. The experiments in MEFs with this system show strong and specific induction, but *in vivo* kinetics could be different. In addition, individual mice self regulate feeding and thus vary dosage to tetracycline. However, similar inter-mouse variability in the *in vivo* mouse model of spontaneous intrachromosomal/sister chromatid HR suggests that I-*Sce*I is not the major determinant of these results [30].

Intrachromosomal HR may occur if homologous repeat sequences lie on the same chromosome in the same direct repeat orientation such as repetitive elements within several kb of each other. Several studies have used *Arabidopsis* and *N. tabacum* models to detect spontaneous and DSB-induced sister chromatid and intrachromsomal HR with spontaneous frequencies estimated at 10^{-5} to 10^{-4} [29,35,71,72] and up to 10,000X stimulation by I-*Sce*I expression [29,35]. Further, similar to *in vitro* findings, SSA was a predominant mode of DSB repair with ectopic joining contributing to a smaller subset of repair events [35]. In mice, spontaneous intrachromosomal and sister chromatid HR have been demonstrated utilizing a yellow fluorescent protein (YFP) reporter or LacZ/β-galactosidase reporter construct [27,30,73–76]. These studies demonstrated median spontaneous HR frequencies of 5 per 10^6 cells in the pancreas [30,73–76]. Ionizing radiation or the interstitial cross-linking agent mitomycin-C led to an increase of recombination suggesting that non-specific DNA damage is also sufficient to promote intrachromsomal HR, at least in pancreatic cells [75]. Although comparisons between different model systems are difficult, these results are surprisingly similar to the findings presented here suggesting that both

Figure 7

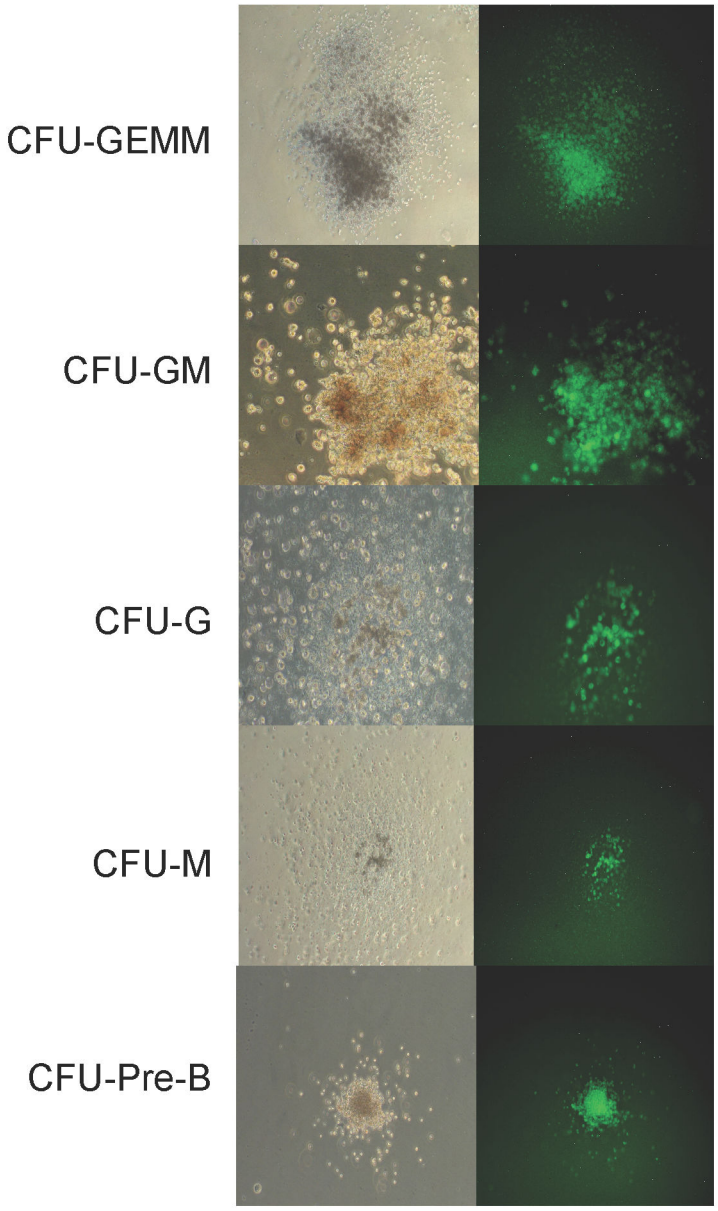

Figure 7. DSB-induced GFP+ recombinants in hematopoietic subpopulations isolated from bone marrow of GS mice. Colonies were scored by inverted fluorescent microscopy and faint background fluorescence of negative controls was subtracted out of total repair frequency. Representative phase contrast and fluorescent microscopy images of GFP+ recombinants from bone marrow CFC assay. Granulocyte-erythrocyte-macrophage-megakaryocyte (GEMM), Granulocyte-macrophage (CFU-GM), Granulocyte (CFU-G), Macrophage (CFU-M), Pre-B cell (Pre-B), and Burst forming unit-erythroid (BFU-E). Magnification 400X.

doi: 10.1371/journal.pone.0084379.g007

types of HR repair are utilized with roughly the same overall efficiency, although likely in different cell types or at different stages of the cell cycle [60].

Cytologic studies indicate that nuclei are ordered, and chromosomes/genomes generally exist within defined nuclear territories [77,78], and single DSBs remain stable in these defined regions [79,80]. Genetic studies seem to support this

Table 1. DSB-induced interchromosomal HR in hematopoietic progenitor cell populations.

	# GFP colonies[a]			
Bone Marrow CFC	**Expt 1**	**Expt 2**	**Expt 3**	**avg. GFP colonies**
CFU-GEMM	47	17	32	32 ± 15
CFU-GM	31	0	35	22 ± 19
CFU-G	23	49	7	26 ± 21
CFU-M	0	4	10	5 ± 5 p value = 0.02[b]
CFU-Pre B	37	21	27	28 ± 8
BFU-E	8	0	40	16 ± 21

GS mice were administered tetracycline via drinking H_2O for 14d. Mice were then sacrificed, and femur bone marrow cells isolated and seeded into methylcellulose colony forming assays. Cells were plated at 1.0 x 10^5 cells/plate. Each experiment included 4 technical replicates and the total number of colonies is shown.

a. GFP+ colony numbers were normalized to account for variation of overall plating efficiency (total number of CFC of each type) between mice.

b. Number of GFP+ CFU-M colonies observed was statistically significantly lower as compared to the number of GFP+ CFU-GEMM observed (student's T test).

doi: 10.1371/journal.pone.0084379.t001

model as repair of a single DSB in mouse and human cells does not promote large scale genome rearrangements between heterologs, although they can be associated with regional loss of heterozygosity (LOH) and insertions with sequences of unknown origin [20,31–33,81]. Similarly, multiple DSBs on the same chromosome do not significantly promote large-scale genome rearrangements in mouse or human cell lines, although the efficiency of repair decreases as the distance between two DSBs increases (up to 9 kb apart) [82,83].

By contrast, cytological analysis indicates chromosome movement is more fluid in DNA repair deficient cells [79]. Chromosome movement has also been observed in the presence of multiple induced DSBs on heterologous chromosomes in mitotic yeast [84] or following global exposure of cells to ionizing radiation or topo II inhibitors [85–87], leading to foci suggestive of repair centers ("repairosomes" [84,88]). The steps by which such repairosomes are initiated by chromatin remodeling programs as a normal step in DNA repair or the biological understanding of how translocations are formed within the ordered nucleus remain unclear [2,89,90]. It is not clear if chromosome movement is in response to multiple breaks in different loci or after prolonged or persistent damage. The established nuclear matrix and chromatin loop structures may also influence choice of recombination partners during DSB repair [89]. In support of the cytologic data, our genetic study here indicates that *in vivo* interaction of DNA sequences and recombination is promoted by multiple DSBs.

A wider range of HR mechanisms are used to repair DSBs on heterologous chromosomes as compared to intrachromosomal HR. In addition, intrachromosomal HR is not typically associated with the genome rearrangements observed in human tumors. DSBs in cultured ES cells and multiple *in vitro* differentiated hematopoietic cell types can stimulate interchromosomal HR as a repair pathway [68]. We observed with this *in vivo* system that repair by HR in multiple hematopoietic lineages is also quite prevalent with observed GFP+ numbers decreasing with differentiation. Similarly, in most organs the number of GFP+ cells decreased with age. These data support other hypotheses that differentiation and age will determine different pathways of repair or utilize apoptotic programs with different frequencies [57–60].

Topo II is an essential cellular enzyme that catalyzes changes in DNA topology via its cleavage-religation equilibrium. Topo II inhibitors convert topo II into a DNA-damaging enzyme by disrupting the cleavage-religation equilibrium, resulting in accumulation of DSBs, activation of DNA damage sensors, cell cycle arrest, and initiation of apoptosis or repair. A wide range of agents, including some chemotherapeutic agents, are classified as topo II inhibitors, and exposure to these is associated with development of secondary leukemias [91,92]. However, they also include benzene metabolites, bioflavinoids, anthraquinone laxatives, podophyllin resins, quinolone antibiotics, pesticides, many phenolic compounds, as well as certain fruits, tea, coffee, wine, soy, and cocoa [11,12,93]. The recent observations that bioflavinoids can stabilize DNA DSBs and promote illegitimate repair and genome rearrangements in cultured cells has led to the hypothesis that exposure to these agents *in utero* or through unregulated high doses as dietary supplements may promote leukemia [15–18]. Further study of this *in vivo* system could determine the potential for exposure to such agents at early stages of development to promote HR *in vivo* and their long-term impact.

Rearrangements resulting from DSB repair that occurs in germ cells can have evolutionary implications. It has been observed that topoII has a role in DSB formation in spermatids [94], and chromatin loop organization is similar between spermatids and somatic cell types [89]. These observations have led to the suggestion that DSB repair pathways and partner choice may be more similar in meiotic and mitotic cells than appreciated and has the potential to result in rearrangements leading to genome variation [89,95]. That this may be universal across multiple kingdoms, is supported by genome analysis of plants that suggests translocations are a regular mechanism of plant evolution [40,41]. In addition, mutation fixation has been implicated during DSB repair in the first zygotic cell division in mice [96]. Our demonstration that interchromosomal HR occurs *in vivo* in response to DSBs at just two loci in a broad range of cell types, particularly progenitor cells, is a novel finding and lends further support to the idea that exposure to the growing list of environmental agents, dietary supplements, or groundwater contaminants that induce or stabilize DSBs may promote potentially tumorigenic rearrangements, accelerate genomic variation, and influence evolution.

Materials and Methods

Ethics Statement

All studies were approved by IACUC (protocol #AAAA0123 Columbia University; protocol #08-035 University of North Carolina at Charlotte). All studies were conducted under supervision of appropriate regulatory bodies and in accordance

to established NIH guidelines for ethical treatment of animals in research.

Transgenic Mice

Transgenic mice for study were generated by establishing three independent transgenic lines of mice: (1) the tetracycline-regulated I-*Sce*I expression gene, (2) 1SGFP with I-*Sce*I cut site 1, and (3) 2SGFP containing I-SceI cut site 2 (1). TET-I-*Sce*I – XbaI-PstI fragment of CBAS containing the I-*Sce*I gene [64,66] sequence was inserted into NheI-BamHI digested pBIG3i bicistronic tetracycline-regulated vector (kindly provided by Craig Strathdee) [65]. DNA was digested with BspHI and the fragment was provided to the Columbia University Transgenic Mouse facility (2). 1SGFP – SacII-HindIII fragment of pCAGGS-NZE-GFP containing the GFP sequence was sub-cloned into SacII-HindIII digested pBluescript SK+, creating SKRGFP(Sac2H3). Single-stranded oligomers BHI-Δ1-ISceI-NcoI P1 (5'-GATCTGGATCCACCGGTCGCAATTACCCTGTTATCCCTAC CATGGAGTAC-3') and BHI-Δ1-ISceI-NcoI P2 (5'-GTACTCCATGGTAGGGATAACAGGGTAATTGCGACCGGT GGATCCAGATC-3') were annealed and digested with BamHI and NcoI. This BamHI-NcoI fragment containing the I-SceI recognition site was ligated into the BamHI-NcoI digested SKRGFP, creating SKRGFP(Sac2H3)Δ1-S. The SacII-HindIII fragment of SKRGFP(Sac2H3)Δ1-S was subcloned back into the SacII-HindIII digested pCAGGS-NZE-GFP plasmid, to create pCAGGS-GFPΔ1-S. DNA was digested with SalI and PstI, and the 3433 bp fragment was provided to the Columbia University Transgenic Mouse facility (3). 2SGFP -- A PvuII site was engineered in pCAGGS-NZE-GFP using annealed single-stranded oligomers GFP-Pvu2-1 (5'-CGCCGACCACTACCAGCTGAACACCCCCATCGGCGAC-3') and GFP-Pvu2-2 (5'-GTCGCCGATGGGGGTGTTCAGCTGGTAGTGGTCGGCG-3 'and QuikChangeII Site-Directed Mutagenesis Kit (Stratagene), following manufacturer's protocol, creating pGFP-Pvu2. Single-stranded oligomers SCE1 (5'-Phos-ATTACCCTGTTATCCCTA)and SCE2 (5'-Phos-TAGGGATAACAGGGTAAT-3') were annealed and ligated into the PvuII blunt end digested pGFP-Pvu2, creating pGFP-Pvu2-S. DNA was digested with SalI and PstI, and the 3433 bp fragment was provided to the Columbia University Transgenic Mouse facility. The Columbia University Transgenic Mouse facility generated transgenic mice in F1 (C57BL/6J-CBA) hybrids, and mice were transferred to University of North Carolina at Charlotte.

The two GFP lines were intercrossed and the resulting line crossed with mice containing the tetracycline regulated I-SceI expression transgene. The resultant triply positive transgenic line was denoted "GS" and used for further study. Genotyping for presence of all three transgenes was performed by PCR and Southern blotting of mouse tail tip genomic DNA and subsequent digestion of PCR products with I-*Sce*I endonuclease (New England Biolabs) to confirm intact I-*Sce*I sites. Amplification was performed by 94°C 5 min; followed by 40 cycles of 94°C 30s, 60°C 30s, 72°C 2 min; and 72°C 15 min. For nested PCR 5uL of the first PCR product was used as template for second round of PCR following the same protocol. PCR primers for each: Sce1F 5'-gtccgaactctaaactgctga-3'; Sce2R 5'-ACCAGTATGCCAGAGACATC-3'; GFP 1F 5'-aaggccaagagggccaa-3'; GFP 2F 5'-TGGACGGCGACGTAAAC-3'; GFP 3R 5'-gtgctcaggtagtggttg-3'; GFP 4R 5-CTCTGTTCCACATACACTTC-3'; GFP 5F 5'-tgaaccgcatcgagctgag-3'; GFP 6R 5'-GACCATGTGATCGCGTTC-3'; GFP 7R 5'-TTCTGATAGGCAGCCTG-3'. Southern blotting to determine copy number utilized a plasmid fragment of full length GFP ORF of 3.07 kb and diluted to pg amounts that approximated 0.2, 1.0, 5.0, 10, 20, and 100 copies per genome spiked into 10µg non-transgenic mouse DNA. Genomic DNA of transgenic mice was digested with restriction endonucleases that flank the GFP promoter and ORF of both transgenes. The GFP probe fragment was an Sph-Not I fragment homologous to both transgenes. Q-PCR for copy number estimation utilized a GFP ORF fragment diluted to pg amounts that approximated 0.2, 1.0, 5.0, 10, 20, and 100 copies per genome to amplify a 296 bp fragment of GFP DNA. Genomic DNA isolated from transgenic mice was utilized for Q-PCR. Fluorescent detection of PCR products was reported using a SYBR® Green PCR kit (Quanti Tect) in 20µL reactions established according to the manufacturer's recommended protocol. A standard curve was generated (n=3) using the control plasmid GFP ORF DNA according to the manufacturer's protocol (QuantiTect). Q-PCR analysis was simultaneously analyzed by a 96 well 7500 Fast Real-Time PCR System (Applied Biosystems) in which transgenic mouse genomic DNA was compared against the standard curve and statistical analysis performed according to the Applied Biosystems protocol for 7500 Fast Real-Time PCR System protocol.

MEFs

Mouse embryonic fibroblasts were isolated from day E13.5 of GS mice and washed with phosphate buffered saline (PBS). The head was removed from isolated embryos and used for DNA genotyping. The body was minced well and 10mL of 0.25% Trypsin-EDTA (Gibco, Grand Island, NY) added. Solution was triturated with a pipette and added to 25 mL of medium [Dulbecco's Modified Eagle Medium (Gibco), 15% FBS (Gemini Bio-Products, West Sacramento, CA), 1.2% 200mM L-Glutamine (Gemini Bio-Products), 1.2% Non-essential Amino Acids (Gibco), and 1.2% Penicillin-Streptomycin (Gibco)]. Cells were then collected by centrifugation (1000 rpm x 10 min), resuspended into 4mL medium, and cultured on a 6-well dish at 37°C with 5%CO_2. MEFs were then passaged onto 10cm dishes after initial growth. Tetracycline HCl (Barr Laboratories) was dissolved in 1x PBS to 1mg/mL and passed through a 0.2 micron filter. MEFs were given a final concentration of 2µg/mL for up to 6 days.

DSB induction in Mice

Tetracycline HCl (Barr Laboratories) was dissolved into .5X PBS/H20/ sucrose at 10mg/mL and passed through a 0.2 micron filter. Mice were administered tetracycline at 2mg/mL in a water bottle for up to 21 days.

Flow cytometry and statistical analysis

MEFs were trypsinized and collected by centrifugation (1000 rpm x 10 min). Cells were resuspended in 1x PBS at a concentration of $1.0x10^6$ cells/mL. Sections of individual organs were harvested and a single cell suspension generated in 5% Bovine Serum Albumin (Gemini Bio-Products)/1x PBS. Suspensions were passed through a 53μM nylon mesh filter (Spectrum Laboratories Inc) and analyzed on a FACSAriaII for GFP positivity. To assess statistical significance of increased numbers of GFP+ cells among organs in tetracycline treated mice (Table S1), we utilized a non-parametric t-test for all mice versus negative controls (Figure 5), and then separately in the young and old cohorts versus negative controls (Figure 6). To assess statistical significance of the probabilities associated with covariance of the number of GFP+ cells in organs of individual mice, we calculated Spearman's nonparametric correlation coefficients for each pair of organs separately in the young and old cohorts, and utilized the false discovery rate procedure to control the proportion of false positive results (Table S2).

Western Immunoblot analysis

Protein was isolated from pelleted cells using Total Protein Extraction Kit (Millipore). Cell lysate proteins were then separated on a 10% NuPage Bis-Tris SDS-Page gel (Invitrogen) and transferred to Amersham Hybond-P membrane (GE Healthcare Life Sciences). The membranes were then blocked in 5% Non-Fat dry milk in 1X tris buffered saline (Bio-Rad). Membranes were probed with a mouse monoclonal IgG anti-HA antibody to detect the HA tag within I-*Sce*I (Cell Signaling Technology) at 1:100 dilutions for 20-22 hours at 4°C or a mouse monoclonal IgG anti-β-actin antibody (Santa Cruz Biotechnology) at 1:400 dilution for 1 hour at room temperature. Blots were subsequently exposed to an anti-mouse IgG HRP-linked secondary antibody (Cell Signaling Technology) at 1:1000 dilutions for 1 hour at room temperature. Blots were washed 3x for five minutes each in a 1x TBS-.05% Tween 20 solution. Membranes were developed using SuperSignal® West Pico Chemiluminescent Substrate (Thermo Scientific).

Bone Marrow-CFC Assay

GS mice (ages 3-5 months) were administered tetracycline through H_2O for 14d. Mice were then sacrificed, and femur bone marrow (BM) cells isolated and seeded into methylcellulose colony forming assays [69,70]. Whole BM was flushed from femurs into IMDM supplemented with 2% FBS and disrupted into a single cell suspension by a 22G needle and syringe. Cell viability counts were performed using .05% trypan blue staining. Total viable BM cells were plated at 1.0 x 10^5 cells per 35mm low adherence tissue culture dishes in hematopoietic differentiation medium (STEMCELL Technologies) containing IMDM, 1% methylcellulose, 15% non-ES qualified FBS, 100U/mL penicillin, 100μg/mL streptomycin, 2mM L-glutamine, 150μM monothioglycerol, 1% bovine serum albumin, 10μg/mL insulin, 200μg/mL transferrin, 150ng/mL mSCF, 30ng/ml mIL-3, 30ng/mL mIL-6, and 3U/ml hEPO for 14 days.

DNA Sequence Analysis of HR Recombinants from BM CFCs

Individual CFU-GEMM expressing GFP were identified by inverted fluorescent microscopy and isolated. Genomic DNA from 24 individual CFU-GEMMs was extracted from each with DNeasy Tissue Kit (Qiagen) followed by whole genome amplification (WGA) with Repli-G Kit (Qiagen) as previously described [68]. 1.0μg of WGA DNA template was used for PCR. Each 25μL PCR reaction contained template DNA, 10X reaction buffer, 1.5mM $MgCl_2$, 200μM each dNTP, 0.48μM each primer, 2.5 units Taq DNA polymerase. PCR primer sets are indicated in Figure 1 and in Methods above. Amplification was performed by 94°C 5 min; followed by 40 cycles of 94°C 30s, 55°C 30s, 72°C 2 min; and 72°C 15 min. For nested PCR 5uL of the first PCR product was used as template for second round of PCR following the same protocol. PCR reaction products were cloned with the TA cloning system (Invitrogen) and blue-white screening used to determine which individual clones to amplify, isolate DNA, and sequence by Sequetech (Mountain View, CA) using M13 forward and M13 reverse primers. Sequencing of up to 10 white colonies from each PCR reaction/TA cloning reaction was sufficient to identify GFP+ recombinants among parental GFP sequences.

Supporting Information

Table S1. Number of GFP+ cells detected per million analyzed by FACS in young and old cohorts. Individual mice are noted with young cohort mice indicated by Y and old cohort mice indicated by O. Organs from which technical error led to no sample recovered for FACS analysis are noted as nd (no data). These values were the basis for the covariance of traits analysis in Table S2.
(DOCX)

Table S2. Covariance of GFP+ cells in organs of young and old cohorts. To assess statistical significance of the probabilities associated with covariance, Spearman's nonparametric correlation coefficients for each pair of traits separately in the young and old cohorts (Table S1), and utilized the false discovery rate procedure to control the proportion of false positive results. Calculated p-values in the young mouse cohort are represented within the top diagonal half of the matrix. Calculated p-values in the old mouse cohort are represented within the bottom diagonal half of the matrix. p-values <0.05 are denoted with **.
(DOCX)

Acknowledgements

We thank Craig Strathdee for providing the bicistronic TET-ON vector backbone. We thank Dr. Larry Leamy for assistance with statistical analysis. We gratefully acknowledge Victor Lin and the Columbia University Transgenic Mouse facility for generation of the relevant transgenic mouse lines used in this study. We gratefully acknowledge Norman LeFebvre and the staff at the University of North Carolina at Charlotte vivarium facility for assistance with animal husbandry.

Author Contributions

Conceived and designed the experiments: RRW PS CR. Performed the experiments: RRW PS CGV GB NC CR. Analyzed the data: RRW CGV GB NC CR. Contributed reagents/materials/analysis tools: PS CR. Wrote the manuscript: RRW PS CGV CR.

References

1. van Gent DC, Hoeijmakers JH, Kanaar R (2001) Chromosomal stability and the DNA double-stranded break connection. Nat Rev Genet 2: 196-206. doi:10.1038/35056049. PubMed: 11256071.
2. Pandita TK, Richardson C (2009) Chromatin remodeling finds its place in the DNA double-strand break response. Nucleic Acids Res 37: 1363-1377. doi:10.1093/nar/gkn1071. PubMed: 19139074.
3. Lieber MR (1992) The mechanism of V(D)J recombination: a balance of diversity, specificity, and stability. Cell 70: 873-876. doi: 10.1016/0092-8674(92)90237-7. PubMed: 1525825.
4. Lieber MR, Yu K, Raghavan SC (2006) Roles of nonhomologous DNA end joining, V(D)J recombination, and class switch recombination in chromosomal translocations. DNA Repair (Amst) 5: 1234-1245. doi: 10.1016/j.dnarep.2006.05.013. PubMed: 16793349.
5. Ames BN, Shigenaga MK, Hagen TM (1993) Oxidants, antioxidants, and the degenerative diseases of aging. Proc Natl Acad Sci U S A 90: 7915-7922. doi:10.1073/pnas.90.17.7915. PubMed: 8367443.
6. Beckman KB, Ames BN (1997) Oxidative decay of DNA. J Biol Chem 272: 19633-19636. doi:10.1074/jbc.272.32.19633. PubMed: 9289489.
7. Waris G, Ahsan H (2006) Reactive oxygen species: role in the development of cancer and various chronic conditions. J Carcinog 5: 14. doi:10.1186/1477-3163-5-14. PubMed: 16689993.
8. Haber JE (1999) DNA recombination: the replication connection. Trends Biochem Sci 24: 271-275. doi:10.1016/S0968-0004(99)01413-9. PubMed: 10390616.
9. Vilenchik MM, Knudson AG (2003) Endogenous DNA double-strand breaks: production, fidelity of repair, and induction of cancer. Proc Natl Acad Sci U S A 100: 12871-12876. doi:10.1073/pnas.2135498100. PubMed: 14566050.
10. Li W, Li F, Huang Q, Shen J, Wolf F et al. (2011) Quantitative, noninvasive imaging of radiation-induced DNA double-strand breaks *in vivo*. Cancer Res 71: 4130-4137. doi: 10.1158/0008-5472.CAN-10-2540. PubMed: 21527553.
11. Gatto B, Capranico G, Palumbo M (1999) Drugs acting on DNA topoisomerases: recent advances and future perspectives. Curr Pharm Des 5: 195-215. PubMed: 10066890.
12. Osheroff N, Corbett AH, Robinson MJ (1994) Mechanism of action of topoisomerase II-targeted antineoplastic drugs. Adv Pharmacol 29B: 105-126. PubMed: 8996604.
13. Sung PA, Libura J, Richardson C (2006) Etoposide and illegitimate DNA double-strand break repair in the generation of *MLL* translocations: New insights and new questions. DNA Repair (Amst) 5: 1109-1118. doi:10.1016/j.dnarep.2006.05.018. PubMed: 16809075.
14. Ward JF (1988) DNA damage produced by ionizing radiation in mammalian cells: identities, mechanisms of formation, and reparability. Prog Nucleic Acid Res Mol Biol 35: 95-125. doi:10.1016/S0079-6603(08)60611-X. PubMed: 3065826.
15. Bandele OJ, Osheroff N (2007) Bioflavonoids as poisons of human topoisomerase IIα and IIβ. Biochemistry 46: 6097-6108. doi:10.1021/bi7000664. PubMed: 17458941.
16. van Waalwijk van Doorn-Khosrovani Barjesteh, S, Janssen J, Maas LM, Godschalk RW, Nijhuis JG et al. (2007) Dietary flavonoids induce *MLL* translocations in primary human CD34+ cells. Carcinogenesis 28: 1703-1709. doi:10.1093/carcin/bgm102. PubMed: 17468513.
17. Ross JA, Potter JD, Reaman GH, Pendergrass TW, Robison LL (1996) Maternal exposure to potential inhibitors of DNA topoisomerase II and infant leukemia (United States): a report from the Children's Cancer Group. Cancer Causes Control 7: 581-590. doi:10.1007/BF00051700. PubMed: 8932918.
18. Strick R, Strissel PL, Borgers S, Smith SL, Rowley JD (2000) Dietary bioflavonoids induce cleavage in the *MLL* gene and may contribute to infant leukemia. Proc Natl Acad Sci U S A 97: 4790-4795. doi:10.1073/pnas.070061297. PubMed: 10758153.
19. Liang F, Han M, Romanienko PJ, Jasin M (1998) Homology-directed repair is a major double-strand break repair pathway in mammalian cells. Proc Natl Acad Sci U S A 95: 5172-5177. doi:10.1073/pnas.95.9.5172. PubMed: 9560248.
20. Richardson C, Moynahan ME, Jasin M (1998) Double-strand break repair by interchromosomal recombination: suppression of chromosomal translocations. Genes Dev 12: 3831-3842. doi:10.1101/gad.12.24.3831. PubMed: 9869637.
21. Weinstock DM, Richardson CA, Elliott B, Jasin M (2006) Modeling oncogenic translocations: distinct roles for double-strand break repair pathways in translocation formation in mammalian cells. DNA Repair (Amst) 5: 1065-1074. doi:10.1016/j.dnarep.2006.05.028. PubMed: 16815104.
22. Clejan I, Boerckel J, Ahmed S (2006) Developmental modulation of nonhomologous end joining in *Caenorhabditis elegans*. Genetics 173: 1301-1317. doi:10.1534/genetics.106.058628. PubMed: 16702421.
23. Saleh-Gohari N, Helleday T (2004) Conservative homologous recombination preferentially repairs DNA double-strand breaks in the S phase of the cell cycle in human cells. Nucleic Acids Res 32: 3683-3688. doi:10.1093/nar/gkh703. PubMed: 15252152.
24. Takata M, Sasaki MS, Sonoda E, Morrison C, Hashimoto M et al. (1998) Homologous recombination and non-homologous end-joining pathways of DNA double-strand break repair have overlapping roles in the maintenance of chromosomal integrity in vertebrate cells. EMBO J 17: 5497-5508. doi:10.1093/emboj/17.18.5497. PubMed: 9736627.
25. Johnson RD, Jasin M (2000) Sister chromatid gene conversion is a prominent double-strand break repair pathway in mammalian cells. EMBO J 19: 3398-3407. doi:10.1093/emboj/19.13.3398. PubMed: 10880452.
26. Kadyk LC, Hartwell LH (1992) Sister chromatids are preferred over homologs as substrates for recombinational repair in *Saccharomyces cerevisiae*. Genetics 132: 387-402. PubMed: 1427035.
27. Brown AD, Claybon AB, Bishop AJ (2011) A conditional mouse model for measuring the frequency of homologous recombination events *in vivo* in the absence of essential genes. Mol Cell Biol 31: 3593-3602. doi:10.1128/MCB.00848-10. PubMed: 21709021.
28. Pontier DB, Tijsterman M (2009) A robust network of double-strand break repair pathways governs genome integrity during *C. elegans* development. Curr Biol 19: 1384-1388. doi:10.1016/j.cub.2009.06.045. PubMed: 19646877.
29. Wehrkamp-Richter S, Degroote F, Laffaire JB, Paul W, Perez P et al. (2009) Characterisation of a new reporter system allowing high throughput in planta screening for recombination events before and after controlled DNA double strand break induction. Plant Physiol Biochem 47: 248-255. doi:10.1016/j.plaphy.2008.11.014. PubMed: 19136269.
30. Wiktor-Brown DM, Hendricks CA, Olipitz W, Engelward BP (2006) Age-dependent accumulation of recombinant cells in the mouse pancreas revealed by *in situ* fluorescence imaging. Proc Natl Acad Sci U S A 103: 11862-11867. doi:10.1073/pnas.0604943103. PubMed: 16882718.
31. Moynahan ME, Jasin M (1997) Loss of heterozygosity induced by a chromosomal double-strand break. Proc Natl Acad Sci U S A 94: 8988-8993. doi:10.1073/pnas.94.17.8988. PubMed: 9256422.
32. Stark JM, Jasin M (2003) Extensive loss of heterozygosity is suppressed during homologous repair of chromosomal breaks. Mol Cell Biol 23: 733-743. doi:10.1128/MCB.23.2.733-743.2003. PubMed: 12509470.
33. Rong YS, Golic KG (2003) The homologous chromosome is an effective template for the repair of mitotic DNA double-strand breaks in *Drosophila*. Genetics 165: 1831-1842. PubMed: 14704169.
34. Haber JE, Leung WY (1996) Lack of chromosome territoriality in yeat: promiscuous rejoining of broken chromosome ends. Proc Natl Acad Sci U S A 93: 13949-13954. doi:10.1073/pnas.93.24.13949. PubMed: 8943041.
35. Pacher M, Schmidt-Puchta W, Puchta H (2007) Two unlinked double-strand breaks can induce reciprocal exchanges in plant genomes via homologous recombination and nonhomologous end joining. Genetics 175: 21-29. PubMed: 17057227.
36. Elliott B, Richardson C, Jasin M (2005) Chromosomal translocation mechanisms at intronic alu elements in mammalian cells. Mol Cell 17: 885-894. doi:10.1016/j.molcel.2005.02.028. PubMed: 15780943.
37. Richardson C, Jasin M (2000) Frequent chromosomal translocations induced by DNA double-strand breaks. Nature 405: 697-700. doi: 10.1038/35015097. PubMed: 10864328.
38. Richardson C, Jasin M (2000) Recombination between two chromosomes: implications for genomic integrity in mammalian cells.

Cold Spring Harb Symp Quant Biol 65: 553-560. doi:10.1101/sqb.2000.65.553. PubMed: 12760073.
39. Cheng Y, Zhang Z, Keenan B, Roschke AV, Nakahara K et al. (2010) Efficient repair of DNA double-strand breaks in malignant cells with structural instability. Mutat Res 683: 115-122. doi:10.1016/j.mrfmmm.2009.10.016. PubMed: 19909760.
40. Blanc G, Barakat A, Guyot R, Cooke R, Delseny M (2000) Extensive duplication and reshuffling in the *Arabidopsis* genome. Plant Cell 12: 1093-1101. doi:10.2307/3871257. PubMed: 10899976.
41. Udall JA, Quijada PA, Osborn TC (2005) Detection of chromosomal rearrangements derived from homologous recombination in four mapping populations of *Brassica napus* L. Genetics 169: 967-979. doi:10.1534/genetics.104.033209. PubMed: 15520255.
42. Schmid CW (1996) Alu: Structure, origin, evolution, significance, and function of one-tenth of human. DNA - Prog Nucleic Acid Res Mol Biol 53: 283-319. doi:10.1016/S0079-6603(08)60148-8.
43. Witherspoon DJ, Watkins WS, Zhang Y, Xing J, Tolpinrud WL et al. (2009) Alu repeats increase local recombination rates. BMC Genomics 10: 530. doi:10.1186/1471-2164-10-530. PubMed: 19917129.
44. Cooper DN, Krawczak M, Antonarkis SE (1998) The nature and mechanisms of human gene mutation. In: B VogelsteinKW Kinsler. The genetic basis of human cancer. New York: McGraw-Hill. pp. 65-94.
45. Hwu HR, Roberts JW, Davidson EH, Britten RJ (1986) Insertion and/or deletion of many repeated DNA sequences in human and higher ape evolution. Proc Natl Acad Sci U S A 83: 3875-3879. doi:10.1073/pnas.83.11.3875. PubMed: 3012536.
46. Nyström-Lahti M, Kristo P, Nicolaides NC, Chang SY, Aaltonen LA et al. (1995) Founding mutations and Alu-mediated recombination in hereditary colon cancer. Nat Med 1: 1203-1206. doi:10.1038/nm1195-1203. PubMed: 7584997.
47. Rüdiger NS, Gregersen N, Kielland-Brandt MC (1995) One short well conserved region of Alu-sequences is involved in human gene rearrangements and has homology with prokaryotic chi. Nucleic Acids Res 23: 256-260. doi:10.1093/nar/23.2.256. PubMed: 7862530.
48. Small K, Iber J, Warren ST (1997) Emerin deletion reveals a common X-chromosome inversion mediated by inverted repeats. Nat Genet 16: 96-99. doi:10.1038/ng0597-96. PubMed: 9140403.
49. Small K, Wagener M, Warren ST (1997) Isolation and characterization of the complete mouse emerin gene. Mamm Genome 8: 337-341. doi:10.1007/s003359900435. PubMed: 9107678.
50. Kolomietz E, Meyn MS, Pandita A, Squire JA (2002) The role of Alu repeat clusters as mediators of recurrent chromosomal aberrations in tumors. Genes Chromosomes Cancer 35: 97-112. doi:10.1002/gcc.10111. PubMed: 12203773.
51. Reichel M, Gillert E, Nilson I, Siegler G, Greil J et al. (1998) Fine structure of translocations breakpoints in leukemic blasts with chromosomal translocation t(4;11): the DNA damage-repair model of translocation. Oncogene 17: 3035-3044. doi:10.1038/sj.onc.1202229. PubMed: 9881706.
52. Elliott B, Jasin M (2002) Double-strand breaks and translocations in cancer. Cell Mol Life Sci 59: 373-385. doi:10.1007/s00018-002-8429-3. PubMed: 11915950.
53. Lovett BD, Lo Nigro L, Rappaport EF, Blair IA, Osheroff N et al. (2001) Near-precise interchromosomal recombination and functional DNA topoisomerase II cleavage sites at *MLL* and *AF-4* genomic breakpoints in treatment-related acute lymphoblastic leukemia with t(4;11) translocation. Proc Natl Acad Sci U S A 98: 9802-9807. doi:10.1073/pnas.171309898. PubMed: 11493704.
54. Rowley JD (1999) The role of chromosome translocations in leukemogenesis. Semin Hematol 36: 59-72. PubMed: 10595755.
55. Scandura JM, Boccuni P, Cammenga J, Nimer SD (2002) Transcription factor fusions in acute leukemia: variations on a theme. Oncogene 21: 3422-3444. doi:10.1038/sj.onc.1205315. PubMed: 12032780.
56. Tycko B, Sklar J (1990) Chromosomal translocations in lymphoid neoplasia: a reappraisal of the recombinase model. Cancer Cells 2: 1-8. PubMed: 2201335.
57. Saintigny Y, Delacôte F, Boucher D, Averbeck D, Lopez BS (2007) XRCC4 in G1 suppresses homologous recombination in S/G^2, in G1 checkpoint-defective cells. Oncogene 26: 2769-2780. doi:10.1038/sj.onc.1210075. PubMed: 17057732.
58. Delacôte F, Lopez BS (2008) Importance of the cell cycle phase for the choice of the appropriate DSB repair pathway, for genome stability maintenance: the trans-S double-strand break repair model. Cell Cycle 7: 33-38. doi:10.4161/cc.7.1.5149. PubMed: 18196958.
59. Rothkamm K, Krüger I, Thompson LH, Löbrich M (2003) Pathways of DNA double-strand break repair during the mammalian cell cycle. Mol Cell Biol 23: 5706-5715. doi:10.1128/MCB.23.16.5706-5715.2003. PubMed: 12897142.
60. Hartlerode A, Odate S, Shim I, Brown J, Scully R (2011) Cell cycle-dependent induction of homologous recombination by a tightly regulated I-SceI fusion protein. PLOS ONE 6: e16501. doi:10.1371/journal.pone.0016501. PubMed: 21408059.
61. Dollé ME, Snyder WK, Gossen JA, Lohman PH, Vijg J (2000) Distinct spectra of somatic mutations accumulated with age in mouse heart and small intestine. Proc Natl Acad Sci U S A 97: 8403-8408. doi:10.1073/pnas.97.15.8403. PubMed: 10900004.
62. Ono T, Uehara Y, Saito Y, Ikehata H (2002) Mutation theory of aging, assessed in transgenic mice and knockout mice. Mech Ageing Dev 123: 1543-1552. doi:10.1016/S0047-6374(02)00090-8. PubMed: 12470892.
63. Choulika A, Perrin A, Dujon B, Nicolas J-F (1995) Induction of homologous recombination in mammalian chromosomes by using the I-SceI system of *Saccharomyces cerevisiae*. Mol Cell Biol 15: 1963-1973. PubMed: 7891691.
64. Rouet P, Smih F, Jasin M (1994) Introduction of double-strand breaks into the genome of mouse cells by expression of a rare-cutting endonuclease. Mol Cell Biol 14: 8096-8106. PubMed: 7969147.
65. Strathdee CA, McLeod MR, Hall JR (1999) Efficient control of tetracycline-responsive gene expression from an autoregulated bi-directional expression vector. Gene 229: 21-29. doi:10.1016/S0378-1119(99)00045-1. PubMed: 10095100.
66. Rouet P, Smih F, Jasin M (1994) Expression of a site-specific endonuclease stimulates homologous recombination in mammalian cells. Proc Natl Acad Sci U S A 91: 6064-6068. doi:10.1073/pnas.91.13.6064. PubMed: 8016116.
67. Hadjantonakis AK, Gertsenstein M, Ikawa M, Okabe M, Nagy A (1998) Generating green fluorescent mice by germline transmission of green fluorescent ES cells. Mech Dev 76: 79-90. doi:10.1016/S0925-4773(98)00093-8. PubMed: 9867352.
68. Francis R, Richardson C (2007) Multipotent hematopoietic cells susceptible to alternative double-strand break repair pathways that promote genome rearrangements. Genes Dev 21: 1064-1074. doi:10.1101/gad.1522807. PubMed: 17473170.
69. Humphries RK, Eaves AC, Eaves CJ (1981) Self-renewal of hemopoietic stem cells during mixed colony formation *in vitro*. Proc Natl Acad Sci U S A 78: 3629-3633. doi:10.1073/pnas.78.6.3629. PubMed: 6943564.
70. Rosenberg N, Baltimore D (1976) A quantitative assay for transformation of bone marrow cells by Abelson murine leukemia virus. J Exp Med 143: 1453-1463. doi:10.1084/jem.143.6.1453. PubMed: 178822.
71. Puchta H (1999) Double-strand break-induced recombination between ectopic homologous sequences in somatic plant cells. Genetics 152: 1173-1181. PubMed: 10388832.
72. Shalev G, Levy AA (1997) The maize transposable element *Ac* induces recombination between the donor site and an homologous ectopic sequence. Genetics 146: 1143-1151
73. Hendricks CA, Almeida KH, Stitt MS, Jonnalagadda VS, Rugo RE et al. (2003) Spontaneous mitotic homologous recombination at an enhanced yellow fluorescent protein (EYFP) cDNA direct repeat in transgenic mice. Proc Natl Acad Sci U S A 100: 6325-6330. doi:10.1073/pnas.1232231100. PubMed: 12750464.
74. Hendricks CA, Engelward BP (2004) "Recombomice": the past, present, and future of recombination-detection in mice. DNA Repair (Amst) 3: 1255-1261. doi:10.1016/j.dnarep.2004.04.006.
75. Kovalchuk O, Hendricks CA, Cassie S, Engelward AJ, Engelward BP (2004) *In vivo* recombination after chronic damage exposure falls to below spontaneous levels in "recombomice". Mol Cancer Res 2: 567-573. PubMed: 15498931.
76. Wiktor-Brown DM, Hendricks CA, Olipitz W, Rogers AB, Engelward BP (2006) Applications of fluorescence for detecting rare sequence rearrangements *in vivo*. Cell Cycle 5: 2715-2719. doi:10.4161/cc.5.23.3527. PubMed: 17172860.
77. Misteli T (2009) Self-organization in the genome. Proc Natl Acad Sci U S A 106: 6885-6886. doi:10.1073/pnas.0902010106. PubMed: 19416923.
78. Cremer T, Cremer C (2001) Chromosome territories, nuclear architecture and gene regulation in mammalian cells. Nat Rev Genet 2: 292-301. doi:10.1038/35066075. PubMed: 11283701.
79. Soutoglou E, Dorn JF, Sengupta K, Jasin M, Nussenzweig A et al. (2007) Positional stability of single double-strand breaks in mammalian cells. Nat Cell Biol 9: 675-682. doi:10.1038/ncb1591. PubMed: 17486118.
80. Nelms BE, Maser RS, MacKay JF, Lagally MG, Petrini JH (1998) *In situ* visualization of DNA double-strand break repair in human fibroblasts. Science 280: 590-592. doi:10.1126/science.280.5363.590. PubMed: 9554850.

81. Varga T, Aplan PD (2005) Chromosomal aberrations induced by double strand DNA breaks. DNA Repair (Amst) 4: 1038-1046. doi:10.1016/j.dnarep.2005.05.004. PubMed: 15935739.
82. Boubakour-Azzouz I, Ricchetti M (2008) Low joining efficiency and non-conservative repair of two distant double-strand breaks in mouse embryonic stem cells. DNA Repair (Amst) 7: 149-161. doi:10.1016/j.dnarep.2007.09.005. PubMed: 17964863.
83. Honma M, Sakuraba M, Koizumi T, Takashima Y, Sakamoto H, Hayashi M (2007) Non-homologous end-joining for repairing I-SceI-induced DNA double strand breaks in human cells. DNA Repair (Amst) 6: 781-788. doi:10.1016/j.dnarep.2007.01.004. PubMed: 17296333.
84. Lisby M, Mortensen UH, Rothstein R (2003) Colocalization of multiple DNA double-strand breaks at a single Rad52 repair centre. Nat Cell Biol 5: 572-577. doi:10.1038/ncb997. PubMed: 12766777.
85. Scully R, Chen J, Plug A, Xiao Y, Weaver D et al. (1997) Association of BRCA1 with Rad51 in mitotic and meiotic cells. Cell 88: 265-275. doi:10.1016/S0092-8674(00)81847-4. PubMed: 9008167.
86. Costes SV, Ponomarev A, Chen JL, Nguyen D, Cucinotta FA et al. (2007) Image-based modeling reveals dynamic redistribution of DNA damage into nuclear sub-domains. PLoS Comput Biol 3: e155. doi:10.1371/journal.pcbi.0030155. PubMed: 17676951.
87. Rubtsov MA, Terekhov SM, Razin SV, Iarovaia OV (2008) Repositioning of ETO gene in cells treated with VP-16, an inhibitor of DNA-topoisomerase II. J Cell Biochem 104: 692-699. doi:10.1002/jcb.21656. PubMed: 18183572.
88. Neumaier T, Swenson J, Pham C, Polyzos A, Lo AT et al. (2012) Evidence for formation of DNA repair centers and dose-response nonlinearity in human cells. Proc Natl Acad Sci U S A 109: 443-448. doi:10.1073/pnas.1117849108. PubMed: 22184222.
89. Kantidze OL, Razin SV (2009) Chromatin loops, illegitimate recombination, and genome evolution. Bioessays 31: 278-286. doi:10.1002/bies.200800165. PubMed: 19260023.
90. Meaburn KJ, Misteli T, Soutoglou E (2007) Spatial genome organization in the formation of chromosomal translocations. Semin Cancer Biol 17: 80-90. doi:10.1016/j.semcancer.2006.10.008. PubMed: 17137790.
91. Celsing F, Widell S, Merk K, Bernell P, Grimfors G et al. (1998) Addition of etoposide to CHOP chemotherapy in untreated patients with high-grade non-Hodgkin's lymphoma. Ann Oncol 9: 1213-1217. doi:10.1023/A:1008446430765. PubMed: 9862052.
92. Kollmannsberger C, Beyer J, Droz JP, Harstrick A, Hartmann JT et al. (1998) Secondary leukemia following high cumulative doses of etoposide in patients treated for advanced germ cell tumors. J Clin Oncol 16: 3386-3391. PubMed: 9779717.
93. Lightfoot TJ, Roman E (2004) Causes of childhood leukaemia and lymphoma. Toxicol Appl Pharmacol 199: 104-117. doi:10.1016/j.taap.2003.12.032. PubMed: 15313583.
94. Har-Vardi I, Mali R, Breietman M, Sonin Y, Albotiano S et al. (2007) DNA topoisomerases I and II in human mature sperm cells: characterization and unique properties. Hum Reprod 22: 2183-2189. doi:10.1093/humrep/dem170. PubMed: 17656417.
95. Ashley T, Gaeth AP, Inagaki H, Seftel A, Cohen MM et al. (2006) Meiotic recombination and spatial proximity in the etiology of the recurrent t(11;22). Am J Hum Genet 79: 524-538. doi:10.1086/507652. PubMed: 16909390.
96. Derijck A, van der Heijden G, Giele M, Philippens M, de Boer P (2008) DNA double-strand break repair in parental chromatin of mouse zygotes, the first cell cycle as an origin of *de novo* mutation. Hum Mol Genet 17: 1922-1937. doi:10.1093/hmg/ddn090. PubMed: 18353795.